



UNIVERSIDAD  
DE BURGOS



ICCRAM  
INTERNATIONAL RESEARCH CENTER IN CRITICAL RAW  
MATERIALS FOR ADVANCED INDUSTRIAL TECHNOLOGIES

Programa de Doctorado en Química Avanzada  
Universidad de Burgos

Doctoral Thesis

# **New Battery Technology Concepts Based on Semi-Solid Electrodes**

**Daniel Pérez Antolín**

Director: **Edgar Ventosa Arbáizar**

**Universidad de Burgos**

**2022**





FACULTAD DE CIENCIAS - DEPARTAMENTO DE QUÍMICA

Dr. EDGAR VENTOSA ARBAIZAR, Professor at the Analytical Chemistry Department of the University of Burgos,

HEREBY CERTIFIES:

That the research work included in the dissertation: “New Battery Technology Concepts Based on Semi-Solid Electrodes” performed by Mr. Daniel Pérez Antolín, in order to apply for the degree of Doctor of Philosophy (PhD) in Chemistry by the University of Burgos,

I give my approval for its submission to be defended as a PhD Thesis.

Burgos, 18th April 2022

Signed. Edgar Ventosa Arbáizar



## Acknowledgements

At this point, close to the end of the PhD it is time to thank all the people who have helped and supported me throughout this intense period of my life. Since this is something personal, let me continue in my native language.

En primer lugar, quiero agradecer a la Unidad de Procesos Electroquímicos de IMDEA Energía, concretamente al Dr. Jesús Palma y al Dr. Edgar Ventosa, por haberme brindado la oportunidad de comenzar esta tesis en 2018 y por haber confiado en mí. En especial a mi director de tesis, el Dr. Edgar Ventosa, que no solo ha sido mi referente y guía durante todo este tiempo, sino que me ha apoyado y ayudado en todo, tanto profesional como personalmente. Este trabajo no habría llegado a su fin si no fuera gracias a él, a su trabajo, a su esfuerzo y, sobre todo, a su paciencia.

Gracias también al resto de compañeros de la Unidad - investigadores postdoctorales, titulares y senior - por todo lo aprendido allí en el ámbito laboral, pero, también en el personal. Principalmente, agradecer a mi primera “familia científica” el haberme ayudado y, sobre todo, aguantado: Dr. Jaime S. Sánchez, Dr. David Muñoz-Torrero, Nacho, Bea, Carlos y Antonio. En especial, dar las gracias a Diana y a Mayte por las horas de charla tanto dentro como fuera del trabajo, por su alegría, por su paciencia y, en particular, porque he sentido siempre su apoyo incondicional. Por último, gracias al resto de Unidades de IMDEA por haber estado a mi lado en el día a día, por vuestra ayuda y por vuestro apoyo.

Por otro lado, me gustaría agradecer también a mi segunda “familia científica” de la Universidad de Burgos. Gracias al Departamento de Química Analítica por haberme acogido, en especial al Dr. Álvaro Colina y a la Dra. Aránzazu Heras por el apoyo que he recibido. Además, gracias al resto del Departamento, especialmente a Sheila, Fabiola,

Martín, Paula, Alba y Lara, por hacer amena mi etapa final de la tesis, tanto dentro de la Universidad como fuera de ella.

No puedo pasar por alto a mis amigos, mis "*Queridas*", que, aunque no han formado parte de mi día a día dentro de un laboratorio, han sido igual de imprescindibles para que este trabajo llegara a buen puerto. Gracias por estar a mi lado siempre. Mario y Nuria, gracias por haberme acompañado y apoyado siempre en toda mi etapa académica. Miriam y Bubu, que también habéis estado encima de mi todo este tiempo, gracias. Finalmente, me gustaría extender este agradecimiento al resto de amigos que han estado junto a mí en algún momento de la tesis.

Por último, pero no menos importante, gracias a mis padres, Miguel Ángel y María, y a mis hermanos, Miguel, Miriam, Raquel y Marcos, por haberme soportado no solo en el periodo de la tesis, sino durante toda mi vida, tanto en los buenos como en los malos momentos.

# Table of Content

<b>Abstract</b>	<b><i>i</i></b>
<b>Chapter 1. Introduction</b>	<b>1</b>
<b>1.1 Present Energy System</b>	<b>2</b>
<b>1.2 Energy Storage: Technologies and Applications</b>	<b>3</b>
1.2.1 Mechanical Energy Storage	4
1.2.2 Thermal Energy Storage (TES)	5
1.2.3 Chemical Energy Storage	5
1.2.4 Electrical Energy Storage	5
1.2.5 Electrochemical Energy Storage	6
<b>1.3 Batteries</b>	<b>8</b>
1.3.1 Primary Batteries	9
1.3.2 Secondary Batteries	10
1.3.3 Historical Development of Batteries	10
<b>1.4 Limitations in Batteries</b>	<b>15</b>
<b>1.5 Emerging Technologies</b>	<b>20</b>
1.5.1 Static Batteries	20
1.5.2 Redox Flow Batteries	23
<b>1.6 Semi-Solid Electrodes</b>	<b>26</b>
1.6.1 Areal Capacity and Cost	27
1.6.2 Limitation of conventional electrodes.	27
1.6.3 Tortuosity, Kinetics and Electrochemical Performance	29
<b>1.7 References</b>	<b>32</b>
<b>Chapter 2. Objectives</b>	<b>41</b>
<b>Chapter 3. Semi-Solid Electrodes for Static Batteries</b>	<b>47</b>
<b>3.1 Introduction</b>	<b>48</b>
<b>3.2 Experimental Procedures</b>	<b>50</b>
3.2.1 Reagents and Materials	50
3.2.2 Rheological Measurements	50
3.2.3 Electrochemical Measurements	50

<b>3.3</b>	<b>Results and Discussion</b>	<b>51</b>
3.3.1	Rheology of Semi-solid Electrodes	51
3.3.2	Electrochemical Cell for Assessment of Electrical and Ionic Properties	52
3.3.3	Electrochemical Impedance Spectroscopy (EIS)	54
3.3.4	Resistance Semi-solid Electrodes	58
<b>3.4</b>	<b>Conclusions</b>	<b>64</b>
<b>3.5</b>	<b>References</b>	<b>65</b>

***Chapter 4. The Injectable Battery. A Conceptually New Strategy in Pursue of a Sustainable and Circular Battery Model*** \_\_\_\_\_ **67**

<b>4.1</b>	<b>Introduction</b>	<b>69</b>
<b>4.2</b>	<b>Experimental Procedures</b>	<b>72</b>
4.2.1	Reagents and materials	72
4.2.2	Preparation of semi-solid electrodes and configuration of battery cell	72
4.2.3	Electrochemical measurements	74
<b>4.3</b>	<b>Results and Discussion</b>	<b>75</b>
4.3.1	The concept of injectable battery	75
4.3.2	Proof of concept for aqueous injectable batteries.	76
4.3.3	Theoretical calculations on the battery cost and energy density	87
4.3.4	Proof of plausibility for non-aqueous battery chemistries	94
<b>4.4</b>	<b>Conclusions</b>	<b>99</b>
<b>4.5</b>	<b>References</b>	<b>100</b>

***Chapter 5. Implementation of Injectable Semi-Solid Electrode for an Ultra-Low-Cost Aqueous Battery Chemistry: The Injectable Zn – MnO<sub>2</sub> battery*** \_\_\_\_\_ **105**

<b>5.1</b>	<b>Introduction</b>	<b>107</b>
<b>5.2</b>	<b>Experimental Procedures</b>	<b>110</b>
5.2.1	Reagents and Materials	110
5.2.2	Preparation of electrodes	110
5.2.3	Electrochemical Measurements	111
<b>5.3</b>	<b>Results and Discussion</b>	<b>112</b>
5.3.1	Semi-solid electrodes in Zn – MnO <sub>2</sub> battery	112
5.3.2	Electrolyte pH in Zn – MnO <sub>2</sub> battery	117
<b>5.4</b>	<b>Conclusions</b>	<b>131</b>

5.5	References	133
-----	------------	-----

## **Chapter 6. Semi-Flowable Zn Semi-Solid Electrodes as Renewable Energy Carrier for**

### **Refillable Zn – Air Batteries** 137

6.1	Introduction	139
-----	--------------	-----

6.2	Experimental Procedures	143
-----	-------------------------	-----

6.2.1	Reagents and materials	143
-------	------------------------	-----

6.2.2	Preparation of semi-solid electrodes	143
-------	--------------------------------------	-----

6.2.3	Materials and fabrication of refillable cells	143
-------	---	-----

6.2.4	Electrochemical measurements	144
-------	------------------------------	-----

6.3	Results and Discussion	145
-----	------------------------	-----

6.3.1	Proof-of-concept for the mechanically rechargeable Zn-Air battery based on Zn semi-solid electrodes	145
-------	---	-----

6.3.2	Tuning of energy density by changing the Zn content in the semi-solid electrode	149
-------	---	-----

6.3.3	Exploring the limits of energy density by X-ray tomography	152
-------	--	-----

6.3.4	Tuning of specific power by changing the content of carbon in semi-solid electrodes	154
-------	---	-----

6.3.5	Boosting the specific power by implementing redox mediators	159
-------	---	-----

6.3.6	Projected specific energy and energy density of mechanically rechargeable Zn-Air batteries based on semi-solid electrodes	161
-------	---	-----

6.3.7	Zn semi-solid electrodes as potential energy vector	163
-------	---	-----

6.4	Conclusions	165
-----	-------------	-----

6.5	References	166
-----	------------	-----

## **Chapter 7. Regenerative Electrochemical Ion Pumping Cell Based on Semi-Solid**

### **Electrodes for Sustainable Li Recovery** 171

7.1	Introduction	173
-----	--------------	-----

7.2	Experimental Procedures	176
-----	-------------------------	-----

7.2.1	Reagents and materials	176
-------	------------------------	-----

7.2.2	Preparation of semi-solid electrodes	177
-------	--------------------------------------	-----

7.2.3	Electrochemical cell	177
-------	----------------------	-----

7.2.4	Electrochemical measurements	180
-------	------------------------------	-----

7.2.5	Figures of merit	181
-------	------------------	-----

7.3	Results and Discussion	183
-----	------------------------	-----

7.3.1	The concept of Regenerative Electrochemical Ion Pumping Cell (REIPC)	183
-------	--	-----

7.3.2	Membrane-Containing Regenerative Electrochemical Ion Pumping Cell (MC-REIPC)	187
-------	--	-----

7.3.3	Membrane-Free Regenerative Electrochemical Ion Pumping Cell (MF-REIPC)	199
7.4	Conclusions	208
7.5	References	209
<b>Chapter 8. Final Conclusions and Future Challenges</b>		<b>213</b>
8.1	Final conclusions	214
8.2	Future challenges	216
<b>Appendix A. Scientific Contributions</b>		<b>217</b>
<b>Appendix B. List of Figures and Tables</b>		<b>221</b>
<b>Appendix C. Acronyms</b>		<b>231</b>

## Abstract

Energy Storage Systems have become essential element in our modern society as power source for number for applications ranging from power electronics to buffering energy for implementing energy generated from intermittent renewable sources. Among the various energy storage systems, batteries are attracting increasing attention since they offer a good compromise of energy efficiency, energy density and cost. Thus, a variety of battery technologies have been developed over the last decades with the aim of improving their key performance indicators (KPIs). Despite the great efforts devoted to this field, many challenges remain in terms of sustainability, energy and power density, eco-friendliness, recyclability, etc.

The overall aim of this Thesis is to develop innovative battery solutions based on semi-solid electrodes and demonstrate their feasibility in different applications. In particular, the unique properties of semi-solid electrodes are exploited in various technologies, i.e. lithium-ion batteries, zinc – manganese dioxide batteries, zinc – air batteries and electrochemical ion pumping system. These properties are easily tunable by changing the formulation of different semi-solid electrodes (rheology, ionic conductivity, and electrical conductivity), and the design of new battery cells prototypes.

This PhD thesis is structured in 8 chapters: **Chapter 1** describes the state-of-art and the current main challenges for electrochemical energy storage devices, focusing on batteries. **Chapter 2** explores the main objectives of this PhD thesis, the initial hypothesis and the scientific questions that are pursued to be answered. **Chapters 3, 4, 5, 6, and 7** contain the main scientific results related to the challenges and the objectives proposed previously, including introduction, experimental procedures, discussion of results and bibliography for each chapter. Finally, **Chapter 8** summarizes the main conclusions

obtained from the work and the future perspectives. In addition, **Appendix A** contains the scientific contributions of this work. Finally, in **Appendix B** the figures and tables are listed and **Appendix C** have the list of the acronyms of the work.

Understanding the nature of the semi-solid electrodes is of primary importance for this thesis. For this reason, rheological, electrical, and ionic properties of semi-solid electrodes have been studied and detailed in **Chapter 3**. By evaluating the viscosity of the electrodes at different shear rate, the thixotropic nature of semi-solid electrodes has been demonstrated. The rheological properties of these electrode, make possible to inject the electrodes inside a preassembled cell. In addition, the studied semi-solid electrodes act as a mixed ionic and electronic conductor. Using models for this type of conductor, the ionic and electrical properties of different formulation of slurries are investigated via Electrochemical Impedance Spectroscopy using a special home-made cell showing the possibility of tuning the electrical and ionic properties by changing its composition: carbon content, electrolyte and additives.

In **Chapter 4**, the injectable battery, in which positive and negative electrode materials are not fixed on a current collector, is for the first time proposed as an innovative concept to facilitate the recycling process enabling the reuse of the entire battery cells. Battery crushing during recycling is no longer needed for the injectable batteries since battery cells are reused, which leads to significant reduction in number of steps, products, energy and thus battery costs. The proof-of-concept for the envisioned strategy is shown for aqueous injectable batteries (standard and super-concentrated electrolytes Zn – LiFePO<sub>4</sub> and LiTi<sub>2</sub>(PO<sub>4</sub>)<sub>3</sub> – LiFePO<sub>4</sub>), as well as its plausibility for non-aqueous injectable battery (Li – LiFePO<sub>4</sub>).

Aqueous rechargeable Zn-MnO<sub>2</sub> batteries are receiving interest due to their high charge storage capacity, non-toxicity, non-flammability, and low cost. **Chapter 5** explores the

possibility of achieving high energy density batteries based on semi-solid electrodes ( $4.6 \text{ mAh}\cdot\text{cm}^{-2}$ ). Our results indicate that the relatively high capacity fading (50 % in 120 cycles) is due to problems derived from pH changes in this mild-acid electrolyte. As a practical solution to investigate semi-solid  $\text{MnO}_2$  electrodes, an innovative hybrid system combining flow (negative side) and injectable electrode (positive side) enables expanding the lifespan of the battery up to 500 cycles with a capacity retention of 80 %. Additionally, the pH changes that occur inside the electrolyte and affect the correct functioning of the battery are investigated in detail. Spontaneous reaction between Zn metal and electrolytes evolving hydrogen and Zn-ions is confirmed to drive the electrolyte pH towards alkaline conditions, which in turn hinders the reversible electrochemical reactions in both positive and negative electrodes. The Oxygen Evolution Reaction (OER) at the positive electrode is proposed as a simple strategy to restore the initial pH by applying a float charging protocol (constant voltage at the end of the charge process). Interestingly, the  $\text{Mn}^{2+}$  dissolved as additive in the electrolyte is unravelled to play an important role in the pH correction. Using a pH indicator dissolved in the electrolyte and assembling the electrochemical cell in a spectrophotometer cuvette, the effect of floating voltage is evaluated in operando, enabling optimization of the floating voltage for the electrolyte pH to remain stable over hundreds of cycles.

Rechargeable Zn–Air batteries have held great promises for a long time. However, the severe challenges related to the reversible  $\text{O}_2$  reactions and poor cyclability at the positive and negative electrodes, respectively, have severely hindered the success of this technology. Herein **Chapter 6**, electrically-conducting and semi-flowable Zn semi-solid electrodes are proposed to revive the appealing concept of a mechanically–rechargeable alkaline Zn–Air battery, in which the spent negative electrodes are easily substituted at the end of the discharge process (refillable primary battery). In this proof-of-concept

study energy densities of *ca.* 1500 Wh L<sup>-1</sup> are achieved using semi-flowable Zn electrodes with a material utilization rate of 85 %. In this way, semi-solid Zn electrodes become a type of green energy carrier since they can be generated elsewhere using renewable sources, easily stored, transported, and used to produce electricity, in form of an electrochemically active flowable semi-solid having intrinsic advantages over gas and liquid fuels.

The last technology in which semi-solid electrode are implemented is the electrochemical ion pumping for Li extraction, which is discussed in **Chapter 7**. Since the lithium demand is expected to increase drastically in coming years driven by the market penetration of electric vehicles which are powered by Li-ion batteries, it is considered that much faster and more efficient Li extraction technologies than conventional ones, i.e. evaporation in brines, will be required to cope with this increasing demand. The Electrochemical Ion Pumping Cell (EIPC) technology based on the use of Faradaic materials is one of the most promising approaches. However, its relatively short life span is one of the major issues preventing its commercial deployment. In **Chapter 7**, a new EIPC concept based on the use of semi-solid electrodes is proposed for the first time, which takes advantage of the rheological characteristics of semi-solid electrodes that enable simple and cheap regeneration of the REIPC systems after reaching its end-of-life. Following this idea, a proof-of-concept of an effective regeneration of the REIPC is accomplished in this work by simple replacement of the semi-solid electrode. The results show that REIPC demonstrated a remarkable electrochemical performance along with a competitive ion separation, even for a solution that emulate typical Atacama's brines. In addition, the use of semi-solid electrode offers other unique features such as a significant cost reduction of 95% for every regeneration regarding conventional EIPC, an excellent value of the areal adsorption capacity (85 g<sub>Li+</sub> m<sup>-2</sup>) and an exceptional versatility that enables to use

different ion-capturing electrodes based on different intercalation materials. These results prove that REIPC concept successfully addresses the issues associated to the sustainability and recyclability of the conventional EIPC's for lithium capturing.









# **Chapter 1. Introduction**

## 1.1 Present Energy System

The current energy model is still dependent on fossil fuels. Although measures to reduce this type of fuel have been in place for some time, the reality remains that coal and natural gas are on the top positions in the energy production division today. Fortunately, the forecasts of the International Energy Agency (IEA) for the year 2040 estimates that the renewable sources will become the major contributors (**Figure 1-1**),<sup>1</sup> thus achieving a reduction in global warming of 2 °C if an increase of the installed capacity of 450 GW is achieved, compared to 140 GW in 2014.<sup>2</sup>

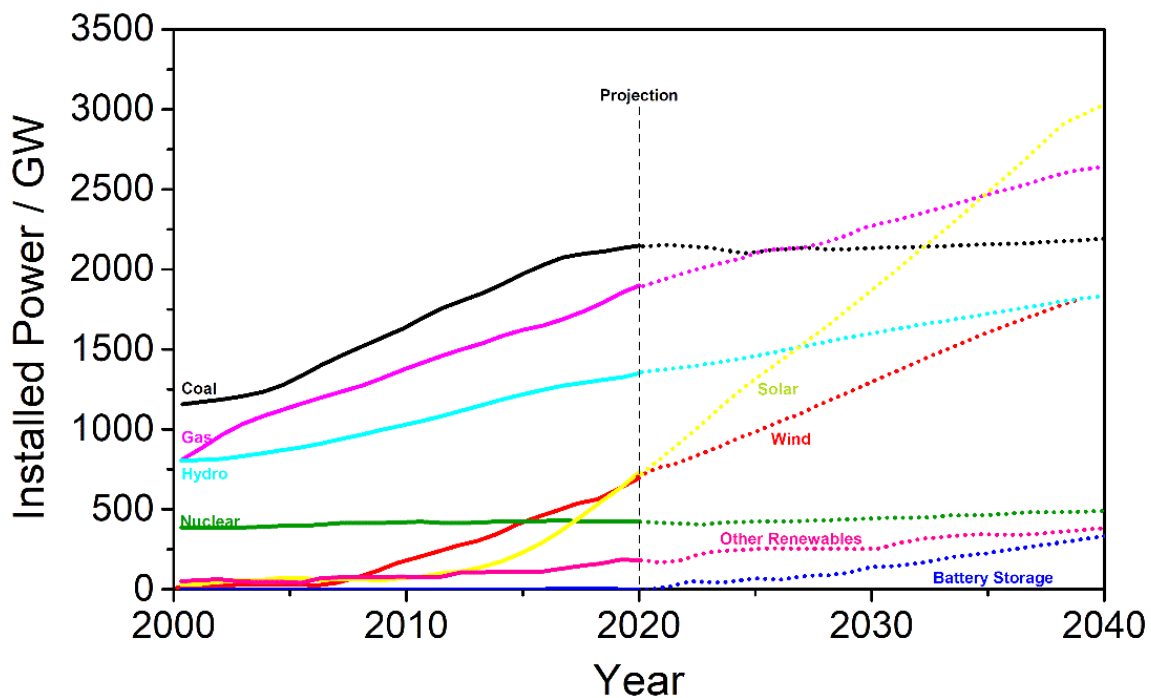


*Figure 1 - 1. Installed power capacity. Adapted with permission from [1].*

The main disadvantage related to the generation of energy from renewable sources is their intermittency and dependency on the climate, since they induce an unstable and fluctuating contribution to the electricity grid, generating a gap between the demand and the supply of electricity that can affect the stability and quality of said network.<sup>3,4</sup> This is the reason why it is necessary to develop energy storage systems that can buffer these

variations, accumulating energy generated when production exceeds demand, being able to release it in a controlled manner when demand increases and exceeds production.<sup>5</sup>

In addition, energy storage systems are needed for a large number of emerging technologies that requires energy storage such as: transport, portable electronics, or the Internet of Things. Indeed, market of energy storage systems for transportation applications will increase its market up to 100 - 200 million electric vehicles, according to the IEA. In addition, considering actions from The European Union for the reduction of emissions derived from the transportation sector by 2035, it will be compulsory the implementation of energy storage systems not only in private cars, but also in heavy-duty transportation.<sup>6,7</sup>

On the other hand, the diversity in power specifications for each application cannot be met with one single energy storage technologies. As consequence, there are different energy storage systems available in the market and a growing number of technologies are being pursued in battery research labs.

## **1.2 Energy Storage: Technologies and Applications**

The foundation of energy storage is the ability to transform one type of energy into another efficiently, so that energy is available at any time.<sup>8</sup> Currently, there are different energy storage technologies, differentiating each other according to certain critical aspects such as power, storage capacity or useful life, that will be the key parameters for the type of application in which it is intended to be used. It will be necessary to find out a compromise between the mentioned variables, so that they perfectly suit the needs of each application. In applications in which the discharge of energy is required for long periods of time, technologies with large storage capacity will be preferred. On the contrary, those application in which fast response is necessary in the accumulation and

releasing of energy, power and time response will be the prime aspects. Also, there are applications such as those related to transportation, in which both energy, power, and useful life are necessary.<sup>2</sup>

Since it is possible to distinguish the different types of energy storage according to the energy that is transformed, energy storage technologies can be arbitrarily categorized in the following types.

### 1.2.1 Mechanical Energy Storage

In this case, mechanical energy (kinetic or potential) is transformed into electrical energy, and vice versa.<sup>9</sup> This type of energy storage has several advantages over other types in terms of environmental impact, cost and sustainability. In this field, the most popular technologies are:

- Flywheel: consists of a rotating disk that quickly accumulates the kinetic energy of its rotation. The main advance of the flywheel is its fast time of response, in the range of minutes (**Figure 1-3**).<sup>10</sup>
- Pumped-hydro: This energy storage system is based on two reservoirs of water located at different heights, storing the energy pumping water from the lower to the upper reservoir, and releasing energy by taking back the water to the lower one. This system is suitable for applications in which long life, flexibility and low maintenance costs are required, but there are geographical limitations for its installation.<sup>4,5</sup>
- Compressed air energy storage (CAES): this system consists of compressed air underground, using the energy released by decompressing the air in a gas turbine for generating electricity. CAES systems are environmentally friendly, with a low maintenance, while having high power rates (**Figure 1-3**)<sup>6-8</sup>

## 1.2.2 Thermal Energy Storage (TES)

This type of energy storage is based on the reversible transformation of electrical energy into heat.<sup>11</sup> Typically, these technologies are grouped in two categories: i) sensible and ii) latent heat technologies. The former uses materials that do not change their phase when capturing heat.<sup>8</sup> In the latter, the materials do change their phase (latent heat), in which the energy released during the phase change in a specific temperature range is used.<sup>12</sup> In addition, it is worth highlighting the thermo-chemical energy storage, based on the accumulation of heat generated / absorbed from a reversible chemical reaction,<sup>13</sup> which allows a high energy density compared to the previous ones, as well as a lower loss of heat in the process.<sup>14</sup>

## 1.2.3 Chemical Energy Storage

Chemical energy accumulated in covalent bonds can be released through a chemical reaction. These systems are mainly based on hydrogen, through its conversion to methane that can be injected into the existing natural gas infrastructure (SNG) or obtaining hydrogen by breaking water molecules usually with electricity (electrolysis). Once the hydrogen has been generated, it can be stored under pressure, at a low temperature or by chemical conversion into other products such as methanol.<sup>4,15</sup>

## 1.2.4 Electrical Energy Storage

The Superconducting Magnetic Energy Storage (SMES) is the most common technology in this field, by passing a current through the coil, an indefinitely high energy efficiency and response speed magnetic field is generated, as well as a high power density (1 - 4 MW m<sup>-3</sup>).<sup>16</sup> In addition, Electrostatic Capacitors (EC) consists of two metal plates with an insulating layer (dielectric) between them. This system can storage electrical energy

from a direct-current source, but it reaches low energy density values ( $0.05\text{-}5\text{ Wh kg}^{-1}$ ) with an efficiency of 60-65 %.<sup>17,18</sup>

## 1.2.5 Electrochemical Energy Storage

In this type of energy storage, it is necessary to make a differentiation between the possible technologies available according to the energy accumulation process, either by a physical process of double layer formation of ions (supercapacitors) or by a chemical reaction through a Faradaic reaction (batteries).<sup>19</sup>

### 1.2.5.1 Supercapacitors

Devices consisting of two electrodes with a separator between them. The separator is soaked in electrolyte thus ensuring ionic contact between the electrodes, while ensuring their electrical isolation (**Figure 1-2**).

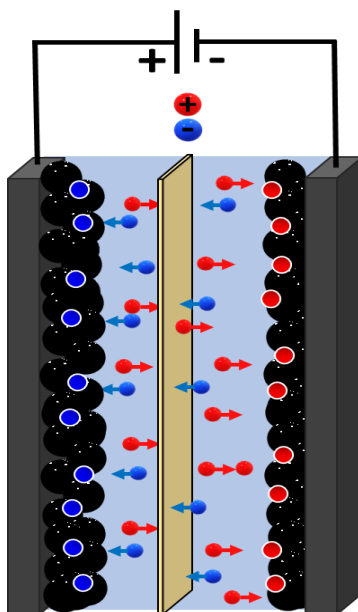


*Figure 1 - 2. Scheme of the charge process of a supercapacitor. Movement of cations (red) and anions (blue).*

When a potential difference is applied between the two electrodes, an electric field is induced that causes the movement of the electrolyte ions, which are reversibly adsorbed

on the surface of the electrodes, so the energy that it is capable of accumulating will depend on the specific surface and specific capacitance of such electrodes.<sup>16</sup> The main advantage of these systems is the great power they can deliver (500 - 10.000 W kg<sup>-1</sup>), with discharge times that do not exceed the order of minutes.<sup>20</sup> This process has a high storage efficiency (> 95 %) and can be cycled even thousands of times without losing energy storage capacity. However, supercapacitors are susceptible to self-discharge and parasitic reactions caused by the applied operating potential, limiting their use in certain applications such as those where high voltage is required.<sup>5,19,21</sup>

#### **1.2.5.2 Batteries**

With a similar configuration as supercapacitors, batteries are mainly composed of two electrodes separated electrically by a separator and connected ionically by an electrolyte. The positive and negative poles are electrically connected by an external electrical circuit through which current flows. Each electrode must have a different chemical potential. The difference between these potentials determines the nominal cell voltage. In the battery discharge process, electrons flow from the negative side (oxidation) to the positive side (reduction) through the external circuit. And ions present into the electrolyte move between the electrodes through the separator for maintaining the electro-neutrality. Batteries that can only release the energy stored (discharging process) are called primary batteries, but if the chemical reactions occurring inside the cell are reversible, it will be possible to recharge the battery. These rechargeable batteries are referred to as secondary batteries.<sup>22-24</sup>

In summary, different technologies are available for storing energy. Each one of them has specific features that make them suitable for specific applications depending on the energy demand. **Figure 1-3a** shows different applications in which energy storage plays an important role, e.g. integrating electricity from renewable energy sources and backup

power with different demand of energy in terms of power and time. Therefore, **Figure 1-3b** shows the rated power and time of energy release corresponding to the technologies above mentioned. As illustrated in **Figure 1-3**, batteries have the widest range of possible applications due to their versatility.

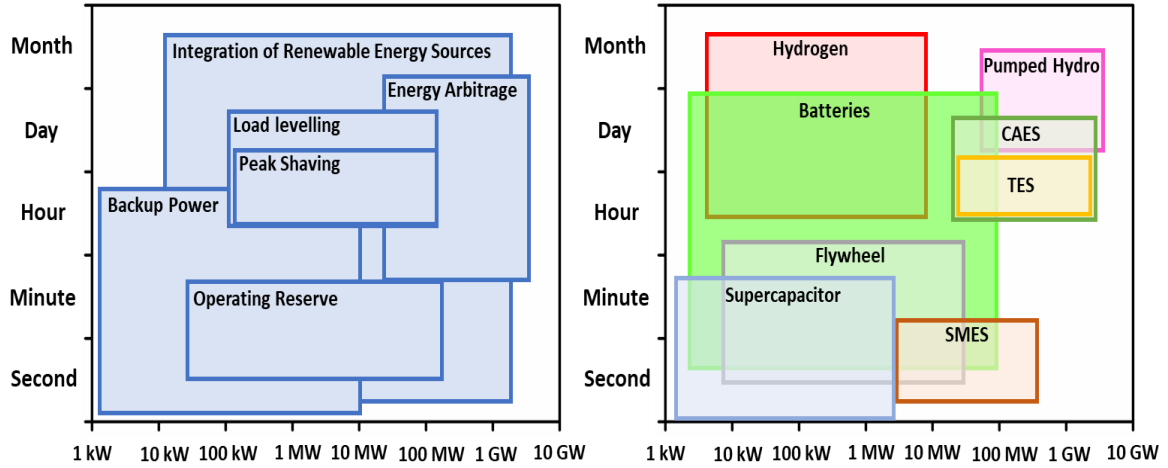


*Figure 1 - 3. Time of energy release and power rate for (a) Energy storage applications and (b) Energy storage systems. Adapted with permission from [25].*

The most mature technologies contribute the most to the global energy storage system. In fact, 169.557 MW of installed power corresponds to hydraulic pumping systems, compared to the total 175.823 MW, which represents approximately 99.3 %.<sup>2</sup> All the systems described above, in addition to other less common, constitute the basis for the decarbonization of the energy system.<sup>26</sup> Each system has its intrinsic properties that make it optimal for each application, so that it is possible to meet energy needs with these systems.

### 1.3 Batteries

A battery is a device capable of directly converting chemical energy stored in its active materials, into electrical energy through electrochemical oxidation and reduction

reactions. These reactions are associated with an electron transfer from one material to another by an external electrical circuit. A battery unit (cell) is composed of:

- *Negative electrode*. It is the electrode with the lowest standard reduction potential. In the discharge process (spontaneous step), an electrochemical oxidation reaction takes place, releasing electrons to the external electrical circuit.
- *Positive electrode*. It is the electrode with the highest standard reduction potential. In the discharge process, an electrochemical reduction reaction takes place, accepting the electrons coming from the external electrical circuit.
- *Electrolyte*. It is an ionic conductor that connects ionically both electrodes.<sup>27</sup> It is essential for the correct operation of a battery since it is responsible for compensating the positive and negative charges generated while charging and discharging the battery.
- *Separator*. This component of the cell is essential, since it electrically isolates the two electrodes to avoid internal short-circuiting, while it allows the passage of ions to maintain the electroneutrality.
- *Current collectors*. It is the element of the electrodes that provides electrical connection between the active materials and the external electrical circuit.

### 1.3.1 Primary Batteries

This type of battery is characterized by being a single-use device since the electrochemical reactions are not reversible. Primary batteries contain a limited amount of electrochemically active compounds that, once consumed in the discharge process of the battery, cannot be used again. The most common example of these batteries is the Daniell Cell (1836), which consists of zinc and copper as active materials. In this system, the reaction at the negative pole (anode) is the oxidation of Zn to  $\text{Zn}^{2+}$  releasing two electrons that flow through the external circuit, reaching the positive pole (cathode) where the reduction of  $\text{Cu}^{2+}$  from the solution of  $\text{CuSO}_4$  to  $\text{Cu}^0$  occurs. This consumption of

copper ions in the positive pole generates a difference in charges between the solutions in both compartments, which is balanced by the transport of ions through the salt bridge.

### 1.3.2 Secondary Batteries

Secondary or rechargeable batteries are devices in which reversible electrochemical reactions take place. As a result, secondary batteries have the ability to electrically charge the system. That is, even though the amount of electrochemically active material is limited in the system, it is possible to force opposite reactions by consuming external energy.<sup>28</sup>

### 1.3.3 Historical Development of Batteries

In the past XVII century, researchers have been pushing the frontier of knowledge in batteries through chemistry and engineering perspectives. The resulting vast diversity of battery technologies shows the versatility of batteries.

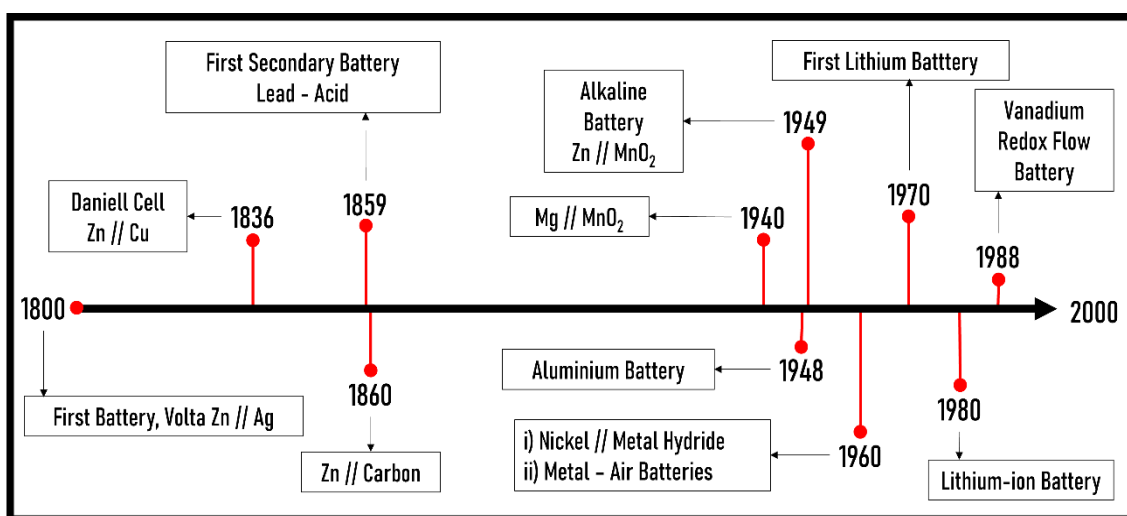


*Figure 1 - 4. History of batteries. Timeline illustrating milestones achieved in the field of batteries in the last 200 years.*

Some of developed battery technologies have had a great impact on society. As a result, they become essential in our day-to-day basis for a multitude of applications, among

which it is worth mentioning lead – acid, alkaline zinc – manganese dioxide, nickel – metal hydride, metal – air, redox flow, and lithium-ion batteries.

#### **Alkaline Zinc – Manganese Dioxide battery**

Manganese dioxide ( $\text{MnO}_2$ ) is the active material for the positive electrode, while the negative electrode consists of zinc particles suspended in a gel concentrated in potassium hydroxide (KOH) that acts as an electrolyte.<sup>29</sup> This battery has dominated the primary battery market for decades, thanks to its low cost, high safety, and simple manufacturing process.<sup>30</sup> These storage systems have an energy density of  $400 \text{ Wh L}^{-1}$  or  $500 \text{ Wh kg}^{-1}$ , due to the high specific capacities of their active materials, in addition, they offer a power density of  $20$  to  $60 \text{ W kg}^{-1}$ , with a cost of  $15 - 30 \text{ USD kWh}^{-1}$ . One of its great advantages, in addition, is the minimal self-discharge that they suffer, losing only  $4 - 7 \%$  of their initial capacity after one year.

#### **Lead – Acid battery**

The lead-acid battery (1859)<sup>31</sup> consists of a positive lead oxide ( $\text{PbO}_2$ ) and a negative lead metal electrode, both immersed in a sulfuric acid solution used as electrolyte.<sup>32</sup> These are secondary batteries since they can be recharged electrically by forcing the opposite redox reactions on the electrodes. With a nominal voltage of approximately  $2 \text{ V}$ , and an energy density of  $30 - 50 \text{ Wh kg}^{-1}$ ,<sup>33</sup> these batteries are widely used for transport ( $82 \%$  including motorcycles and electric bicycles, machinery and conventional vehicles), and they also find their space in applications in Uninterrupted Power Supply (UPS) systems among others.<sup>34</sup>

#### **Nickel – Metal Hydride battery**

This battery consists of a positive electrode of nickel hydroxide ( $\text{Ni(OH)}_2$ ) and a negative electrode of metal hydrides, while using an aqueous alkaline electrolyte ( $30 \%$  KOH (wt. %)).<sup>35</sup> This battery has a nominal voltage of  $1.2 \text{ V}$ , while an energy density of  $130 - 170$

Wh L<sup>-1</sup> (volumetric), specific energy density of 60 -70 Wh kg<sup>-1</sup> and 150 - 300 W kg<sup>-1</sup> for its power density.<sup>36</sup> Due to these characteristics, this battery chemistry reached a production of more than 10<sup>9</sup> batteries in 2009.

### Metal – Air batteries

This type of batteries have a particular characteristic that differentiates it from the others; one of its electrochemically active materials is not stored in the device since it is the oxygen present in the air.<sup>37</sup> This is beneficial for the energy density and the cost. Also, metal – air batteries employ metals as negative electrodes, e.g. Zn (820 mAh g<sup>-1</sup>), Li (3861 mAh g<sup>-1</sup>), Al (2981 mAh g<sup>-1</sup>) or Mg (2200 mAh g<sup>-1</sup>), which contributes to increasing the energy density. During discharge, the metal is oxidized in the negative electrode while oxygen present in the air is reduced in the positive electrode. (**Figure 1-5**).

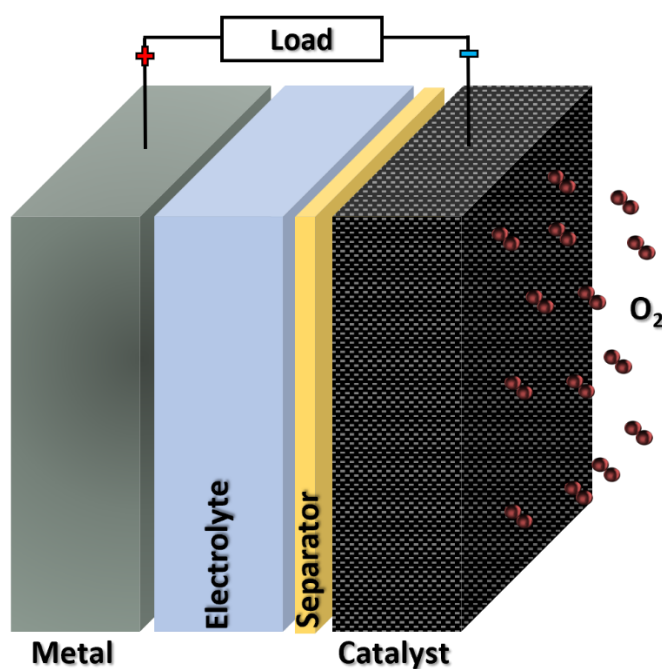


*Figure 1 - 5. Illustration of the elements of a Metal - Air battery.*

One of main challenges of the family of technologies is the sluggish oxygen reaction in the positive electrode. Electrocatalyst are needed in the positive electrode to improve the kinetics. The difficulties for achieving reversible oxygen reaction (both oxygen reduction

and oxygen evolution) in the same electrode leads to success commercialization of primary metal – air batteries, in which only oxygen reduction reaction takes place. Obviously, the goal is to achieve electrically rechargeable metal - air battery.<sup>38</sup>

### Redox flow batteries

Redox flow batteries represented a great change with respect to the conventional battery concept in its design and operation. In contrast to other types of batteries, the electrochemically active materials are dissolved into the electrolyte and stored in external tanks. These electrolytes are pumped into an electrochemical reactor in which energy conversion take place through the redox reactions (**Figure 1-6**). Having the electroactive species dissolved in the electrolyte enables the decoupling of power (defined by the size of the reactor) and energy (limited by the amount of active material stored in the external tanks). This unique feature of redox flow batteries provide them with high versatility which is of great interest for multiple applications.<sup>39</sup>

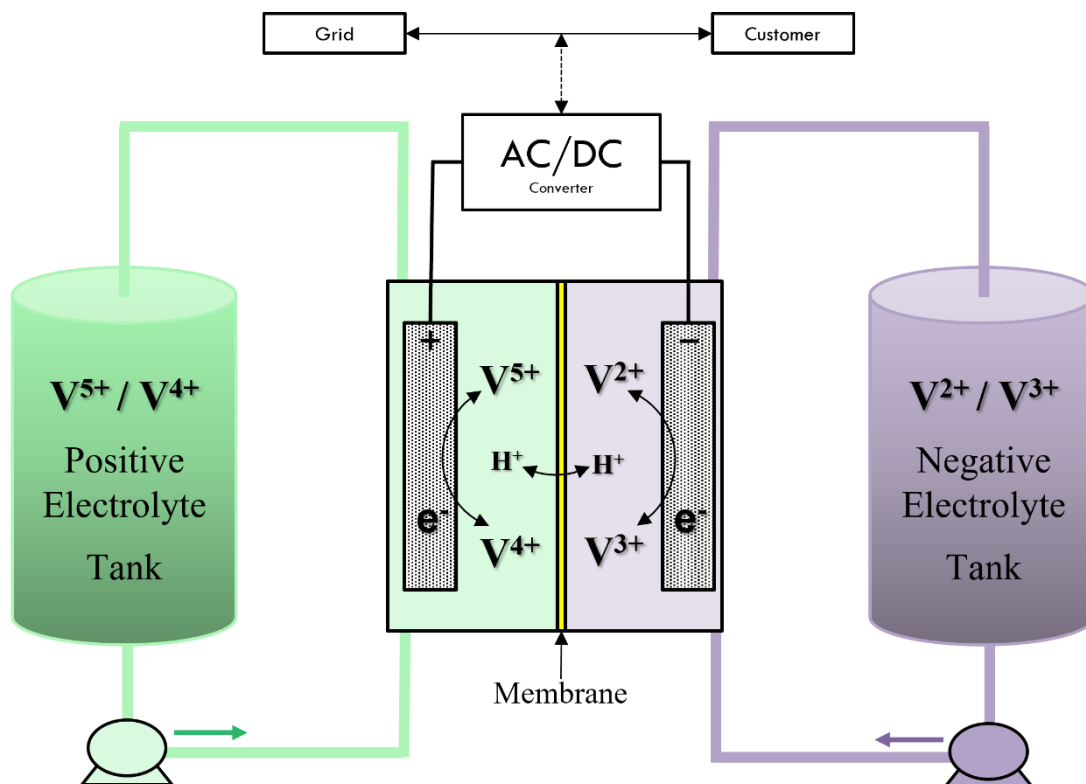


*Figure 1 - 6. Scheme of an all-Vanadium redox flow battery.*

The most mature battery chemistry in redox flow batteries is on the all-vanadium. The electrochemical reactions that occur in this battery chemistry are the oxidation and reduction of vanadium species ( $V^{5+} / V^{4+}$  for the positive,  $V^{3+} / V^{2+}$  for the negative). All Vanadium species are dissolved in an strongly acidic aqueous media (5-8 M sulfuric acid), while positive and negative compartment are separated by a selective proton exchange membrane.<sup>40</sup> Despite the benefits of all-vanadium, there are certain disadvantages associated with this system, e.g the cost of the membrane and availability of vanadium (critical material for the USA and EU).

### **Lithium – ion Battery**

As recognition of the great milestone that LIBs mean for the society some of the pioneers (John B. Goodenough, M. Stanley Whittingham, and Akira Yoshino) received the Nobel Prize in Chemistry in 2019. In 1976, S. Whittingham published his research devoted to the study of the intercalation of lithium in different materials.<sup>41,42</sup> Two years later (1980), JB Goodenough studied the use of "Lithium Cobalt Oxide" as a lithium intercalation material to be used as a cathode for high energy density batteries,<sup>43</sup> but it was not until 1982 when A. Yoshino patented the first rechargeable lithium ion battery.<sup>44</sup>

The lithium-ion battery is fundamentally based on the intercalation / deintercalation process of Li-ions in different active materials that are fixed in battery electrodes. The great variety of existing intercalation materials generates many possible combinations for this type of batteries, each combination with different performance in terms of voltage and energy density (**Figure 1-7**). The electrolyte used in these batteries, unlike the previous aqueous ones, is a non-aqueous media which enables larger nominal cell voltages.

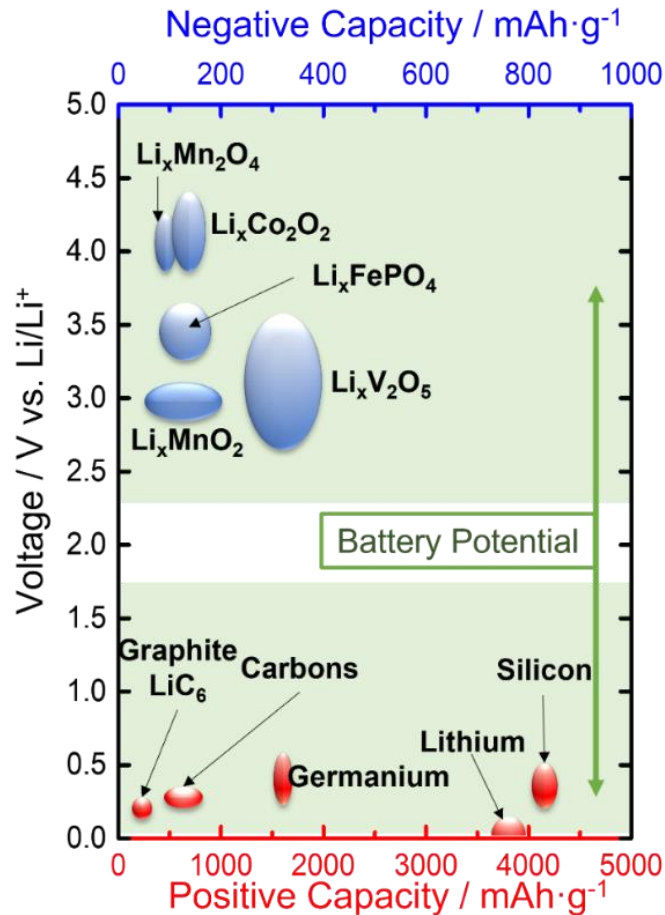


*Figure 1 - 7. Representation of specific capacity and operating redox potential of various materials for Li-ion batteries, adapted with permission from [45].*

Today, this mature battery technology dominates the market for mobile applications thanks to its high energy density, relatively long cycle life and its moderate cost (< 150 USD kW h<sup>-1</sup>). Indeed, the increase in production, forecasted to reach more than 1.2 TWh in 2030,<sup>46-48</sup> is driving a significant decrease in cost which has triggered the use of Li-ion batteries in other application such as stationary energy storage.

## 1.4 Limitations in Batteries

Considering all the technologies mentioned, batteries can be categorized as a function of its operation: static batteries and flow batteries. Static batteries are characterized by having the active material (positive and negative electrodes) fixed on the current collector,

confined, and sealed inside the battery cell. On the other hand, in the case of flow batteries, the active materials are dissolved in the electrolyte, which is stored in the external tanks.<sup>49</sup>

The most commercially used technologies for static and flow batteries are lithium-ion batteries and all-vanadium redox flow batteries, respectively. **Table 1-1** summarizes the key performance indicators (KPIs) for each type of battery. Advantageous characteristics are marked in green, while limitations are marked in red. Yellow represents KPIs that are improvable.

*Table 1 - 1. Comparison of the key performance indicators of state-of-art static batteries and flow batteries: Lithium-ion vs. All-vanadium.*

	<b>Lithium - ion</b>	<b>All - Vanadium</b>	<b>Objective</b>
<b>Sustainability</b>	<b>Co, Li, Graphite</b>	<b>Vanadium</b>	
<b>Recyclability</b>	<b>Sealed Cell</b>		
<b>Eco-Friendliness</b>	<b>Life Cycle Assessment</b>	<b>Electrolyte</b>	
<b>Energy Density</b>		<b>Dissolved Species</b>	
<b>Cyclability</b>			
<b>Energy Efficiency</b>			
<b>Cost</b>			
<b>Energy and Power</b>	<b>Coupled</b>		
<b>Temperature Range</b>		<b>&lt; 40 °C</b>	
<b>Safety</b>	<b>Thermal Runaway</b>		

**Sustainability** In this regard, both systems are considered negative due to the use of critical materials such as cobalt, lithium, graphite, and vanadium. These materials are on the list of fundamental raw materials because of their economic importance and the risk in their supply.<sup>50</sup>

**Recyclability.** The possibility of recycling in flow batteries is simple for the electrolyte since it is in the external tanks and is easily removable. However, in static batteries, as they are sealed cells, materials cannot be extracted without breaking the battery cell, so several separation stages are added in their recycling process.

**Eco-Friendliness.** Relative to this parameter, the two types of storage are negative. First, according to the Life Cycle Assessment study conducted by Peters et al. (2017),<sup>46</sup> the production of 1 kWh of storage capacity in lithium ion batteries requires a total energy of 328 kWh on average, with greenhouse gas emissions of 110 kg CO<sub>2</sub> equivalent. On the other hand, in vanadium flow batteries, greenhouse gas emissions are approximately 90 kg CO<sub>2</sub> kWh<sup>-1</sup>, of which the electrolyte used (dissolution of vanadium species in sulfuric acid) corresponds to a 89 %.<sup>51,52</sup>

**Energy Density.** Currently, practically any type of commercial lithium ion battery has a specific energy of 100 - 265 Wh kg<sup>-1</sup>, they have no memory effect and their self-discharge is only 1.5 – 2 % month<sup>-1</sup>.<sup>53</sup> Regarding the vanadium flow battery, the energy density is much lower than the static batteries, since it depends directly on the solubility of the species in the electrolyte (1.7 M for vanadium), limiting the energy density of the system. at 25 - 35 Wh L<sup>-1</sup>.<sup>54</sup>

**Cyclability.** Regarding lithium-ion batteries, their cyclability is limited due to the side reactions produced by the large operating potentials that may result in a decay of the coulombic efficiency, and the usable capacity.<sup>55,56</sup> In addition, the common intercalation/deintercalation process occurring in the charging/discharging processes,

could lead to a structural changes in the electrode that could be associated with low energy efficiencies.<sup>57</sup> On the other hand, the use of the same metal in both negative and positive electrolytes in the vanadium redox flow battery, allows longer cyclability than solid-state batteries. This system is capable of maintaining its capacity for 15.000 – 20.000 cycles.<sup>54</sup>

**Cost.** In the case of static batteries, taking as reference a  $\text{Li}_{1.05}(\text{Ni}_{0.6}\text{Co}_{0.2}\text{Mn}_{0.2})_{0.95}\text{O}_2$  (NMC622) - Graphite battery, the total cost of the system including materials (32 %), hardware (20 %), labor (5 %), general expenses (29 %) and battery (13 %) and temperature (1 %) monitoring/controlling systems amounts to 240 USD  $\text{kWh}^{-1}$ .<sup>58</sup> On the other hand, in vanadium flow batteries the cost power accounts for 3.430 USD  $\text{kW}^{-1}$  for power plus 858 USD  $\text{kWh}^{-1}$  for energy.<sup>59</sup> As a result, all-V redox flow batteries are especially suitable for long cycles (> 5 hours) so that the power cost is minimized.

**Ratio between Energy and Power.** As explained above, energy and power are decoupled in redox flow batteries since the energy depends on the active material found in the external tanks, and power depends on the active reaction surface (reactor size). However, in static batteries, the active material is fixed on the current collectors. Decoupling of energy and power requires changing the mass loading (or areal capacity,  $\text{mAh cm}^{-2}$ ). Unfortunately internal resistance increases significantly above certain values of mass loading so that the ratio between power and energy is very limited in static batteries.<sup>49</sup>

**Temperature Range and Safety.** Since energy density in all-vanadium flow batteries is limited by the solubility of vanadium species in the electrolyte, temperature variations can lead to precipitation of species. In particular,  $\text{VO}^{2+}$  at the employed concentration of 1.5 - 1.6 M precipitates above 40° C as  $\text{V}_2\text{O}_5$ , and the crystallization of  $\text{V}^{2+}$ ,  $\text{V}^{3+}$  and  $\text{V}^{4+}$  at lower temperatures.<sup>60</sup> As for static batteries, the working temperature range may be a bit wider. Below 0 °C the reaction kinetics get much worse, favoring lithium deposition. Furthermore, although the battery can operate up to 90 °C before overheating,

when the temperature is above 40 °C the battery life is shortened due to parasitic reactions.<sup>61</sup>

In terms of safety, the great advantage of all-vanadium flow batteries is the use of aqueous electrolyte, as well as the separation between the tanks and the reactor, which make these types of batteries safe thanks to heat dissipation made by the liquid electrolyte from the cell to the external reservoirs.<sup>62</sup> On the contrary, lithium-ion batteries use organic and flammable electrolytes making them less safe since a series of exothermic reactions can cause increase in pressure and temperature inside the cell leading to the evaporation of the electrolyte and even the explosion of the battery.<sup>61</sup>

As a consequence, it is necessary to propose different systems, modifications, adaptations, and new disruptive concepts that make the way of understanding, designing, and using these energy storage systems evolve with regard to the discussed KPIs.

## **1.5 Emerging Technologies**

If non incremental improvements in the KPIs are pursued, innovative concept and technologies are required. Below, some alternative battery technologies as non-incremental approach to state-of-the-art are discussed.

### **1.5.1 Static Batteries**

Despite commercial lithium-ion batteries are reaching the maximum theoretical value in terms of energy density and energy efficiency,<sup>63</sup> there are still negative aspects in this technology, especially in the field of safety and the environmental issues, as well as aspects related to new social needs. For this reason, much of the research related to the study and development of static lithium-ion batteries aims to mitigate these limiting aspects implementing modifications and improvements in every element of the cell:

cathode, anode, electrolyte, and separator as well as in the battery design. Some of the proposals are:

- Aqueous Lithium-ion Batteries. The use of organic solvents in the electrolytes of lithium-ion batteries entails lower ionic conductivity and high manufacturing costs due to the absence of oxygen and moisture, apart from the safety and environmental problems. Therefore, the idea of using aqueous electrolytes for lithium ion batteries arises due to its high power and low flammability, allowing the manufacture in the presence of water and oxygen.<sup>64</sup> However, the great limitation of this technology is the water stability window (evolution of oxygen and hydrogen reactions), which limits the battery voltage.<sup>65</sup> Since the first aqueous lithium ion battery ( $\text{LiNO}_3$  as electrolyte),<sup>66</sup> different strategies have been developed to improve the operation of this type of system, such as the concentration of salt in the electrolyte to increase the stability window and improve battery cyclability,<sup>64</sup> or the search for new materials with optimal properties for these batteries.<sup>67</sup>

- Flexible Batteries. The current increase in the market of portable devices, phones, or flexible displays has generated great interest in the design of flexible storage systems.<sup>68</sup> Currently commercial lithium-ion batteries have cylindrical or prismatic shapes that, together with the rigidity of their components, make it difficult to apply them in this type of devices. To face these limitations, the research focuses on two aspects: improving the mechanical resistance of the electrodes and designing new battery configurations. However, the low energy density and cyclability, the safety problems,<sup>69</sup> and the complexity of the new manufacturing methods required for this type of cells, do not currently reach the necessary standards for their possible commercialization.<sup>70</sup>

- Post-Lithium-ion Batteries. The so-called post-lithium-ion technologies are those that present non-incremental improvements compared to conventional lithium-ion batteries (LIB). These technologies include sodium ion batteries (SIB), lithium sulfur

batteries (LSB), solid-state batteries (SSB) and lithium-Air batteries (LAB).<sup>48</sup> **Table 1-2** shows the main KPIs for these technologies.

*Table 1 - 2. Key performance indicators for post-lithium-ion battery technologies. Adapted with permission from [48].*

	<b>LIB</b>	<b>SIB</b>	<b>LSB</b>	<b>SSB</b>	<b>LAB</b>
<b>Nominal Voltage / V</b>	3.2-3.85	3.1-3.3	2.1-2.2	3.7-3.8	2.6-2.9
<b>Areal Capacity / mAh cm<sup>-2</sup></b>	3-5	3-4	5-8	0.5-14	2-4
<b>Power / kW · kg<sup>-1</sup></b>	1-20	2-5	0.1-1	0.01-3	-
<b>Cyclability</b>	1.000-6.000	500-4.000	100-500	100-1.000	5-100
<b>Energy Efficiency</b>	> 90 %	> 90 %	70-95 %	50-76 %	60-80 %
<b>Self-discharge</b>	Low	Low	High	Low	-

Sodium-ion batteries have the great advantage of the low cost and availability of Na<sub>2</sub>CO<sub>3</sub>, Na<sub>2</sub>SO<sub>4</sub> and NaCl salts for their electrolyte. But they still have an inferior electrochemical performance, in terms of energy density, compared with the conventional Li-ion batteries.<sup>58,71</sup>

In the case of lithium-sulfur batteries, their great advantage lies on the high theoretical energy density (2800 Wh L<sup>-1</sup>) apart from the low cost and abundance of sulfur cathodes. However, the sulfur suffers from volume expansion (80 %) during discharge, and its poor conductivity leading to low sulfur utilization are still the main drawbacks of this chemistry.<sup>72-75</sup>

Solid-state batteries enable high durable and safe batteries due to the use of non-flammable solid electrolytes. In addition, this kind of electrolytes help to preventing the crossover of species across the cell and internal short-circuiting. However, there is still

problems regarding the physical contact between the parts of the cell and the electrochemical stability of the system.<sup>76,77</sup>

Finally, in lithium-air batteries, the use of metallic lithium as anode, due to its low potential ( $\approx 3.04$  V vs SHE), high energy density ( $3,860$  mAh  $g^{-1}$ ), and the high theoretical specific energy density ( $3,505$  Wh  $kg^{-1}$ ) combined with the unlimited oxygen in the air, make this system one of the most promising for high energy density required applications. However, the energy efficiency that offers Li-air batteries is low due to problems related to the air-cathode and the overpotential obtained in the charge and discharge processes.<sup>78–</sup>

81

## 1.5.2 Redox Flow Batteries

Different redox flow battery technologies have been proposed and developed to address the negative aspects of all-vanadium chemistry. Some of these systems are:

- Redox Flow Batteries based on Organic Electroactive Molecules. The accessibility and sustainability issues related to the use of metal electroactive materials was proposed to be addressed by using organic-based materials. These organic molecules can be dissolved in both aqueous and organic solvents. The use of organic molecules has great advantages such as the low cost, the sustainability of the compounds and easily tunability of their properties, being able to increase the cell voltage and solubility or even improve the stability and the reaction kinetics.<sup>54,82–84</sup> The most widely used and studied organic molecules include: anthraquinone ( $C_{14}H_8O_2$ ), thyron ( $C_6H_4Na_2O_8S_2$ ), phenazine ( $C_{12}H_8N_2$ ), aloxazine ( $C_{10}H_6N_4O_2$ ), methyl viologen ( $C_{12}H_{14}C_{12}N_2$ ), TEMPO ( $C_9H_{18}NO$ ) as well as polymers based on these single-molecules.<sup>85–90</sup>

- Membrane-Free Redox Flow Batteries. The membrane in redox flow batteries is a fundamental part. Ion-selective membranes avoid the crossover of electroactive species between the positive and negative compartments, while they allow selectively for passage

of ions to balance the charges of the system. The great problem associated with this element of the battery is the high cost. To remove the need for expensive ion-selective membrane, two different strategies have been proposed. On the one hand, application of laminar flow in catholyte and anolyte avoids the mixture of both currents.<sup>91</sup> On the other hand, the use of immiscible electrolytes forming two phases separate the electrolyte of the positive and negative electrolytes.<sup>92</sup>

- Hybrid-flow Batteries. While the configuration of a hybrid-flow battery is similar to redox flow batteries, the electroactive material is stored inside the electrochemical reactor in one of the two compartments. This fact limits to some extent the decoupling of energy and power. On the other hand, hybrid-flow batteries offers the possibility of using abundant, cheap and environmentally friendly metals such as copper, zinc or iron in their solid-state, combining them with the advantages offered by flow systems.<sup>93-95</sup> Typically these metals are used as negative electrode, combined with a positive electrode in solution. Within this type of batteries, there are multiple different combinations regarding the design of the device such as static or particulate metallic electrodes that flow, a single flow channel, more than one flow channel, the possibility of using organic and aqueous electrolytes and a combination of both, etc. The most promising metals are zinc and lithium due to their high energy densities.<sup>95-98</sup>

- Redox-mediated Flow Batteries. This technology accumulates energy in solid materials that are confined in the external tanks. For this, it uses dissolved species (redox-mediators) as charge transport. The dissolved redox-mediator is pumped into the battery cell for charge transfer reaction transporting these charges to the external tank in which redox reaction between redox-mediator and solid electroactive materials occurs. This transfer of charge from the liquid to the solid occurs spontaneously, accumulating the

energy without the need for an electrical contact of the solid material, increasing the energy density of the battery.<sup>99–103</sup>

- Semi-solid Redox Flow Batteries. This technology is based on replacing dissolved active species by suspensions that contain solids active compounds and conductive activated carbon. This suspension forms a "slurry", which is stored in the external tanks and is pumped into the reactor (**Figure 1-8**). This system involves a large increase in energy density, since solids can store more energy per volume unit than liquids. In addition, the use of semi-solid electrodes allows the use of microporous separators instead of ion-selective membranes, thus reducing the cost of the battery cell.<sup>104–107</sup> However, the technical feasibility of this technology must be evaluated when considering its long-term use and in large-scale storage devices, due to the problems derived from the use of very viscous suspensions in terms of pumping, corrosion, and sedimentation.<sup>108</sup>

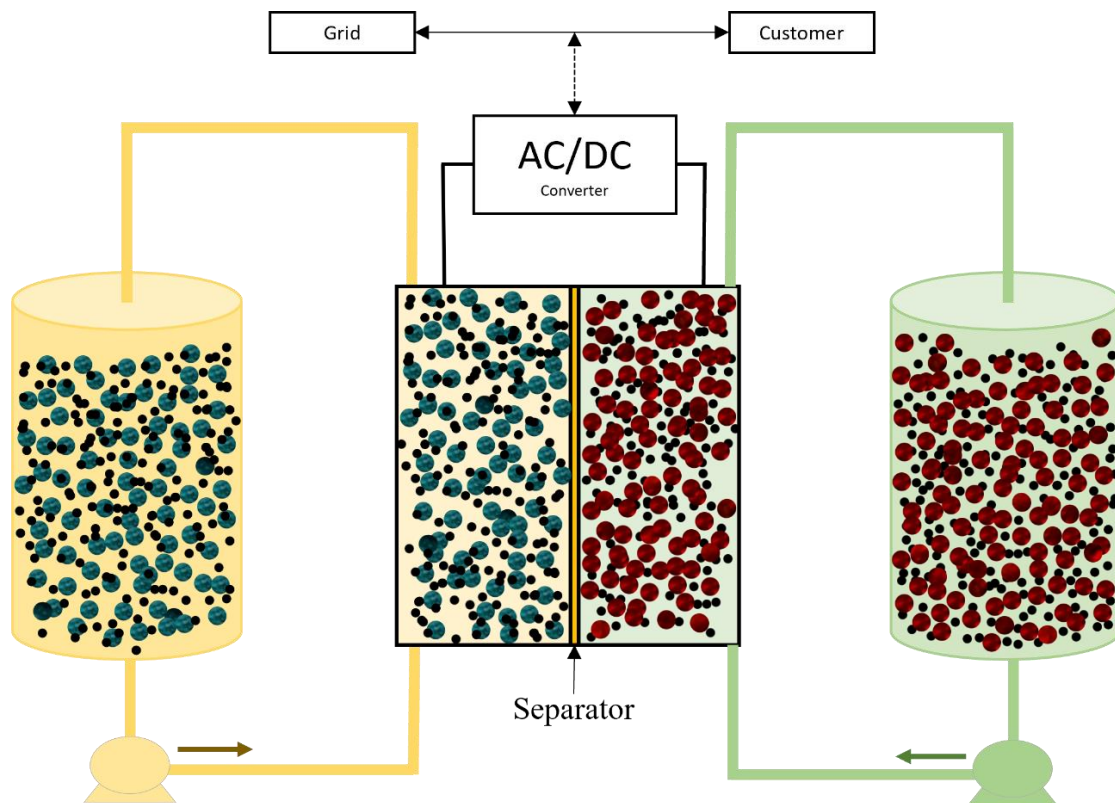


*Figure 1 - 8. Scheme of a semi-solid redox flow battery.*

All the emerging technologies discussed involve improving one, or more, of the limiting aspects of state-of-the-art batteries (**Table 1-1**).

## 1.6 Semi-Solid Electrodes

The first battery concept based on the use of semi-solid electrodes was “the semi-solid flow battery” (2011). This new battery technology emerged as a solution for combining the high energy density of solid active materials and the advantages of the redox flow battery configuration.<sup>106</sup> After the proof-of-concept accomplished by Chiang et.al, there has been attempts to extend the concept of semi-solid flow battery to other battery chemistries in non-aqueous sodium-ion batteries,<sup>107</sup> lithium-polysulfide,<sup>109</sup> lithium-oxygen,<sup>110</sup> aqueous-hypersaline lithium ion,<sup>111</sup> zinc-nickel batteries,<sup>112</sup> or even their use in water-related technologies such as capacitive water deionization or wastewater treatment.<sup>113</sup>

The use of semi-solid electrodes was demonstrated to be very useful. However, challenges associated with pumping viscous suspensions have hindered commercial deployment. On the other hand, it was found out that semi-solid electrode possesses other advantages over conventional electrodes resulting in a new type of static batteries commercialized by the company 24M.

The semi-solid electrodes are based on the absence of binder in their formulation, unlike in conventional static batteries. That is, semi-solid electrode consists of directly mixing the active material, a conductive additive and electrolyte. The tunable porosity and lack of binder lead to enhanced mass transport across the electrode which enables the fabrication of batteries with thicker electrodes.<sup>114</sup> The increase in areal capacity due to thicker electrode results in a reduction in the costs of this system. In contrast, increase in

thickness of conventional electrodes faces certain challenges : such as weakness, delamination, high tortuosity, and slow kinetics.<sup>115</sup>

### 1.6.1 Areal Capacity and Cost

The areal capacity of a static battery is defined by the amount of charge stored per unit area, which in turn depends on the amount of active material per area. In conventional electrode, the amount of active material is at least  $10 \text{ mg}_{\text{material}} \text{ cm}^{-2}$  for high areal capacity electrode.<sup>116</sup> For a given energy storage capacity, e.g. 1 kWh, the total area decreases as the areal capacity increase (**Figure 1-9**). In this way, the total cost will significantly decrease with increasing areal capacity since the costs associated with those parts directly dependent on the surface (current collectors and separator) will be reduced. Therefore, the cost reduction will largely depend on the areal capacity of the system.

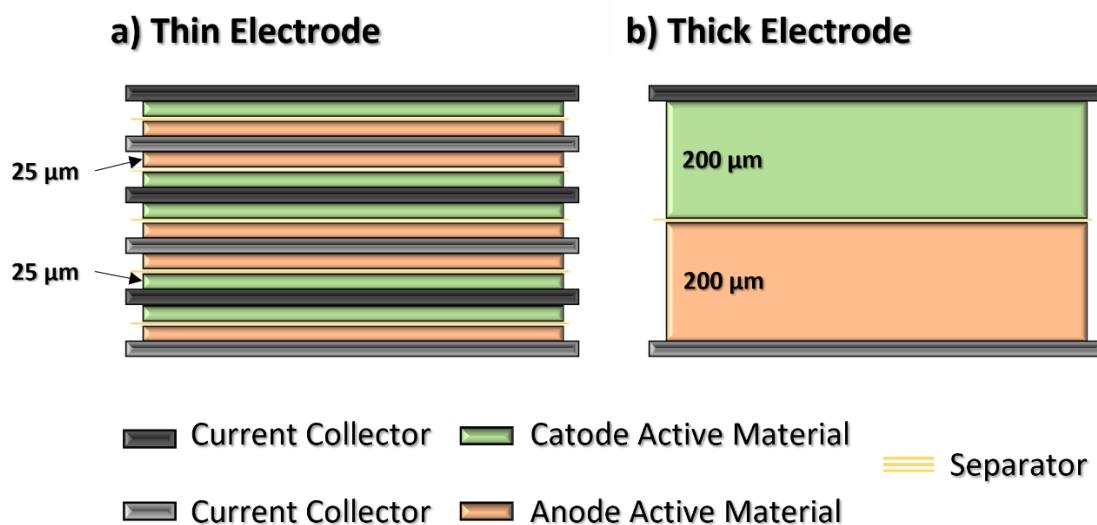


*Figure 1 - 9. Different configurations of static battery (a) Conventional thin electrodes vs. (b) Thick electrodes. Adapted with permission from [115].*

### 1.6.2 Limitation of conventional electrodes.

The manufacturing process for conventional electrodes (**Figure 1-10**) consists of several steps. First, the active material is mixed with the additive conductive carbon, and binder

using a solvent in which the binder is dispersed with the solvent. The current collector is coated using this suspension. Precise control over this process is important since it not only influences the quality of the electrode, but also cost (minimum residence times are around 1-2 minutes). Once the solvent has evaporated, the electrodes are compressed (calendaring) to improve the physical properties of the electrode (porosity, adhesion, or conductivity). It is important to bear in mind that this type of process involves the application of mechanical stress on the electrode, which will directly affect its adherence, causing a loss of battery capacity as well as a reduction in its useful life.<sup>117</sup> Finally, the electrode goes to a dry room where its humidity is reduced ( $< 500$  ppm).<sup>118</sup>

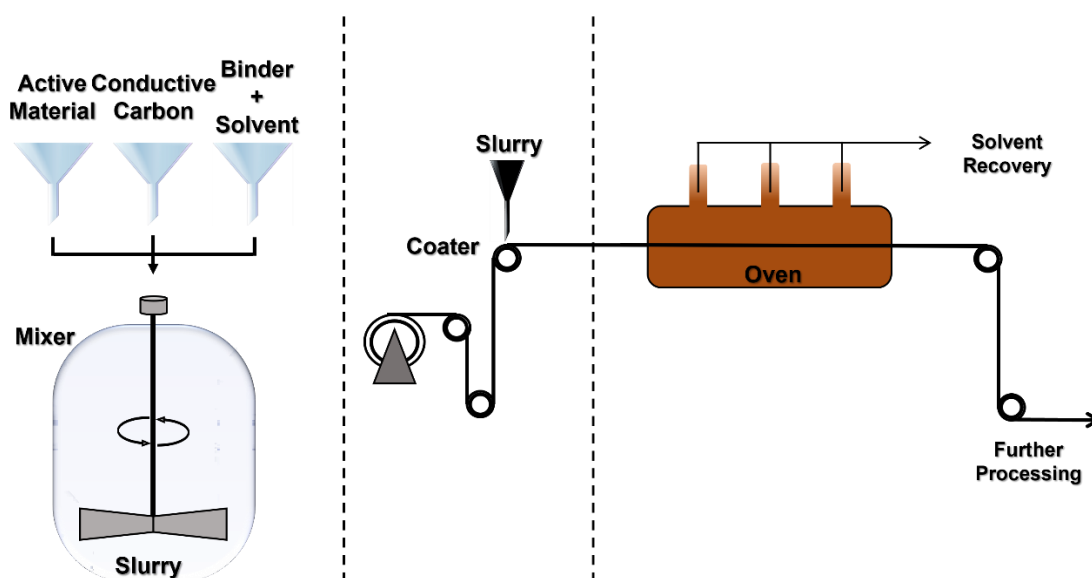


*Figure 1 - 10. Illustration of the manufacturing process of conventional electrodes. Adapted from [119].*

Potential batteries based on semi-solid electrodes completely changes the manufacturing process due to the absence of binder. The elimination of solvents and evaporation reduce the number of steps and make it environmentally friendlier.

### 1.6.3 Tortuosity, Kinetics and Electrochemical Performance

For conventional electrodes, the increasing internal resistance mainly driven by hindered mass transport of ion through the porous electrode limits the maximum thickness accessible.<sup>120</sup>

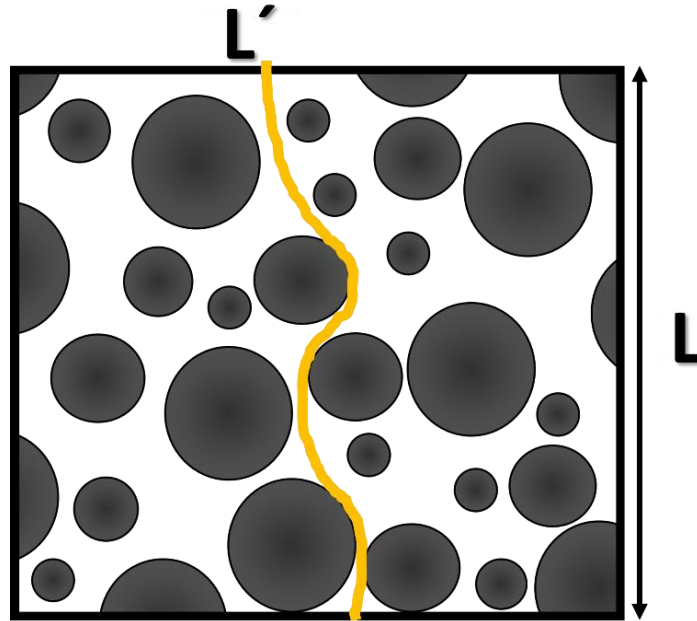


*Figure 1 - 11. Drawing representing the tortuosity of a porous media.*

The tortuosity is an intrinsic property of a porous media that defines the real path between two points. **Figure 1-11** shows the tortuosity as the ratio between the path of the real flow (yellow  $L'$ ) and the distance, in a straight line, from the beginning to the end of said path ( $L$ ).<sup>121</sup> This relationship is expressed according to the Bruggeman equation (**Equation 1-1**):

$$\tau = \varepsilon^{-\alpha} \quad [1-1]$$

Where  $\tau$  is the tortuosity,  $\varepsilon$  the porosity of the medium and  $\alpha$  the Bruggeman coefficient, (0.5 for spherical particles).<sup>122</sup> This relationship changes with the shape of the particles, as well as with the porosity of the electrode. Several studies were carried out to modify

this equation for fitting perfectly with experimental results obtained. From these studies, there is an upgraded equation for the tortuosity (**Equation 1-2**).<sup>123</sup>

$$\tau^2 = \gamma \cdot \varepsilon^{1-\alpha} \quad [1-2]$$

Being  $\gamma$  a correcting parameter calculated experimentally for each material individually as show in **Table 1-3**.

**Table 1 - 3. Value of “ $\gamma$ ” for different materials [123].**

<i>Material</i>	<i><math>\gamma</math></i>
<i>Battery Electrode / LiMn<sub>2</sub>O<sub>4</sub></i>	1
<i>Battery Electrode / LiFePO<sub>4</sub></i>	1.8
<i>Battery Electrode / LiCoO<sub>2</sub></i>	2.5
<i>Battery Electrode / Graphite</i>	0.11
<i>Battery Separator / Celgard 3501</i>	0.58

From these tortuosity values calculated for each individual case, it is possible to extract the effective diffusion coefficient of the ions (**Equation 1-3**) through the electrode.<sup>124</sup>

$$D_{eff} = \frac{\varepsilon}{\tau} D_0 \quad [1-3]$$

Where  $D_0$  is the diffusion coefficient of an ion in the electrolyte. As a result, the effective diffusivity through a porous electrode is always lower than that in the electrolyte. In a battery, the lower effective diffusivity limits the transport of ions along the electrode, generating concentration gradients and inducing overpotentials.<sup>125</sup> The thicker the electrode is, the higher gradient and the larger overpotentials.

Semi-solid electrodes address the issue of mass transport via double aspect. On the one hand, the binder was reported to increase the tortuosity so that the absence of binder in semi-solid electrode should lead to lower tortuosity.<sup>107</sup> On the other hand, the porosity

plays a key role in the effective diffusion coefficient, so that semi-solid electrodes having easily tunable porosities can be designed to maximize diffusivity.

As discussed, semi-solid electrodes possess intrinsic advantages over conventional electrode, but they can offer untapped features and characteristics that could be used as foundations of innovative technologies.<sup>126,127</sup>

## 1.7 References

1. Installed power generation capacity by source in the Stated Policies Scenario, 2000-2040 – Charts – Data & Statistics - IEA.
2. Olabi, A. G. *et al.* Critical review of energy storage systems. *Energy* **214**, 118987 (2021).
3. Rugolo, J. & Aziz, M. J. Electricity storage for intermittent renewable sources. *Energy Environ. Sci.* **5**, 7151–7160 (2012).
4. Guney, M. S. & Tepe, Y. Classification and assessment of energy storage systems. *Renew. Sustain. Energy Rev.* **75**, 1187–1197 (2017).
5. Koochi-Fayegh, S. & Rosen, M. A. A review of energy storage types, applications and recent developments. *J. Energy Storage* **27**, 101047 (2020).
6. European Commission, official website. [https://ec.europa.eu/info/index\\_en](https://ec.europa.eu/info/index_en).
7. The European Association for Storage of Energy. <https://ease-storage.eu/>.
8. Gür, T. M. Review of electrical energy storage technologies, materials and systems: Challenges and prospects for large-scale grid storage. *Energy Environ. Sci.* **11**, 2696–2767 (2018).
9. Stys, Z. S. Mechanical energy storage. 29–46 (1980) doi:10.1016/b978-0-12-814100-7.00003-1.
10. Mahmoud, M., Ramadan, M., Olabi, A. G., Pullen, K. & Naher, S. A review of mechanical energy storage systems combined with wind and solar applications. *Energy Convers. Manag.* **210**, 112670 (2020).
11. Henry, A., Prasher, R. & Majumdar, A. Five thermal energy grand challenges for decarbonization. *Nat. Energy* **5**, 635–637 (2020).
12. Jouhara, H., Żabnieńska-Góra, A., Khordehgah, N., Ahmad, D. & Lipinski, T. Latent thermal energy storage technologies and applications: A review. *Int. J. Thermofluids* **5–6**, 100039 (2020).
13. Abedin, A. H. & Rosen, M. A. A Critical Review of Thermochemical Energy Storage Systems. *Open Renew. Energy J.* **4**, 42–46 (2011).
14. Malley-Ernewein, A. & Lorente, S. Analysis of thermochemical energy storage in an elemental configuration. *Sci. Rep.* **9**, 1–9 (2019).
15. Mohtadi, R. & Orimo, S. I. The renaissance of hydrides as energy materials. *Nat. Rev. Mater.* **2**, 1–15 (2016).

16. Gallo, A. B., Simões-Moreira, J. R., Costa, H. K. M., Santos, M. M. & Moutinho dos Santos, E. Energy storage in the energy transition context: A technology review. *Renew. Sustain. Energy Rev.* **65**, 800–822 (2016).
17. Chen, H. *et al.* Progress in electrical energy storage system: A critical review. *Prog. Nat. Sci.* **19**, 291–312 (2009).
18. Hameer, S. & van Niekerk, J. L. A review of large-scale electrical energy storage. *Int. J. Energy Res.* **39**, 1179–1195 (2015).
19. González, A., Goikolea, E., Barrena, J. A. & Mysyk, R. Review on supercapacitors: Technologies and materials. *Renew. Sustain. Energy Rev.* **58**, 1189–1206 (2016).
20. Béguin, F., Presser, V., Balducci, A. & Frackowiak, E. Carbons and Electrolytes for Advanced Supercapacitors. *Adv. Mater.* **26**, 2219–2251 (2014).
21. Aneke, M. & Wang, M. Energy storage technologies and real life applications – A state of the art review. *Appl. Energy* **179**, 350–377 (2016).
22. He, P. *et al.* Building Better Zinc-ion Batteries: A Materials Perspective. *EnergyChem* **100022**, 100022 (2019).
23. Luo, X., Wang, J., Dooner, M. & Clarke, J. Overview of current development in electrical energy storage technologies and the application potential in power system operation. *Appl. Energy* **137**, 511–536 (2015).
24. Chen, H. *et al.* Progress in electrical energy storage system: A critical review. *Prog. Nat. Sci.* **19**, 291–312 (2009).
25. M. G. Molina. Energy Storage and Power Electronics Technologies: A Strong Combination to Empower the Transformation to the Smart Grid. in *Proceedings of the IEEE* vol. 105 2191–2219 (2017).
26. de Sisternes, F. J., Jenkins, J. D. & Botterud, A. The value of energy storage in decarbonizing the electricity sector. *Appl. Energy* **175**, 368–379 (2016).
27. Reddy, T. B. LINDEN’S HANDBOOK OF BATTERIES. (2011).
28. Palacín, M. R. Recent advances in rechargeable battery materials: A chemist’s perspective. *Chem. Soc. Rev.* **38**, 2565–2575 (2009).
29. Cheng, F., Chen, J., Gou, X. & Shen, P. High-power alkaline Zn-MnO<sub>2</sub> batteries using  $\gamma$ -MnO<sub>2</sub> nanowires/nanotubes and electrolytic zinc powder. *Adv. Mater.* **17**, 2753–2756 (2005).
30. Zhang, N. *et al.* Rechargeable aqueous zinc-manganese dioxide batteries with high energy and power densities. *Nat. Commun.* **8**, 1–9 (2017).

31. Kurzweil, P. Gaston Planté and his invention of the lead-acid battery-The genesis of the first practical rechargeable battery. *J. Power Sources* **195**, 4424–4434 (2010).
32. Bullock, K. R. Lead/acid batteries. *J. Power Sources* **51**, 1–17 (1994).
33. Battery Comparison of Energy Density - Cylindrical and Prismatic Cells. <https://www.epectec.com/batteries/cell-comparison.html>.
34. Jung, J., Zhang, L. & Zhang, J. Lead-Acid Battery Technologies. *Lead-Acid Batter. Technol.* (2015).
35. Ovshinsky, S. R., Fetcenko, M. A. & Ross, J. A nickel metal hydride battery for electric vehicles. *Science (80-. )*. **260**, 176–181 (1993).
36. Chan, C. C. & Wong, Y. S. Electric vehicles charge forward. *IEEE Power Energy Mag.* **2**, 24–33 (2004).
37. Blurton, K. F. & Sammells, A. F. Metal/air batteries: Their status and potential - a review. *J. Power Sources* **4**, 263–279 (1979).
38. Liu, Q., Pan, Z., Wang, E., An, L. & Sun, G. Aqueous metal-air batteries: Fundamentals and applications. *Energy Storage Mater.* **27**, 478–505 (2020).
39. Skyllas-Kazacos, M. Electro-chemical energy storage technologies for wind energy systems. *Stand-Alone Hybrid Wind Energy Syst.* 323–365 (2010) doi:10.1533/9781845699628.2.323.
40. Skyllas-Kazacos, M., Rychcik, M., Robins, R. G., Fane, A. G. & Green, M. A. New All-Vanadium Redox Flow Cell. *J. Electrochem. Soc.* **133**, 1057–1058 (1986).
41. Whittingham, M. S. The Role of Ternary Phases in Cathode Reactions. *J. Electrochem. Soc.* **123**, 315–320 (1976).
42. Whittingham, M. S. Chemistry of intercalation compounds: Metal guests in chalcogenide hosts. *Prog. Solid State Chem.* **12**, 41–99 (1978).
43. Mizushima, K., Jones, P. C., Wiseman, P. J. & Goodenough, J. B.  $\text{Li}_x\text{CoO}_2$  ( $0 < x < 1$ ): A new cathode material for batteries of high energy density. *Mater. Res. Bull.* **15**, 783–789 (1980).
44. Yoshino, A., Sanechika, K. & Nakajima, T. US4668595A - Secondary battery. No. 19 (1986).
45. Hawley, G. C. & Associates, &. Natural Graphite versus Synthetic, Silicon and Others in Lithium Ion Battery Anodes.
46. Peters, J. F., Baumann, M., Zimmermann, B., Braun, J. & Weil, M. The

- environmental impact of Li-Ion batteries and the role of key parameters – A review. *Renew. Sustain. Energy Rev.* **67**, 491–506 (2017).
47. Pillot, C. The Rechargeable Battery Market and Main Trends 2012-2025. *Avicenne Energy* (2019).
  48. Duffner, F. *et al.* Post-lithium-ion battery cell production and its compatibility with lithium-ion cell production infrastructure. *Nat. Energy* **6**, 123–134 (2021).
  49. Ponce de León, C., Frías-Ferrer, A., González-García, J., Szánto, D. A. & Walsh, F. C. Redox flow cells for energy conversion. *J. Power Sources* **160**, 716–732 (2006).
  50. COMMITTEE AND THE COMMITTEE OF THE REGIONS Critical Raw Materials Resilience: Charting a Path towards greater Security and Sustainability 1.
  51. Arbabzadeh, M., Johnson, J. X., De Kleine, R. & Keoleian, G. A. Vanadium redox flow batteries to reach greenhouse gas emissions targets in an off-grid configuration. *Appl. Energy* **146**, 397–408 (2015).
  52. Fernandez-Marchante, C. M., Millán, M., Medina-Santos, J. I. & Lobato, J. Environmental and Preliminary Cost Assessments of Redox Flow Batteries for Renewable Energy Storage. *Energy Technol.* **8**, 1900914 (2020).
  53. Lithium-Ion Battery - Clean Energy Institute.
  54. Sánchez-Díez, E. *et al.* Redox flow batteries: Status and perspective towards sustainable stationary energy storage. *J. Power Sources* **481**, (2021).
  55. Yang, G. *et al.* Improving the cyclability performance of lithium-ion batteries by introducing lithium difluorophosphate (LiPO<sub>2</sub>F<sub>2</sub>) additive. *RSC Adv.* **7**, 26052–26059 (2017).
  56. Xu, J., Deshpande, R. D., Pan, J., Cheng, Y.-T. & Battaglia, V. S. Electrode Side Reactions, Capacity Loss and Mechanical Degradation in Lithium-Ion Batteries. *J. Electrochem. Soc.* **162**, A2026–A2035 (2015).
  57. Pender, J. P. *et al.* Electrode Degradation in Lithium-Ion Batteries. *ACS Nano* **14**, 1243–1295 (2020).
  58. Vaalma, C., Buchholz, D., Weil, M. & Passerini, S. A cost and resource analysis of sodium-ion batteries. *Nat. Rev. Mater.* **3**, 1–11 (2018).
  59. Mongird, K. *et al.* Energy Storage Technology and Cost Characterization Report. (2019).
  60. Yang, Y. *et al.* Improved energy density and temperature range of vanadium redox

- flow battery by controlling the state of charge of positive electrolyte. *J. Power Sources* **450**, 227675 (2020).
61. Lyu, P. *et al.* Recent advances of thermal safety of lithium ion battery for energy storage. *Energy Storage Mater.* **31**, 195–220 (2020).
  62. Wang, W. *et al.* Recent progress in redox flow battery research and development. *Adv. Funct. Mater.* **23**, 970–986 (2013).
  63. Ponrouch, A. & Rosa Palacín, M. Post-Li batteries: Promises and challenges. *Philos. Trans. R. Soc. A Math. Phys. Eng. Sci.* **377**, (2019).
  64. Zhang, H., Liu, X., Li, H., Hasa, I. & Passerini, S. Challenges and Strategies for High-Energy Aqueous Electrolyte Rechargeable Batteries. *Angew. Chemie - Int. Ed.* **60**, 598–616 (2021).
  65. Alias, N. & Mohamad, A. A. Advances of aqueous rechargeable lithium-ion battery: A review. *J. Power Sources* **274**, 237–251 (2015).
  66. Li, W. & Dahn, J. R. Lithium-Ion Cells with Aqueous Electrolytes. *J. Electrochem. Soc.* **142**, 1742–1746 (1995).
  67. Wang, Y., Yi, J. & Xia, Y. Recent progress in aqueous lithium-ion batteries. *Adv. Energy Mater.* **2**, 830–840 (2012).
  68. Islam, J., Chowdhury, F. I., Uddin, J., Amin, R. & Uddin, J. Review on carbonaceous materials and metal composites in deformable electrodes for flexible lithium-ion batteries. *RSC Adv.* **11**, 5958–5992 (2021).
  69. Zeng, L., Qiu, L. & Cheng, H. M. Towards the practical use of flexible lithium ion batteries. *Energy Storage Mater.* **23**, 434–438 (2019).
  70. Cha, H., Kim, J., Lee, Y., Cho, J. & Park, M. Issues and Challenges Facing Flexible Lithium-Ion Batteries for Practical Application. *Small* **14**, 1702989 (2018).
  71. Skundin, A. M., Kulova, T. L. & Yaroslavtsev, A. B. Sodium-Ion Batteries (a Review). *Russ. J. Electrochem.* **54**, 131–174 (2018).
  72. Li, F. *et al.* Recent advances in cathode materials for rechargeable lithium–sulfur batteries. *Nanoscale* **11**, 15418–15439 (2019).
  73. Peng, H. J., Huang, J. Q., Cheng, X. B. & Zhang, Q. Review on High-Loading and High-Energy Lithium–Sulfur Batteries. *Adv. Energy Mater.* **7**, 1700260 (2017).
  74. Park, J., Yu, S. H. & Sung, Y. E. Design of structural and functional nanomaterials for lithium-sulfur batteries. *Nano Today* **18**, 35–64 (2018).
  75. Cano, Z. P. *et al.* Batteries and fuel cells for emerging electric vehicle markets. *Nat. Energy* **3**, 279–289 (2018).

76. Kim, J. G. *et al.* A review of lithium and non-lithium based solid state batteries. *J. Power Sources* **282**, 299–322 (2015).
77. Lim, H. D. *et al.* A review of challenges and issues concerning interfaces for all-solid-state batteries. *Energy Storage Mater.* **25**, 224–250 (2020).
78. Aurbach, D., McCloskey, B. D., Nazar, L. F. & Bruce, P. G. Advances in understanding mechanisms underpinning lithium-air batteries. *Nat. Energy* **1**, 1–11 (2016).
79. Lee, Y. G. *et al.* High-energy long-cycling all-solid-state lithium metal batteries enabled by silver–carbon composite anodes. *Nat. Energy* **5**, 299–308 (2020).
80. Geng, D. *et al.* From Lithium-Oxygen to Lithium-Air Batteries: Challenges and Opportunities. *Adv. Energy Mater.* **6**, 1502164 (2016).
81. Imanishi, N. & Yamamoto, O. Perspectives and challenges of rechargeable lithium–air batteries. *Mater. Today Adv.* **4**, 100031 (2019).
82. Winsberg, J., Hagemann, T., Janoschka, T., Hager, M. D. & Schubert, U. S. Redox-Flow Batteries: From Metals to Organic Redox-Active Materials. *Angew. Chemie - Int. Ed.* **56**, 686–711 (2017).
83. Wang, W. & Sprenkle, V. Redox flow batteries go organic. *Nat. Chem.* **8**, 204–206 (2016).
84. Brushett, F. R., Aziz, M. J. & Rodby, K. E. On Lifetime and Cost of Redox-Active Organics for Aqueous Flow Batteries. *ACS Energy Lett.* **5**, 879–884 (2020).
85. Kwabi, D. G. *et al.* Alkaline Quinone Flow Battery with Long Lifetime at pH 12. *Joule* **2**, 1894–1906 (2018).
86. Xu, Y., Wen, Y. H., Cheng, J., Cao, G. P. & Yang, Y. S. A study of tiron in aqueous solutions for redox flow battery application. *Electrochim. Acta* **55**, 715–720 (2010).
87. Hollas, A. *et al.* A biomimetic high-capacity phenazine-based anolyte for aqueous organic redox flow batteries. *Nat. Energy* **3**, 508–514 (2018).
88. Lin, K. *et al.* A redox-flow battery with an alloxazine-based organic electrolyte. *Nat. Energy* **1**, 1–8 (2016).
89. Liu, T., Wei, X., Nie, Z., Sprenkle, V. & Wang, W. A Total Organic Aqueous Redox Flow Battery Employing a Low Cost and Sustainable Methyl Viologen Anolyte and 4-HO-TEMPO Catholyte. *Adv. Energy Mater.* **6**, 1501449 (2016).
90. Janoschka, T. *et al.* An aqueous, polymer-based redox-flow battery using non-corrosive, safe, and low-cost materials. *Nature* **527**, 78–81 (2015).

91. Ferrigno, R., Stroock, A. D., Clark, T. D., Mayer, M. & Whitesides, G. M. Membraneless vanadium redox fuel cell using laminar flow. *J. Am. Chem. Soc.* **124**, 12930–12931 (2002).
92. Navalpotro, P., Palma, J., Anderson, M. & Marcilla, R. A Membrane-Free Redox Flow Battery with Two Immiscible Redox Electrolytes. *Angew. Chemie Int. Ed.* **56**, 12460–12465 (2017).
93. Dinesh, A. *et al.* Iron-based flow batteries to store renewable energies. *Environ. Chem. Lett.* **16**, 683–694 (2018).
94. Lloyd, D., Magdalena, E., Sanz, L., Murtomäki, L. & Kontturi, K. Preparation of a cost-effective, scalable and energy efficient all-copper redox flow battery. *J. Power Sources* **292**, 87–94 (2015).
95. Khor, A. *et al.* Review of zinc-based hybrid flow batteries: From fundamentals to applications. *Mater. Today Energy* **8**, 80–108 (2018).
96. Yu, W. *et al.* Toward a new generation of low cost, efficient, and durable metal-air flow batteries. *J. Mater. Chem. A* **7**, 26744–26768 (2019).
97. Wang, Y., He, P. & Zhou, H. Li-Redox Flow Batteries Based on Hybrid Electrolytes: At the Cross Road between Li-ion and Redox Flow Batteries. *Adv. Energy Mater.* **2**, 770–779 (2012).
98. Xue, T. & Fan, H. J. From aqueous Zn-ion battery to Zn-MnO<sub>2</sub> flow battery: A brief story. *J. Energy Chem.* **54**, 194–201 (2021).
99. Páez, T., Martínez-Cuezva, A., Palma, J. & Ventosa, E. Mediated alkaline flow batteries: From fundamentals to application. *ACS Appl. Energy Mater.* **2**, 8328–8336 (2019).
100. Jia, C. *et al.* High-energy density nonaqueous all redox flow lithium battery enabled with a polymeric membrane. *Sci. Adv.* **1**, e1500886 (2015).
101. Zanzola, E. *et al.* Solid electrochemical energy storage for aqueous redox flow batteries: The case of copper hexacyanoferrate. *Electrochim. Acta* **321**, 134704 (2019).
102. Zhu, Y. G. *et al.* Unleashing the Power and Energy of LiFePO<sub>4</sub>-Based Redox Flow Lithium Battery with a Bifunctional Redox Mediator. *J. Am. Chem. Soc.* **139**, 6286–6289 (2017).
103. Cheng, Y. *et al.* Redox Targeting-Based Vanadium Redox-Flow Battery. *ACS Energy Lett.* **4**, 3028–3035 (2019).
104. Ventosa, E. *et al.* Solid electrolyte interphase in semi-solid flow batteries: A Wolf

- in sheep's clothing. *Chem. Commun.* **51**, 14973–14976 (2015).
105. Ventosa, E., Amedu, O. & Schuhmann, W. Aqueous Mixed-Cation Semi-solid Hybrid-Flow Batteries. *ACS Appl. Energy Mater.* **1**, (2018).
  106. Duduta, M. *et al.* Semi-solid lithium rechargeable flow battery. *Adv. Energy Mater.* **1**, 511–516 (2011).
  107. Ventosa, E. *et al.* Non-aqueous semi-solid flow battery based on Na-ion chemistry. P2-type  $\text{Na}_x\text{Ni}_{0.22}\text{Co}_{0.11}\text{Mn}_{0.66}\text{O}_2\text{-NaTi}_2(\text{PO}_4)_3$ . *Chem. Commun.* **51**, 7298–7301 (2015).
  108. Park, M., Ryu, J., Wang, W. & Cho, J. Material design and engineering of next-generation flow-battery technologies. *Nat. Rev. Mater.* **2**, 16080 (2016).
  109. Dong, K., Wang, S. & Yu, J. A lithium/polysulfide semi-solid rechargeable flow battery with high output performance. *RSC Adv.* **4**, 47517–47520 (2014).
  110. Soavi, F., Ruggeri, I. & Arbizzani, C. Design Study of a Novel, Semi-Solid Li/O<sub>2</sub> Redox Flow Battery. *ECS Trans.* **72**, 1–9 (2016).
  111. Wei, J. *et al.* Hypersaline Aqueous Lithium-Ion Slurry Flow Batteries. *ACS Energy Lett.* **7**, 862–870 (2022).
  112. Zhu, Y. G. *et al.* High-energy and high-power Zn–Ni flow batteries with semi-solid electrodes. *Sustain. Energy Fuels* **4**, 4076–4085 (2020).
  113. Hatzell, K. B., Boota, M. & Gogotsi, Y. Materials for suspension (semi-solid) electrodes for energy and water technologies. *Chem. Soc. Rev.* **44**, 8664–8687 (2015).
  114. 24M Technologies.
  115. Kuang, Y., Chen, C., Kirsch, D. & Hu, L. Thick Electrode Batteries: Principles, Opportunities, and Challenges. *Adv. Energy Mater.* **9**, 1–19 (2019).
  116. Cheng, H. M. & Li, F. Charge delivery goes the distance. *Science (80-. )*. **356**, 582–583 (2017).
  117. Schilling, A., Schmitt, J., Dietrich, F. & Dröder, K. Analyzing Bending Stresses on Lithium-Ion Battery Cathodes induced by the Assembly Process. *Energy Technol.* **4**, 1502–1508 (2016).
  118. Kwade, A. *et al.* Current status and challenges for automotive battery production technologies. *Nat. Energy* **3**, 290–300 (2018).
  119. Costa, C. M. *et al.* Recycling and environmental issues of lithium-ion batteries: Advances, challenges and opportunities. *Energy Storage Mater.* **37**, 433–465 (2021).

120. Bae, C. J., Erdonmez, C. K., Halloran, J. W. & Chiang, Y. M. Design of battery electrodes with dual-scale porosity to minimize tortuosity and maximize performance. *Adv. Mater.* **25**, 1254–1258 (2013).
121. Kia, A., Wong, H. S. & Cheeseman, C. R. Clogging in permeable concrete: A review. *J. Environ. Manage.* **193**, 221–233 (2017).
122. Ebner, M., Chung, D. W., García, R. E. & Wood, V. Tortuosity anisotropy in lithium-ion battery electrodes. *Adv. Energy Mater.* **4**, 1301278 (2014).
123. Tjaden, B., Brett, D. J. L. & Shearing, P. R. Tortuosity in electrochemical devices: a review of calculation approaches. (2016) doi:10.1080/09506608.2016.1249995.
124. Ebner, M. & Wood, V. Tool for Tortuosity Estimation in Lithium Ion Battery Porous Electrodes. *J. Electrochem. Soc.* **162**, A3064–A3070 (2015).
125. Landesfeind, J., Ebner, M., Eldiven, A., Wood, V. & Gasteiger, H. A. Tortuosity of Battery Electrodes: Validation of Impedance-Derived Values and Critical Comparison with 3D Tomography. *J. Electrochem. Soc.* **165**, A469–A476 (2018).
126. Muñoz-Torrero, D., Palma, J., Marcilla, R. & Ventosa, E. Al-Ion Battery Based on Semisolid Electrodes for Higher Specific Energy and Lower Cost. *ACS Appl. Energy Mater.* **3**, 2285–2289 (2020).
127. Landesfeind, J., Eldiven, A. & Gasteiger, H. A. Influence of the Binder on Lithium Ion Battery Electrode Tortuosity and Performance. *J. Electrochem. Soc.* **165**, A1122–A1128 (2018).



## **Chapter 2. Objectives**

The main objective of this doctoral dissertation is to contribute to push the boundaries of knowledge in batteries by the development of innovative battery technologies based on the use of semi-solid electrodes. To achieve this overall goal, specific objectives were defined and described as follows:

### **Objective 1. Understanding and tuning of semi-solid electrodes properties**

The performance of any device based on semi-solid electrodes will be highly dependent on the properties of these electrode. Thus, the tunable properties need to be first investigated separately, adopting the necessary analytical techniques when no standard methods were established. **Chapter 3** aims to this objective, in which three key parameters are studied: rheology, ionic conductivity, and electrical conductivity. This objective pursues to find answer to the following questions: Do semi-solid electrodes behave as a solid or a liquid? What about electrical and ionic conductivities of this kind of electrodes? And is it possible to tune the properties of the electrodes?

The initial hypotheses are: i) Semi-solid electrodes have a non-newtonian behavior, changing their rheology depending on the pressure applied. ii) Electrical and ionic conductivities should be able to be achieved, so that these electrodes can be implemented in a battery. iii) The rheology, electrical conductivity, and ionic conductivity of semi-solid electrodes can be tuned by adjusting the composition of the slurries.

### **Objective 2. Improvement in battery recyclability by demonstrating a new concept**

Battery recyclability has gained importance in pursue of advancing towards circularity in this field. Thus, the second specific objective is to demonstrate a new battery concept designed to facilitate static battery recyclability by the use of semi-solid electrodes. In **Chapter 4** of this thesis, the injectable battery concept based on easily replaceable semi-solid electrode is explored. Instead of fixing active materials inside the battery, a pre-assembled cell is filled with “semi-flowable” semi-solid electrode, which largely

facilitate recyclability after the end-of-life is reached. In this chapter answers for the following questions will be searched: It is possible to replace the active material of a static battery? Can the battery recovery its initial performance after a simple substitution of semi-solid electrodes? How can affect this on the economic perspective? And what about the environmental perspective?

The initial hypotheses considered here are: i) The semi-solid electrodes will enable the replacement of the active material via removal of spent electrode and injection of fresh semi-solid electrodes thanks to their flowable properties. ii) Proper formulation of semi-solid electrodes will allow for high areal capacity batteries, reducing the cost of the system. iii) The possibility of extracting the semi-solid electrodes from the battery will simplify the recycling process and reduce the number of steps.

**Objective 3. Extending the use of semi-solid electrodes for low-cost battery chemistries:**

**Zn – MnO<sub>2</sub>**

Since the injectable battery should enable direct reuse of the battery cell, this concept should be especially suitable for cheap battery chemistries in which the contribution of the cell cost (inactive materials) is more pronounced. This objective covered in **Chapter 5** aims to evaluate the feasibility of using semi-solid electrodes for low-cost Zn – MnO<sub>2</sub> battery. Chapter 5 answers the following questions: Are electrochemical reaction involved in Zn and MnO<sub>2</sub> proceed in the form of semi-solid electrodes? Does the pH of the electrolyte affect negatively to the electrochemical performance of the battery? Is it possible to control the pH while the battery is cycling to expand its lifespan?

The initial hypotheses considered here are: i) Semi-solid electrodes should be compatible with any electrochemical charge storage mechanism. ii) Semi-solid electrodes enabling high areal capacities and direct reuse of the entire battery cell have a great economic impact for Zn – MnO<sub>2</sub> batteries. iii) There is spontaneous reaction that increase the pH

value of the electrolyte in this battery that can lead to an alkaline value which generates insoluble and undesired products.

**Objective 4. Exploiting the features of semi-solid electrodes for zinc – air battery**

The concept of mechanically rechargeable zinc – air batteries have been long pursued as a holistic solution to overcome the limiting aspects of this technology. The specific objective discussed in **Chapter 6** aims to revive this long-desired concept by exploiting the unique features of semi-solid electrodes. In chapter 6, answers for the following questions are sought: Is it possible to design an operational mechanically recharge Zn - Air battery using semi-solid electrode? Do Zn semi-solid electrode possess enough specific charge capacity and specific power? And what about the possibility of power density improvements?

The initial hypotheses considered here are: i) Zn semi-solid electrodes will allow the zinc – air system to be mechanically recharged in a simple way. ii) The tunable properties of semi-solid electrodes will enable boosting performance of mechanically rechargeable Zn – Air batteries. iii) The use of molecular wiring in the negative electrode will increase the power density of the system.

**Objective 5. Implementation of semi-solid electrodes in electrochemical ion pumping technology for Li recovery**

The increasing demand of Li may not be met by conventional slow and inefficient Li extraction currently used. The electrochemical ion pumping technique is a very promising technique for efficient Li recovery. The main challenge is the relatively short cycle life. The implementation of semi-solid electrodes in this technology will thus address this main issue since the regeneration of the systems will be largely facilitate. The specific objective pursued in **Chapter 7** aims to explore the implantation of semi-solid electrode in electrochemical ion pumping for Li recovery. In chapter 7, answers for the following

questions are sought: Is it possible to replace the active-faradaic materials of an electrochemical ion pumping cell when the life of the battery ends? How can affect the use of semi-solid electrodes in ion capturing technologies?

The initial hypotheses considered here are: i) Semi-solid electrodes allow the system to be regenerated easily while prolonging the life of the device. ii) The possibility of increasing the mass loading of active materials in semi-solid electrodes leads to an improvement of lithium-ion capturing capacity iii) The versatility of semi-solid electrodes makes them compatible with different configurations and cell design of this technology.





# **Chapter 3. Semi-Solid Electrodes for Static Batteries**

### 3.1 Introduction

As detailed in **Chapter 1**, the possibility of making thicker electrodes when using semi-solid electrode in static batteries have a great impact in the system, affecting the areal capacity, energy density and cost.<sup>1</sup> In addition mechanical stability of thick conventional electrodes can be problematic.<sup>2-4</sup> This is the reason why it is necessary to look for a new solutions when thicker electrodes are going to be used in static batteries.

Semi-solid flow electrodes were proposed in 2011 as a new technology for their use in flow batteries, merging the benefits of using solid materials and flow battery configuration. These electrodes were composed by less than 1 % of carbon additive to create the percolating network necessary for the electrical conductivity between active materials and current collectors.<sup>5</sup>

The concepts developed along this thesis employs this kind of electrodes, but their unique features are exploited for static batteries. As demonstrated by the company 24M technologies founded in 2010, the implementation of semi-solid electrodes in static lithium-ion batteries implies advantages, e.g. increase in thickness of the electrodes. However, the electrodes employed by 24M sacrifice another unique characteristic, i.e. flowability.<sup>6</sup> Therefore, the aim in this thesis is to develop semi-solid electrode having the advantageous features of semi-solid electrode in terms of tunable porosity and maintain enough flowability to be injected in pre-assembled battery cells. In this way, not only batteries of high areal capacities will be pursued, but the manufacturing process and more importantly the recycling process will be radically changed with respect to conventional static batteries.

Achieving semi-solid electrode having the desired properties (in between flow and static semi-solid electrodes) requires the tuning of their formulation. For this reason, this **Chapter 3** is dedicated to investigating the influence of the formulation on of the semi-

solid electrodes on their final characteristics. While electrical and ionic conductivity are known to play a critical role in the electrochemical performance of batteries,<sup>7,8</sup> in our case the rheological properties are also considered.

The key differentiation of semi-solid electrodes is the absence of binder. The type of electrodes is composed by electrolyte (liquid), solid active material, carbon additive. Obviously different types of additives can be added in the formulation such as stabilizer. The ions-containing electrolyte provides the necessary ionic conductivity, while the carbon additive not only enhances electrical conductivity, but also strongly influences the texture of the suspension.<sup>9</sup>

Since the field of semi-solid electrode is still emerging, there is a lack of established methodology for fundamental studies. Electrochemical Impedance Spectroscopy has been widely used in the field of batteries to study a variety of processes occurring at different timescales. In addition, this highly sensitive and non-invasive technique has been used to study mixed ionic-electric conductor.<sup>10</sup> Both contribution can be evaluated as EIS enable deconvoluting their contribution as a function of the timescale.<sup>11,12</sup> Therefore, EIS is chosen as the main tool for developing a methodology that enable investigating the properties of semi-solid electrodes in this chapter.

## 3.2 Experimental Procedures

### 3.2.1 Reagents and Materials

The electrochemical cell. The external case was designed and printed by 3D-Printing machine (MakerBot Replicator™ 2X) using ABS as plastic material. Expanded graphite (Sigracet TF6) was used as current collector. Materials. Reagents were used as received: carbon additive KetjenBlack EC-600 JD (Azelis and AkzoNovel polymer chemicals), polyvinylpyrrolidone (Sigma Aldrich),  $\text{Zn}_2\text{SO}_4 \cdot 7\text{H}_2\text{O}$  ( $\geq 99.5\%$ , Sigma Aldrich), KOH ( $\geq 85\%$ , Sigma Aldrich).

Electrode preparation. Semi-solid electrodes (slurry) with different compositions were prepared containing carbon (KetjenBlack) and in some cases polyvinylpyrrolidone as stabilizer. The solid particles were dispersed in the electrolyte. The suspension was mixed with Ultra-Turrax IKA T18-Basic during three periods of 10 minutes resting 5 minutes between periods. The slurries were prepared directly in a syringe to facilitate the injection of the electrode into the battery pre-assembled.

### 3.2.2 Rheological Measurements

The rheological measurements were conducted by using a Rheometer HAAKE RheoStress RS600 from Thermo Electron Corp.

### 3.2.3 Electrochemical Measurements

Electrochemical impedance Spectroscopy with two electrode experiments were conducted by using one of the current collectors as working electrode, and the other one as reference and counter electrode. The frequency ranges from 100 kHz to 100 mHz, and amplitude of 20 mV starting from 0V vs. reference electrode were the conditions imposed. The potentiostat used for these experiments was an Autolab PGSTAT302N model.

### 3.3 Results and Discussion

In this section, the properties of semi-solid electrodes used in this doctoral thesis are studied. While rheological properties are evaluated using an established technique (rheometer), a home-made separator-free cell is fabricated to assess ionic and electrical properties of this new type of electrodes.

#### 3.3.1 Rheology of Semi-solid Electrodes

Rheological properties of semi-solid electrodes have been previously studied for their deployment in flow batteries,<sup>13–15</sup> While the absolute values of our semi-flowable electrode will certainly be different, it is expected that the non-Newtonian behavior is maintained. Previously studied flowable semi-solid electrode were classified as thixotropic, defined as a “term used in rheology which means that the viscosity of a material decreases significantly with the time of shearing and then, increases significantly when the force inducing the flow is removed”.<sup>16</sup> To explore whether our semi-flowable semi-solid electrode maintained this type of rheological behavior, a formulation of slurry that will be implemented in injectable batteries in the following chapter was studied. **Figure 3-1** show the viscosity of a semi-solid electrode containing Lithium iron Phosphate (LFP) and carbon additive (KetjenBlack), 77 wt.% ( $0.195 \text{ g mL}^{-1}$ ) and 23 wt.% ( $0.0625 \text{ g mL}^{-1}$ ) respectively, mixed into a water-based electrolyte as a function of the shear rate.

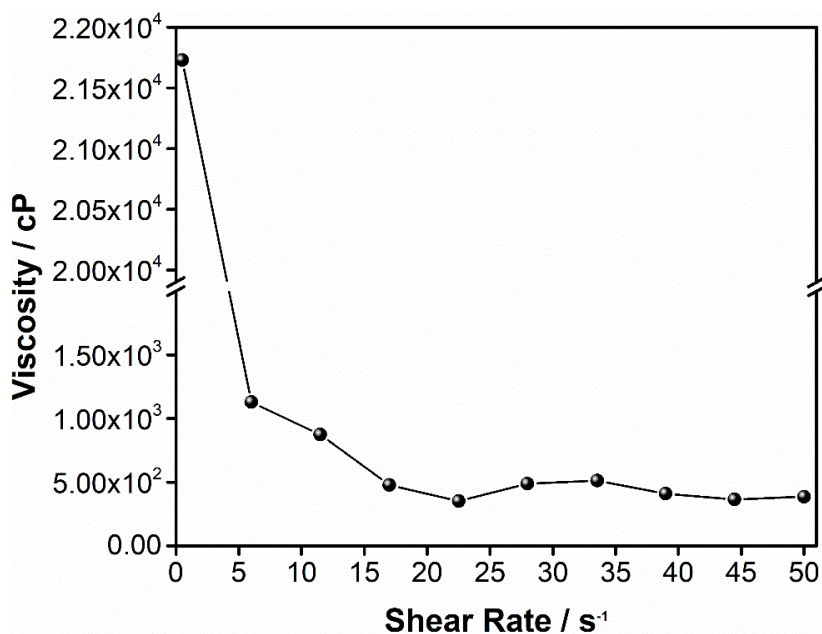


*Figure 3 - 1. Rheological behavior of a semi-solid electrode containing LFP, carbon additive, and electrolyte.*

The results confirmed that the behavior of this electrode is thixotropic, decreasing its viscosity when the shear rate increases.<sup>17</sup> This means that viscosity of the semi-solid electrode will increase when the flow stopped after the injection. This behavior is very beneficial for our application since it will facilitate the injection process, while the increase in viscosity once the cell is completely filled with semi-solid electrode will help preventing sedimentation during operation of the static battery.

### 3.3.2 Electrochemical Cell for Assessment of Electrical and Ionic Properties

Conventional battery cells are composed of current collectors, porous electrodes and separator packed as shown in **Figure 3-2a**. This configuration complicates the estimation and quantification of the electrical resistance of the system by Electrochemical Impedance Spectroscopy (EIS) techniques. Specifically, the presence of the separator impedes the flow of electrons between current collectors. This element is necessary for

avoiding short-circuit in an operation battery, but it hinders determination of their electrical properties.

Thus, it is necessary to design a cell without separator which also enable being filled with semi-solid electrodes. Only two elements are required for this cell: two current collector and a semi-solid electrode filling the gap between them, as illustrated in **Figure 3-2b**. The use of Electrochemical Impedance Spectroscopy in this new cell configuration will allow determination of both ionic and electrical properties of the semi-solid electrodes by using the theory developed for mixed ionic-electric conductors.



*Figure 3 - 2. Cell design for (a) Conventional battery and (b) Separator-free configuration for determination of electrical properties of semi-solid electrodes.*

**Figure 3-3** shows the scheme of the cell designed for this work and its components. This cell consists of two expanded graphite electrodes used as blocking electrodes, separated by a gasket in which the semi-solid electrode is located (2 mm thick and 7.5 cm<sup>2</sup> area). Two end-plates fabricated using 3D FDM printing are used to keep the part together.

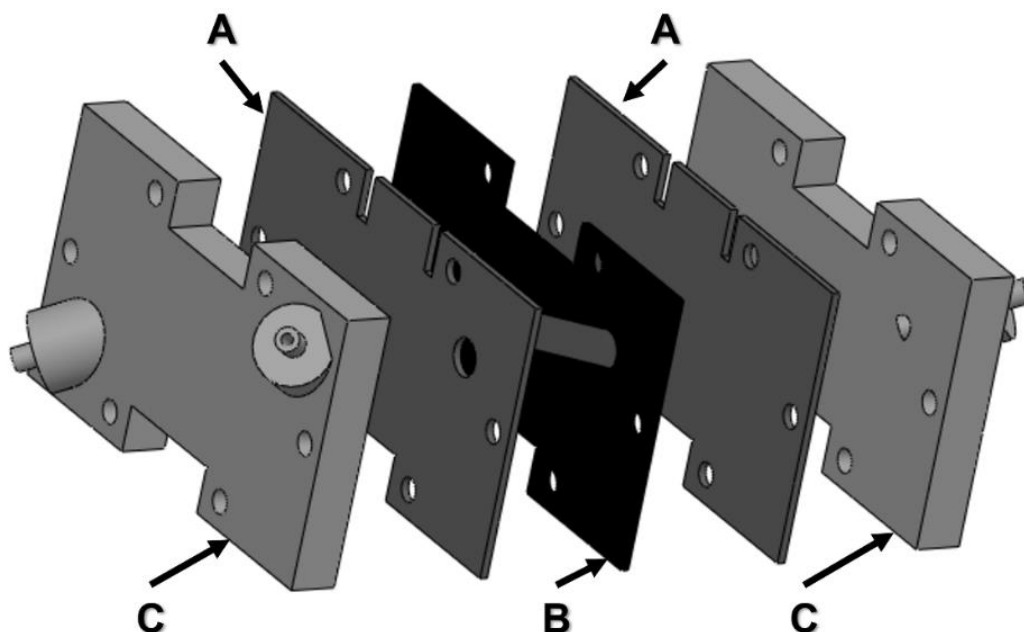


*Figure 3 - 3. Design scheme of the separator-free symmetrical cell containing (A) Expanded graphite, (B) Gasket and (C) ABS 3D printed case.*

### 3.3.3 Electrochemical Impedance Spectroscopy (EIS)

Electrochemical Impedance Spectroscopy (EIS) is an Alternating Current (AC) technique, so that it is used for measuring the response of a system to a sinusoidal perturbation as function of the frequency. This frequency domain, allows to evaluate different processes that take place at different time scales (charge transfer or mass transport), and even other electrical contributions will be visible.<sup>18</sup> Specifically, in this work, potentiostatic EIS was used which is based in applying an alternating voltage signal at around a given voltage value (open circuit voltage) given by the **Equation 3-1**.

$$E (V) = E_{ocv} + E_0 \cdot \sin(\omega \cdot t) \quad [3-1]$$

Where  $E_{ocv}$  is the open circuit voltage,  $E_0$  is the amplitude of the applied sinusoidal signal (Volts), and  $\omega$  the angular frequency defined as  $\omega = 2 \cdot \pi \cdot f$ , being  $f$  the alternating frequency of the voltage signal ( $s^{-1}$ ).

In a lineal system, it is possible to obtain a current defined by **Equation 3-2**.<sup>19</sup>

$$I(A) = I_0 \cdot \sin(\omega \cdot t + \phi) \quad [3-2]$$

Where I is the current response (Ampere),  $I_0$  its amplitude and  $\phi$  the phase shift between both E and I signals. It is possible to define the value of the Impedance (Z) of the system by the **Equation 3-3**.<sup>19</sup>

$$Z = \frac{E}{I} = \frac{E_0 \cdot \sin(\omega \cdot t)}{I_0 \cdot \sin(\omega \cdot t + \phi)} = Z_0 \cdot \frac{\sin(\omega \cdot t)}{\sin(\omega \cdot t + \phi)} \quad [3-3]$$

In order to simplify the calculation of impedances, it is necessary to change to complex notation, where the impedance of the system could be expressed as follows (**Equation 3-4**).<sup>19</sup>

$$Z (\Omega) = Z' + j \cdot Z'' \quad [3-4]$$

Where  $j = \sqrt{-1}$ . Since the electrochemical systems are complex, the way for calculating the impedance is to translate the real electrochemical components of the system studied into its equivalents of a typical electronic circuit, by using four individual components: resistance, capacitor, inductor, and Warburg.<sup>20</sup>

- **Resistance:** The impedance of this component is defined as  $Z = R$ , so is independent of frequency, having only real part.
- **Capacitor:** For this component, the impedance is defined as  $Z = 1/(j \cdot \omega \cdot C)$ , decreasing when the frequency is increased, having only the imaginary part.
- **Inductor:** As the previous component, it only has imaginary part, but its impedance increases when the frequency increases. The impedance of this component is  $Z = j \cdot \omega \cdot L$ .
- **Warburg:** This component mixes both real and imaginary part, with a constant phase shift ( $\phi = 45^\circ$ ).

Due to the complexity of the electrochemical systems and the fact of working on the imaginary plane, there is diverse ways of representing the response of the system. One of the most used is the called “Nyquist plot” that shows the real part of the impedance ( $Z'$ )

on the x-axes and the negative imaginary part ( $-Z''$ ) on the y-axes for each frequency used in the experiment (**Figure 3-4a**).<sup>21</sup>

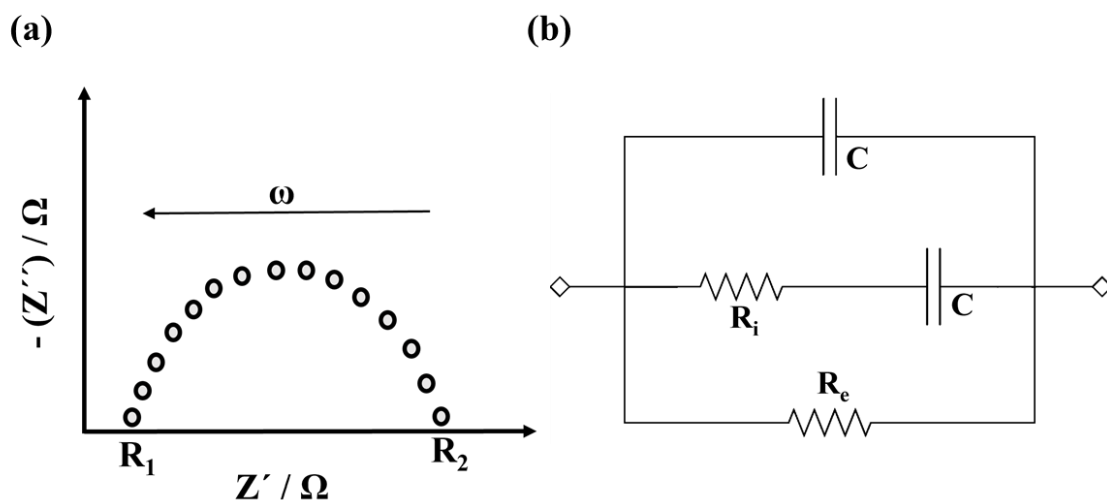


**Figure 3 - 4.** (a) Typical Nyquist plot for mixed ionic and electronic conductors, and (b) Equivalent electrical circuit.

This Nyquist plot shows the response of an electrochemical system, in this case, both real and imaginary parts are necessary to solve it. Among the various pieces of information to extract from this plot, some of the most relevant information is the related to the interceptions with the x-axes:  $R_1$  and  $R_2$ . These two values are used for calculating both ionic and electronic resistances of a mixed electric and ionic conductor. Specifically, the Nyquist plot represented in **Figure 3-4a**, correspond to the equivalent electrical circuit shown in **Figure 3-4b**, called “Debye circuit”. This equivalent circuit is used for mixed ionic and electronic conductors, being appropriate an model for this work,<sup>22</sup> where  $R_e$  and  $R_i$  are the electronic and ionic resistances, respectively.

The shape of the Nyquist plot can vary even when using the same equivalent circuit. The shape will be dependent on the ratio between electrical and ionic resistances.<sup>22</sup> Thus, there is three possibilities:

A) **Electrical resistance > Ionic resistance**: The shape of the Nyquist plot for this scenario is shown in the previous **Figure 3-4a**. At high frequencies, the current will flow

though the ionic resistance line, as  $R_i < R_e$ . At low frequency, the capacitor related to the ionic resistance will act as an open circuit impeding the flow of current through the ionic lines. Thus, the current at low frequencies will go through the electrical resistance line. In this case, both ionic and electrical resistance can be determined directly from the Nyquist plot:  $R_1 = R_i$  and  $R_2 = R_e$ .

B) **Electrical resistance < Ionic resistance**: In this case, the shape of the Nyquist plot resultant is the same as in scenario A). However, the high ionic resistance will impede flow of current through this line. As a result, the semicircle obtained is only due to the electronic resistance. Ideally, the origin of such semicircle should be 0 in X-axis since the current will flow through the capacitor at high frequencies (no real part). However, in practice the origin is never 0 since there is always either a small electrical resistance due to connection of cables and/or a small current leakage through the ionic line.

C) **Electrical resistance  $\approx$  Ionic resistance**: This is the most complex scenario due to the similar contribution of both electronic and ionic resistances. As a result, a second semicircle emerges in the Nyquist plot as shown in **Figure 3-5a**. These two semicircles represent the combination of resistances and capacitors, following the Debye equivalent circuit (**Figure 3-4b**).

At low frequencies, the current flow goes only through the resistance  $R_e$  of the circuit (equivalent to DC resistance). Therefore, the interception of the graph at low frequencies ( $R_2$ ) is directly the electrical resistance of the system. On the other hand, at high frequencies the current flow through different lines. Thus, the interception with the x-axis  $R_1$  is a combination of two parallel resistances, so that the ionic resistance must be calculated solving the equivalent circuit by the **Equation 3-5**.<sup>22</sup>

$$R_i = \frac{R_1 \cdot R_2}{R_2 - R_1} \quad [3-5]$$

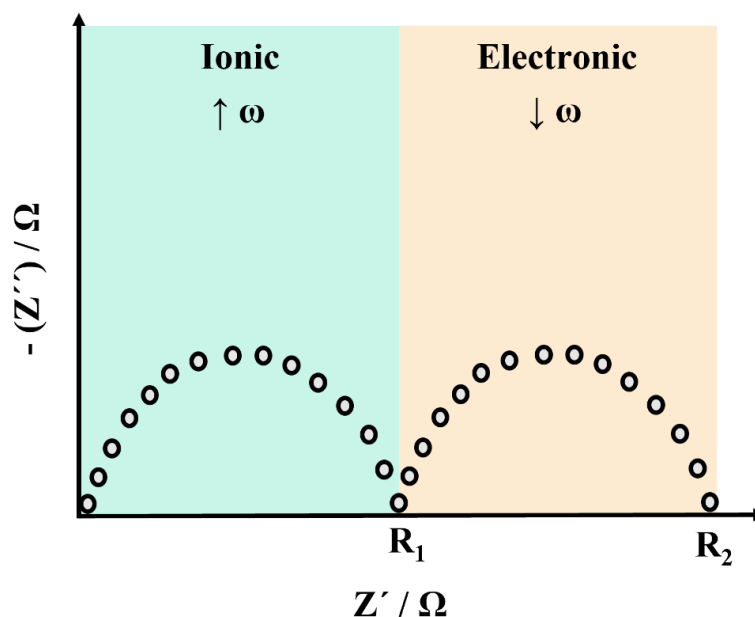


Figure 3 - 5. Nyquist plot for relevant mixed ionic and electronic transport.

### 3.3.4 Resistance Semi-solid Electrodes

In the conventional porous electrodes, electrical resistance is lower than the ionic resistance due to their low porosity. Semi-solid electrodes with higher porosity are anticipated to possess poorer electrical contacts. Thus, both electrical and ionic resistance of semi-solid electrode should be tunable by changing the carbon content.

#### 3.3.4.1 Effect of carbon content

The electrical percolation network of the semi-solid electrodes is one of the most important parameters to be study. To illustrate the effect of carbon content in the electrical and ionic resistance of the semi-solid electrode, the content of carbon KetjenBlack added into the formulation of the semi-solid electrode based on 6 M KOH was evaluated. **Figure 3-6** shows the Nyquist plot of different semi-solid electrodes with an electrolyte (6 M KOH in this case) containing suspended carbon particles as a function of the carbon content.

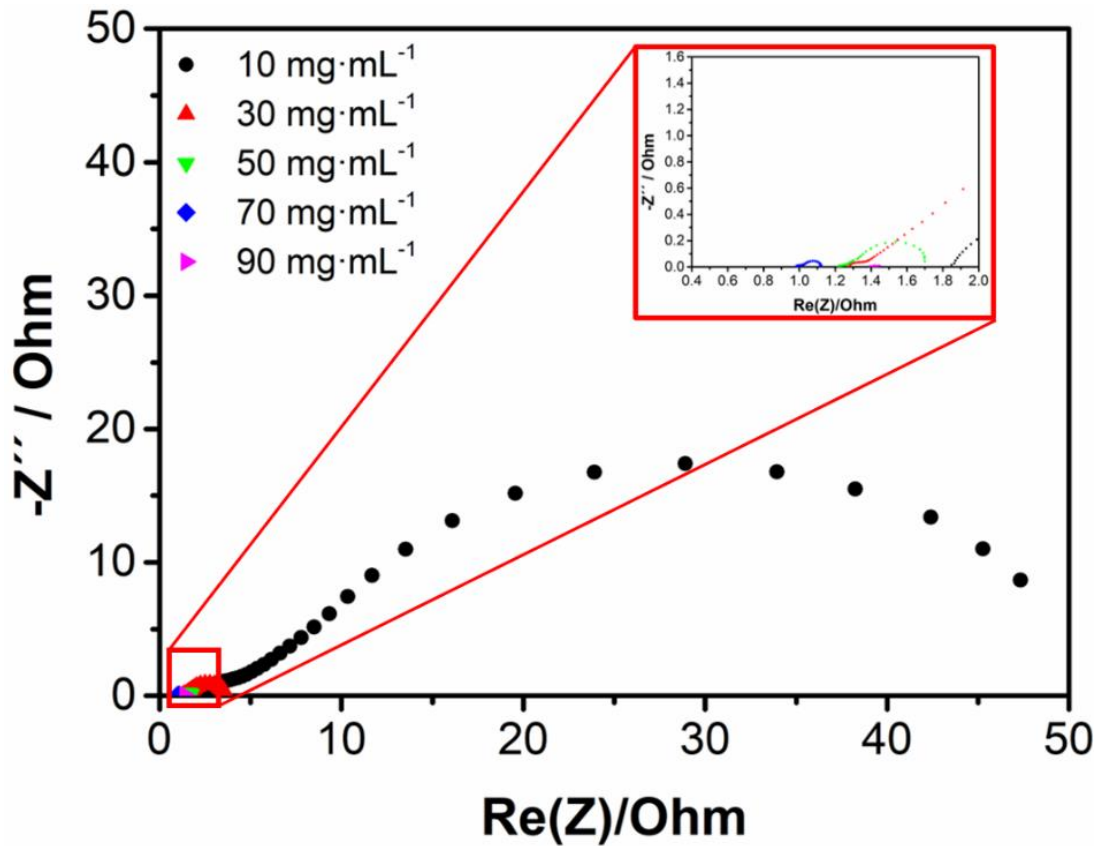


*Figure 3 - 6. Nyquist plots of the EIS measurements for semi-solid electrodes containing 10, 30, 50, 70 and 90  $\text{mg}_{\text{carbon}} \text{mL}^{-1}$*

These semi-solid electrodes show two semicircles, indicating that both electrical and ionic conductivities have a relevant contribution to the total conductivity of the system. Solving the equivalent Debye circuit for this set of measurements, quantitative values of electrical and ionic resistances are calculated. **Figure 3-7** shows the resistance values, normalized by area, obtained from these calculations.

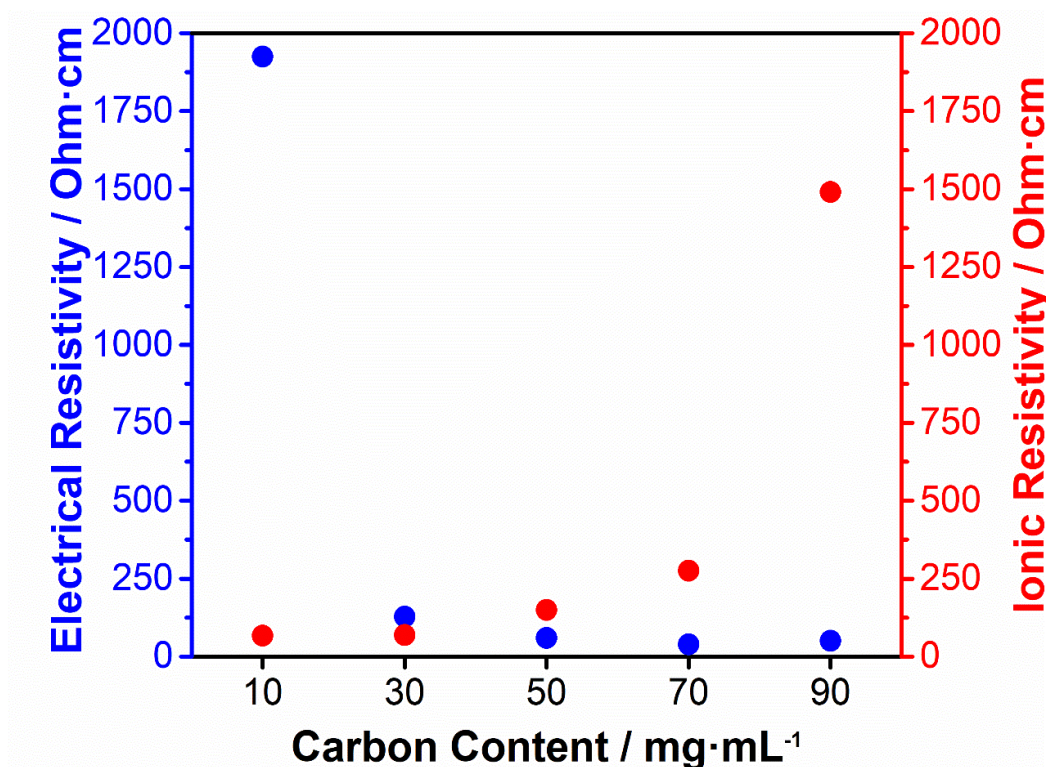


*Figure 3 - 7. Electrical and ionic conductivities for semi-solid electrodes containing 10, 30, 50, 70 and 90 mg<sub>carbon</sub> mL<sup>-1</sup>.*

Whereas the ionic resistivity increases with increasing carbon content due to decreasing tortuosity, electrical resistivity increases with increasing carbon content. This reveals that the ionic and electrical properties of flowable semi-solid electrodes can be easily tuned by adjusting the carbon content.

#### **3.3.4.2 Effect of stabilizer**

The influence of dispersant (polyvinylpyrrolidone) was evaluated by adding different amounts in a semi-solid electrode composed of the carbon additive (KetjenBlack) in an aqueous electrolyte containing 2 M Zn<sub>2</sub>SO<sub>4</sub> + 0.2 M Li<sub>2</sub>SO<sub>4</sub>. The Nyquist plots obtained for various formulation are shown in **Figure 3-8**.

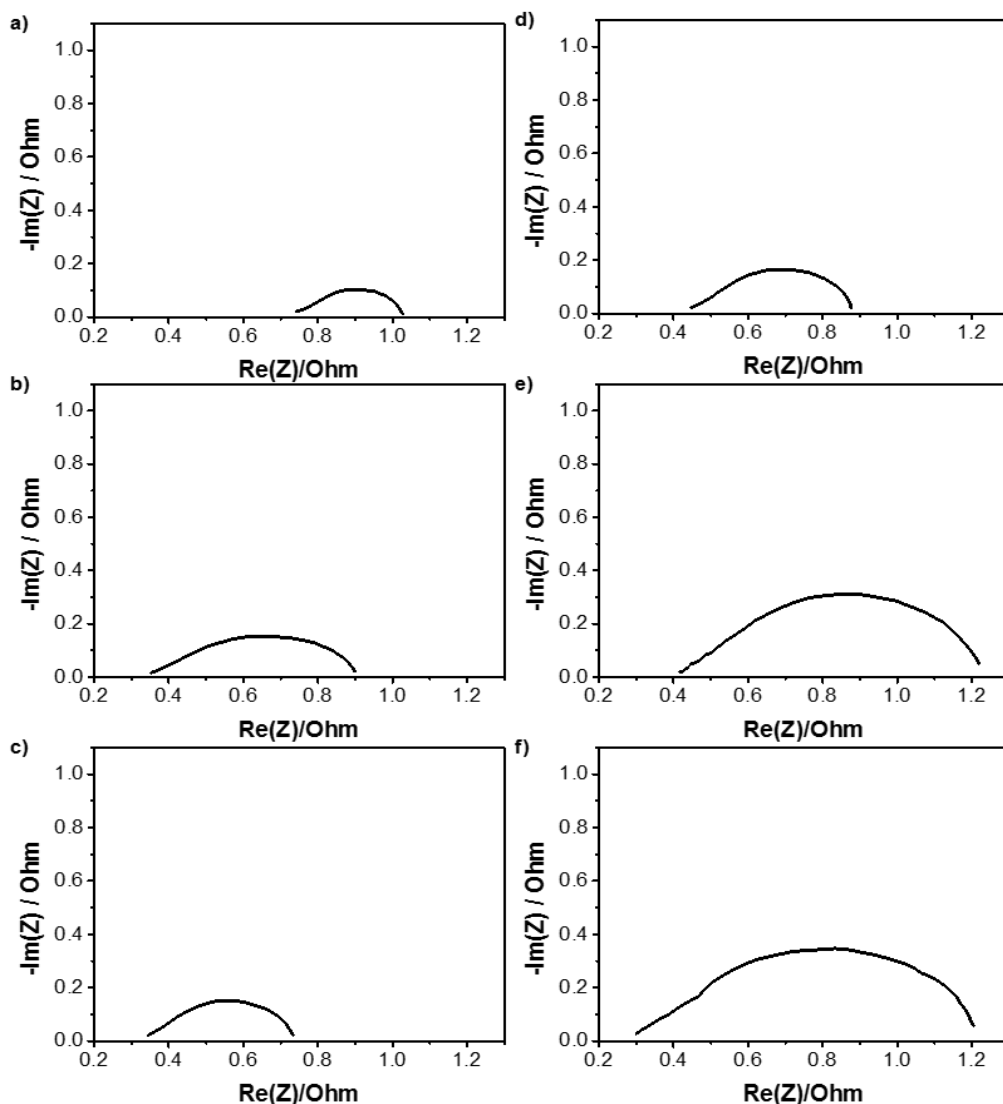


**Figure 3 - 8.** Nyquist plot of EIS measurements of semi-solid electrodes containing: (a) 53 mg mL<sup>-1</sup> carbon additive and 0 mg mL<sup>-1</sup> stabilizer. (b) 53 mg mL<sup>-1</sup> carbon additive and 1.5 mg mL<sup>-1</sup> stabilizer. (c) 53 mg mL<sup>-1</sup> carbon additive and 2.3 mg mL<sup>-1</sup> stabilizer. (d) 42 mg mL<sup>-1</sup> carbon additive and 0 mg mL<sup>-1</sup> stabilizer. (e) 42 mg mL<sup>-1</sup> carbon additive and 1.5 mg mL<sup>-1</sup> stabilizer. (f) 42 mg mL<sup>-1</sup> carbon additive and 2.3 mg mL<sup>-1</sup> stabilizer.

For the Nyquist plot, it is clearly shown how small changes in the materials have great impact in the EIS results. For a quantitative comparison of the results, ionic and electrical resistance were calculated (**Figure 3-9a and 3-9b**). As expected, in the absence of stabilizer (0 %), an increase the carbon additive content results in a reduction of electrical resistance and an increase in ionic resistance. As anticipated, the increasing amount of conducting particles is beneficial for the electrical conductivity but it hinders the

displacement of ions due to the reduction of the porosity of the electrode that affects directly on the ion's mobility. While the absolute values and changes are different for **Figure 3-9a and 3-9b**, the same general trend are observed for these two carbon contents: the addition of polyvinylpyrrolidone to the formulation decreases the ionic resistance but it increases the electrical resistance.

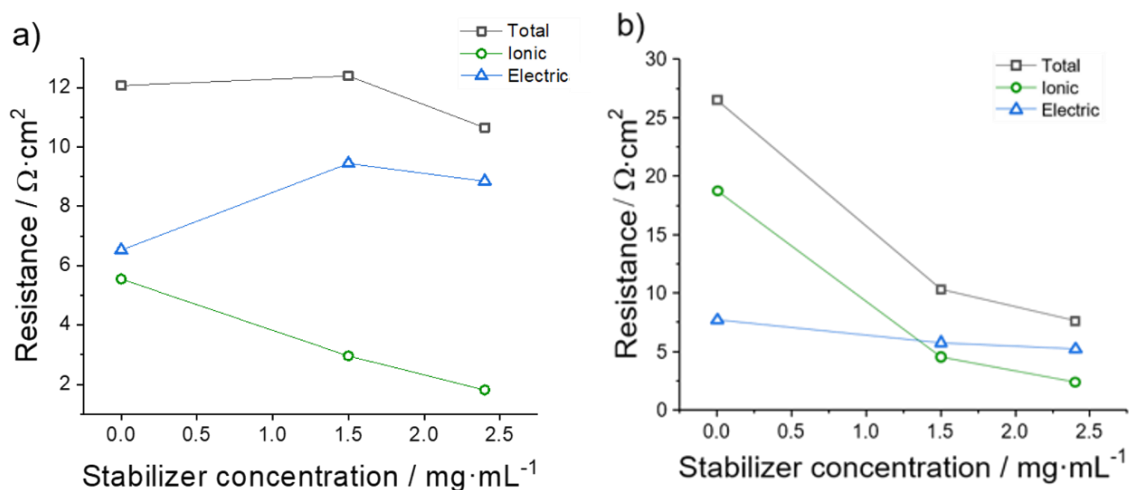


**Figure 3 - 9. (a) Ionic, electrical, and total conductivity of a semi-solid electrode for 42 mg mL<sup>-1</sup> carbon additive. (b) Ionic, electrical, and total conductivity of a semi-solid electrode for 53 mg mL<sup>-1</sup> carbon additive.**

The trend can be explained based on the action of non-ionic surfactant as polyvinylpyrrolidone on the suspended particles since the polymer keeps particles of the suspension separated from each other.<sup>23</sup> As a result, ions move easier but electron may have more difficulties for transferring between particles. Interestingly, the influence of surfactant in the electrical resistance changes with the carbon content. For lower carbon content, the described phenomenon is clearly show in the electrical one (blue line, **Figure 3-9a**). For higher carbon content (blue line, **Figure 3-9b**), the impact of the stabilizer in the electrical percolation network is much smaller since the higher concentration of particles ensure facile electron transfer.

It should be noted that the configuration of our cell does not allow assessment of electrical conductivity of semi-solid electrodes that contain electroactive materials. The sinusoidal voltage applied during EIS measurement can oxidize and/or reduce the active species generating a current. Unfortunately, this current cannot be deconvoluted from the ohmic current from the ionic and electrical resistors. In the framework of this thesis, the first steps towards the validation of a method allowing evaluation of semi-solid electrodes containing electroactive materials were taken. Unfortunately, this work has been delayed so that it is not included.

### 3.4 Conclusions

In summary, rheological, electrical, and ionic properties of semi-solid electrodes has been studied. First of all, the thixotropic nature of these kind of electrodes has been confirmed by measuring their viscosity at different shear rates, revealing that it decreases when force is applied, recovering its initial value when the force ceases. This parameter is crucial for the concept developed in this thesis because it will facilitate the injection of semi-solid electrodes into a preassembled cell. On the other hand, a specific cell for assessing the ionic and electrical conductivity of semi-solid electrodes by using Electrochemical Impedance Spectroscopy measurements was designed. This cell allow for evaluation of intrinsic ionic and electrical properties of semi-solid electrodes. In this case, the studied semi-solid electrodes behaves as a mixed ionic and electronic conductor, so the Debye circuit is used for fitting the data. Different formulation of slurries have been prepared and measured using the proposed methodology, showing the possibility of tuning the electrical and ionic properties of the electrode. For the studied formulations, the addition of Ketjenblack results in an decrease in electrical resistance but an increase in ionic resistance due to the increasing concentration of carbon particles. On the other hand, when non-ionic surfactant used as stabilizer (polyvinylpyrrolidone) is added into the formulation, the opposite behavior is obtained: the ionic resistance decreases, while the electrical resistance increases due to the presence of the stabilizer in the suspension. For higher carbon content, the influence of the stabilizer in the electrical resistance is minimized. This methodology for understanding the properties of the semi-solid electrodes will be necessary for various chapters of this thesis, since it will be used for the optimization of each slurry developed along the work.

### 3.5 References

1. Kuang, Y., Chen, C., Kirsch, D. & Hu, L. Thick Electrode Batteries: Principles, Opportunities, and Challenges. *Adv. Energy Mater.* **9**, 1–19 (2019).
2. Chiu, R. C., Garino, T. J. & Cima, M. J. Drying of Granular Ceramic Films: I, Effect of Processing Variables on Cracking Behavior. *J. Am. Ceram. Soc.* **76**, 2257–2264 (1993).
3. Wood, D. L., Li, J. & Daniel, C. Prospects for reducing the processing cost of lithium ion batteries. *J. Power Sources* **275**, 234–242 (2015).
4. Molina, A. *et al.* Electrode Engineering of Redox-Active Conjugated Microporous Polymers for Ultra-High Areal Capacity Organic Batteries. *ACS Energy Lett.* **5**, 2945–2953 (2020).
5. Duduta, M. *et al.* Semi-solid lithium rechargeable flow battery. *Adv. Energy Mater.* **1**, 511–516 (2011).
6. 24M Technologies.
7. Ma, J., Wang, C. & Wroblewski, S. Kinetic characteristics of mixed conductive electrodes for lithium ion batteries. *J. Power Sources* **164**, 849–856 (2007).
8. Park, M., Zhang, X., Chung, M., Less, G. B. & Sastry, A. M. A review of conduction phenomena in Li-ion batteries. *J. Power Sources* **195**, 7904–7929 (2010).
9. Muñoz-Torrero, D., Palma, J., Marcilla, R. & Ventosa, E. Al-Ion Battery Based on Semisolid Electrodes for Higher Specific Energy and Lower Cost. *ACS Appl. Energy Mater.* **3**, 2285–2289 (2020).
10. Lasia, A. Electrochemical impedance spectroscopy and its applications. *Electrochem. Impedance Spectrosc. its Appl.* **9781461489337**, 1–367 (2014).
11. Barai, A., Uddin, K., Widanage, W. D., MCGordon, A. & Jennings, P. A study of the influence of measurement timescale on internal resistance characterisation methodologies for lithium-ion cells OPEN. *Sci. RepoRts /* **8**, 21 (2018).
12. Meddings, N. *et al.* Application of electrochemical impedance spectroscopy to commercial Li-ion cells: A review. *J. Power Sources* **480**, 228742 (2020).

13. Narayanan, A., Mugele, F. & Duits, M. H. G. Mechanical History Dependence in Carbon Black Suspensions for Flow Batteries: A Rheo-Impedance Study. *Langmuir* **33**, 1629–1638 (2017).
14. Biendicho, J. J., Flox, C., Sanz, L. & Morante, J. R. Static and dynamic studies on LiNi<sub>1/3</sub>Co<sub>1/3</sub>Mn<sub>1/3</sub>O<sub>2</sub>-based suspensions for semi-solid flow batteries. *ChemSusChem* **9**, 1938–1944 (2016).
15. Youssry, M. *et al.* Formulation of flowable anolyte for redox flow batteries: Rheo-electrical study. *J. Power Sources* **274**, 424–431 (2015).
16. Barnes, H. A. Thixotropy—a review. *J. Nonnewton. Fluid Mech.* **70**, 1–33 (1997).
17. Akuzum, B. *et al.* Percolation Characteristics of Conductive Additives for Capacitive Flowable (Semi-Solid) Electrodes. *ACS Appl. Mater. Interfaces* **12**, 5866–5875 (2020).
18. Homepage - Biologic. <https://www.biologic.net/>.
19. Basics of Electrochemical Impedance Spectroscopy. <https://www.c3-analysentechnik.eu/downloads/applikationsberichte/gamry/5657-Application-Note-EIS.pdf>.
20. (PDF) Electrochemical impedance spectroscopy I. Basic elements. [https://www.researchgate.net/publication/343685142\\_Electrochemical\\_impedance\\_spectroscopy\\_I\\_Basic\\_elements](https://www.researchgate.net/publication/343685142_Electrochemical_impedance_spectroscopy_I_Basic_elements).
21. Bard, A. J., Faulkner, L. R. & Wiley, J. ELECTROCHEMICAL METHODS Fundamentals and Applications. (2001).
22. Huggins, R. A. Simple method to determine electronic and ionic components of the conductivity in mixed conductors a review. *Ionics 2002 83* **8**, 300–313 (2002).
23. Wu, Y. *et al.* Effects of Non-Ionic Surfactants on the Rheological, Electrical and Electrochemical Properties of Highly Loaded Silicon Suspension Electrodes for Semi-Solid Flow Batteries. *ChemElectroChem* **7**, 3623–3631 (2020).

**Chapter 4. The Injectable Battery. A  
Conceptually New Strategy in Pursue of a  
Sustainable and Circular Battery Model**

The results obtained in this chapter have been published in an international peer-reviewed journal (Journal of Power Sources, IF:9.127). Basic information about this publication can be found as follows.

**D. Perez-Antolin**, R. Trócoli, J. Palma, E. Ventosa. (2020). The injectable battery. A conceptually new strategy in pursue of a sustainable and circular battery model. *Journal of Power Sources*, 480, 228839. DOI: 10.1016/j.jpowsour.2020.228839.

<https://www.sciencedirect.com/science/article/pii/S0378775320311435>

## 4.1 Introduction

Electric vehicles and renewable energy sources play a vital role in the transition towards a sustainable and environmentally friendly energy and transportation model. In both cases, batteries are key elements, powering electric vehicles and storing energy to balance production and demand from renewable sources. As both the electric vehicle and renewable energy penetrate in the market, a larger amount of batteries will be demanded. In fact, if projections are met in the Li-ion battery market “*alone*”, the global battery factory capacity would reach 1700 GWh per year by 2028,<sup>1</sup> leading to a production capacity of 7 million tonnes of batteries a year. At this production scale, linear economy will obviously not be sustainable considering that battery contain high-value and energy-intensive materials. Unfortunately, recycling processes currently available are not highly efficient from an environmental and economical perspective<sup>2</sup> hindering the implementation of circular economy for batteries.

Achieving a sustainable and circular battery model will require efforts in several aspects, i.e. development of sustainable active materials, battery chemistries as well as cost and energy - efficient recycling processes. I) Much efforts has been recently devoted to the development of sustainable organic-based electroactive materials, which can potentially replace metal-based cathode materials, obtaining promising results<sup>3-5</sup> II) Alternative greener battery chemistries are being explored. The use of the universal solvent is obviously preferred from a sustainability perspective, although the lower cell voltage limits their use to stationary energy storage applications. Despite the long-term efforts in aqueous chemistries, e.g. aqueous Li-ion<sup>6</sup> or Zn-ion,<sup>7</sup> these technologies did not success commercially. A recent study evaluating the use of low-cost Prussian Blue Analogues for aqueous batteries revealed that the contribution of inactive materials, e.g. current collector, in aqueous systems is very large increasing battery costs.<sup>8</sup> III) Battery

recyclability is essential for the sustainability of any battery chemistry, but surprisingly this topic did not attract sufficient attention so far.

Several recent review articles have covered the state-of-the-art battery recycling techniques.<sup>9-13</sup> Currently, the pyro-hydrometallurgical route represents the most widely used recycling processes.<sup>14</sup> In the initial pyrometallurgical step, batteries are burnt. The burnt-out batteries are combined with reducing agents and slowly heated up to ca. 1500 °C, resulting in two fractions; a slag containing metals such as Al, Si, and Fe, and an alloy fraction composed of transition metals, e.g. Cu, Co, and Ni. The alloy fraction is then refined in a hydrometallurgical process involving dissolution of the alloy in sulfuric acid to extract the transition metals in various steps. The mechanical-hydrometallurgical route is a growing alternative to the energy-demanding pyrometallurgical route,<sup>15</sup> which generally consists of several steps: deep discharge, dismantling, shredding (or some kind of milling to access the inside of the cell), mechanical separation (magnetic and/or gravimetric) and hydrometallurgical methods for metals recovery. In all recycling routes, the inside of the battery cells needs to be accessed to extract and recycled the elements of interest since active materials are fixed onto the current collectors inside the cells. This necessary step prevents direct reuse of the battery cells, i.e. inactive materials (current collector, separator, casing), and complicates the recycling process since these elements needs to be separated from the spent electrodes. Once spent electrodes are collected, recovery of the elements can be achieved by a variety of hydrometallurgical methods. Direct relithiating and healing of cathode materials to be reused is another promising approach.<sup>16,17</sup> Although incremental improvements are expected, a breakthrough in battery recycling will require a change in the battery cell concept to facilitate its recyclability.

In this context, we propose an innovative battery concept based on the use of semi-solid electrodes which aims to facilitate battery recycling.

Since semi-solid electrodes does not contain any binder and active materials are not fixed onto the current collectors, direct recovery of active materials is enabled by dejection of the flowable electrodes from the battery cell. Importantly, battery cells remain intact allowing its reuse including all inactive elements, e.g. current collectors, separators, casing, and simplifying the recycling process by eliminating several steps (**Figure 4-1**). The reuse of the battery cells also leads to significant reductions in the battery cost as well. The proof of concept focuses on aqueous based battery chemistries since inactive materials have a large contribution to cost for this type of batteries so that direct reuse of battery cell is of special interest.

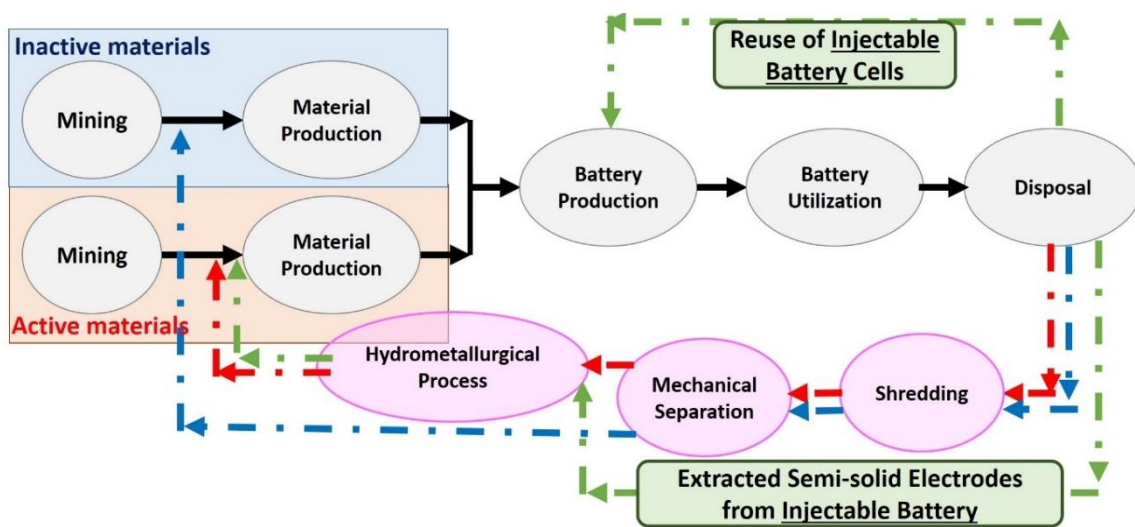


*Figure 4 - 1. General illustration of life cycle of battery materials and components, adapted with permission from [18]. Red and blue arrows show the path for the mechanical-hydrometallurgical recycling route of active and inactive materials, respectively. Green arrows represent the new path for the recycling of the injectable battery. Recycling of inactive materials is not required for injectable battery since battery cells are reused, while shredding and mechanical separation are not necessary since spent electrodes are extracted without damaging the cells.*

## 4.2 Experimental Procedures

### 4.2.1 Reagents and materials

Lithium Iron Phosphate ( $\text{LiFePO}_4$ , Advanced Lithium Electrochemistry), KetjenBlack EC-600 JD (Azelis and AkzoNovel polymer chemicals), Zinc powder (99.9 % -100 mesh, Alfa Aesar),  $\text{Li}_2\text{SO}_4 \cdot \text{H}_2\text{O}$  ( $\geq 99$  %, Sigma Aldrich),  $\text{Zn}_2\text{SO}_4 \cdot 7\text{H}_2\text{O}$  ( $\geq 99.5$  %, Sigma Aldrich), Lithium(I) bis(trifluoromethanesulfonyl)imide (99.9 %, Solvionic), Polyvinylpyrrolidone (Sigma Aldrich), Zinc Foil (99.98 %, Alfa Aesar), Lithium (99.9 %, Sigma Aldrich) were used as-received. Lithium Titanium phosphate ( $\text{LiTi}_2(\text{PO})_4$ ) was synthesized following the route described by Jiayang Sun *et al.*<sup>19</sup>. The non-aqueous electrolyte was prepared by dissolving 1 M Lithium hexafluorophosphate in (1:1 vol. %) Ethylene carbonate: Diethyl carbonate (- 99.9 % Solvionic). Expanded graphite (Sigracet TF6) was used as current collector, and Celgard 3501 and 2500 as separator in aqueous and non-aqueous systems, respectively.

### 4.2.2 Preparation of semi-solid electrodes and configuration of battery cell

Semi-solid electrodes with different compositions were prepared: 55 – 95 wt.% active material, 45 – 5 wt.% Ketjenblack and in some cases 0 – 0.6 wt.% polyvinylpyrrolidone. The solid particles were dispersed in 6 mL of electrolyte: i) 2M  $\text{Zn}_2\text{SO}_4$  and 0.2 M  $\text{Li}_2\text{SO}_4$  (proof of concept for aqueous systems), ii) 1.5 M  $\text{Li}_2\text{SO}_4$  (Symmetrical cell measurements) and iii) 1M Lithium hexafluorophosphate in EC : DEC 1:1 vol.% for non-aqueous system. The suspension was mixed with Ultra-Turrax IKA T18-Basic during three periods of 10 minutes resting 5 minutes between periods. The slurries were prepared directly in a syringe to facilitate the injection of the electrode into the battery pre-assembled. The external case of the battery was designed and printed by 3D-Printing

machine (MakerBot Replicator™ 2X) using ABS as plastic material for aqueous media. Equivalent pieces consisted in Teflon for non-aqueous media due to dissolution of ABS-based pieces in the organic solvent. The battery cell contained the following parts. First, one of the current collectors (expanded graphite) with two holes through which the slurry has to pass, then a gasket is placed onto the current collector taking in account the dimensions of the hole of the gasket that defines the shape of the final electrodes. Then, a microporous separator (Celgard) needed for isolating electrically positive and negative compartments is put onto the mentioned gasket. This part corresponds to half-cell, so the rest of the battery has the same components. The final device is assembled by pressing all these parts. Empty space defined by the gaskets is filled with semi-solid electrode, ranging a thickness of 1 – 2 mm and an area of 7 – 7.5 cm<sup>2</sup>. Postmortem images of the dismantled cells (**Figure 4-2**) show how the semi-solid electrodes fill the empty space.

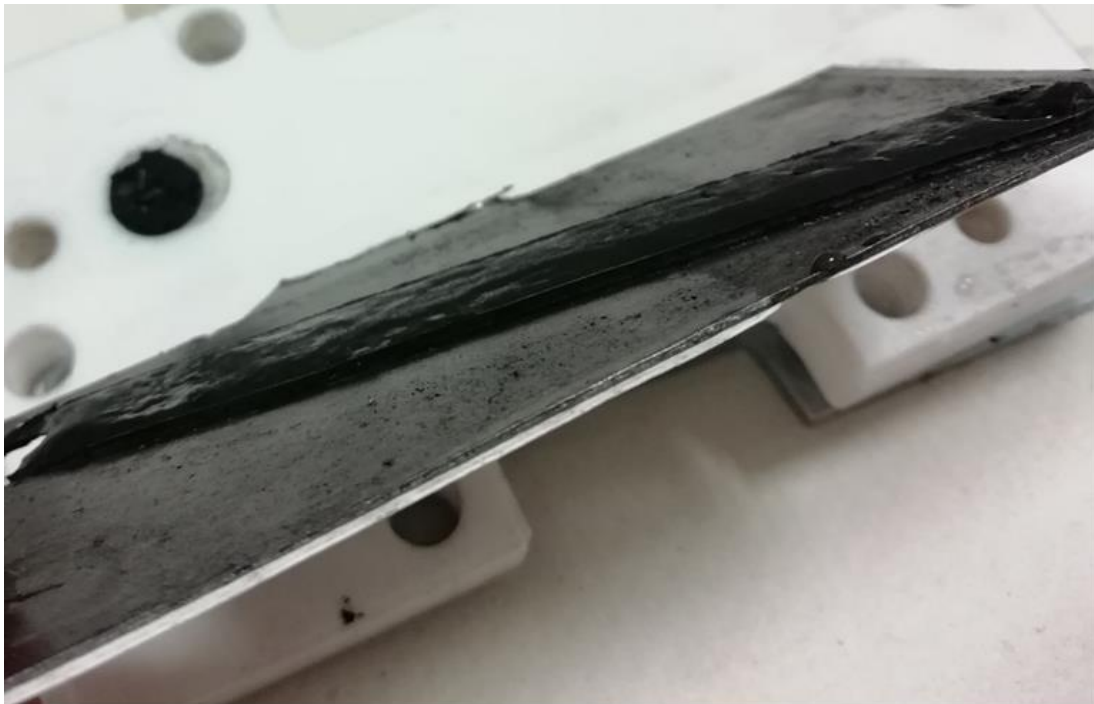


*Figure 4 - 2. Photograph of the semi-solid electrode after dismantling the cell.*

### 4.2.3 Electrochemical measurements

Galvanostatic charge/discharge as well as electrochemical impedance spectroscopy measurements were carried out using an EC-Biologic potentiostat.

- The Zn-LiFePO<sub>4</sub> battery was cycled between 0.7 V and 1.5 V at 1.3 C (5 mA cm<sup>-2</sup> or 260 mA g<sup>-1</sup>). The semi-solid electrode for this experiment contained 21.1 wt.%, 78.3 wt. % and 0.6 wt. % of KetjenBlack, LiFePO<sub>4</sub> and Polyvinylpyrrolidone respectively.
- The Zn-LiFePO<sub>4</sub> in super concentrated aqueous electrolyte battery was cycled between 0.7 V and 1.6 V at 1.5 C (2 mA cm<sup>-2</sup> or 60 mA g<sup>-1</sup>). The semi-solid electrode for this experiment contained 21.1 wt. %, 78.3 wt. % and 0.6 wt. % of KetjenBlack, LiFePO<sub>4</sub> and Polyvinylpyrrolidone respectively.
- The FePO<sub>4</sub> – LiFePO<sub>4</sub> was cycled between + 0.3 V / -0.3 V at 0.66 C (2 mA cm<sup>-2</sup> or 60 mA g<sup>-1</sup>). The semi-solid electrode for this experiment contained 25.3 wt.%, 74.1 wt.% and 0.6 wt.% of KetjenBlack, LiFePO<sub>4</sub> and Polyvinylpyrrolidone respectively.
- The Li – LiFePO<sub>4</sub> was cycled between 2.5 / and 3.6 V at 0.57 C (0.28 mA cm<sup>-2</sup> or 40 mA g<sup>-1</sup>). The semi-solid electrode for this experiment contained 42.9 wt.% and 57.1 wt.% of KetjenBlack and LiFePO<sub>4</sub> respectively.
- The LiTi<sub>2</sub>(PO<sub>4</sub>)<sub>3</sub> – LiFePO<sub>4</sub> was cycled between 0.5 / and 1.2 V at 1.6 C (1 mA cm<sup>-2</sup> or 52 mA g<sub>LTP</sub><sup>-1</sup>). The positive semi-solid electrode for this experiment contained 23 wt.% and 77 wt.% of Ketjen Black and LiFePO<sub>4</sub> respectively. The negative semi-solid electrode for this experiment contained by 37.4 wt.% and 62.6 wt.% of Ketjen Black and LiTi<sub>2</sub>(PO<sub>4</sub>)<sub>3</sub> respectively All chemicals were purchased from Sigma Aldrich and Alfa Aesar, and used as received, except for the Lithium Titanate phosphate (LiTi<sub>2</sub>(PO)<sub>4</sub>) that was synthesized following the route described by Jiayang Sun *et al.*<sup>19</sup>

## 4.3 Results and Discussion

### 4.3.1 The concept of injectable battery

In contrast to redox flow batteries in which active materials are flowable and easily accessible, the configuration of non-flow batteries, e.g. Li-ion battery, prevents the direct substitution of spent end-of-life electrodes. Battery cells need to be crushed to recover the valuable elements, since active materials are fixed onto current collectors located inside, hindering the recycling process. We propose the use of flowable semi-solid electrodes in the absent of binder. The fabrication and recycling of the injectable battery concept is illustrated in **Figure 4-3**. A battery cell is pre-assembled and then filled with semi-solid electrodes. Once injected, the battery cell will be sealed operating normally until it reaches its end-of-life. Then, the flowable semi-solid electrodes will be substituted by fresh semi-solid electrodes. In this way, spent semi-solid electrodes will be directly extracted from the inside leaving the cell intact. By this, recycling process will be largely facilitated since separation of spent active materials from other elements, e.g. current collector, separator, or casing, will not be necessary. The elements of interest such as Li can be recovered via established hydrometallurgical methods from the extracted semi-solid electrodes. Additionally, active materials from positive and negative electrodes are extracted separately so that they can be processed independently. Thus, relithiation of cathode materials<sup>16,17</sup> would be facilitated by the proposed concept avoiding the synthesis process of new cathode materials from its elemental components. Importantly, direct extraction of semi-solid electrodes also allows the reuse of cells contributing to reducing costs since new cells will not need to be fabricated. Similar type of flowable electrodes were used for redox flow batteries,<sup>20-22</sup> but the uninterrupted flow of suspensions poses several drawbacks (e.g. erosion and high pumping energy cost) compared to other redox flow battery systems. Although energy and power are not

decoupled for the case of the injectable battery (in contrast to redox flow batteries), a major advantage of the proposed technology is achieved, i.e., the slurries only flow during the regeneration process.

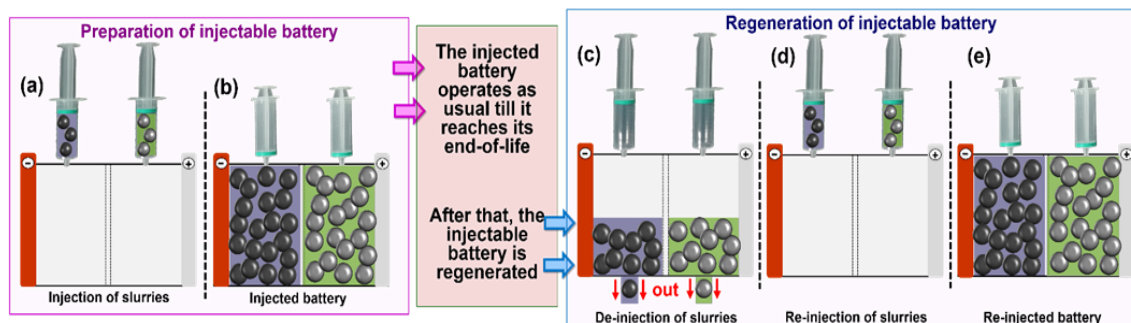


*Figure 4 - 3. Illustration of the injectable battery concept. (a) The preassembled cell is fabricated, which is (b) filled with semi-solid electrode. After end-of-life (several years), the injectable battery regenerated by (c) removing the spent semi-solid electrodes, (d-e) having the cell ready for injecting fresh one.*

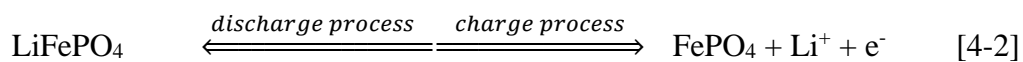
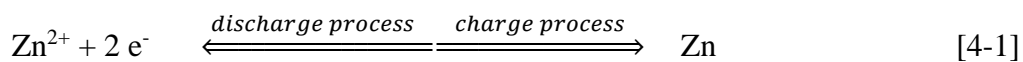
In other words, the limitation related to the continuous flow of viscous suspensions are minimized since the proposed technology is a non-flow (static) battery during its years of operation and pumping is only required once every several years. In non-flow batteries, non-flowable semi-solid electrodes were used for enhancing mass transport of ions and thus increasing areal capacity of the battery (lower cost).<sup>23,24</sup> However, the lack of flowability of these semi-solid electrodes prevented any possibility of facilitating recyclability and reusing the battery cells.

## 4.3.2 Proof of concept for aqueous injectable batteries.

### 4.3.2.1 Aqueous Zn – LiFePO<sub>4</sub> injectable battery

The chemistry Zn – LiFePO<sub>4</sub> was chosen for the first proof of concept due to its intrinsic features: i) the chemistry of these materials, Zn and LiFePO<sub>4</sub>, is well known for conventional battery electrode<sup>25</sup> ii) it is an aqueous system facilitating the development of a prototype, and iii) it suffers from poor cycle life simplifying the demonstration of

recyclability of our injectable battery concept. The overall reaction in the positive and negative electrodes of the Zn – LiFePO<sub>4</sub> system are shown in **Equation 4-1** and **Equation 4-2**, respectively. Since the cation is not common for the positive and negative electrode reactions, this battery chemistry is not a rocking chair concept, and the energy density may be limited by the solubility of the salt. Considering the solubility of Li<sub>2</sub>SO<sub>4</sub> (6.6 M Li<sup>+</sup>), in semi-solid electrodes with electrode porosity of *ca.* 75 vol% the amount of electrolyte is enough to reach a utilization rate of LiFePO<sub>4</sub> of 148 mAh g<sup>-1</sup>. Thus, a value of electrode porosities > 75 vol% were used for the proof of concept of Zn – LiFePO<sub>4</sub> injectable battery.



The content of carbon additive and stabilizer agent is of key importance for the ionic and electrical conductivity of a semi-solid electrode as discussed in **Chapter 3**, while the content of active material plays a key role in the energy density and specific energy (discussed below).

Semi-solid electrodes (**Figure 4-5a**) containing a mixture of LiFePO<sub>4</sub>, carbon additive, stabilizer, and electrolyte (78.3 wt.%, 21.1 wt.% and 0.6 wt.%, respectively) were prepared directly in a syringe by stirring with a high-shear homogenizer. A pre-assembled injectable battery cell (**Figure 4-4**) was filled with this semi-solid electrode using a Zn plate as counterpart.

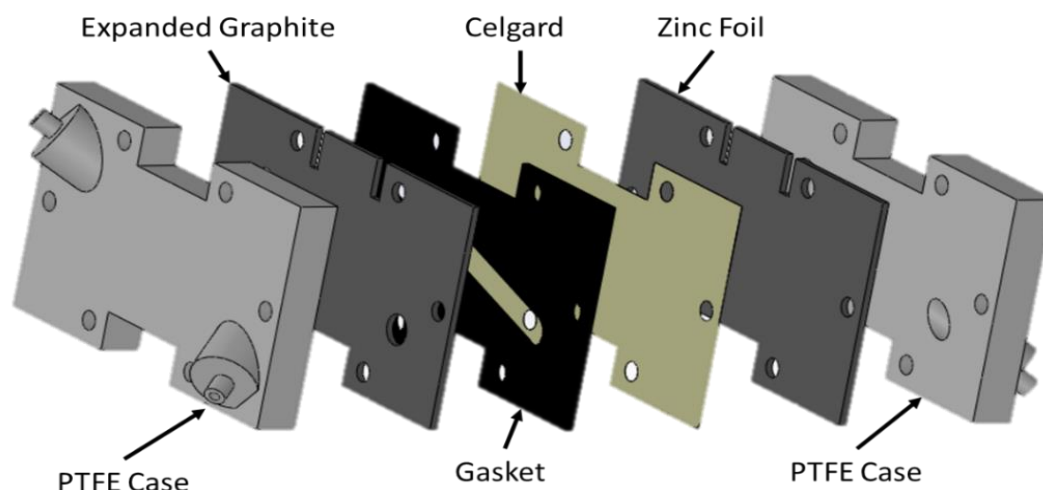


**Figure 4 - 4.** Schematic representation of the cell design of the Zn – LiFePO<sub>4</sub> injectable battery.

In the first cycle, the injected battery delivered an areal capacity of 2.5 mAh cm<sup>-2</sup> and specific capacity of 130 mAh g<sub>LiFePO<sub>4</sub></sub><sup>-1</sup> at 1C (**Figure 4-5b**). However, the capacity rapidly faded dropping below 0.2 mAh cm<sup>-2</sup> in 50 cycles. After 50 cycles, the spent semi-solid cathode was removed by circulating tap water. Then, the battery cell was filled again with a fresh LiFePO<sub>4</sub> semi-solid electrode (Regeneration 1 – R1 in **Figure 4-5b**). The areal capacity increased from 0.1 to 2.7 mAh cm<sup>-2</sup> after substitution of the semi-solid electrode, reaching the value of the first cycle of the initial battery cell. The regenerated battery followed similar capacity fading as the initial cell, leading to a value below 0.2 mAh cm<sup>-2</sup> after 50 cycles. The regeneration / recycling procedure was applied 4 times following each time the same behavior: recovery of the initial capacity after regeneration of the battery cell followed by a rapid capacity fading. The overpotentials shown in Figure 3b were used to make an estimation of the internal resistance, which do not vary significantly between injections (**Figure 4-5c**). The slight variations in areal capacity (2.5 ± 0.25 mAh cm<sup>-2</sup>) between regenerations are attributed to the reproducibility of this home-made regeneration process since there is no trend along the 5 injections. Consequently,

the concept of battery regeneration / recycling by simple substitution of the semi-solid electrode was shown to be feasible.

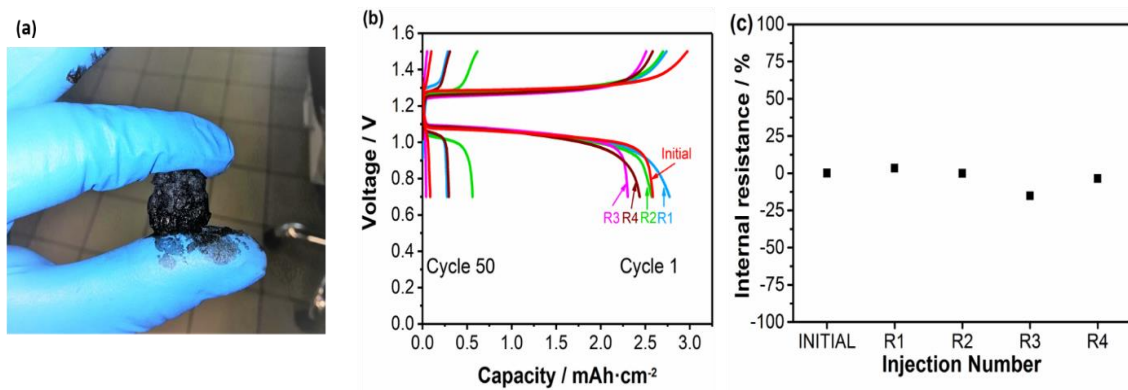


**Figure 4 - 5.** (a) Photograph of a semi-solid electrode. (b) Voltage profile of an injected Zn – LiFePO<sub>4</sub> battery in the 1<sup>st</sup> and 50<sup>th</sup> cycle for the initial battery and after 4 subsequent regenerations (R1, R2, R3 and R4) at IC (2.5 mA cm<sup>-2</sup>). (c) Variation of the internal resistance of the injectable battery with respect to initial value when semi-solid electrodes are substituted.

#### 4.3.2.2 Super-concentrated Zn – LiFePO<sub>4</sub> injectable battery

The poor cycle life of the aqueous Zn – LiFePO<sub>4</sub> injectable battery was likely associated with the changes in pH due to the hydrogen evolution reaction occurring at the Zn electrode. The use of super-concentration aqueous electrolytes has been recently shown to mitigate this issue.<sup>26</sup> Thus, we prepared a super-concentrated Zn – LiFePO<sub>4</sub> injectable battery, in which both Zn and LiFePO<sub>4</sub> materials were injected as semi-solid electrodes (Figure 4-6).

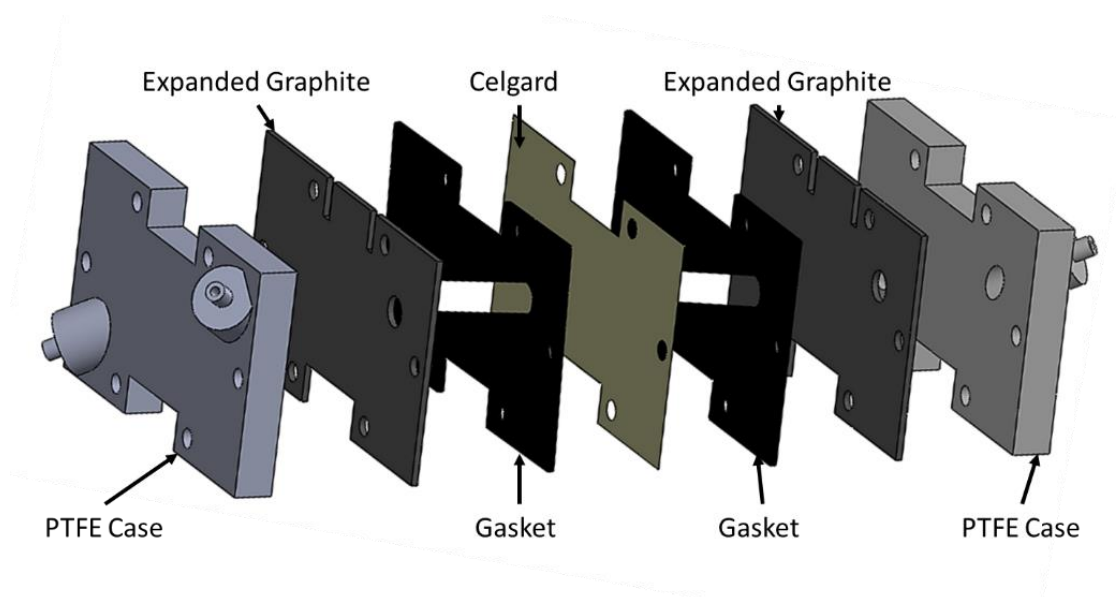


**Figure 4 - 6.** Schematic representation of the cell design of the aqueous super-concentrated Zn – LiFePO<sub>4</sub>, FePO<sub>4</sub> – LiFePO<sub>4</sub> and LiTi<sub>2</sub>(PO<sub>4</sub>)<sub>3</sub> – LiFePO<sub>4</sub> injectable battery.

The cycle stability of the resulting injectable battery was significantly increased (**Figure 4-7**) with respect to the injectable battery using standard electrolyte (**Figure 4-5b**). Specifically, a capacity retention value of 70 % was reached after 10 and 300 cycles for standard (**Figure 4-5b**) and super-concentrated (**Figure 4-7b**) electrolytes, respectively. These results clearly indicate that the use of super-concentrated electrolytes is a promising strategy to prevent side reactions in semi-solid electrodes.

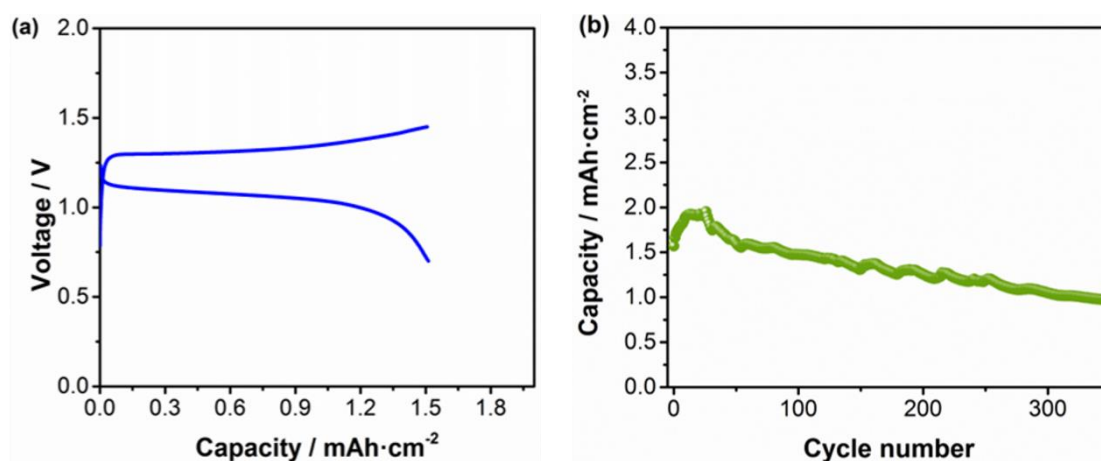


**Figure 4 - 7.** (a) Voltage profile and (b) evolution of the areal capacity with cycles for the super-concentration Zn – LiFePO<sub>4</sub> injectable battery in 21 m LiTFSI and 1 m ZnTFSI.

#### 4.3.2.3 Aqueous $\text{LiTi}_2(\text{PO}_4)_3$ – $\text{LiFePO}_4$ injectable battery

The injectable battery concept was further implemented for an aqueous Li-ion battery chemistry:  $\text{LiFePO}_4$  –  $\text{LiTi}_2(\text{PO}_4)_3$  (LFP – LTP) (**Figure 4-8a** and **4-8b**). Since LTP is not commercially available and several milliliters of semi-solid electrode are required, the areal capacity (mass loading) needed to be decreased. Both LTP and LFP were injected as semi-solid electrodes (**Figure 4-6**).

The typical nominal voltage of *ca.* 0.9 V was delivered (**Figure 4-8a**), while the specific capacity ( $45 \text{ mAh g}_{\text{LTP}}^{-1}$ ) was at the lower end of the variety of values reported in other studies ( $60 - 100 \text{ mAh g}^{-1}$ )<sup>27,28</sup> due to the unexpected difficulties in the synthesis of LTP. The capacity fading was improved with respect to the Zn – LFP injectable battery (**Fig 4-5b**) confirming that the Zn electrode in neutral pH electrolytes limits the cycle life of that battery chemistry when standard electrolyte is used.

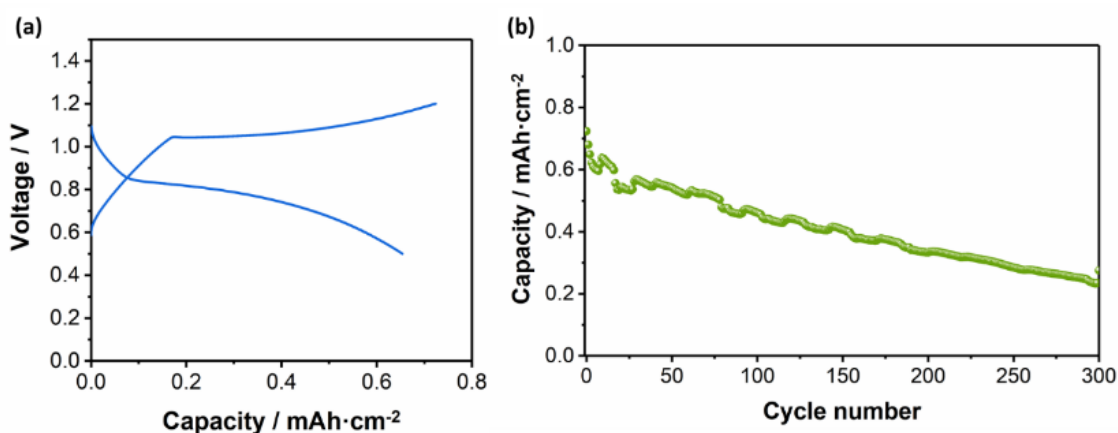


**Figure 4 - 8. (a) Voltage profile and (b) evolution of the areal capacity with cycles for the  $\text{LiTi}_2(\text{PO}_4)_3$  –  $\text{LiFePO}_4$  injectable battery.**

Both aqueous injected battery cells, i.e. the super-concentrated Zn – LFP and the LTP – LFP, delivered > 99 % coulombic efficiency (**Figure 4-9**). The evolution of the energy and coulombic efficiency with the number of cycles for the aqueous  $\text{LiTi}_2(\text{PO}_4)_3$  –  $\text{LiFePO}_4$  and super-concentrated Zn –  $\text{LiFePO}_4$  injectable battery are shown in **Figure 4-**

**9a and Figure 4-9b**, respectively. In both cases, the coulombic efficiency remained above 99 %. As for the energy efficiency, the  $\text{LiTi}_2(\text{PO}_4)_3 - \text{LiFePO}_4$  battery and super-concentrated  $\text{Zn} - \text{LiFePO}_4$  battery delivered values of *ca.* 65 % and > 75 %, respectively. The lower energy efficiency is attributed to the  $\text{LiTi}_2(\text{PO}_4)_3$  semi-solid electrode. It should be noted that  $\text{LiTi}_2(\text{PO}_4)_3$  was home-made (not commercially available) and will probably need to be further optimized. In addition, the low nominal voltage of this battery chemistry penalizes the energy efficiency.

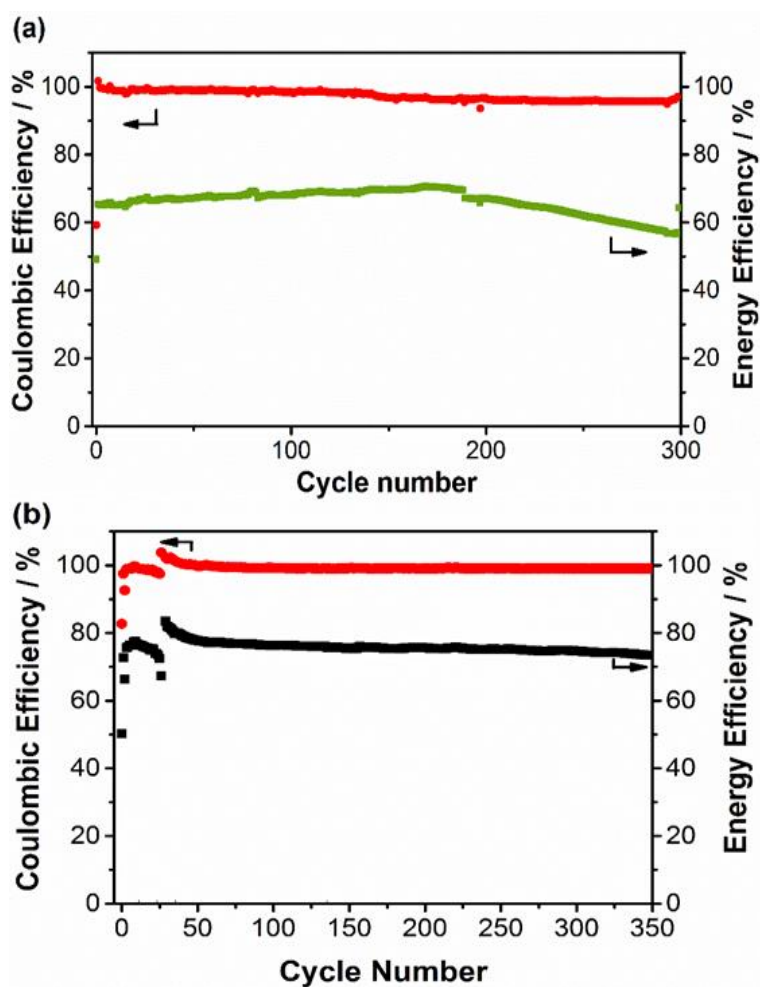


*Figure 4 - 9. Energy and coulombic efficiency of aqueous (a)  $\text{LiTi}_2(\text{PO}_4)_3 - \text{LiFePO}_4$  and (b) super-concentrated  $\text{Zn} - \text{LiFePO}_4$  injectable battery operated at  $1 \text{ mA cm}^{-2}$  and  $2 \text{ mA cm}^{-2}$ , respectively.*

#### 4.3.2.4 Symmetrical LiFePO<sub>4</sub> – FePO<sub>4</sub> injectable battery

The capacity fading observed for the super-concentrated Zn – LiFePO<sub>4</sub> and the LiTi<sub>2</sub>(PO<sub>4</sub>)<sub>3</sub>-LiFePO<sub>4</sub> injectable batteries were comparable. To elucidate the contribution of semi-solid LiFePO<sub>4</sub> electrodes to the capacity fading and deconvolute it from electrode unbalancing due to parasitic side reactions or degradation of negative electrode material, we deployed a symmetrical injectable battery using FePO<sub>4</sub> (pre-oxidized) and LiFePO<sub>4</sub> in the negative and positive compartment. In this cell (**Figure 4-5**), both compartments are filled with semi-solid electrode: LiFePO<sub>4</sub>-based semi-solid electrode will be oxidized in one compartment while FePO<sub>4</sub>-based semi-solid electrode will be reduced in the other compartment. The symmetrical injectable cell does not store energy since the cell voltage should be zero (**Figure 4-10**). Nevertheless, this configuration allows us to elucidate the intrinsic cycle life of LiFePO<sub>4</sub> semi-solid electrodes. It should be noted that symmetrical cells have been successfully used in redox flow batteries to evaluate the intrinsic stability of active materials.<sup>29,30</sup> **Figure 4-10** shows the differential voltage curves of the for the 1<sup>st</sup> and 300<sup>th</sup> cycle. From this plot, the oxidation / reduction voltage can be easily obtained. Since the cell is symmetrical, the cell voltage is zero and the recorded voltage corresponds directly to the overpotential of two symmetrical electrodes. The results confirmed that the lower energy efficiency is attributed to the LiTi<sub>2</sub>(PO<sub>4</sub>)<sub>3</sub> since the symmetrical system aqueous FePO<sub>4</sub> – LiFePO<sub>4</sub> injectable battery showed small overpotential of 100 mV. Also, an internal resistance for the entire cell of 3.5 Ohm cm<sup>-2</sup> and 5.5 Ohm cm<sup>-2</sup> are calculated for the 1<sup>st</sup> and 300<sup>th</sup> cycle. The entire internal resistance increases 2 Ohm cm<sup>-2</sup> (4 mV in this case) after 300 cycles (> 500 hours), indicating that major sedimentation of solid particles did not occur.

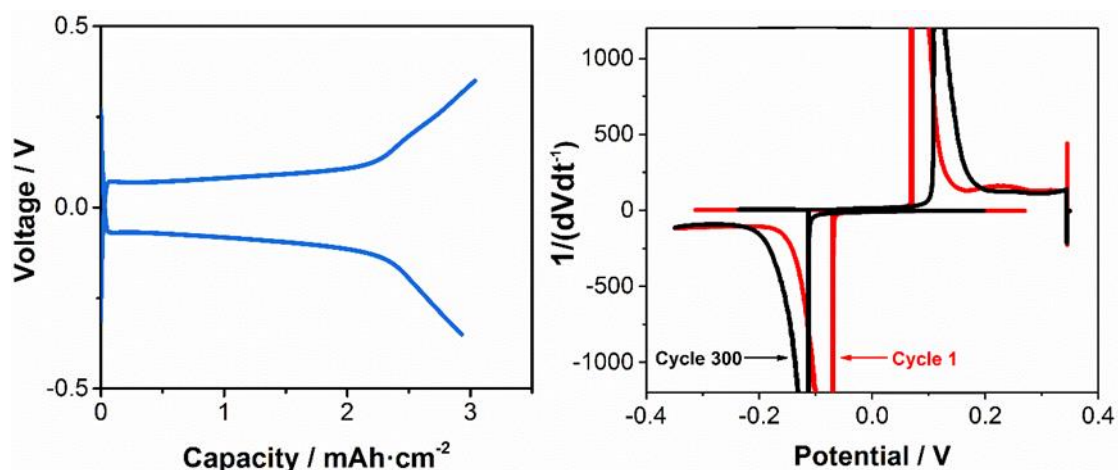


Figure 4 - 10. Voltage profile and differential voltage curves of the aqueous  $\text{FePO}_4 - \text{LiFePO}_4$  injectable battery for the 1<sup>st</sup> and 300<sup>th</sup> cycle at  $2 \text{ mA cm}^{-2}$ . Electrode thickness: 2 mm and 1 mm for  $\text{FePO}_4$  and  $\text{LiFePO}_4$  semi-solid electrode, respectively.

Figure 4-11 shows the evolution of capacity retention for the super-concentrated Zn –  $\text{LiFePO}_4$ , the  $\text{LiTi}_2(\text{PO}_4)_3 - \text{LiFePO}_4$  and the  $\text{FePO}_4 - \text{LiFePO}_4$  injectable batteries.

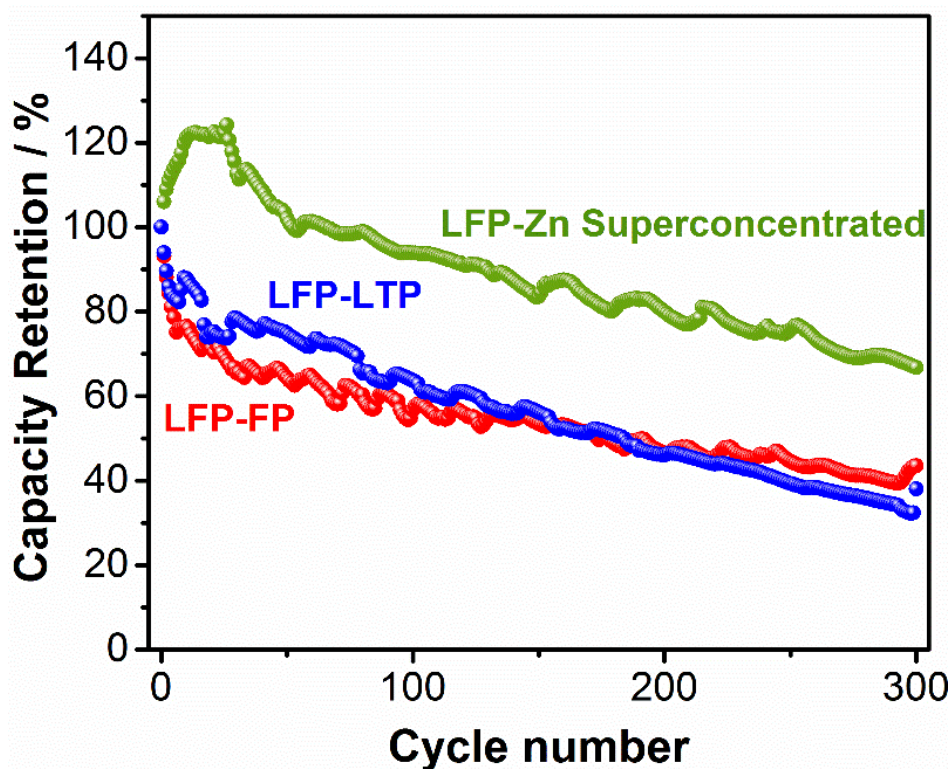


Figure 4 - 11. Comparison of capacity retentions for the  $\text{LiTi}_2(\text{PO}_4)_3 - \text{LiFePO}_4$ , the super-concentrated Zn –  $\text{LiFePO}_4$  and the  $\text{FePO}_4 - \text{LiFePO}_4$  injectable batteries. An average capacity decay of  $0.15$ ,  $0.13$  and  $0.08 \text{ \% cycle}^{-1}$ , respectively, was calculated for the last 200 cycles.

Obviously, the capacity retention for the Zn – LiFePO<sub>4</sub> (standard electrolyte) is much poorer than rest of battery chemistries due to the significant hydrogen evolution reaction at Zn electrode (neutral pH), so that it was excluded from the comparison. An average capacity fading was estimated for the last 200 cycle (from cycle 100 to 300) to facilitate the comparison. An average capacity decay of 0.15, 0.13 and 0.08 % cycle<sup>-1</sup> was obtained for the LiTi<sub>2</sub>(PO<sub>4</sub>)<sub>3</sub> – LiFePO<sub>4</sub>, the super-concentrated Zn – LiFePO<sub>4</sub>, and the FePO<sub>4</sub> – LiFePO<sub>4</sub> injectable battery, respectively. The symmetric FePO<sub>4</sub> –LiFePO<sub>4</sub> reveals the intrinsic cycle stability of LiFePO<sub>4</sub> in aqueous media, which establishes the best-case scenario. In this case, hydrogen evolution reaction (HER) is prevented, while oxygen reduction reaction (ORR) may occur, which would lead to a change in pH.

The resulting capacity decay of 0.08 % cycle<sup>-1</sup> is well-below the average decay reported in literature for aqueous LiFePO<sub>4</sub>-based batteries using conventional electrodes (**Table 4-1**). In the case of Zn – LFP in super concentrated electrolyte, HER is mitigated but not prevented, which leads to a slight worsening of the capacity decay (0.13 % cycle<sup>-1</sup>).

Since there is a large excess of Zn metal, the capacity decay derives from the positive electrode. Consequently, small amounts of parasitic reactions affect the capacity retention of LiFePO<sub>4</sub>. In the case of Zn – LFP in conventional electrolyte, side reactions occurring at the Zn electrode, especially HER, results in the highest capacity decay for the LiFePO<sub>4</sub>. Therefore, these results reveal three important points.

I) LiFePO<sub>4</sub> is not stable in aqueous media as previously reported. He *et. al*<sup>31</sup> concluded that the reduction of oxygen leads to changes in pH (small volumes of electrolyte, not in flooded cells), which induces a capacity fading by modification of the LiFePO<sub>4</sub> surface, which is consistent with our findings.

II) Side reactions occurring at the negative electrode play an essential role in the cycle stability of the  $\text{LiFePO}_4$  since they not only may unbalance the cell,<sup>32</sup> but also induce changes in pH.

III) The intrinsic stability of semi-solid  $\text{LiFePO}_4$  electrode is not the source of the rapid capacity fading observed in some of the tested batteries (**Figure 4-5**).

**Table 4 - 1. Comparison of electrochemical performance of state-of-the-art aqueous  $\text{LiFePO}_4$ -based batteries.**

<i>Ref.</i>	<i>System</i>	<i>Electrolyte</i>	<i>Capacity Fading</i> (%·cycle <sup>-1</sup> )	<i>C-rate</i>	<i>Capacity</i> (mAh·g <sup>-1</sup> )
<sup>32</sup>	$\text{LiTi}_2(\text{PO}_4)_3/\text{LiFePO}_4$	$\text{LiSO}_4$	0.70	6 C	110
<sup>33</sup>	$\text{LiTi}_2(\text{PO}_4)_3/\text{LiFePO}_4$	$\text{LiNO}_3$	0.34	7 C	130
<sup>34</sup>	$\text{LiFePO}_4/\text{LiFePO}_4$	$\text{LiSO}_4$ (Without $\text{O}_2$ )	0.20	1.1 C	--
<sup>31</sup>	$\text{LiFePO}_4$	$\text{LiSO}_4$	3.70	5 C	130
<sup>35</sup>	Pt / $\text{LiFePO}_4$	$\text{LiNO}_3$	0.90	0.5 C	84
<sup>25</sup>	Zn / $\text{LiFePO}_4$	ZnCl / LiCl	0.19	6 C	170
<i>Our work</i>	$\text{LiTi}_2(\text{PO}_4)_3/\text{LiFePO}_4$	$\text{LiSO}_4$	0.15	1.6 C	46 (normalized by LTP)
<i>Our work</i>	$\text{LiFePO}_4/\text{LiFePO}_4$	$\text{LiSO}_4$	0.08	0.6 C	116
<i>Our work</i>	Zn / $\text{LiFePO}_4$	LiTFSI /ZnTFSI	0.13	1.5 C	50

Indeed, the symmetrical cell reveals a capacity fading for semi-solid  $\text{LiFePO}_4$  electrodes of 0.04 % cycle<sup>-1</sup> (0.04 % in each LFP electrode). Importantly, the semi-solid electrodes in the symmetrical cell did not show indications of sedimentation as the internal resistance did not increase drastically over long cycling (**Figure 4-10**).

### 4.3.3 Theoretical calculations on the battery cost and energy density

The use of semi-solid electrodes not only facilitates the recyclability of the battery which clearly has a tremendously positive environmental impact, but also influences the battery cost and energy density. The porosity of semi-solid electrodes plays an important role in both the battery cost and energy density, referring to electrode porosity (vol. %) as the fraction between volume of active material and total volume of electrode in percentage. Since active materials are denser than carbon and electrolyte, the content of active material influences the electrode porosity and, thus, plays a key role in the energy density and specific energy. As a proof of versatility, we increased the content of  $\text{LiFePO}_4$  (wt.%) in the semi-solid electrode to decrease the electrode porosity (vol.%) from 90 vol.% (78 wt.%) to 70 vol.% (95 wt.%) and tested it in a symmetrical injectable cell ( $\text{LiFePO}_4 - \text{FePO}_4$ ). The areal capacity achieved for an electrode porosity of 70 vol% (95 wt.% of  $\text{LiFePO}_4$ ) was  $14 \text{ mAh cm}^{-2}$  while a material utilization of  $140 \text{ mAh g}^{-1}$  was delivered (**Figure 4-12 and Figure 4-13**). The total resistance was  $62 \text{ Ohm cm}^2$  and  $87 \text{ Ohm cm}^2$  for higher and lower electrode porosity, respectively, calculated as the ratio between overpotential and current density. This increase of 40 % in total resistance could be mitigated by further optimization of the electrode formulation for low porosity. This indicates that i) it is feasible to work with these values of electrode porosity and ii) the high mass transport of ions through semi-solid electrodes allows high areal capacities. Further decrease in electrode porosity may be possible for thinner electrode. Nevertheless, we believe that it will be very challenging to obtain semi-solid electrodes with an electrode porosity below 60 % while maintaining the flowability. Therefore, we take values of electrode porosity between 60 – 70 % and areal capacities between 10 – 15  $\text{mAh cm}^{-2}$  for the theoretical calculations below.

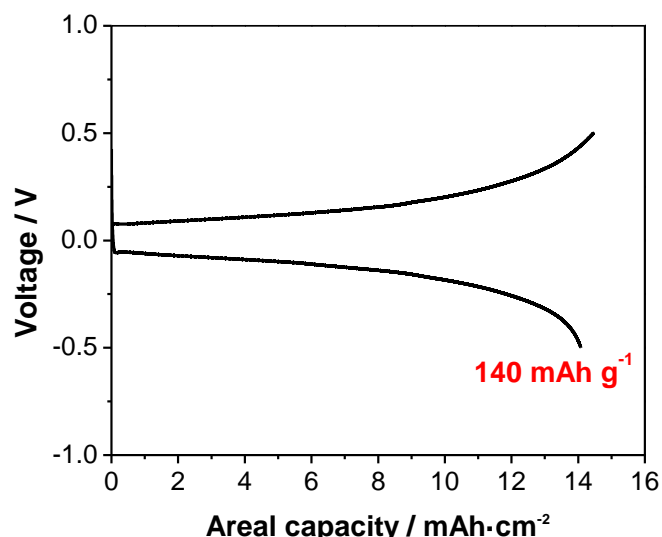


Figure 4 - 12. Voltage profile of a  $\text{FePO}_4$  –  $\text{LiFePO}_4$  injected battery with an electrode porosity of 70 vol% cycled at  $C/14$  ( $1 \text{ mA cm}^{-2}$ ) reaching a utilization rate of  $\text{LiFePO}_4$  of  $140 \text{ mAh g}^{-1}$  for the limiting side (the 1 mm-thick electrode vs the 2 mm-thick electrode).

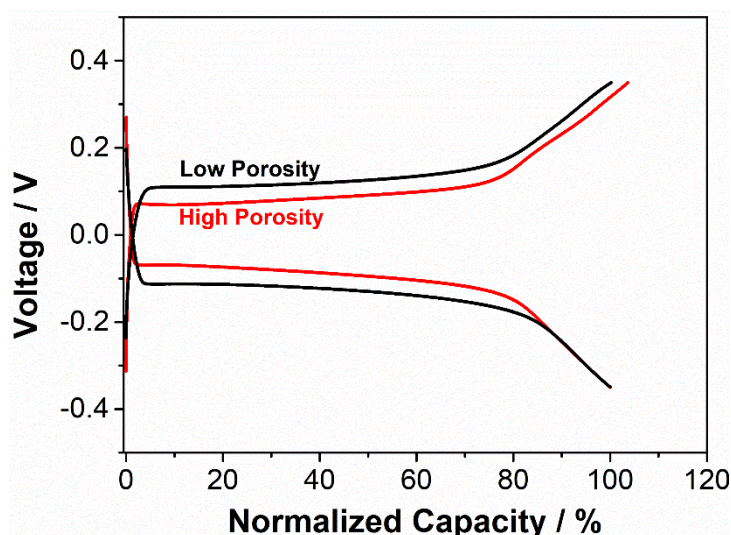


Figure 4 - 13. Normalized voltage profile of a  $\text{FePO}_4$  –  $\text{LiFePO}_4$  injected battery with lower electrode porosity (70 vol%) cycled at  $1 \text{ mA cm}^{-2}$  and higher electrode porosity (90 vol%) at  $2 \text{ mA cm}^{-2}$ .

#### 4.3.3.1 Battery cost

We conducted theoretical calculations on the contribution of the main elements of a battery to the cost of materials for the aqueous  $\text{LiTi}_2(\text{PO}_4)_3$  –  $\text{LiFePO}_4$  battery (**Figure 4-14a**). The “inactive materials”, e.g. current collector and separator, have a large

contribution (80 %) which is mainly due to the price of the positive current collector (expanded graphite) for neutral pH media. When a battery cell is reused after substitution of the semi-solid electrode, the costs related to inactive materials are completely eliminated. Thus, the contribution of inactive materials to the overall cost of materials represents the reduction in materials cost for each regeneration.

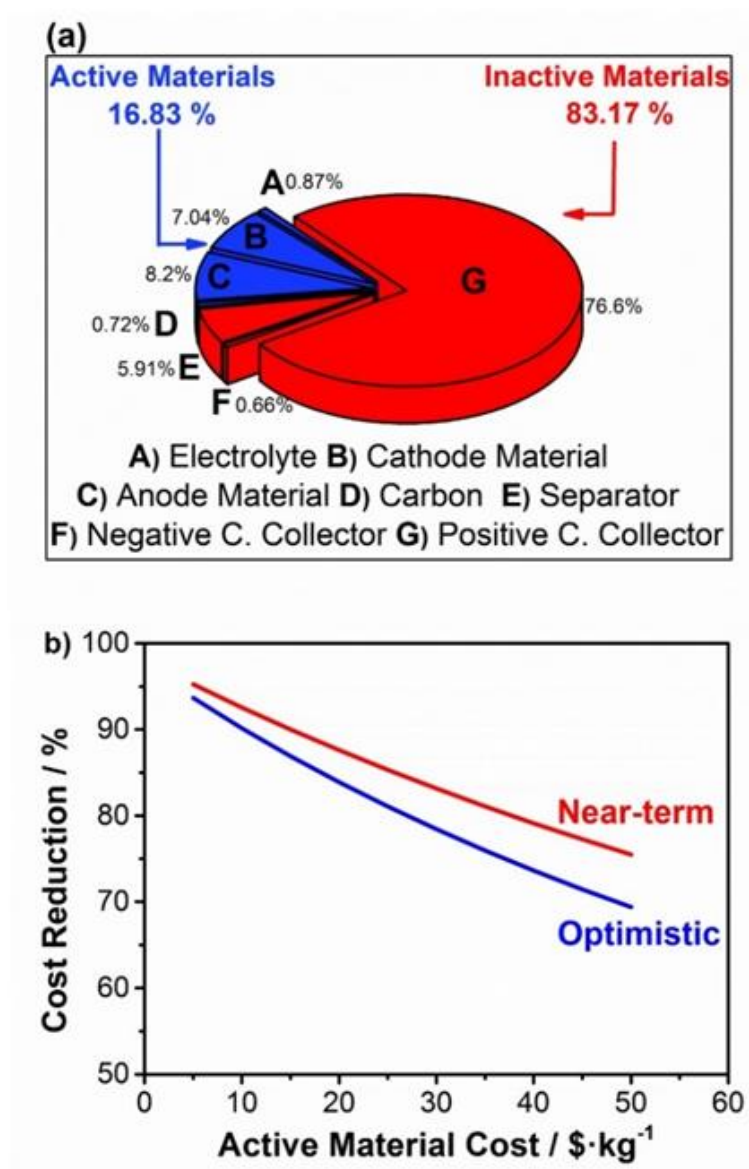


Figure 4 - 14. (a) Contributions of different elements to the cost of materials for the aqueous  $\text{LiTi}_2(\text{PO}_4)_3 - \text{LiFePO}_4$  battery. (b) Evolution of the contribution of inactive materials, which represents the reduction in battery costs, as a function of the active materials cost for an aqueous battery (neutral pH electrolyte). The values were calculated using prices of materials shown in Table 4-2.

The purchase cost per kWh of battery (USD kWh<sup>-1</sup>) was calculated according to the **Equation 4-3** and does not include any processing cost, assuming an average discharge voltage of 0.9 V for LFP-LTP batteries and 3.4 V for Li-ion batteries (Li – LiFePO<sub>4</sub>). Since an areal capacity of 1 mAh cm<sup>-2</sup> and 1 cm<sup>2</sup> of battery were selected, the capacity was 1 mAh.

$$Purchase\ cost\ per\ kWh = \frac{(Cost_{cathode} + Cost_{anode} + Cost_{electrolyte} + Cost_{current\ collector} + Cost_{separator})}{Capacity \cdot Discharge\ Voltage} \quad [4-3]$$

The procedure used to calculate the purchase cost of each component is described as follows:

- Cathode Material Cost ( $Cost_{cathode}$ ), the total cost of the LFP ( $Cost_{LFP}$ ) was calculated by **Equation 4-4**.

$$Cost_{LFP} = \frac{C_{Battery}}{C_{LFP}} \cdot P_{LFP} \quad [4-4]$$

Where,  $Cost_{LFP}$  is the active material cost,  $C_{Battery}$  is the capacity of the battery (1 mAh),  $C_{LFP}$  is the specific capacity of LiFePO<sub>4</sub> (140 mAh g<sup>-1</sup>) extracted from literature, and  $P_{LFP}$  is the cost of LFP per kg (USD kg<sup>-1</sup>) according to literature. The cost of the carbon (KetjenBlack), assuming that represents the 10% of the cathode weight, was calculated following the **Equation 4-5**.

$$Cost_{LFP} = \frac{C_{Battery}}{C_{LFP}} \cdot \frac{0.1}{0.9} \cdot P_{Carbon} \quad [4-5]$$

Where, the  $P_{Carbon}$  is the cost of the carbon per kg (USD kg<sup>-1</sup>).

- Current collector ( $Cost_{current\ collector}$ ): The purchase cost of current collector was extracted from the cost in USD m<sup>-2</sup>, depending on the system studied.
- Anode Material Cost ( $Cost_{anode}$ ): The total cost of the anode ( $Cost_{anode}$ ) was calculated by **Equation 4-6**.

$$Cost_{anode} = \frac{C_{Battery}}{C_{anode}} \cdot P_{anode} \quad [4-6]$$

Where, the  $Cost_{anode}$  is the active material cost, the  $C_{Battery}$  is the capacity of the battery (1 mAh), the  $C_{anode}$  is the specific capacity of LTP for aqueous system and Li for the non-aqueous one extracted from literature, and the  $P_{anode}$  is the costs of anode material per kg (USD kg<sup>-1</sup>) according to literature.

- Separator ( $Cost_{separator}$ ): The separator membrane cost was 2.7 USD m<sup>-2</sup>.
- Electrolyte cost: The volume of the electrolyte necessary to fill the electrodes of the battery was estimated as follows. Then, the grams of electrolyte necessary to fill the free volume depending on the porosity of the electrodes were calculated assuming a density of the electrolyte of 1.1 g cm<sup>-3</sup> and 1.28 g cm<sup>-3</sup> for the aqueous and non-aqueous system, respectively. Finally, the cost of electrolyte was calculated from the cost of 1 kg of material. The raw material cost of each component of the battery (USD kg<sup>-1</sup> or USD MT<sup>-1</sup>) is summarized in **Table 4-2**.

**Table 4 - 2. Prices of materials for the analysis of costs**

<i>Material</i>	<i>Cost (USD·kg<sup>-1</sup>)</i>	<i>Reference</i>
<i>Lithium Iron Phosphate</i>	15	36
<i>Lithium Titanium Phosphate</i>	15*	37
<i>Graphite</i>	10	36
<i>Carbon</i>	7,15	36
<i>Aqueous Electrolyte</i>	0,9	38
<i>Non-Aqueous Electrolyte</i>	19,5	36
<i>Material</i>	<b>Cost (USD·m<sup>2</sup>)</b>	<b>Reference</b>
<i>Aqueous Current Collector</i>	35	39
<i>Non-Aqueous Positive Current Collector</i>	0,3	36
<i>Non-Aqueous Negative Current Collector</i>	1,2	36
<i>Separator</i>	2,7	36

\* *Since LTP is not commercially available, we use the price of another lithium titanate (LTO (Lithium Titanate Oxide)).*

We also made a general estimation of the injectable concept for potential emerging aqueous battery chemistries in mild pH media. **Figure 4-14b** shows the evolution of the battery cost reduction as function of the cost of active materials (cathode + anode) for two scenarios: Near Term Price of Current Collector and Optimistic Price of Current Collector, which represent the prices of the needed expended graphite: 35 USD m<sup>-2</sup> and 25 USD m<sup>-2</sup> for a near-term and optimistic scenario, respectively<sup>39</sup>.

For injectable batteries, the reduction in battery cost for each regeneration increases as the cost of active materials decreases, which makes the injectable concept very attractive for future emerging battery technologies deploying cheap active materials, e.g. Zn–MnO<sub>2</sub> and all-organic batteries. In addition, there is a further reduction of costs associated with the manufacturing (not calculated in the present work), since a new injectable battery cell does not need to be manufactured. On the other hand, the higher porosity of semi-solid electrodes requires the use of more electrolyte.

**Figure 4-15** shows that the impact of electrode porosity in battery cost is negligible for aqueous systems. Also, this figure shows that the cost decreases with increasing areal capacity. We have demonstrated that semi-solid electrode having areal capacities of 14 mAh cm<sup>-2</sup> operates normally. Therefore, easy regeneration/recycling of the injectable battery not only has a positive environmental impact but also economic advantages.

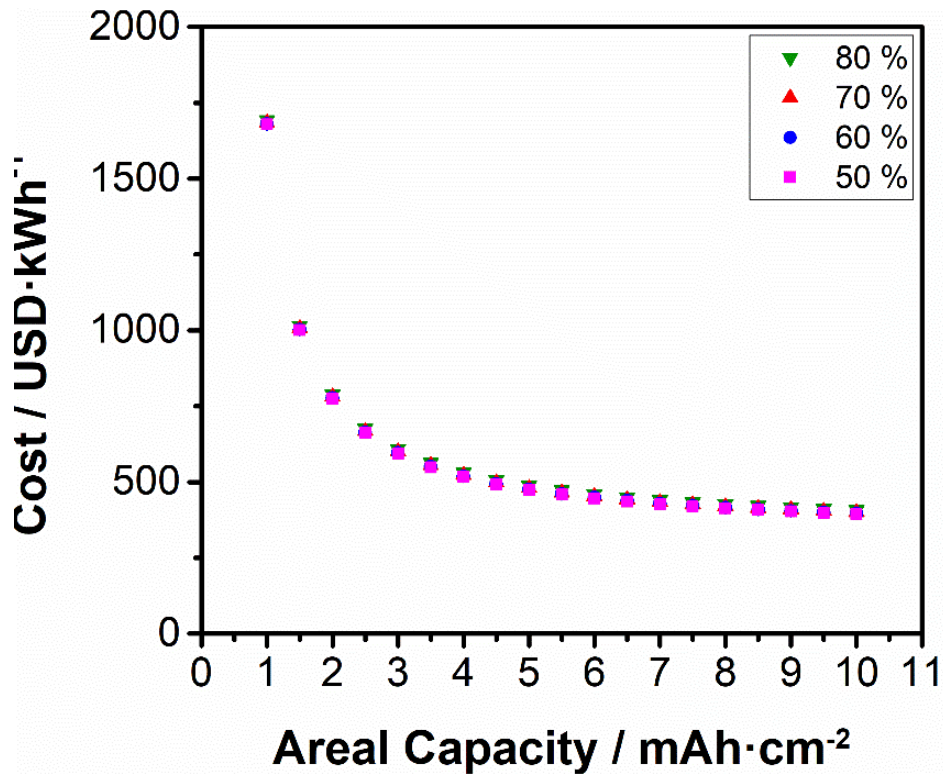


*Figure 4 - 15. Evolution of cost of materials as a function of the areal capacity and electrode porosity for an aqueous  $\text{LiTi}_2(\text{PO}_4)_3 - \text{LiFePO}_4$  battery.*

#### 4.3.3.2 Energy density

The higher electrode porosity of semi-solid electrodes is clearly a penalty for the energy density (**Figure 4-16a**). For the sake of the analysis, we take an electrode porosity value of 65 % and 45 % for semi-solid and conventional electrode, respectively. On the other hand, the areal capacity is expected to be higher for semi-solid electrode due to the enhanced mass transport (higher porosity) so that an areal capacity of 10 mAh cm<sup>-2</sup> and 3 mAh cm<sup>-2</sup> are assumed for injectable batteries and high-energy conventional batteries<sup>40</sup>. Under these conditions, the increase in energy density derived from the higher areal capacity of injectable batteries does not compensate the effect of the lower electrode porosity of conventional batteries. For instance, the energy density obtained using conventional electrode of 45 vol.% and 3 mAh cm<sup>-2</sup> (74 Wh L<sup>-1</sup>) is still higher than the value for semi-solid electrodes of 65 vol.% and 10 mAh cm<sup>-2</sup> (61 Wh L<sup>-1</sup>).

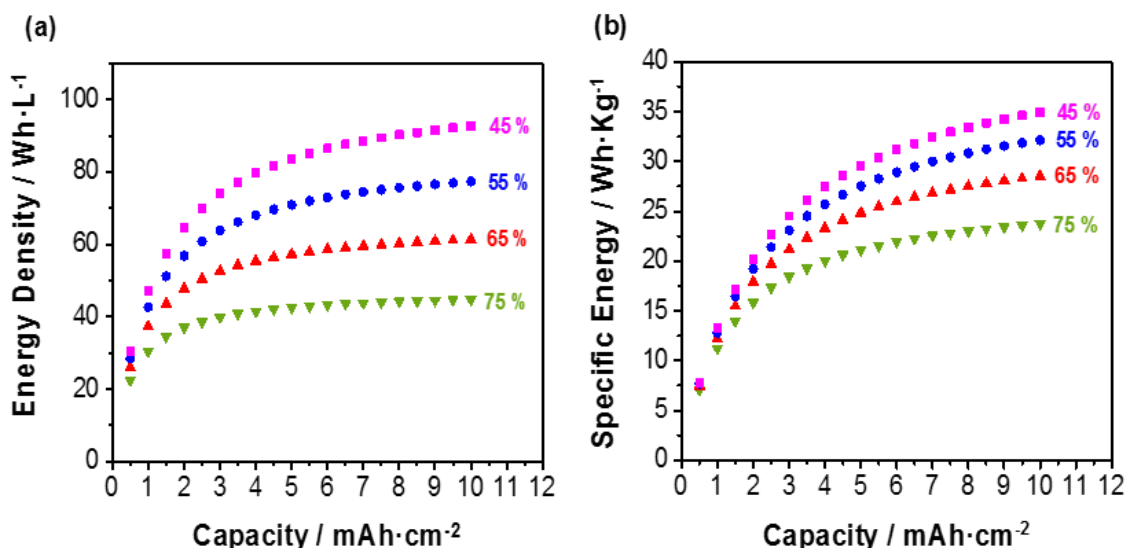


Figure 4 - 16. Evolution of (a) energy density and (b) specific energy as a function of the areal capacity and electrode porosity for the aqueous  $\text{LiTi}_2(\text{PO}_4)_3 - \text{LiFePO}_4$ .

Thus, much work will be necessary to increase the areal capacity and especially decrease the electrode porosity of injectable battery for the latter technology to compete with conventional batteries in terms of energy density. In the case of specific energy, the impact of electrode porosity is less severe (**Figure 4-16b**). The differences in specific energy using conventional and semi-solid electrodes can be minimized by realizing higher areal capacities. Using the same example (conventional electrodes of  $3 \text{ mAh cm}^{-2}$  and semi-solid electrodes of  $10 \text{ mAh cm}^{-2}$ ), the specific energy using conventional electrodes is only 5-10 % higher than that using semi-solid electrodes. In stationary energy storage applications, differences of 10 – 30 % in specific and energy density are assumable since battery cost is the most pressing parameters.

#### 4.3.4 Proof of plausibility for non-aqueous battery chemistries

We focused on aqueous systems for the first proof-of-concept of the injectable battery due to the safety concerns that the injectable approach may raise for non-aqueous systems at larger scale, which will require to be carefully evaluated in a specific study.

Nevertheless, we decided to show a concept of plausibility for non-aqueous battery chemistries. As a case study, the non-aqueous Li – LiFePO<sub>4</sub> injectable battery was investigated in the absence of air (Ar-filled glovebox). Due to the nature of the non-aqueous electrolyte, PTFE and expanded PTFE were used for the main body and gaskets, respectively (**Figure 4-17**).

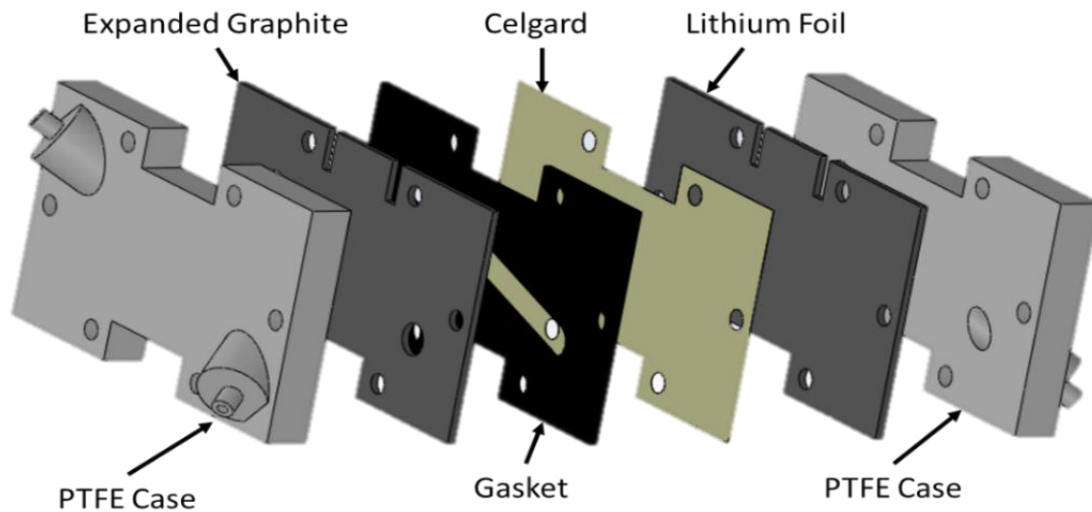


**Figure 4 - 17.** Schematic representation of the cell design of the non-aqueous Li – LiFePO<sub>4</sub> injectable battery.

The mass loading was adjusted to deliver an areal capacity below 1 mAh cm<sup>-2</sup> to avoid short-circuiting originated from the Li metal anode. The voltage profiles for an injected Li –LFP cell (**Figure 4-18a**) showed the voltage profile of a charge – discharge process revealing a plateau at *ca.* 3.4 V, similarly to conventional Li – LFP cells.

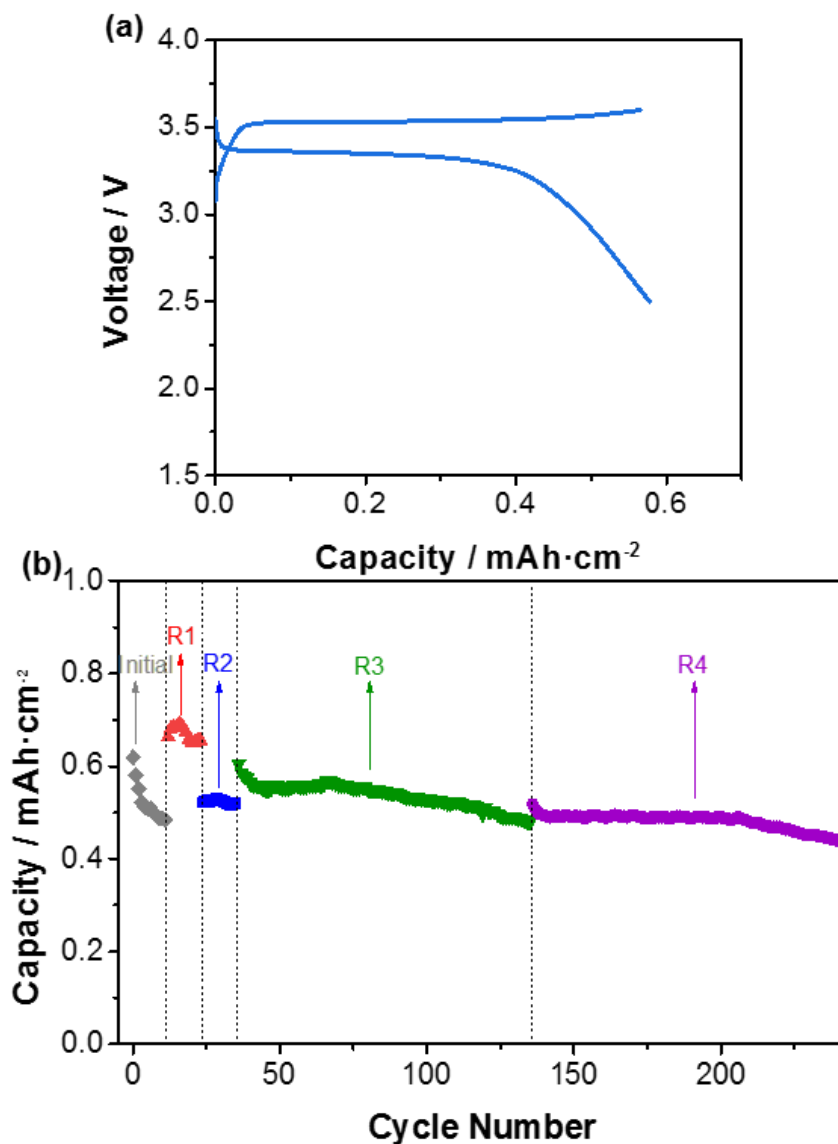


**Figure 4 - 18.** (a) Voltage profile and (b) evolution of the area capacity with cycles for 4 subsequent regenerations for the non-aqueous Li – LiFePO<sub>4</sub> injectable battery electrode.

After a slight capacity decrease during the first few cycles that is attributed to the Li metal anode (SEI thickening), the capacity stabilized at *ca.* 0.5 mAh cm<sup>-2</sup> / 80 mAh g<sup>-1</sup> (**Figure 4-18b**). The regeneration/recycling protocol was adapted to non-aqueous media: the spent semi-solid electrode was removed using compressed-Ar followed by circulating dimethyl carbonate for a minute. Several regenerations (**Figure 4-18b**) were successfully accomplished. The content of LiFePO<sub>4</sub> was increased in R1, and decreased back to its initial value for R2, R3 and R4. The increase in LiFePO<sub>4</sub> content for R1 led to an increase

in areal capacity, which confirmed the substitution of the semi-solid electrode during the regeneration.

The evolution of the energy and coulombic efficiency with the number of cycles for the non-aqueous Li – LiFePO<sub>4</sub> injectable battery are shown in **Figure 4-19**. The coulombic efficiency remained above 99 %. As for the energy efficiency, the battery delivered values of *ca.* > 90 %.

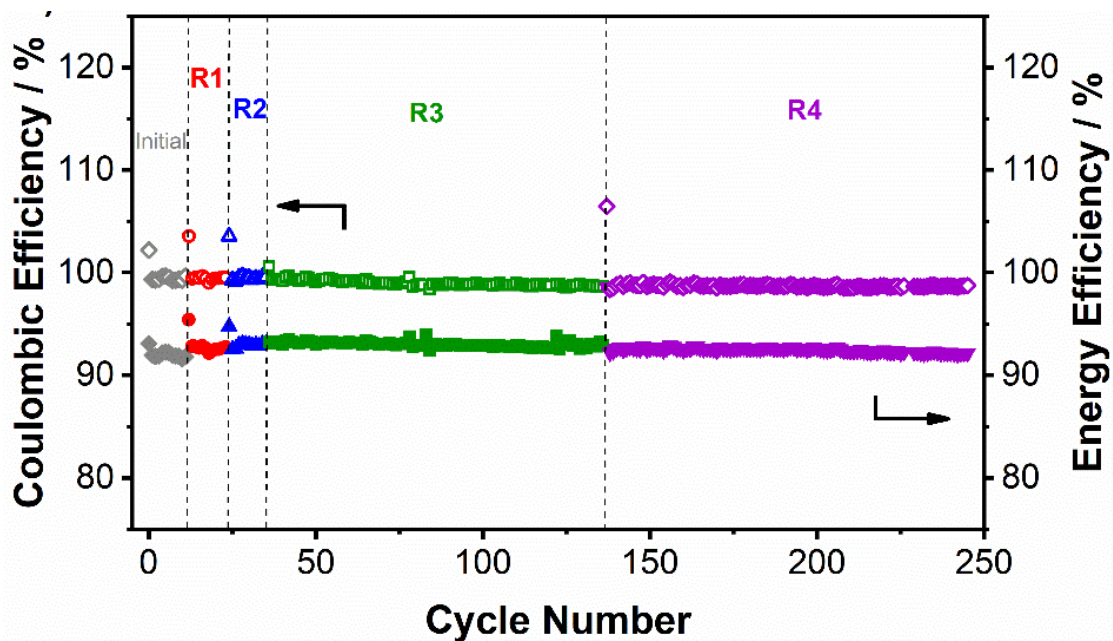


**Figure 4 - 19.** Energy and coulombic efficiency of Li - LiFePO<sub>4</sub> 0.3 mA cm<sup>-2</sup>.

The theoretical analysis of the battery cost for non-aqueous system was made by using the values of **Table 4-2** and **Equations 4-3 to 4-6**, separating the cost in active materials (carbon, active materials, and electrolyte) and inactive materials (current collectors and separator). The reduction in battery costs between 25 – 40 % are expected from our calculations (**Figure 4-20**)

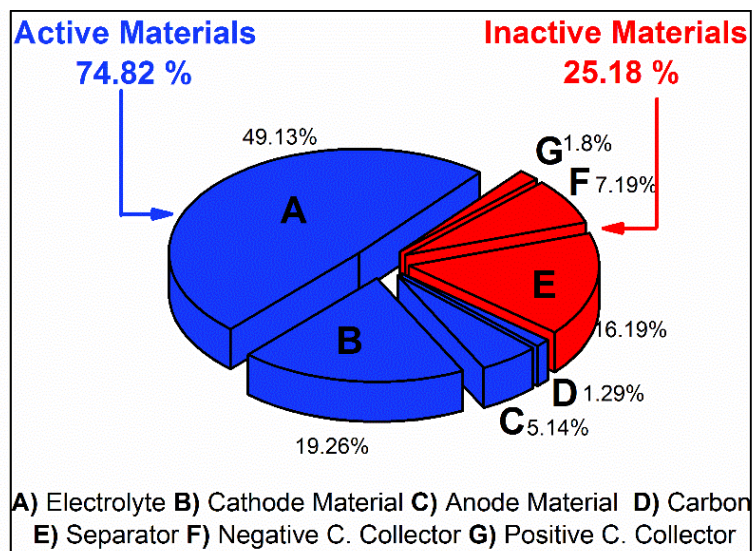


Figure 4 - 20. Contributions of different elements to the cost of materials for a non-aqueous Li – LiFePO<sub>4</sub> battery.

Specific and energy density will be penalized by the higher porosity of semi-solid electrodes. Theoretical analysis of the evolution evolution of energy density and specific energy were carried out for the non-aqueous system when the electrode porosity changes (Figure 4-21).

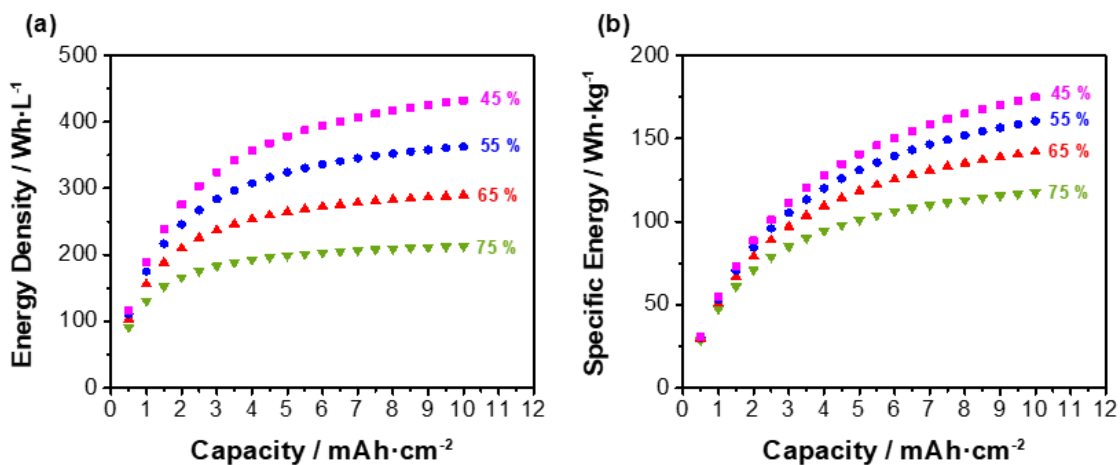


Figure 4 - 21. Evolution of (a) Energy density and (b) Specific energy as a function of the areal capacity and electrode porosity for a non-aqueous Li – LiFePO<sub>4</sub> battery.

Therefore, the injectable battery concept should be explored for low-cost non-aqueous battery chemistries which target stationary energy storage applications.

## 4.4 Conclusions

In summary, an innovative battery concept is proposed to address the issue of sustainability and circular economy of batteries. The proof-of-concept for aqueous injectable batteries shown for aqueous injectable batteries ( $\text{Zn} - \text{LiFePO}_4$  and  $\text{LiTi}_2(\text{PO}_4)_3 - \text{LiFePO}_4$ ) is successfully demonstrated, while preliminary results are presented for non-aqueous batteries ( $\text{Li} - \text{LiFePO}_4$ ). The electrochemical performance of injectable battery cells is shown to be comparable to conventional batteries even after being subjected to several recycling process. The higher intrinsic electrode porosity (ratio between volume of active material and total volume) of semi-solid electrodes necessary for the injectable battery is identified as the main drawback of this concept since it penalizes the specific and energy density, with respect to conventional battery. Most importantly, the cost of the regenerated battery (second, third and so on spent battery) may be reduced up to 80 % due to the reuse of battery cells (inactive materials). In addition to this essential advantage, costs related to battery manufacturing will be also reduced since the fabrication of a new injectable battery cell is not required. Therefore, easy regeneration/recycling of the injectable battery not only has a positive environmental impact but also economic advantages. Elucidating ageing mechanism of static semi-solid electrodes in emerging aqueous battery chemistries with low-cost active materials will be of special interest for this concept holding the key for success of this conceptually new family of batteries.

## 4.5 References

1. Benchmark Mineral Intelligence | Price Reporting Agency.
2. Ciez, R. E. & Whitacre, J. F. Examining different recycling processes for lithium-ion batteries. *Nat. Sustain.* **2**, 148–156 (2019).
3. Yang, Z. *et al.* Electrochemical energy storage for green grid. *Chem. Rev.* **111**, 3577–3613 (2011).
4. Larcher, D. & Tarascon, J. M. Towards greener and more sustainable batteries for electrical energy storage. *Nat. Chem.* **7**, 19–29 (2015).
5. Kim, J., Kim, J. H. & Ariga, K. Redox-Active Polymers for Energy Storage Nanoarchitectonics. *Joule* **1**, 739–768 (2017).
6. Wu Li, j. R. Dahn, D. S. W. Rechargeable Lithium batteries with aqueous electrolytes. *Science* (80-. ). **264**, 1–4 (1994).
7. Xu, C., Li, B., Du, H. & Kang, F. Energetic zinc ion chemistry: The rechargeable zinc ion battery. *Angew. Chemie - Int. Ed.* **51**, 933–935 (2012).
8. Hurlbutt, K., Wheeler, S., Capone, I. & Pasta, M. Prussian Blue Analogs as Battery Materials. *Joule* **2**, 1950–1960 (2018).
9. Velázquez-Martínez *et al.* A critical review of lithium-ion battery recycling processes from a circular economy perspective. *Batteries* **5**, 5–7 (2019).
10. Larouche, F. *et al.* Progress and status of hydrometallurgical and direct recycling of Li-Ion batteries and beyond. *Materials (Basel)*. **13**, (2020).
11. Asadi Dalini, E., Karimi, G., Zandevakili, S. & Goodarzi, M. A Review on Environmental, Economic and Hydrometallurgical Processes of Recycling Spent Lithium-ion Batteries. *Miner. Process. Extr. Metall. Rev.* **00**, 1–22 (2020).
12. Huang, B., Pan, Z., Su, X. & An, L. Recycling of lithium-ion batteries: Recent advances and perspectives. *J. Power Sources* **399**, 274–286 (2018).
13. Sommerville, R., Shaw-Stewart, J., Goodship, V., Rowson, N. & Kendrick, E. A review of physical processes used in the safe recycling of lithium ion batteries. *Sustain. Mater. Technol.* **25**, e00197 (2020).
14. Rothermel, S., Krüger, S., Winter, M. & Nowak, S. Recycling of Lithium-Ion

- Batteries: The LithoRec Way. 219–246 (2018).
15. Hanisch, C., Diekmann, J., Stieger, A., Haselrieder, W. & Kwade, A. Recycling of Lithium-Ion Batteries. *Handb. Clean Energy Syst.* 1–24 (2015) doi:10.1002/9781118991978.hces221.
  16. Sloop, S. Giga Life Cycle: Manufacture of Cells from Recycled EV Li-ion Batteries. (2015).
  17. Sloop, S. E. *et al.* Cathode healing methods for recycling of lithium-ion batteries. *Sustain. Mater. Technol.* **22**, (2019).
  18. Dühren, S. *et al.* Toward Green Battery Cells: Perspective on Materials and Technologies. *Small Methods* **4**, (2020).
  19. Sun, J., Sun, Y., Gai, L., Jiang, H. & Tian, Y. Carbon-coated mesoporous LiTi<sub>2</sub>(PO<sub>4</sub>)<sub>3</sub>nanocrystals with superior performance for lithium-ion batteries. *Electrochim. Acta* **200**, 66–74 (2016).
  20. Duduta, M. *et al.* Semi-solid lithium rechargeable flow battery. *Adv. Energy Mater.* **1**, 511–516 (2011).
  21. Ventosa, E. *et al.* Non-aqueous semi-solid flow battery based on Na-ion chemistry. P2-type Na<sub>x</sub>Ni<sub>0.22</sub>Co<sub>0.11</sub>Mn<sub>0.66</sub>O<sub>2</sub>-NaTi<sub>2</sub>(PO<sub>4</sub>)<sub>3</sub>. *Chem. Commun.* **51**, 7298–7301 (2015).
  22. Ventosa, E., Amedu, O. & Schuhmann, W. Aqueous Mixed-Cation Semi-solid Hybrid-Flow Batteries. *ACS Appl. Energy Mater.* **1**, (2018).
  23. Home - 24M.
  24. Muñoz-Torrero, D., Palma, J., Marcilla, R. & Ventosa, E. Al-Ion Battery Based on Semisolid Electrodes for Higher Specific Energy and Lower Cost. *ACS Appl. Energy Mater.* **3**, 2285–2289 (2020).
  25. Yesibolati, N. *et al.* High performance Zn/LiFePO<sub>4</sub> aqueous rechargeable battery for large scale applications. *Electrochim. Acta* **152**, 505–511 (2014).
  26. Wang, F. *et al.* Highly reversible zinc metal anode for aqueous batteries. *Nat. Mater.* **17**, 543–549 (2018).
  27. Chen, L. *et al.* Electrochemical profile of LiTi<sub>2</sub>(PO<sub>4</sub>)<sub>3</sub> and NaTi<sub>2</sub>(PO<sub>4</sub>)<sub>3</sub> in lithium, sodium or mixed ion aqueous solutions. *J. Electrochem. Soc.* **163**, A904–

- A910 (2016).
28. Sun, J., Sun, Y., Gai, L., Jiang, H. & Tian, Y. Carbon-coated mesoporous  $\text{LiTi}_2(\text{PO}_4)_3$  nanocrystals with superior performance for lithium-ion batteries. *Electrochim. Acta* **200**, 66–74 (2016).
  29. Goulet, M.-A. & Aziz, M. J. Flow Battery Molecular Reactant Stability Determined by Symmetric Cell Cycling Methods. *J. Electrochem. Soc.* **165**, A1466–A1477 (2018).
  30. Páez, T., Martínez-Cuezva, A., Palma, J. & Ventosa, E. Mediated alkaline flow batteries: From fundamentals to application. *ACS Appl. Energy Mater.* **2**, 8328–8336 (2019).
  31. He, P., Liu, J. L., Cui, W. J., Luo, J. Y. & Xia, Y. Y. Investigation on capacity fading of  $\text{LiFePO}_4$  in aqueous electrolyte. *Electrochim. Acta* **56**, 2351–2357 (2011).
  32. Luo, J. Y., Cui, W. J., He, P. & Xia, Y. Y. Raising the cycling stability of aqueous lithium-ion batteries by eliminating oxygen in the electrolyte. *Nat. Chem.* **2**, 760–765 (2010).
  33. Li, Z. *et al.* Aqueous Semi-Solid Flow Cell : Demonstration and Analysis. 2–7 (2013).
  34. Gordon, D. *et al.* Enhancing cycle stability of lithium iron phosphate in aqueous electrolytes by increasing electrolyte molarity. *Adv. Energy Mater.* **6**, 1–11 (2016).
  35. Alias, N. & Mohamad, A. A. Synthesis and electrochemical behavior of  $\text{LiFePO}_4/\text{C}$  with an air-electrode in an aqueous lithium ion battery. *Ceram. Int.* **40**, 13089–13096 (2014).
  36. Patry, G., Romagny, A., Martinet, S. & Froelich, D. Cost modeling of lithium-ion battery cells for automotive applications. *Energy Sci. Eng.* **3**, 71–82 (2015).
  37. Vaalma, C., Buchholz, D., Weil, M. & Passerini, S. A cost and resource analysis of sodium-ion batteries. *Nat. Rev. Mater.* **3**, 1–11 (2018).
  38. Weng, G. M., Li, Z., Cong, G., Zhou, Y. & Lu, Y. C. Unlocking the capacity of iodide for high-energy-density zinc/polyiodide and lithium/polyiodide redox flow batteries. *Energy Environ. Sci.* **10**, 735–741 (2017).

39. Viswanathan, V. *et al.* Cost and performance model for redox flow batteries. *J. Power Sources* **247**, 1040–1051 (2014).
40. Park, S. H. *et al.* High areal capacity battery electrodes enabled by segregated nanotube networks. *Nat. Energy* (2019) doi:10.1038/s41560-019-0398-y.



**Chapter 5. Implementation of Injectable  
Semi-Solid Electrode for an Ultra-Low-Cost  
Aqueous Battery Chemistry: The Injectable  
Zn – MnO<sub>2</sub> battery**

The results obtained in this chapter have been published in an international peer-reviewed journal (Electrochemistry Communications, IF:4.724). Basic information about this publication can be found as follows.

**D. Perez-Antolin**, I. Sáez-Bernal, A. Colina, E. Ventosa. (2022). Float-charging protocol in rechargeable Zn–MnO<sub>2</sub> batteries: unraveling the key role of Mn<sup>2+</sup> additives in preventing spontaneous pH changes. *Electrochemistry Communications*, 107271. DOI: 10.1016/j.elecom.2022.107271.

<https://www.sciencedirect.com/science/article/pii/S138824812200073X>

## 5.1 Introduction

Energy Storage Systems have become key elements in the transition to a more sustainable energy model,<sup>1</sup> by *i*) buffering energy to match the demand and intermittent production of energy from renewable sources, and *ii*) powering electric vehicles. Batteries, and Li-ion batteries in particular, are considered an excellent compromise due to their relatively high energy density, cycle stability, energy efficiency and cost. On the other hand, this technology still faces important challenges, i.e. safety issues related to the use of flammable organic solvents and availability of critical raw materials (e.g. Li, Co).<sup>2,3</sup> To overcome these challenges, much effort has been devoted to the development of battery chemistries based on abundant elements and aqueous electrolytes.<sup>4</sup> Rechargeable Zinc-Ion batteries are an attractive alternative owing to the intrinsic characteristics of Zn as negative electrode material: high specific capacity (820 mAh g<sup>-1</sup>), relatively cathodic redox potential (-0.76 V vs Standard Hydrogen Electrode in neutral pH), non-toxicity, non-flammability and low cost due to its high abundance and the well-known commercial processes for producing and recycling.<sup>5-7</sup>

The Zinc-Manganese Oxide battery is commercially available as alkaline primary battery due to its low-cost cost and specific capacity (100-300 mAh g<sup>-1</sup> depending on its structure). Therefore, the development of rechargeable Zn-MnO<sub>2</sub> batteries have focused much attention in the last decade as low-cost and safe energy storage solution.<sup>8</sup> This rechargeable battery was reported the first time using ZnSO<sub>4</sub> as mild-acidic electrolyte<sup>5,9,10</sup> instead of the alkaline media used in non-rechargeable commercial Zn-MnO<sub>2</sub> batteries. In neutral and mild-acidic electrolyte, Zn is reversibly plated and stripped on the negative electrode while charge storage mechanism in the positive electrode material is still under debate: possible Zn<sup>2+</sup> intercalation<sup>11,12</sup> and Mn

electrodissolution/electroplating.<sup>13–16</sup> In any case, insulating layers have been identified on the electrode surfaces during the discharge process,<sup>17</sup> e.g. Zn<sub>12</sub>(CF<sub>3</sub>SO<sub>3</sub>)<sub>9</sub>(OH)<sub>15</sub> · nH<sub>2</sub>O,<sup>18</sup> Zn<sub>4</sub>ClO<sub>4</sub>(OH)<sub>7</sub>,<sup>19</sup> or Zn<sub>4</sub>SO<sub>4</sub>(OH)<sub>6</sub> · nH<sub>2</sub>O (ZHS),<sup>20–22</sup> in Zn(CF<sub>3</sub>SO<sub>3</sub>)<sub>2</sub>, ZnSO<sub>4</sub> and Zn(ClO<sub>4</sub>)<sub>2</sub> electrolytes, respectively. These compounds are usually generated when the solution becomes alkaline.<sup>23</sup> Thus, changes of the electrolyte pH towards alkaline values must be avoided to retain the reversibility of the electrochemical reactions in Zn-MnO<sub>2</sub> batteries. Since charge storage in MnO<sub>2</sub> involves protons uptake and release, evolution of the electrolyte pH during charge / discharge process has been studied.<sup>24–26</sup> Surprisingly, changes in the electrolyte pH due to possible spontaneous reaction between Zn metal and protons in neutral pH, which should thermodynamically occur according to the Pourbaix diagram for Zn in “mild-acidic” pH,<sup>8</sup> have not been investigated. This reaction is very relevant considering that spontaneous oxidation of Zn metal would consume protons leading to an increase in the electrolyte pH.

Here we report the use of injectable semi-solid electrodes for high-energy Zn – MnO<sub>2</sub> batteries that can decrease the production cost and turns the system into a recyclable battery. Since the semi-solid electrodes can be injected into a pre-assembled cell and removed once a battery failure occurs, the inactive materials of the cell can be reused, and the active materials can be directly recycled as demonstrated in **Chapter 4**. In addition, evolution of the electrolyte pH over time is investigated by dissolving a pH indicator in the electrolyte and assembling the electrochemical cell in a spectrophotometer cuvette. This setup not only allows for confirmation of pH drift towards alkaline values, but it clearly reveals that changes in the electrolyte pH is originated at the Zn metal electrode. Based on this, a simple charging protocol is proposed to maintain the pH value of the electrolyte constant, which consists in

implementing a float charging step (constant voltage) at the end of the charge process. By holding the voltage at fully charged state, the oxygen evolution reaction is promoted at the positive electrode, which release protons and compensate the pH change provoked at the negative electrode.

## 5.2 Experimental Procedures

### 5.2.1 Reagents and Materials

For the injectable battery part: MnSO<sub>4</sub> · H<sub>2</sub>O (≥ 99 %, Sigma Aldrich), ZnSO<sub>4</sub> · 7H<sub>2</sub>O (≥ 99.5 %, Sigma Aldrich), Zinc Foil (99.98 %, Alfa Aesar), Zinc powder (-100 mesh, 99.9 %, Alfa Aesar), KetjenBlack EC-600 JD (Azelis and AkzoNovel polymer chemicals), and polyvinylpyrrolidone (Sigma Aldrich) were used as received. Expanded graphite (Sigracet TF6) was used as current collector, and Celgard 3501 as separator.

Regarding the pH evaluation part: MnSO<sub>4</sub> · H<sub>2</sub>O (≥ 99 %, Sigma Aldrich), ZnSO<sub>4</sub> · 7H<sub>2</sub>O (≥ 99.5 %, Sigma Aldrich), Zinc Foil (99.98 %, Alfa Aesar), NaCl (99 %, Alfa Aesar), KCl (99 %, Alfa Aesar), LiCl (99 %, Alfa Aesar), Bromocresol green (Panreac). UV-Vis cuvette was used as open electrochemical cell and expanded graphite (Sigracet TF6) was used as substrate for the electrodeposition of MnO<sub>2</sub>. Aqueous solution 2 M ZnSO<sub>4</sub> + 0.1 M MnSO<sub>4</sub> is used as electrolyte in this part of the work, with a measured pH of 3.74.

### 5.2.2 Preparation of electrodes

Semi-solid electrodes. MnO<sub>2</sub> electrode: 72 wt.% active material, 27.3 wt.% KetjenBlack and 0.7 wt.% stabilizing polyvinylpyrrolidone. Zn electrode: 79 wt.% active material, 21 wt.% KetjenBlack. Solid particles were dispersed in 6 mL of electrolyte (2M ZnSO<sub>4</sub> and 0.1 M MnSO<sub>4</sub>). The suspension was mixed with Ultra-Turrax IKA T18-Basic during three periods of 10 minutes resting 5 minutes between periods. The slurries were prepared directly in a syringe to facilitate the injection of the electrode into the battery pre-assembled. The external case of the battery was

designed and printed by 3D-Printing machine (MakerBot Replicator TM 2X) using ABS as plastic material.

MnO<sub>2</sub> solid electrodes were made by electrodeposition in three electrodes. Introducing the expanded graphite (working electrode) into a solution of KMnO<sub>4</sub> 0.5 M (Panreac, 98.5 %) for the reduction following **Equation 5-1**. Platinum wire and Ag/AgCl were used as counter and reference electrodes, respectively.<sup>27</sup>



Electrodes of MnO<sub>2</sub> electrodeposited are rectangles of 1 x 5 cm, that were immersed into the electrolyte just to 3 cm leaving the other two for the electrical connection. Therefore, their active area is 3 cm<sup>2</sup> (3 mL of volume).

### 5.2.3 Electrochemical Measurements

For the injectable battery part of the work, galvanostatic charge/discharge measurements were carried out using an EC-Biologic potentiostat. In the pH evaluation part of the work, an Autolab PGSTAT302N model was used.

## 5.3 Results and Discussion

This work is structured in two sections. The first section is dedicated to exploring the feasibility of using semi-solid injectable electrodes for rechargeable Zn – MnO<sub>2</sub> batteries. And the second section deals with the issues related to the changes of the electrolyte pH; shedding light into the key process and proposing approaching to mitigate it.

### 5.3.1 Semi-solid electrodes in Zn – MnO<sub>2</sub> battery

#### 5.3.1.1 High-energy injectable Zn – MnO<sub>2</sub> battery

First, the proof-of-concept of a Zn – MnO<sub>2</sub> battery using semi-solid electrode in both sides was aimed. For that purpose, the cell design detailed in **Figure 4-5 (Chapter 4)** was used. In this way, both electrodes are injected inside the cell and a cyclability test was carried out (**Figure 5-1**) at 2.5 mA cm<sup>-2</sup> (81 mA g<sup>-1</sup>), obtaining for the first cycle an areal capacity of 4.6 mAh cm<sup>-2</sup> in the first cycle (152 mAh g<sup>-1</sup>).

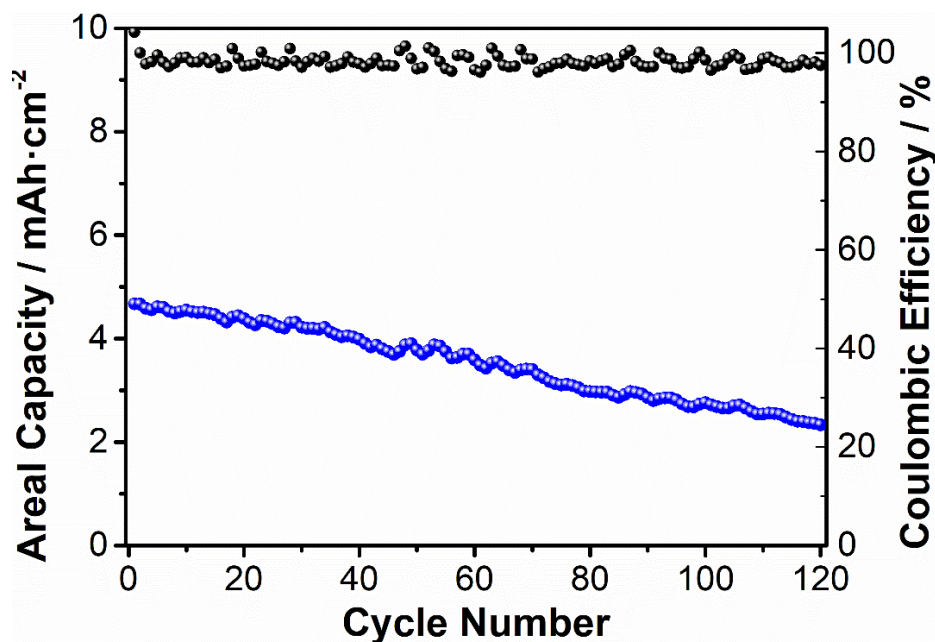


*Figure 5 - 1 Cyclability test of an injectable Zn – MnO<sub>2</sub> battery using semi-solid electrodes at 0.5 C.*

These results demonstrate the feasibility of using injectable semi-solid electrodes of zinc and manganese dioxide in rechargeable batteries. However, the capacity fade in this case is 50 % in 120 cycles (340 hours), which are likely associated with the corrosion of Zn in neutral media. It should be noted that the use of Zn powder in contrast with Zn foil typically used in conventional rechargeable Zn – MnO<sub>2</sub> batteries accelerate the corrosion process. To evaluate whether parasitic reactions at the negative electrode are responsible for the battery failure, a new configuration was designed and evaluated: the Zn hybrid-flow battery using MnO<sub>2</sub> semi-solid electrode.

### ***5.3.1.2 Hybrid flow-injectable battery***

An approach to mitigate the issues related with the hydrogen evolution reaction and changes in pH at the Zn electrode, flow of electrolyte at the negative electrode using a Zn foil. By this, the concentration gradients, and the pH variations (excess of electrolyte) are mitigated so that longer stability is expected. **Figure 5-2**). Shows the configuration for this hybrid-flow Zn-MnO<sub>2</sub> battery.

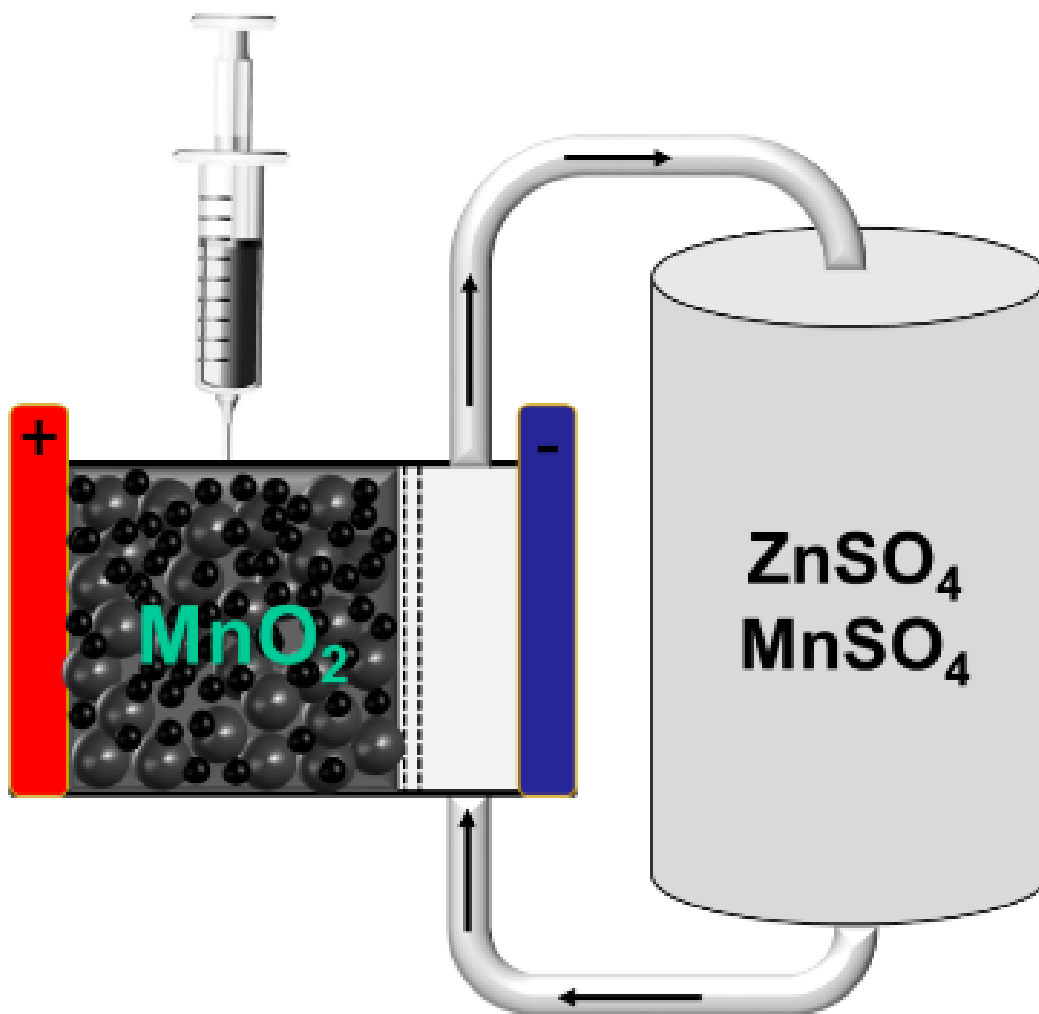


*Figure 5 - 2 Scheme of the battery cell design for the hybrid-flow injectable Zn - MnO<sub>2</sub> battery.*

This new configuration consists of a positive side of injected semi-solid MnO<sub>2</sub>, and a negative side of Zinc foil combined with a flow-channel for the electrolyte for the negative electrode. Regarding the internal parts of the cell, the design is based on that deployed in **Chapter 4**. The battery cell contains the following parts. First, one of the current collectors (expanded graphite) with two holes through which the semi-solid MnO<sub>2</sub> electrode is injected. A gasket is placed onto the current collector. This gasket is cut creating a channel, which defines the dimensions of the injected semi-solid electrode. A microporous separator (Celgard 3501) needed for isolating electrically

positive and negative compartments is put onto the mentioned gasket. This part corresponds to half-cell, so that the other half contain the same elements to compete the full cell. The final device is assembled by pressing all these parts. In one side, the empty space defined by the gaskets is filled with semi-solid electrode (2 mm thick) and an area of 7.5 cm<sup>2</sup> (**Figure 5-3**). On the other side, electrolyte continuously flows (Figure 5-3, inlet-outlet) from/to an external reservoir. In this side, a Zn foil is placed on top of the current collector.

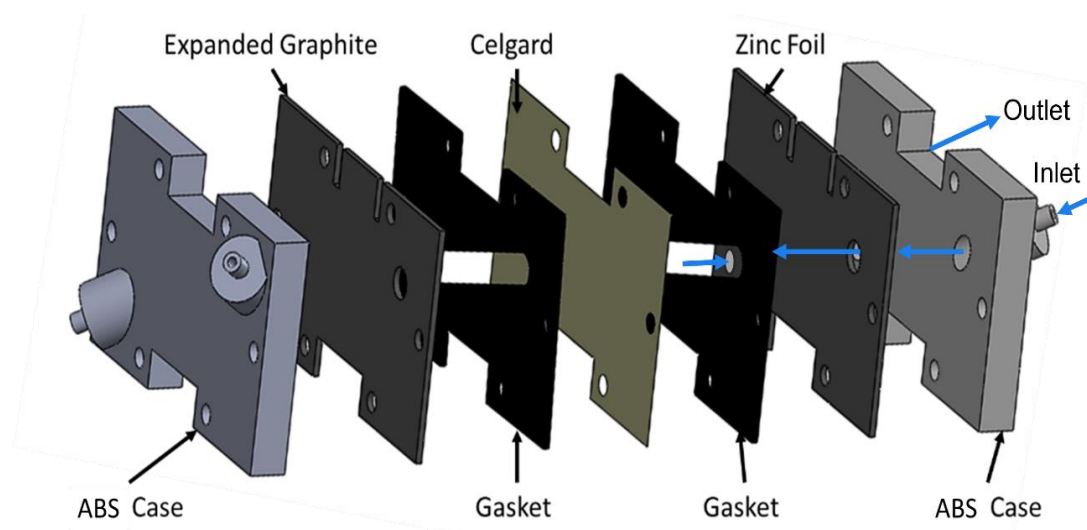


**Figure 5 - 3** Internal design of the cell.

Using this configuration, with 2 M ZnSO<sub>4</sub> + 0.1 M MnSO<sub>4</sub> as electrolyte, and a positive semi-solid electrode (72 wt.% MnO<sub>2</sub>, 27.3 wt.% KetjenBlack and 0.7 wt.% polyvinylpyrrolidone) a cyclability test was performed applying constant current of 5 mA·cm<sup>-2</sup> (≈ 1C). The high capacity of this cathode (4.55 mAh cm<sup>-2</sup> or 160 mAh g<sup>-1</sup> for the first cycle) is maintained (**Figure 5-4a**) upon cycling achieving a capacity retention of 83 % after 500 cycles (3.78 mAh cm<sup>-2</sup> or 129 mAh g<sup>-1</sup>).

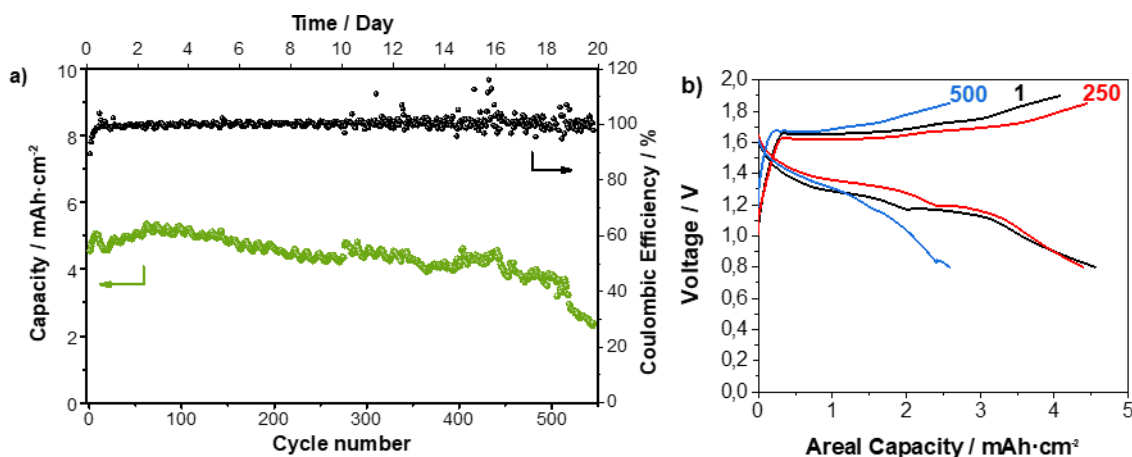


**Figure 5 - 4** (a) Cyclability test of the hybrid system: injected MnO<sub>2</sub> - Zn-foil with electrolyte flow. (b) Voltage profiles of 1<sup>st</sup>, 250<sup>th</sup> and 500<sup>th</sup> cycles.

Regarding the voltage profiles (**Figure 5-4b**), the discharge characteristic for this chemistry having two distinct plateaus ( $\approx 1.4$  V and  $\approx 1.2$  V). This behavior was analyzed during 500 cycles and while the charge plateau is maintained until the end, the discharges plateaus can be clearly identified also up to cycle 250. At the end of the experiment (cycle 500<sup>th</sup>), they almost disappeared resulting in a capacity fade of approximately 50 %. Visual inspection (**Figure 5-5**) revealed that the channel in which the flow passed through the cell was obstructed due to the formation of a thick layer of material ( $\approx 2$  mm thick) during cycling, The capacity loss occurring after 500 cycles is thus associated the formation of this thick film at the negative electrode. Although the electrolyte tank used contained 40 mL (compared to 1.5 mL of injected MnO<sub>2</sub> electrode), apparently it was not enough to compensate the change in system pH, which ended up in alkaline values with the consequent generation of by-products such as Zn<sub>4</sub>SO<sub>4</sub>(OH)<sub>6</sub> · nH<sub>2</sub>O.

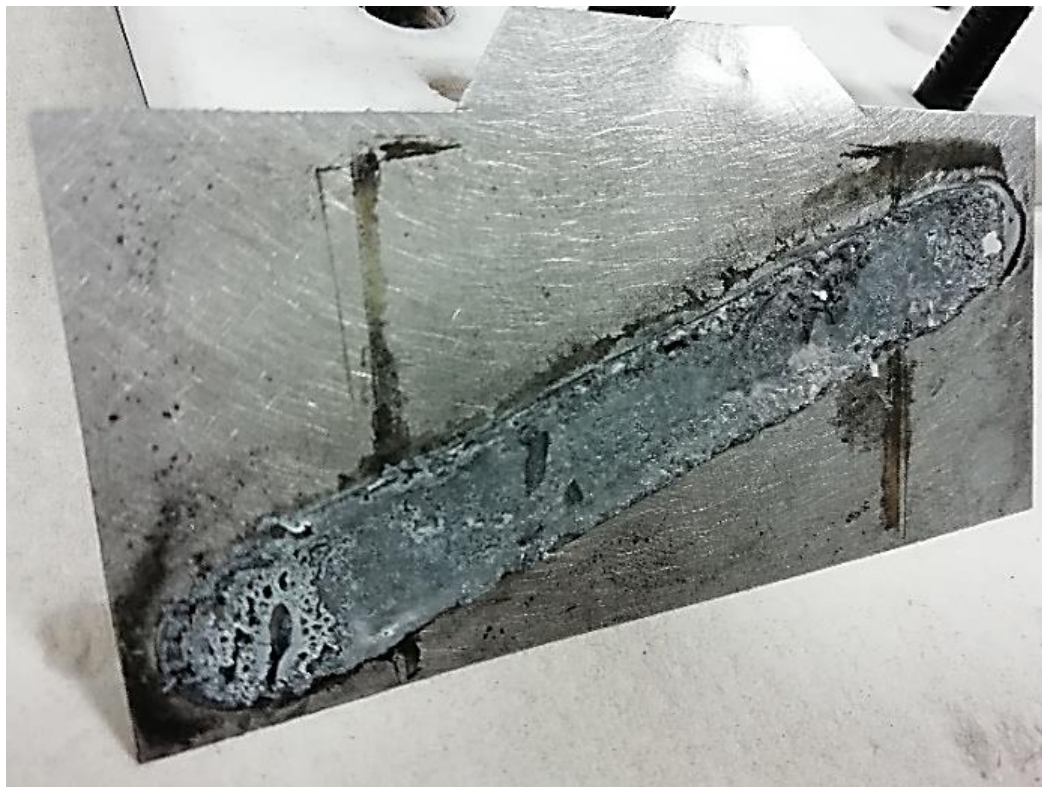


*Figure 5 - 5 Photograph of the negative zinc electrode after 500 cycles.*

In addition, the higher the areal capacity of the battery, the higher the amount of material generated inside, leading to the collapse of this system. These results motivated us to investigate the role of pH changes of the electrolyte in this chemistry.

### **5.3.2 Electrolyte pH in Zn – MnO<sub>2</sub> battery**

#### **5.3.2.1 Monitoring of electrolyte pH in Zn-MnO<sub>2</sub> batteries**

The electrolyte pH plays a critical role in the reversibility of Zn-MnO<sub>2</sub> batteries since insulating products having poor electrochemical reversibility are obtained in alkaline media. Lee *et al.* studied the changes in the electrolyte pH associated with charge storage mechanism of MnO<sub>2</sub> during charge and discharge.<sup>25</sup> This work confirmed the evolution of the electrolyte pH upon charge and discharge process: “During discharge, unstable trivalent manganese deprotonates and dissolves into the electrolyte resulting in a gradual increase in the pH value of the electrolyte. This triggers precipitation of

*zinc hydroxide sulfate from the electrolyte on the electrode surface. During charging, the pH value of the electrolyte reverts to being acidic as a result of manganese recombination on the cathode that causes zinc hydroxide sulfate to re-dissolve into the electrolyte".* While it was not analyzed in detail, their results also showed that the overall pH value of the electrolyte was turning alkaline over time, that is, there was an accumulated increase in the pH value upon subsequent cycles. This observation motivated us to assemble an electrochemical cell in a spectrophotometer cuvette using MnO<sub>2</sub> film electrodeposited on expanded graphite and Zn foil as positive and negative electrodes, respectively, and dissolving a pH indicator (Bromocresol green) in the electrolyte (**Figure 5-6a**). It should be noted that a similar setup was reported by Bischoff, C. F. *et al.*<sup>26</sup> which was proven to be of highly suitable. However, this previous study focused on the evolution of the electrolyte pH upon charge – discharge process, overlooking the spontaneous reaction between Zn metal and water. In our work, since the color range of Bromocresol green as indicator is yellow (pH < 3), green (3 < pH < 5), and blue (pH > 5), the electrolyte (pH ≈ 4 – 4.5) is initially green (**Figure 5-6b**).

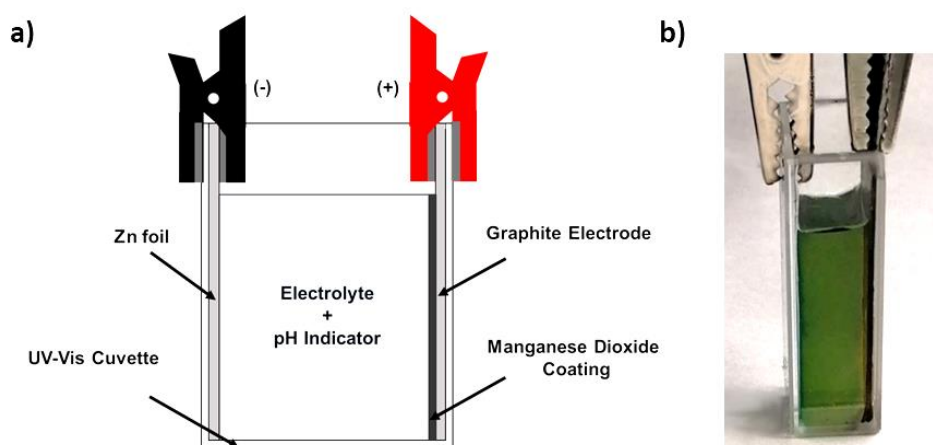


**Figure 5 - 6 (a) Scheme of the Zn-MnO<sub>2</sub> cell assembled in a UV-Vis Cuvette. (b) Picture of the cell filled with electrolyte containing pH indicator. Green color indicates that the pH value is between 3 and 5.**

While several reactions driven by the charge / discharge processes can induce changes in the pH value,<sup>24–26</sup> the spontaneous evaluation should be first assessed. Therefore, the cell was first left at open circuit voltage (OCV) for 22 hours (**Figure 5-7**).

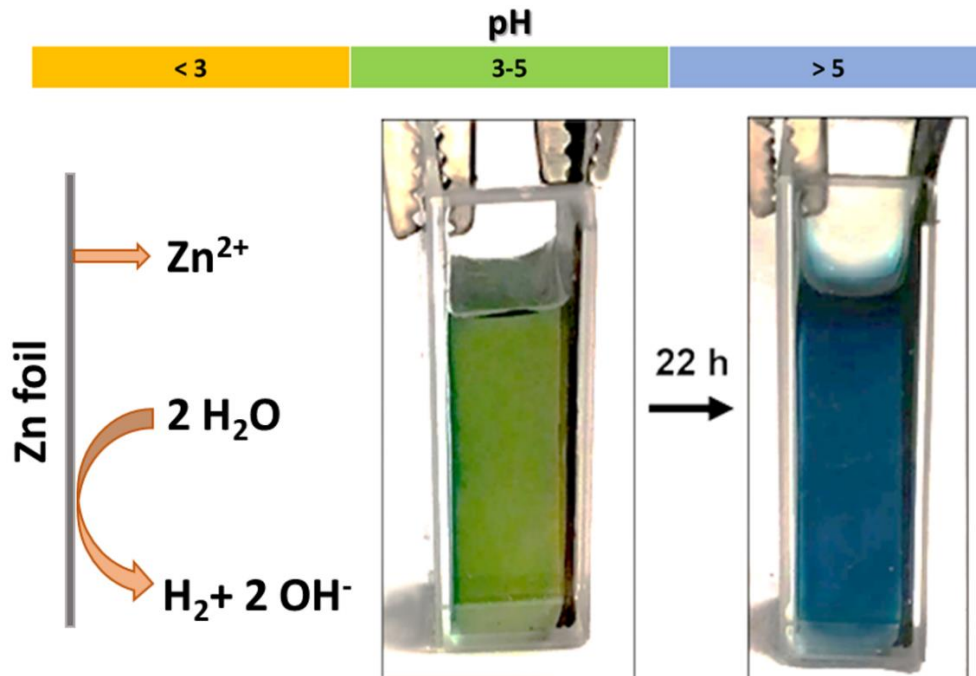


*Figure 5 - 7 Spontaneous evolution of the electrolyte pH without the application of an external bias.*

Without the application of an external bias, the color of the electrolyte changed from green to blue after 22 hours indicating the pH value is spontaneously turning alkaline. This change is attributed to the reaction between Zn metal and protons from the electrolyte giving rise to Zn-ions and hydrogen as illustrated in the scheme of **Figure 5-7**. A closer look at the picture of the initial state, in which the electrolyte is green, reveals that electrolyte near the Zn electrode (left electrode) forms a thin blue layer. This indicates that the origin of the changes in the electrolyte pH is the spontaneous reaction at the Zn metal electrode. Additional experiments using Zn powder clearly illustrate that kinetics of the spontaneous reaction are not as slow as one could assumed. When 500 mg of Zn powder are added to 20 mL of electrolyte (2 M ZnSO<sub>4</sub>

+ 0.1 M MnSO<sub>4</sub>), the spontaneous oxidation of Zn particles is immediate (**Figure 5-8a** and **Figure 5-8b**). The evolution of bubbles when the vial is shaken clearly shows that the reaction between Zn metal and water is kinetically not as slow as one could assume (**Figure 5-8c** and **Figure 5-8d**).

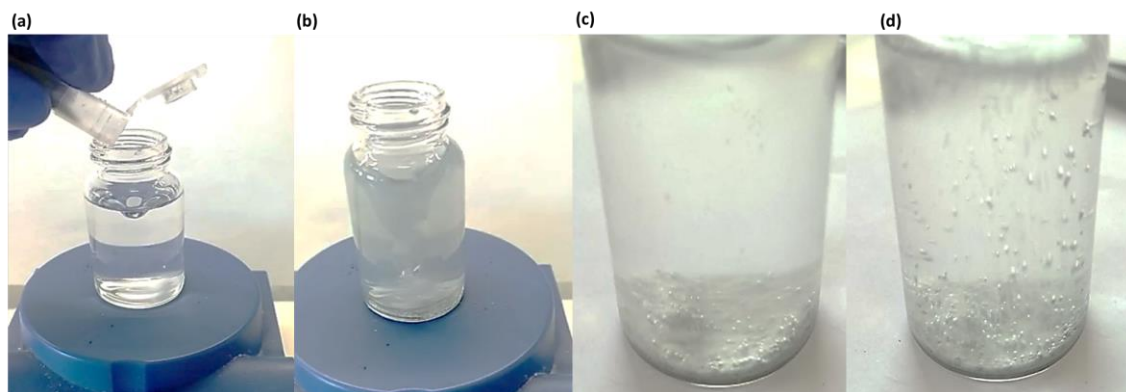


*Figure 5 - 8. Pictures of evaluation of a solution when Zn particles are added.*

The changes in pH value can be used to monitor the spontaneous reaction. The pH value was measured before the addition of Zn and 2 minutes after the addition of 500 mg of Zn powder. The reaction was evaluated for six different solutions (distilled H<sub>2</sub>O, 1M LiCl, 1M NaCl, 1M KCl, H<sub>2</sub>O + H<sub>2</sub>SO<sub>4</sub> (pH 3.73) and 2 M ZnSO<sub>4</sub> + 0.1M MnSO<sub>4</sub>), and the results are shown in **Table 5-1**. A clear change in pH values was observed for all samples. The change in concentration of protons is related to the initial pH of the solution: the lower the initial pH, the higher the change in pH value.

**Table 5 - 1. Changes in pH for 6 solution (20 mL) before and 2 minutes after the addition of Zn particles.**

	$pH_{initial}$	$pH_{final}$	$\Delta[H^+] / M$
$H_2O$	6.91	8.89	1.22E-07
1M LiCl	6.99	9	1.01E-07
1M NaCl	6.42	8.09	3.72E-07
1M KCl	7.14	9.07	7.16E-08
$H_2O + H_2SO_4$ (pH 3.73)	3.73	7.62	1.86E-04
2M $ZnSO_4 + 0.1M MnSO_4$	3.74	5.03	1.73E-04

The higher surface area of particles accelerates the spontaneous reaction which is convenient for illustrating that the reaction is not intrinsically slow. Nevertheless, Zn foil is often used in rechargeable Zn-MnO<sub>2</sub> batteries. Thus, Zn foil (2.5 cm<sup>2</sup>) was also introduced in an electrolyte (without stirring). After 72 h, a weight loss of 0.28 mg<sub>zn</sub>·cm<sup>-2</sup> was observed. Mass losses for Zn foil over 3 days in static conditions confirms that spontaneous reaction between water and Zn metal is an important issue for long-term operation. In addition, with this experiment it is possible to estimate the amount of protons consumed (or OH<sup>-</sup> released) through the atomic weight of Zn (g mol<sup>-1</sup>). Starting from a pH value of 4 for the initial electrolyte and considering that a pH value of 10 may compromise the battery operation as alkaline media, it is possible to calculate the volume of electrolyte necessary to avoid the pH raising above 10 assuming that the corrosion rate remains constant. While this is a simple estimation (kinetics is assumed to be independent of the evolving pH value), it clearly shows that the needed volume of water would be too much for long-term operation so that a mitigating strategy should be developed to correct spontaneous change of the pH (Table 5-2).

**Table 5 - 2. Volume of electrolyte necessary for long-life battery**

<i>Time / h</i>	<i>Consumed H<sup>+</sup> / mol cm<sup>-2</sup></i>	<i>Electrolyte Volume / L cm<sup>-2</sup></i>
10	2.38E-06	0.02
1000	2.38E-04	2
4380	1.04E-03	10
6570	1.56E-03	15
8760	2.08E-03	20
17520	4.17E-03	40
26280	6.25E-03	60
35040	8.34E-03	80
43800	1.04E-02	104
65700	1.56E-02	156
87600	2.08E-02	208

Since the reduction of water (hydrogen evolution reaction) at the negative electrode drives the changes in the electrolyte pH, the opposite reaction taking place at the opposite electrode can potentially compensate these changes in the pH value. Therefore, we explored the promotion of the oxygen evolution reaction at the positive electrode as solution to restore the pH value by holding the voltage at the end of the charge process. This strategy is based on floating protocols employed on Lead-acid battery technology,<sup>28</sup> which was never explored for Zn – MnO<sub>2</sub> as an approach to control changes in the electrolyte pH and prolong cycle life. **Figure 5-9** shows the influence of the value of the float voltage on the electrolyte pH. A cell was left at OCV for 22 h turning spontaneous to blue (alkaline). Then, different constant voltages were applied i.e., 1.7 V, 1.8 V, 1.9 V and 2.0 V. The electrolyte pH near the positive electrode (right side electrode in **Figure 5-9**) turned yellow indicating acidification.

The higher the voltage was applied; the thicker the acid layer was. This set of pictures reveals that float charging protocol can be used as an effective strategy to acidify the electrolyte.

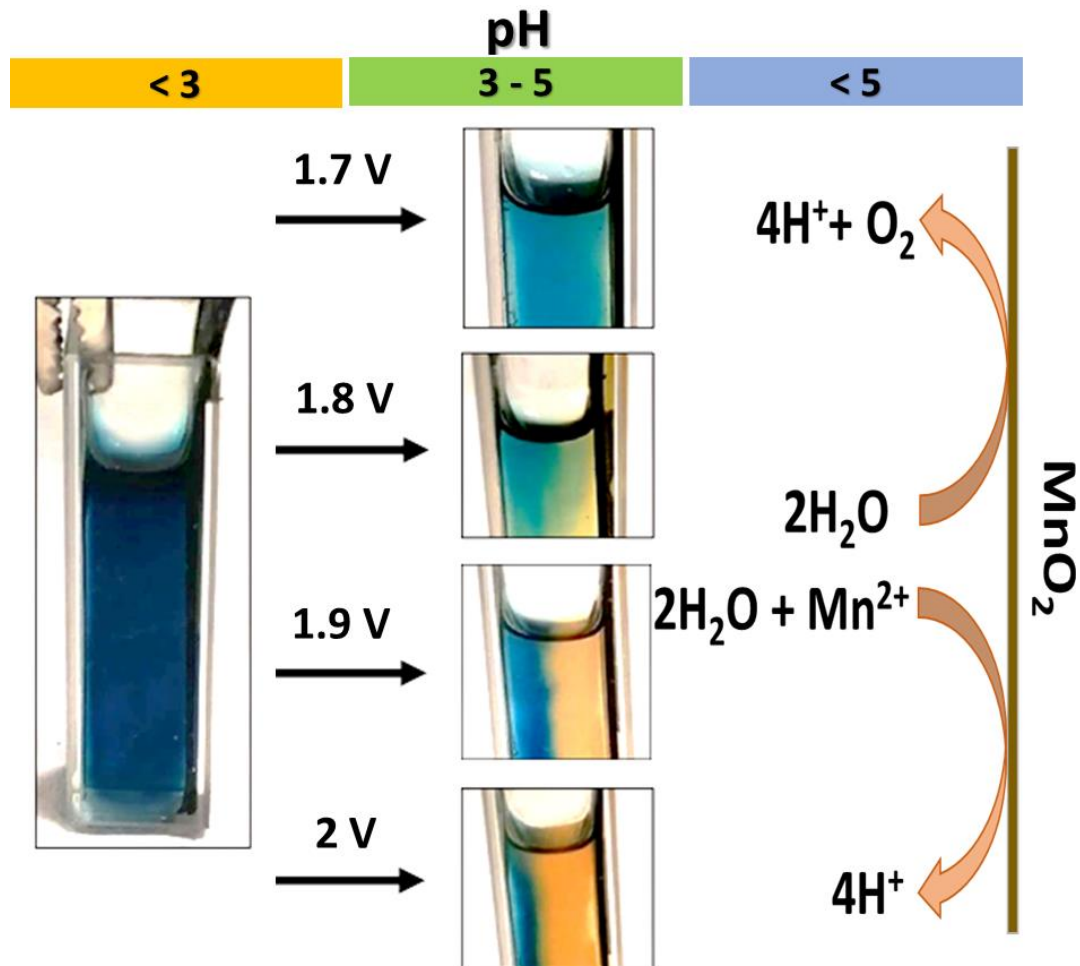
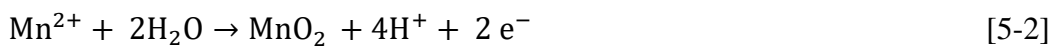


*Figure 5 - 9. Pictures of the cuvette cell after open circuit voltage (left) and when a constant voltage of 1.7 V, 1.8 V, 1.9 V and 2.0 V was applied to the cell. Zn foil and MnO<sub>2</sub> electrode are located at the left and right side of the cuvette. Right: scheme of the electrochemical reaction taking place at the positive electrode.*

The presence of Mn<sup>2+</sup> dissolved in the electrolyte was originally proposed to suppress dissolution of MnO<sub>2</sub> during cycling.<sup>20</sup> Later on, it was reported to provide additional capacity since Mn<sup>2+</sup> is able to be electrodeposited.<sup>13-16,29</sup> As oxidation of Mn<sup>2+</sup> to MnO<sub>2</sub> involved the release of H<sup>+</sup> (Equation 5-2), oxidation of Mn<sup>2+</sup> additive during the float charging step can also contribute to acidification of the electrolyte.



It has been shown that the pH value decreases significantly at the positive electrode when a float charging protocol at 1.8 V is applied. However, this change in pH value could be driven by the oxidation of the Mn<sup>2+</sup> present in the electrolyte, or by the Oxygen Evolution Reaction (OER). For elucidating the contribution of each reaction for this protocol, four blank experiments were carried out. For all cells, zinc foil was placed as negative electrode. For the positive side, either an electrode having electrodeposited-MnO<sub>2</sub> on graphite or a bare graphite electrode was used. For the electrolyte, two different compositions were studied: 0.1 M Mn<sup>2+</sup> (0.1 M MnSO<sub>4</sub>) + 2 M ZnSO<sub>4</sub> and Mn<sup>2+</sup>- free 2 M ZnSO<sub>4</sub>. **Figure 5-10** shows the accumulate charge consumed in the 4 experiments when a constant voltage of 1.8 V was applied for one hour. In the absence of Mn<sup>2+</sup> in the electrolyte, the charge is attributed to the OER. The larger amount of charge consumed when a MnO<sub>2</sub> electrode was used in the absence of Mn<sup>2+</sup> could be related to the rougher surface and/or the catalytic activity of MnO<sub>2</sub> towards the OER. In the presence of Mn<sup>2+</sup> in the electrolyte, the charge consumed, regardless the electrodes used, was significantly larger than those experiments in the absence of Mn<sup>2+</sup>. Again, the use of MnO<sub>2</sub> electrode led to higher amount of charge, which can be attributed to the same reasons. For experiments using the same electrode (either graphite or MnO<sub>2</sub> on graphite), the presence of Mn<sup>2+</sup> in the electrolyte led to a significant increase in the consumed charge. In both cases, the contribution of the OER to the overall accumulated charge at 1.8 V was *ca.* 20 %. Therefore, oxidation of Mn<sup>2+</sup> is attributed as the main promoter of the change in pH during the float charging voltage protocol at 1.8 V.

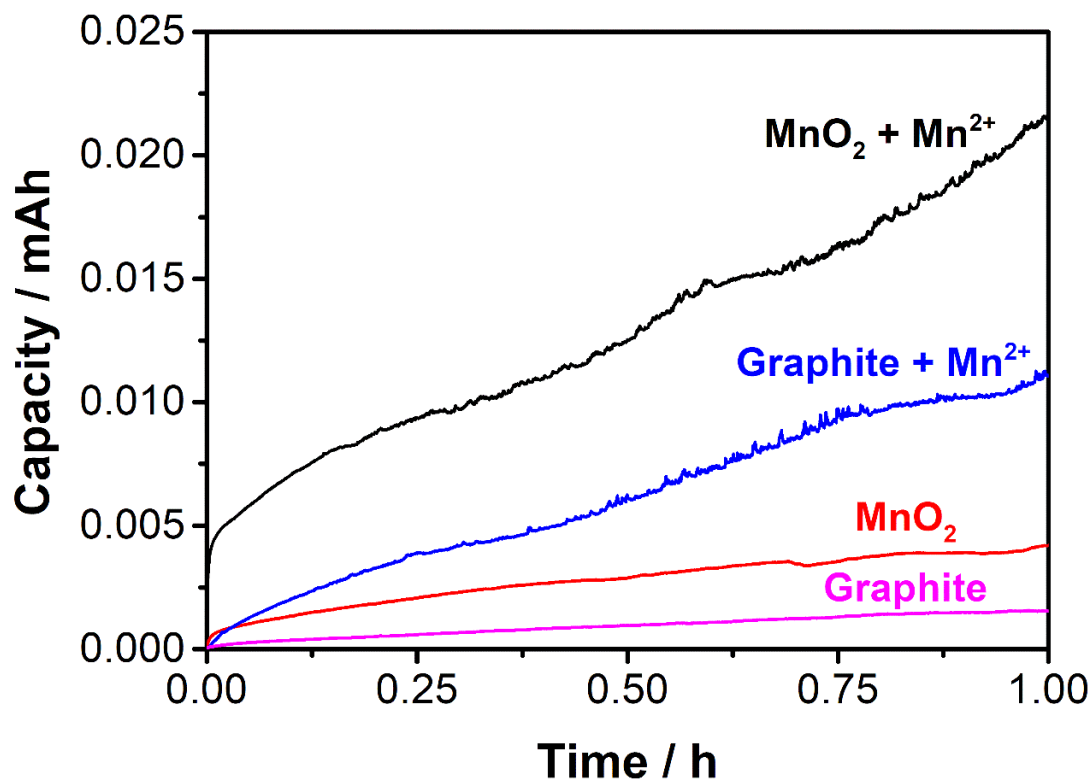


*Figure 5 - 10. Accumulated charge consumed with time when a constant voltage of 1.8 V is applied during one hour in four systems: Graphite as positive electrode with (blue) and without (pink) Mn<sup>2+</sup> additive in the electrolyte, and MnO<sub>2</sub> electrode as positive side with (black) and without (red) Mn<sup>2+</sup> additive in the electrolyte.*

These experiments reveal that approximately 80 % of the charge consumed when a constant voltage of 1.8 V is applied during 1 h are attributed to the oxidation of Mn<sup>2+</sup>. Thus, both the OER and oxidation of Mn<sup>2+</sup> are responsible for correction of pH values during the float charging step. Indeed, our estimation indicate that oxidation of Mn<sup>2+</sup> is the main contributor unraveling an unknown key role of Mn<sup>2+</sup> additive for cycle stability. However, the amount of Mn<sup>2+</sup> is limited so that its depletion may eventually prevent the correction of the spontaneous pH drift. Using the corrosion rate determined for a Zn foil one can make a rough estimation of the amount of Mn<sup>2+</sup> required for correcting the pH value for long-term. With this corrosion rate (0.28 mg<sub>Zn</sub>·cm<sup>-2</sup>) the protons consumed are calculated (**Table 5-2**). In this case, the estimation is based on

assuming 10  $\mu\text{L cm}^{-2}$  of electrolyte and the stoichiometry of the Mn<sup>2+</sup> oxidation reaction (4 mol H<sup>+</sup> released for 1 mol Mn<sup>2+</sup> oxidized). With this information, it is possible to calculate the Mn<sup>2+</sup> necessary for correcting the pH value. **Table 5-3** indicates that 1 mM Mn<sup>2+</sup> would be sufficient to maintain the pH value. Thus, the concentration of Mn<sup>2+</sup> most often used in literature (0.1 M) should be more than enough for several years.

*Table 5 - 3. Estimation of number of protons spontaneously consumed based on the corrosion rate of Zn, the amount of Mn<sup>2+</sup> necessary to correct the pH change, and concentration assuming 10  $\mu\text{L cm}^{-2}$  of electrolyte for long-life battery.*

<i>Years</i>	<i>Mol H<sup>+</sup> cm<sup>-2</sup></i>	<i>Mol Mn<sup>2+</sup> cm<sup>-2</sup></i>	<i>[Mn<sup>2+</sup>] / mM</i>
0.5	1.04E-03	2.61E-04	2.61E-02
1	2.08E-03	5.21E-04	5.21E-02
2	4.17E-03	1.04E-03	1.04E-01
3	6.25E-03	1.56E-03	1.56E-01
4	8.34E-03	2.08E-03	2.08E-01
5	1.04E-02	2.61E-03	2.61E-01
6	1.25E-02	3.13E-03	3.13E-01
7	1.46E-02	3.65E-03	3.65E-01
8	1.67E-02	4.17E-03	4.17E-01
9	1.88E-02	4.69E-03	4.69E-01
10	2.08E-02	5.21E-03	5.21E-01

The float charging protocol should be able to compensate the changes in the electrolyte pH originated in the negative electrode and restore the initial value of pH. To assess this, the electrolyte pH was evaluated after different float voltages were applied for 2 h (**Figure 5-11**). When a constant voltage of 2.0 V was applied for 2 h, the electrolyte

pH turned acid as indicated by the color of the electrolyte (yellow indicates pH < 3). The same result was obtained for a float voltage of 1.9 V. On the other hand, a constant voltage of 1.7 V applied for 2 h was not able to completely restore the initial value of pH as indicated by the color of the electrolyte (Blue Turquoise indicates pH close-to-but-above 5). Only when a constant voltage of 1.8 V was applied to the cell, the electrolyte pH was restored as confirmed by the color of the electrolyte (green indicates pH between 3 and 5). According to these results, the application of a float charging protocol that consist in holding the voltage at 1.8 V at the end of the charge process should lead to improved electrochemical performances.

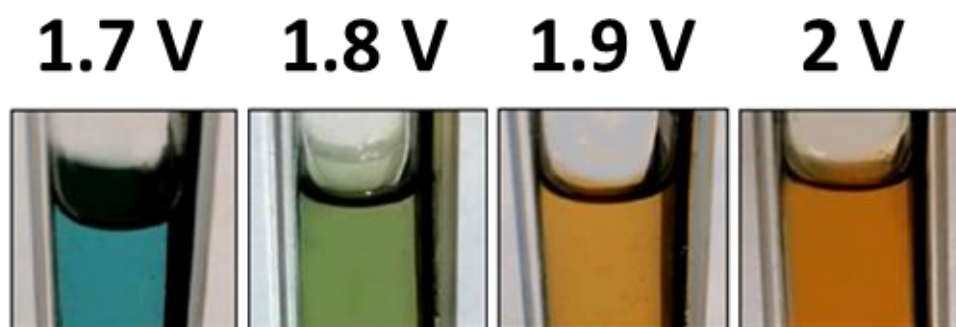


*Figure 5 - 11. Pictures of the electrolyte after a constant voltage of 1.7 V, 1.8 V 1.9 V and 2.0 V was applied for 2 h.*

### **5.3.2.2 Preventing pH Drift via Float Charging Protocols in Zn-MnO<sub>2</sub> batteries**

The evaluation of the electrolyte pH indicates that the electrolyte is spontaneously changing towards alkaline values, while the application of a constant voltage at the end of the charge process can be used to restore the initial values of pH. Thus, this finding should translate into stable pH over cycling. To explore this, cuvette electrochemical cells were galvanostatically charged and discharged under float charging protocols consisting in holding the voltage at 1.8 V for 15 min at the end of the charge step (**Figure 5-12**). In this figure, a picture of i) initial electrolyte and ii) a cell left at open circuit voltage during 22 h are included to illustrate the relevant

timescale of the experiment since a spontaneous drift towards alkaline values was already observed after 22 h. **Figure 5-12** shows the evolution of the specific charge capacity upon cycling when float charging protocol was applied (a cut-off voltage of 1.8 V was held for 15 min at the end of the charge step). A slight but steady increase in specific capacity was observed. This behavior has been previously reported and it is associated with the electrodeposition of Mn<sup>2+</sup>,<sup>29</sup> which is present in the electrolyte in the form of MnSO<sub>4</sub> as standard additive in most of the reported Zn-MnO<sub>2</sub> batteries. According to **Equation 5-2**, electrodeposition of additional MnO<sub>2</sub> from Mn<sup>2+</sup> in the electrolyte leads to acidification of the media, which is the main sources of protons to correct the spontaneous drift of the potential towards alkaline values.

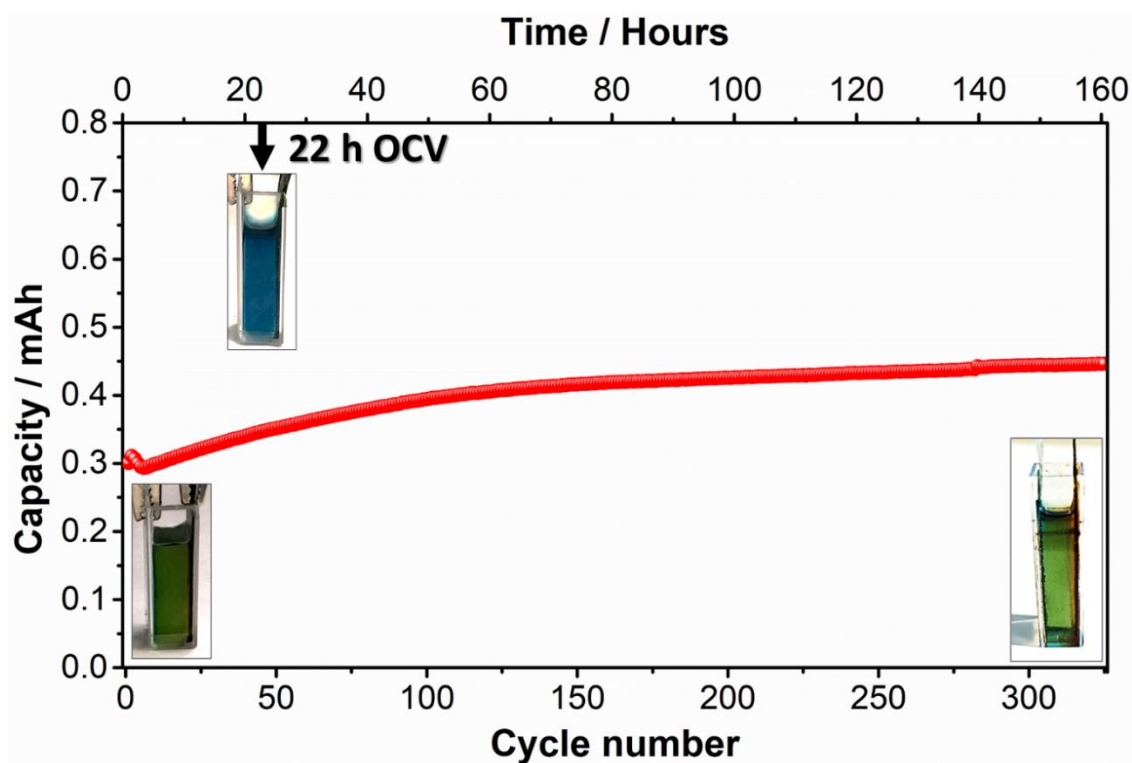


*Figure 5 - 12 Evolution of the charge capacity when a float charging protocol is applied (1.8 V for 15 min). Inset: color of the electrolyte at the beginning, after 22 h at open circuit voltage (spontaneous drift towards alkaline values) and after 300 cycles implementing the float charging protocol. Total duration of the experiment was >160 h.*

Indeed, the green color of the electrolyte after 300 cycles and > 160 h reveals that the implementation of a constant voltage step at the end of the charge process effectively prevents changes of pH values towards alkaline media. Note that the timescale of the experiment was 160 h, which is relevant for the timescale of Zn corrosion. For this cyclability test, the results of coulombic efficiency and the voltage profile are shown in **Figure 5-13** and **Figure 5-14**, respectively. Assuming a specific capacity of 200 mAh g<sup>-1</sup>, a mass loading range of these electrodes is: 0.24 mg<sub>MnO<sub>2</sub></sub> cm<sup>-2</sup>.

Since accumulation of MnO<sub>2</sub> from the Mn<sup>2+</sup> from the electrolyte has been unraveled as the main contributor, the coulombic efficiencies are *ca.* 100 % (additional electrodeposited MnO<sub>2</sub> from Mn<sup>2+</sup> contributes to the subsequent discharge process).

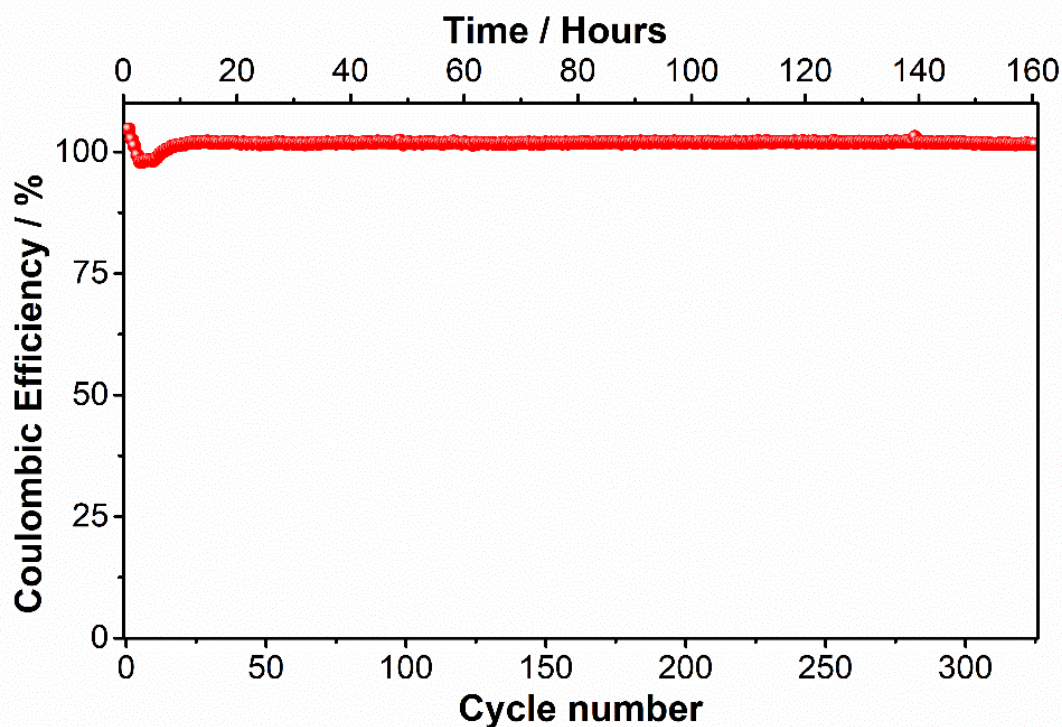


**Figure 5 - 13.** Coulombic efficiency for a Zn-MnO<sub>2</sub> cell when a float charging protocol is applied (1.8 V for 15 min).

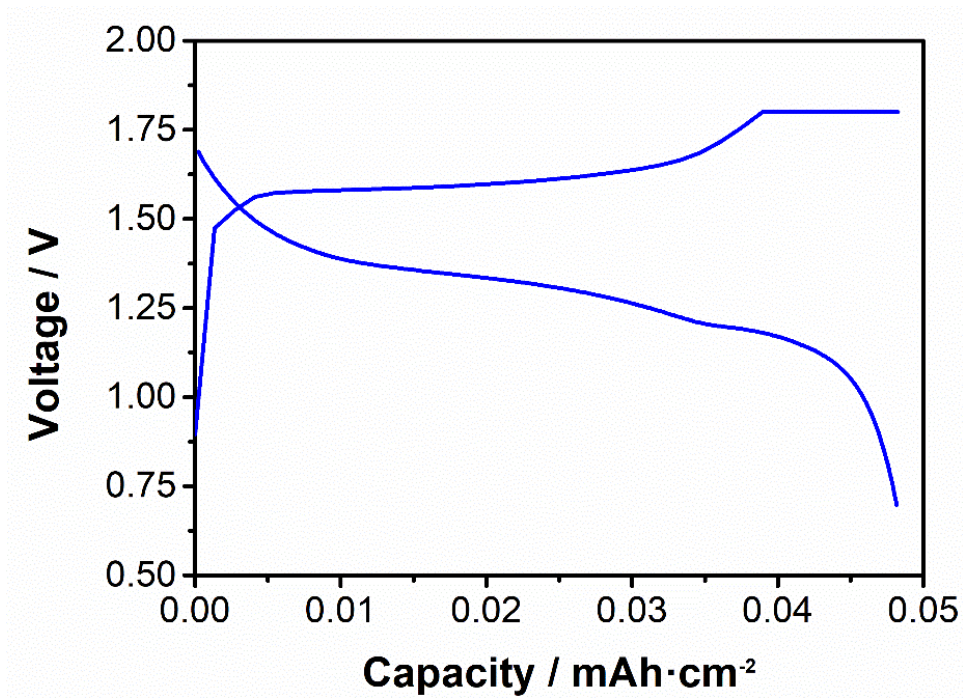


*Figure 5 - 14. Voltage profiles for full cycles when a float charging protocol is applied (1.8 V for 15 min).*

## 5.4 Conclusions

In summary, it has been demonstrated the possibility of making an injectable battery with high energy density (4.6 mAh cm<sup>-2</sup>) for this chemistry (Zn – MnO<sub>2</sub>). However, this battery chemistry suffers from capacity fading (50 % in 120 cycles), which is attributed to parasitic reactions and by-products at the negative electrode. To explore this hypothesis, an innovative hybrid-flow MnO<sub>2</sub> semi-solid battery that combines an injectable positive electrode with a flow negative electrode was designed and testing leading to a significant increase in the lifespan. However, there are still issues related with the negative electrode derived from the pH variation that finally provoke the collapse of the system after 500 cycles (3.78 mAh cm<sup>-2</sup>) with a capacity retention of 83 %.

It was shown that the electrolyte pH value in rechargeable Zn–MnO<sub>2</sub> batteries evolves spontaneously towards alkaline values due to the reaction between Zn metal and protons. This is an intrinsic issue related to the use of metal Zn and aqueous electrolyte with neutral and mild-acid pH. Research on material science by the development of artificial solid electrolyte interphase could prevent it, as the SEI prevents spontaneous reaction between organic electrolytes and Li metal. Alternatively, a simpler and straightforward approach that was explored and demonstrated to be useful in this work is the implementation of float charging protocols for Zn–MnO<sub>2</sub> batteries, in which a constant voltage is held at the end of the charge process. In a spectrophotometer cuvette, a pH indicator was dissolved in the electrolyte of a cell containing Zn foil and MnO<sub>2</sub> previously electrodeposited on expanded graphite. In this cell, several charging protocols were studied realizing that oxidation of Mn<sup>2+</sup> additive dissolved in the electrolyte and occurrence of the oxygen evolution reaction (OER) that is controlled by the applied charging protocol is able to acidify the electrolyte. The use of this cell

enabled the understanding of the role of the cut-off voltage and float voltage in the change of the electrolyte pH. Intermediate values for the float voltage (e.g. 1.8 V) gave rise to the results as higher values led to acidification of the electrolyte while lower values were not able to restore the initial pH value. Our estimation indicates that the amount of Mn<sup>2+</sup> most often used in literature (0.1 M) should be sufficient to correct the pH value for several years. Oxidation of Mn<sup>2+</sup> and promotion of the OER taking place during the float voltage protocol also address losses of Zn metal due to spontaneous corrosion since Zn deposition should occur during the float voltage (if the HER takes place, pH value will not be restored). Consumption of water should be small considering the amount of required Mn<sup>2+</sup> for long-term operation (1 mM Mn<sup>2+</sup> → 4 mM H<sub>2</sub>O (72 mg<sub>H<sub>2</sub>O</sub> L<sup>-1</sup>)) and the fact that the oxygen released during float voltage is expected to recombine with hydrogen from the Zn corrosion.

## 5.5 References

1. Dunn, B., Kamath, H. & Tarascon, J. M. Electrical energy storage for the grid: A battery of choices. *Science* (80-. ). **334**, 928–935 (2011).
2. Kim, H. *et al.* Aqueous rechargeable Li and Na ion batteries. *Chem. Rev.* **114**, 11788–11827 (2014).
3. Yabuuchi, N., Kubota, K., Dahbi, M. & Komaba, S. Research development on sodium-ion batteries. *Chem. Rev.* **114**, 11636–11682 (2014).
4. Feng, Y. *et al.* A novel aqueous sodium-manganese battery system for energy storage. *J. Mater. Chem. A* **7**, 8122–8128 (2019).
5. Selvakumaran, D., Pan, A., Liang, S. & Cao, G. A review on recent developments and challenges of cathode materials for rechargeable aqueous Zn-ion batteries. *J. Mater. Chem. A* **7**, 18209–18236 (2019).
6. Wang, F. *et al.* Highly reversible zinc metal anode for aqueous batteries. *Nat. Mater.* **17**, 543–549 (2018).
7. Petrescu, M. I., Ghica, G. V & Buzatu, T. Recovery of zinc and manganese from spent batteries by reductive leaching in acidic media. *J. Power Sources* **247**, 612–617 (2014).
8. Blanc, L. E., Kundu, D. & Nazar, L. F. Scientific Challenges for the Implementation of Zn-Ion Batteries. *Joule* **4**, 771–799 (2020).
9. He, P. *et al.* Building Better Zinc-ion Batteries: A Materials Perspective. *EnergyChem* **100022**, 100022 (2019).
10. Fang, G., Zhou, J., Pan, A. & Liang, S. Recent Advances in Aqueous Zinc-Ion Batteries. *ACS Energy Lett.* **3**, 2480–2501 (2018).
11. Xu, C., Li, B., Du, H. & Kang, F. Energetic zinc ion chemistry: The rechargeable zinc ion battery. *Angew. Chemie - Int. Ed.* **51**, 933–935 (2012).
12. Tafur, J. P., Abad, J., Román, E. & Fernández Romero, A. J. Charge storage mechanism of MnO<sub>2</sub> cathodes in Zn/MnO<sub>2</sub> batteries using ionic liquid-based gel polymer electrolytes. *Electrochem. commun.* **60**, 190–194 (2015).
13. Guo, X. *et al.* Zn/MnO<sub>2</sub> battery chemistry with dissolution-deposition

- mechanism. *Mater. Today Energy* **16**, (2020).
14. Wu, D. *et al.* Quantitative temporally and spatially resolved X-ray fluorescence microprobe characterization of the manganese dissolution-deposition mechanism in aqueous Zn/a-MnO<sub>2</sub> batteries †. *This J. is Cite this Energy Environ. Sci* **13**, 4322–4333 (2020).
  15. Mateos, M., Harris, K. D., Limoges, B. & Balland, V. Nanostructured Electrode Enabling Fast and Fully Reversible MnO<sub>2</sub>-to-Mn<sup>2+</sup> Conversion in Mild Buffered Aqueous Electrolytes. *ACS Appl. Energy Mater.* **3**, 7610–7618 (2020).
  16. Mateos, M., Makivic, N., Kim, Y. S., Limoges, B. & Balland, V. Accessing the Two-Electron Charge Storage Capacity of MnO<sub>2</sub> in Mild Aqueous Electrolytes. *Adv. Energy Mater.* **10**, (2020).
  17. Huang, J. *et al.* A calcium hydroxide interlayer as a selective separator for rechargeable alkaline Zn/MnO<sub>2</sub> batteries. *Electrochem. commun.* **81**, 136–140 (2017).
  18. Liu, Y., Li, Q., Ma, K., Yang, G. & Wang, C. Graphene oxide wrapped Cu<sub>2</sub>O nanobelts as high-capacity and long-life cathode materials of aqueous zinc-ion batteries. *ACS Nano* **13**, 12081–12089 (2019).
  19. Wei, T., Li, Q., Yang, G. & Wang, C. Pseudo-Zn–Air and Zn-Ion Intercalation Dual Mechanisms to Realize High-Areal Capacitance and Long-Life Energy Storage in Aqueous Zn Battery. *Adv. Energy Mater.* **9**, 1901480 (2019).
  20. Pan, H. *et al.* Reversible aqueous zinc/manganese oxide energy storage from conversion reactions. *Nat. Energy* **1**, 1–7 (2016).
  21. Soundharajan, V. *et al.* Na<sub>2</sub>V<sub>6</sub>O<sub>16</sub>·3H<sub>2</sub>O Barnesite Nanorod: An Open Door to Display a Stable and High Energy for Aqueous Rechargeable Zn-Ion Batteries as Cathodes. *Nano Lett.* **18**, 2402–2410 (2018).
  22. Jo, J. H., Sun, Y. K. & Myung, S. T. Hollandite-type Al-doped VO<sub>1.52</sub>(OH)<sub>0.77</sub> as a zinc ion insertion host material. *J. Mater. Chem. A* **5**, 8367–8375 (2017).
  23. Yang, G., Li, Q., Ma, K., Hong, C. & Wang, C. The degradation mechanism of vanadium oxide-based aqueous zinc-ion batteries. *J. Mater. Chem. A* **8**, 8084–8095 (2020).

24. Fitz, O. *et al.* Electrolyte Study with in Operando pH Tracking Providing Insight into the Reaction Mechanism of Aqueous Acidic Zn//MnO<sub>2</sub> Batteries. *ChemElectroChem* **8**, 3553–3566 (2021).
25. Lee, B. *et al.* Critical Role of pH Evolution of Electrolyte in the Reaction Mechanism for Rechargeable Zinc Batteries. *ChemSusChem* **9**, 2948–2956 (2016).
26. Bischoff, C. F. *et al.* Revealing the Local pH Value Changes of Acidic Aqueous Zinc Ion Batteries with a Manganese Dioxide Electrode during Cycling. *J. Electrochem. Soc.* **167**, 020545 (2020).
27. Ali, G. A. M., Yusoff, M. M. & Chong, K. F. Electrochemical Properties of Electrodeposited MnO<sub>2</sub> Nanoparticles. *Adv. Mater. Res.* **1113**, 550–553 (2015).
28. Liu, X. *et al.* A new dynamic SOH estimation of lead-acid battery for substation application. *Int. J. Energy Res.* **41**, 579–592 (2017).
29. Qiu, C. *et al.* The function of Mn<sup>2+</sup> additive in aqueous electrolyte for Zn/ $\delta$ -MnO<sub>2</sub> battery. *Electrochim. Acta* **351**, 136445 (2020).



**Chapter 6. Semi-Flowable Zn Semi-Solid  
Electrodes as Renewable Energy Carrier  
for Refillable Zn – Air Batteries**

The results obtained in this chapter have been published in an international peer-reviewed journal (Journal of Power Sources, IF:9.127). Basic information about this publication can be found as follows.

**D. Perez-Antolin**, W. Schuhmann, J. Palma, E. Ventosa (2022). Semi-Flowable Zn Semi-Solid Electrodes as Renewable Energy Carrier for Refillable Zn–Air Batteries. *Journal of Power Sources*. Accepted:14/04/2022

## 6.1 Introduction

Energy storage has become one of the main technological pillars of our society due to the increasing energy demand, the need for a sustainable energy model, and the emerging of off-grid power-demanding gadgets. Obviously, the combination of a number of energy storage technologies will be required in the future to fulfill the various requirements of each specific application. Rechargeable batteries are the power sources of choice for portable electronics, and they are called to power the upcoming generation of electric vehicles, most likely together with hydrogen fuel cells. Metal–Air batteries can be considered to be a nexus between the two named electrochemical technologies. As a result, metal–air batteries possess high specific energy ( $1084 \text{ Wh kg}^{-1}$  for Zn–Air)<sup>1–3</sup> because of the use of atmospheric air like in a fuel cell, while having a simple sealed architecture and a solid electroactive material, e.g. Zn or Li, like in a rechargeable battery. On the other hand, rechargeable metal–air batteries also have distinct disadvantages, i.e. lower energy efficiency related to the reversible  $\text{O}_2$  reactions (both the OER and the ORR are using the same electrode) and poorer cycle stability associated with the reversible Zn reaction in a static configuration (sealed) cell.<sup>4,5</sup> In an attempt for overcoming the major challenges at once, the mechanically–rechargeable Zn–Air battery was proposed a long time ago, in which the spent negative electrodes are replaced at the end of the discharge process.<sup>6–</sup>

<sup>13</sup> By doing this, two major issues are addressed: i) the poor cyclability of the Zn electrode in a static negative electrode, and ii) avoiding the oxygen evolution reaction in the air-breathing electrode during the charging process. In this way, spent Zn material can be collected and regenerated electrically in a separate cell specially designed for this process (e.g. electrowinning of Zn) or thermally in a concentrated solar power plant.<sup>2,11,14–17</sup> Two categories can be distinguished: i) substitution of the

entire negative compartment, and ii) substitution of the spent negative electrode materials, also referred to as Zn/Air Fuel Cell (ZAFC).<sup>7</sup> The latter approach has demonstrated to be suitable for practical implementation as several companies based their technology in this concept: the Electric Fuel Ltd., the Power Zinc, the Power Air Co., the Metallic Power Inc., and the Zinc8.<sup>7,18–22</sup> In all cases, the poor electrical conductivity of ZnO locks achieving high volumetric capacities since large excess of electrolyte is used to promote the formation of dissolved zincates as discharge product and prevent ZnO formation. In this way, the volumetric capacity is largely locked by the solubility of zincates, which can be incrementally improved by using electrolyte additives or increasing the operating temperature.<sup>23</sup> However, the achieved volumetric capacities ( $100 - 150 \text{ Ah L}^{-1}$ )<sup>24</sup> are very far from the highly appealing value of Zn ( $5800 \text{ Ah L}^{-1}$ ). Thus, innovative approaches are required to address this issue, which in turn will unlock the energy density of mechanically-rechargeable Zn-Air batteries.

In 2011, a pioneering work led by Chiang proposed for the first time the use of slurries in redox flow batteries.<sup>25</sup> These slurries contained solid redox-active particles, conducting additive and electrolyte forming flowable electrode, which were referred to as “semi-solid electrode”. Since then, the higher energy density of flowable semi-solid electrodes, compared to electrolytes containing dissolved species, have been exploited for different redox flow battery chemistries.<sup>26–28</sup> In addition, semi-solid electrodes offer other unique advantages such as enhanced mass transport due to their tunable porosity compared to conventional porous electrodes.<sup>29</sup> For instance, the company 24M seizes the enhanced mass transport in semi-solid electrodes to manufacture Li-ion batteries having high areal capacities using non-flowable semi-solid electrodes.<sup>30</sup> So far, the two extreme cases have been used to develop innovative batteries, i.e. either highly flowable semi-solid electrodes or non-flowable semi-solid

electrodes for redox flow and static batteries, respectively. Each case possesses pros and cons: flowable semi-solid electrodes results in lower energy density, while denser semi-solid electrodes that have higher energy density lacks the ability to flow. For instance, flowable Zn semi-solid electrodes have been deployed for Zn-Ni,<sup>31-33</sup> and Zn-MnO<sub>2</sub><sup>34</sup> redox flow batteries. The need for flowability resulted in Zn semi-solid electrodes of limited specific capacity. Specifically, values of 44.8 Ah L<sup>-1</sup> (52.4 % utilization rate),<sup>31</sup> 40 Ah L<sup>-1</sup> (3 % utilization rate),<sup>32</sup> 127.3 Ah L<sup>-1</sup> (58.44 % utilization rate),<sup>33</sup> were achieved for redox flow Zn-Ni batteries. Note that static Zn pellets were used for the proof-of-concept of the semi-solid flow Zn-MnO<sub>2</sub> likely due to corrosion issues in neutral electrolyte. Recently, our group proposed the deployment of semi-solid electrodes of intermediate flowability to be used in static batteries. On the one hand, the resulting electrical percolation enables excellent electrochemical performance and, on the other hand, they still present sufficient flowability to be injected and removed from the battery cell at the end-of-life to largely facilitate recyclability of static batteries<sup>35</sup>. This type of semi-flowable semi-solid electrodes is not feasible for redox flow batteries since the pumping consumption would be too high, but it enables eventual substitution.

In this context, our goal is to revive the promising concept of mechanically-rechargeable Zn-Air batteries that implies the use of Zn as energy carrier. To regain attention, high practical energy densities need to be achieved. With this aim, we propose for the first time the use of electrically-conducting and semi-flowable semi-solid electrodes in non-flow Zn-Air batteries (refillable primary battery). Previous studies on Zn semi-solid electrodes achieved relatively low energy density due to constrictions derived from the need for continuous flow and for its electrochemical recharging process in the same device. Our concept of using Zn semi-solid electrode

in non-flow mechanically rechargeable Zn-Air batteries widens the range of carbon content since semi-flowable viscous slurries are valid for our case. The semi-solid and semi-flowable nature of our electrodes provides not only the proposed Zn-based electrodes with sufficient flowability to recharge mechanically a Zn/Air battery, but also the electrical percolating network and deformability to minimize passivation of remaining active material by formation of ZnO. By this, the volumetric capacity in semi-flowable Zn electrodes is boosted opening up a new research direction for reaching the full potential of mechanically-rechargeable Zn-Air batteries. Alkaline Zn-based semi-solid electrodes are suggested to act as green energy carriers since Zn metal can be electrochemically generated (Zn electrowinning) from discharge products. This concept may become of high interest for a number of emerging applications in which neither batteries nor fuel cells completely fulfill the requirements.

## 6.2 Experimental Procedures

### 6.2.1 Reagents and materials

Zinc powder (99.9 % -100 mesh, Alfa Aesar), Carbon additive KetjenBlack EC-600 JD (Azelis and AkzoNovel polymer chemicals), KOH ( $\geq 85$  %, Sigma Aldrich), were used as-received. Expanded graphite (Sigracet TF6) was used as negative current collector, Celgard 3501 as separator and E4B (ElectricFuel) as air electrode. Gaskets were made of Viton<sup>®</sup> due to its resistance to alkaline conditions.

### 6.2.2 Preparation of semi-solid electrodes

Semi-solid electrodes with different compositions were prepared using 6, 20, 26, 42 wt.% active material, corresponding with 0.1, 0.33, 0.5 and 1  $\text{kg}_{\text{Zn}} \text{L}_{\text{electrode}}^{-1}$ . In addition, 4.5, 2.9, 3.7 and 1.4 wt.% of carbon additive, respectively, was used. Active material proportion was calculated by dividing the amount of active material (grams of Zn or carbon additive) by the total weight of the solid materials (carbon additive and zinc) following **Equation 6-1**.

$$\text{wt. \%}_A = \frac{g_A}{g_{\text{Solid}}} \cdot 100 \quad [6-1]$$

The solid particles were dispersed in 6 mL of electrolyte (6 M KOH) and mixed with Ultra-Turrax IKA T18-Basic during three periods of 10 minutes resting 5 minutes between periods. The slurries were prepared directly in a syringe to facilitate the injection of the electrode into the battery pre-assembled.

### 6.2.3 Materials and fabrication of refillable cells

The external casing of the battery was designed and printed by FDM-3D-Printing machine (MakerBot Replicator<sup>TM</sup> 2X) using Acrylonitrile butadiene styrene (ABS) for planar configuration and by Selective Deposition Lamination-3D-Printing machine

(Anycubic: Photon Mono SE) using Grey Colored UV resin (Anycubic) for the tubular one.

### **6.2.4 Electrochemical measurements**

Electrochemical testing of the battery was carried out using a battery tester (Neware BTS4000 5V6A).

## 6.3 Results and Discussion

### 6.3.1 Proof-of-concept for the mechanically rechargeable Zn-Air battery based on Zn semi-solid electrodes

Implementation of the new vision for a mechanically-rechargeable Zn-Air battery chemistry requires the design and fabrication of a reusable primary battery cell. The design of the cell is shown in the **Figure 6-1a**, **Figure 6-1b** and **Figure 6-1c**. One end-plate of the cell (positive end-plate, 120 mm x 70 mm) has a large opening (item 1, 8.28 x 1 cm) to allow air to reach the air-breathing electrode. The other end-plate (negative end-plate, 120 mm x 70 mm) has two small openings (item 2a and 2b, 1 cm diameter) to allow the semi-solid electrode to be injected inside the cell. A rectangular plate (10 x 12 cm) of expanded graphite (including two opening of 1 cm diameter, item 3, for enabling injection of semi-solid electrode) is placed onto the negative end-plate to act as current collector. A compartment of 8.28 x 1 x 0.2 cm (item 4) is created using Viton gaskets to be filled with Zn-based semi-solid electrode. A separator (Celgard 3500) of 120 mm x 70 mm is placed between the compartment and the air-breathing electrode. The two end-plates are pressed against each other to seal the systems. Once the semi-solid electrode is injected inside the cell, the two small openings at the negative side are sealed using stoppers for the battery to be operated in non-flow conditions.

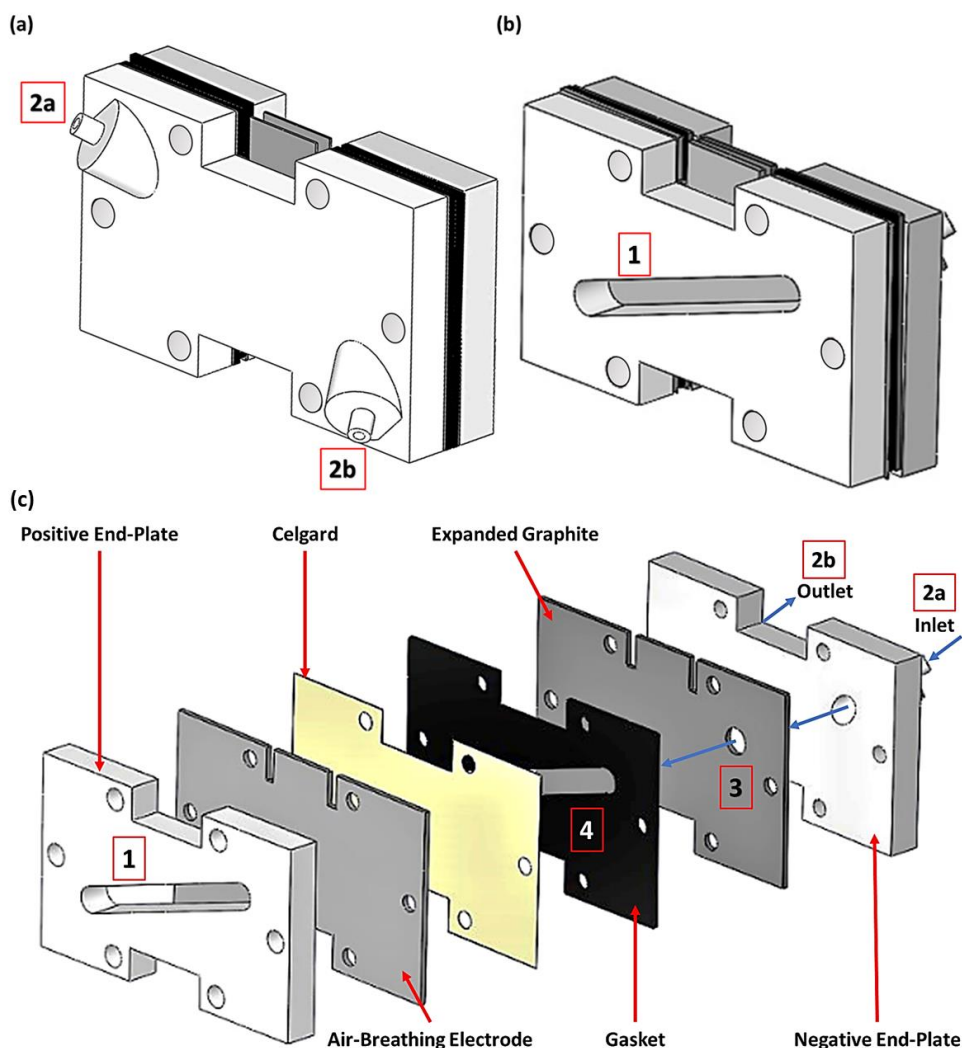


**Figure 6 - 1.** Design of the semi-solid Zn-air device fabricated using 3-D Fused Deposition Modelling Printing. (a) Packed cell (negative end-plate view). (b) Packed cell (positive end-plate view). (c) Internal part of the cell.

**Figure 6-2a** shows the evolution of the ionic and electrical resistivity of an electrolyte containing suspended carbon particles as a function of the carbon content (**Chapter 3, Figure 3-6, and Figure 3-7**). Whereas the ionic resistivity increased with increasing carbon content due to the hinderance of the solid particles as in conventional porous battery electrodes, electrical resistivity decreased with increasing carbon content. This reveals that electrochemically active and flowable semi-solid electrodes can be obtained through tuning of composition formulation. In our case, the value of  $70 \text{ mg mL}^{-1}$  represents a balanced trade-off between electrical and ionic resistivity, so that

carbon contents around this value were explored in further formulations containing Zn particles (below). In a way, this easily refillable primary battery becomes a fuel cell, in which the typically employed gas or liquid fuel (e.g. H<sub>2</sub>, methanol) is replaced by a semi-solid *fuel*. As a result, cheap microporous separator can be used instead of an ion-selective membrane. **Figure 6-2b** illustrates the working principle in a sequence of 4 steps. The key technology enabler proposed in our work is the use of electrically percolated and flowable Zn semi-solid electrodes (dense suspension of Zn and carbon additive in an alkaline electrolyte), which allows for the realization of the sequence of steps shown in **Figure 6-2b**. **Figure 6-2c** shows the voltage profiles of 5 subsequent refilling cycles using the same cell but substituting the Zn semi-solid electrode according to the refilling procedure illustrated in **Figure 6-2b**.

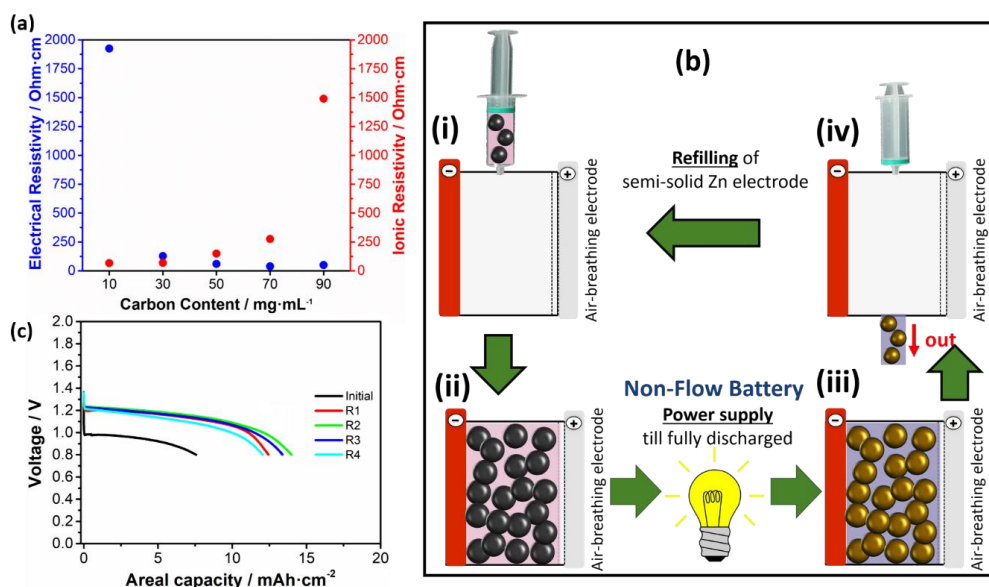


**Figure 6 - 2.** (a) Electrical and ionic resistivities of semi-solid electrodes containing different carbon contents (10, 30, 50, 70, 90 mg·cmL<sup>-1</sup>) (b) Schematic representation of the working principle of the mechanically-rechargeable semi-solid Zn-Air battery. (i) A pre-assembled electrochemical cell is filled with flowable semi-solid Zn electrode. (ii) The cell is sealed and ready to deliver energy in static (non-flow) configuration. (iii) The sealed cell reaches full state of discharge. (iv) The spent semi-solid Zn electrode is removed from the cell, which is then ready to be refilled in step (i). (c) Voltage profile of 5 subsequent refilling using a semi-solid electrode containing 0.1 kg<sub>Zn</sub> L<sup>-1</sup><sub>electrode</sub> in 6 M KOH.

After a first slightly poorer-performing discharge, the operating voltage and areal capacity remained stable. A value of  $13 \text{ mAh cm}^{-2}$  with a high Zn utilization rate in the range of  $67 - 77 \%$  ( $546 - 633 \text{ mAh g}_{\text{Zn}}^{-1}$ ) for R1- R4 were achieved at *ca.*  $0.1 \text{ C}$  ( $16 \text{ mA cm}^{-2}$ ). It should be noted that the reproducibility is limited by the oversimplified refilling method was applied in this work.

The method for the replacement and refilling of semi-solid electrodes is based on the removal of spent semi-solid electrode using a stream of tap water and the refilling of fresh semi-solid electrode using a simple syringe.

Subtraction process. The cell is connected to the tap through its inlet opening. The pressure of the tap water entering into the cell forces the semi-solid electrode to be removed from the cell through the outlet opening until the system is clean and ready for the next injection (**Figure 6-3**).

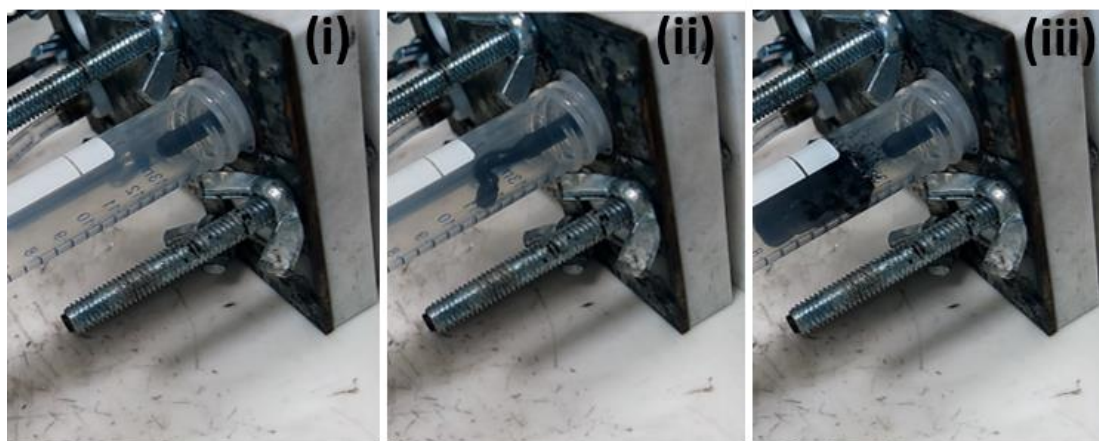


**Figure 6 - 3.** Removal of the semi-solid electrode from a filled battery cell. (i) Initially, the cell is filled with a semi-solid electrode. (ii) Air pressure is applied inside the cell through the one of the inlets, and the semi-solid electrode starts to come out of the cell. (iii) Finally, all the spent semi-solid electrode is removed from the cell, which is then empty and ready for being used again.

Injection process: the slurry is well mixed inside the syringe. Then, the syringe is attached to the inlet opening of the cell, and pressure is applying, so that the semi-solid electrode is inserted into pre-assembled cell (**Figure 6-4**). Pressure is continuously applied until the semi-solid electrode comes out through the outlet opening. Then, the cell is assumed to be correctly filled.

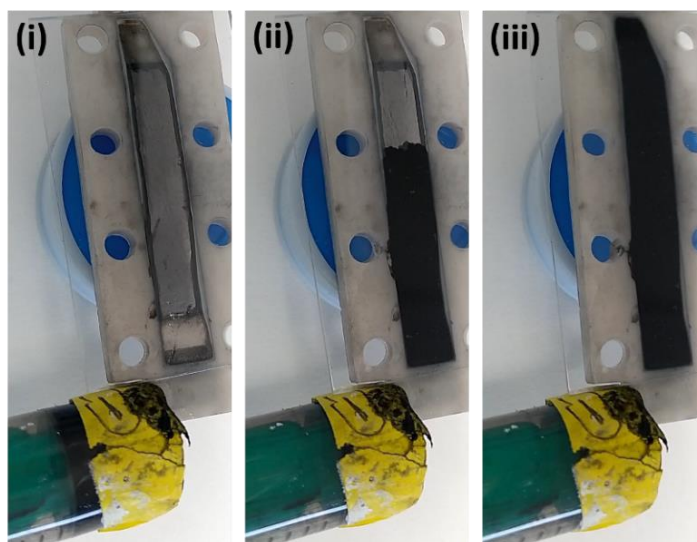


*Figure 6 - 4. Refilling process of a battery cell using semi-solid electrodes. (i) Initially, the cell is empty, and the syringe that contains the semi-solid electrode is connected to the inlet. (ii) Pressure is applied to the syringe and the semi-solid electrode is introduced inside the cell. (iii) Finally, the cell is fulfilled by the semi-solid electrode. It should be noted that a modified version of the cell displayed in Figure 6-1 was used here. The air-breathing electrode is replaced by a glass plate to visualize the filling process of the cavity left inside the cell.*

Although the method enabled substitution of semi-solid electrodes for the-proof-of-concept, much effort is required from an engineering perspective to improve the reproducibility and overall performance of the system.

### **6.3.2 Tuning of energy density by changing the Zn content in the semi-solid electrode**

The independent content of Zn and carbon additive enables tuning of energy density and specific power, separately. The energy density of a semi-solid electrode is

determined by the content of Zn. That is, the higher content ( $\text{kg}_{\text{Zn}} \text{L}_{\text{electrode}}^{-1}$ ), the higher volumetric charge capacity ( $\text{Ah L}^{-1}$ ), and thus higher energy density ( $\text{Wh L}^{-1}$ ).

**Figure 6-5a** shows typical voltage profiles, which were used to calculate the energy density as integral under the curves. Note that volume is calculated as area by thickness of the cavity in which the semi-solid electrode is injected:  $7 \text{ cm}^2 \times 0.2 \text{ cm}$ . **Figure 6-5b** shows the evolution of the energy density achieved as a function of the content of Zn ( $\text{kg}_{\text{Zn}} \text{L}_{\text{electrode}}^{-1}$ ).

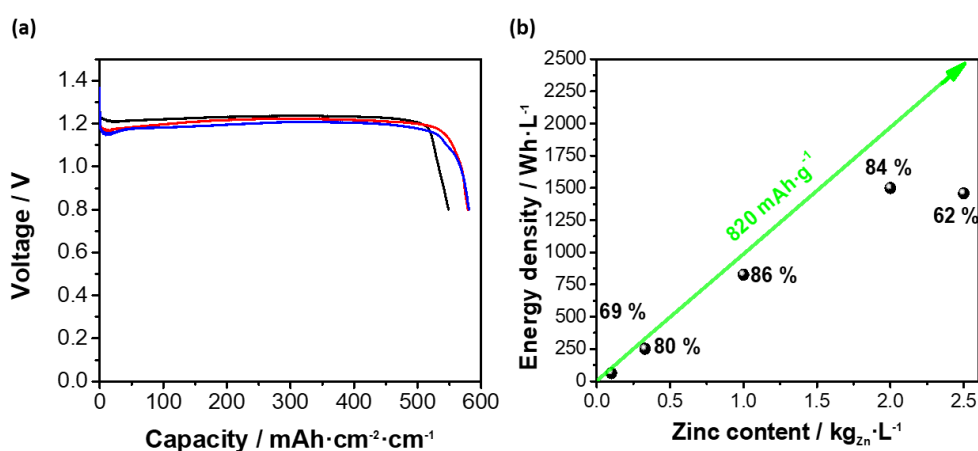


**Figure 6 - 5.** (a) Voltage profiles of three subsequent injections. (b) Energy density evolution for semi-solid electrodes with different zinc content ( $0.1 \text{ kg}_{\text{Zn}} \text{L}^{-1}$ ,  $0.33 \text{ kg}_{\text{Zn}} \text{L}^{-1}$ ,  $1 \text{ kg}_{\text{Zn}} \text{L}^{-1}$ ,  $2 \text{ kg}_{\text{Zn}} \text{L}^{-1}$  and  $2.5 \text{ kg}_{\text{Zn}} \text{L}^{-1}$ ).

The increase in energy density was almost perfectly linear with increasing Zn content, being close to the theoretical values represented as a green arrow in **Figure 6-5b**. At higher value of Zn content ( $2 \text{ kg}_{\text{Zn}} \text{L}^{-1}$ ), higher material utilization of 84 % ( $687 \text{ mAh g}_{\text{Zn}}$ ) was achieved at  $32 \text{ mA cm}^{-2}$  (*ca.*  $0.1 \text{ C}$ ). This resulted in a value of energy density of  $1500 \text{ Wh L}^{-1}$ , that is calculated considering the volume of carbon, Zn, and electrolyte. Voltage profiles **Figure 6-6**.

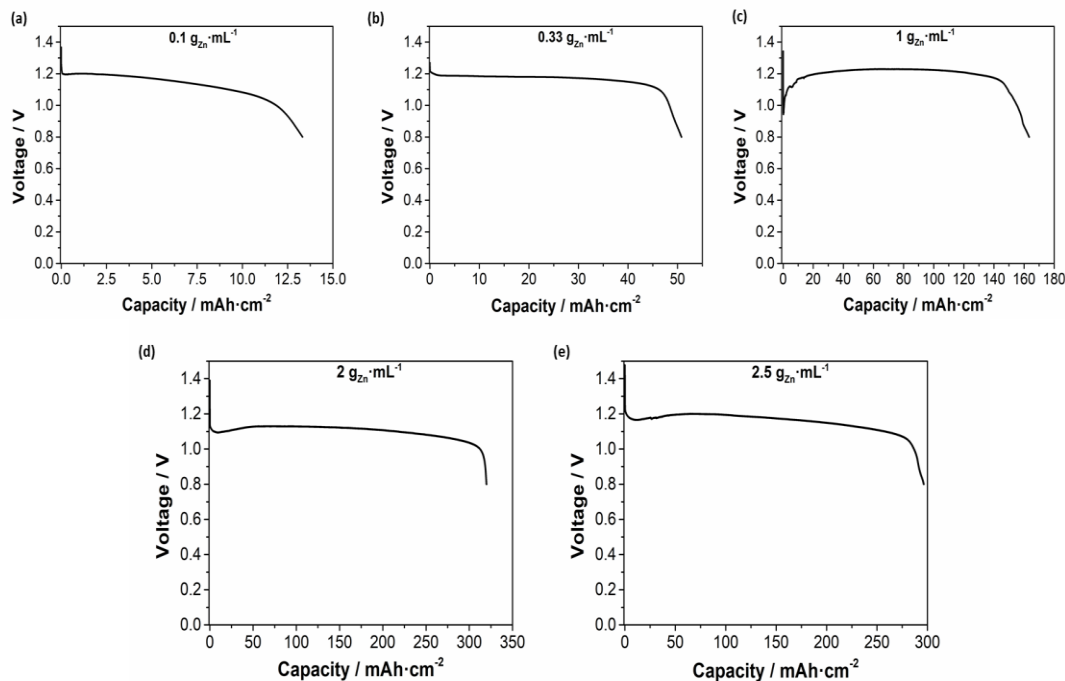


**Figure 6 - 6. Voltage profiles of 100 % discharged batteries with different Zn content. (a) 0.1 kg<sub>Zn</sub> L<sup>-1</sup> (b) 0.33 kg<sub>Zn</sub> L<sup>-1</sup> (c) 1 kg<sub>Zn</sub> L<sup>-1</sup> (d) 2 kg<sub>Zn</sub> L<sup>-1</sup> (e) 2.5 kg<sub>Zn</sub> L<sup>-1</sup>.**

Values of energy density at cell level (including separator, current collector, and air-breathing electrode) are discussed below. Note that the value of energy density only decreases a 5 % at cell level. It should also be noted that a remarkable areal capacity of 303 mAh cm<sup>-2</sup> was here demonstrated at 0.1 C (32 mA cm<sup>-2</sup>), which is relevant for the energy density of the entire device. This value not only largely exceeds typical values reported for conventional Zn-Air batteries, but also recent reports using solid-state electrolyte. That is, the value achieved in our work (303 mAh cm<sup>-2</sup> at 32 mA cm<sup>-2</sup>) is 3-fold higher than the state-of-the-art value of 133 mAh cm<sup>-2</sup> at the current density of 4 mA cm<sup>-2</sup>, which is in turn 100 times higher than that of the Zinc-Air battery using zinc foil as anode (1-2 mAh cm<sup>-2</sup>).<sup>36</sup>

### 6.3.3 Exploring the limits of energy density by X-ray tomography

For Zn content above  $2 \text{ kg L}^{-1}$ , the utilization rate of Zn significantly decreased, i.e. 62 % at  $2.5 \text{ kg}_{\text{Zn}} \text{ L}^{-1}$ . This is likely due to clogging issue related to the formation of ZnO as discharge product. X-ray computed tomography analysis was carried out to investigate the microstructures of Zn semi-solid electrodes and the changes upon discharge process.

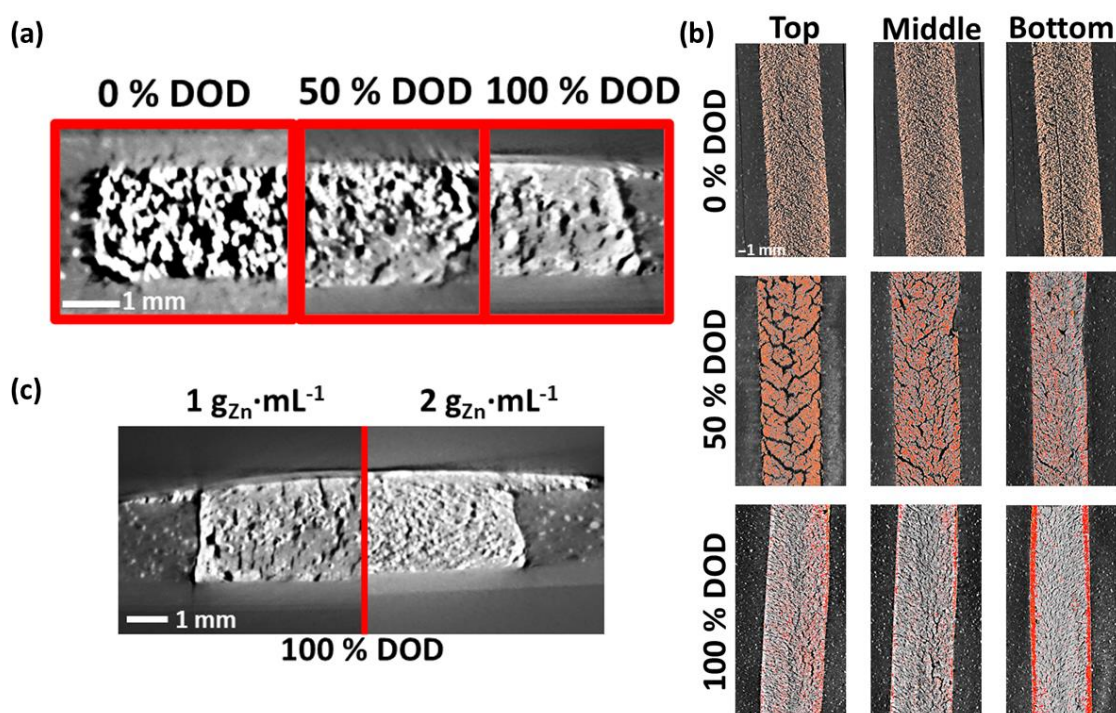


**Figure 6 - 7.** X-ray computed tomography (a) Cross section of semi-solid electrodes at different Depth-Of-Discharge (0 %, 50 % and 100 %). (b) Top-view of electrodes at different semi-solid heights (top, bottom, and middle) with different DOD. (c) Cross section of two electrodes with different Zn content ( $1 \text{ kg}_{\text{Zn}} \text{ L}^{-1}$  and  $2 \text{ kg}_{\text{Zn}} \text{ L}^{-1}$ ) at 100 % DOD.

To facilitate the visualization, the evolution of microstructure of the semi-solid electrode with the depth-of-discharge (DOD) was first studied for intermediate Zn content ( $1 \text{ kg}_{\text{Zn}} \text{ L}^{-1}$ ). **Figure 6-7a** shows the cross-section images of a Zn semi-solid Zn electrode ( $1 \text{ kg}_{\text{Zn}} \text{ L}^{-1}$ ) at various depth-of-discharge (DOD). And **Figure 6-7b** shows top-views of these 3 samples shown in **Figure 6-7a** at 3 different electrode depth (top:

near Air-breathing electrode, middle: between current collector and air-breathing electrode and bottom: near current collector). At 0 % DOD (fully charged), a homogenous distribution of Zn particles, which are visualized as bright areas in **Figure 6-7a** and orange spots in **Figure 6-7b** was observed. At 100 % DOD, Zn particles were almost completely oxidized leading to the disappearance of the bright areas (orange spots in **Figure 6-7b**). The most interesting image corresponds to 50 % DOD. Two regions are distinguished in this image: top is brighter (intense orange in **Figure 6-7b**), and bottom is darker (lighter orange in **Figure 6-7b**). This indicates that Zn particles were preferentially oxidized at the bottom. The air breathing electrode (and separator) was located at the top while negative current collect was located at the bottom. This means that the ionic transport ( $\text{OH}^-$  anions) from the air-breathing electrode to the current collectors across the semi-solid electrode is sufficient so that the reaction takes place preferentially close to the current collector. This special feature of semi-solid electrodes is due to the higher porosity and enhanced mass transport of semi-solid electrodes, compared to conventional electrodes, and enable progressive transformation from the current collector towards the air-breathing electrode. This is highly beneficial since the opposite behavior (formation of ZnO near the air-breathing electrode) that is observed for thick conventional electrodes leads to blockage of ionic pathways from the air-breathing electrode to the rest of the electrode.<sup>37</sup> The preferential formation of ZnO starting from the current collector towards the air-breathing electrode avoid this blockage for anion transport to active Zn particles, which results in deep discharge and high utilization of Zn. **Figure 6-7c** shows the cross-section images of semi-solid electrode at 100 % DOD (fully discharged) for 2 different Zn contents, i.e.  $1 \text{ kg}_{\text{zn}} \text{ L}^{-1}$  and  $2 \text{ kg}_{\text{zn}} \text{ L}^{-1}$ . While micro-channels were still visible for  $1 \text{ kg}_{\text{zn}} \text{ L}^{-1}$ , the spent electrode for  $2 \text{ kg}_{\text{zn}} \text{ L}^{-1}$  is completely dense.

Consequently, maintaining high utilization rates (e.g. > 80 %) becomes difficult for this electrode composition when Zn contents are higher than  $2 \text{ g}_{\text{zn}} \text{ mL}^{-1}$ , as shown in **Figure 6-5a**. Reformulation and re-optimization of the semi-solid electrode is therefore necessary to achieve high utilization rates for higher Zn content.

### 6.3.4 Tuning of specific power by changing the content of carbon in semi-solid electrodes

The specific power and voltage efficiency of the proposed concept will largely depend on the overall resistance of the semi-solid electrodes. **Figure 6-8a** and **Figure 6-8b** display the evolution of the operating voltage and the corresponding evolution of specific power, respectively, as a function of the applied current density for various formulations. Due to the balanced trade-off between electrical and ionic conductivity shown for semi-solid electrode containing  $70 \text{ mg mL}^{-1}$ , the content of Zn was fixed at  $0.5 \text{ g mL}^{-1}$  and the carbon content was varied around  $70 \text{ mg mL}^{-1}$ , i.e. 60, 70 and 80  $\text{mg mL}^{-1}$ , to illustrate the influence of carbon content in the specific power. For comparison, the specific power measurements were carried out at 50 % depth of discharge (DOD).

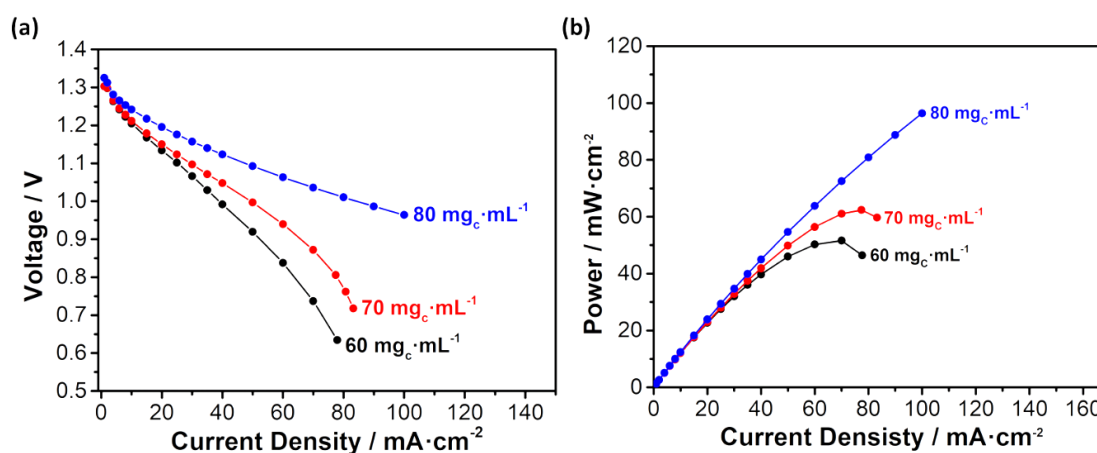


**Figure 6 - 8.** Performance of semi-solid electrodes with different formulation in terms of (a) Evolution of the operating voltage (b) Evolution of the specific power with the applied current density for a Zn content of  $0.5 \text{ kg L}^{-1}$ .

**Figure 6-9** shows the evolution of the internal resistance with the DOD revealing stable resistance from 0 % to 90.

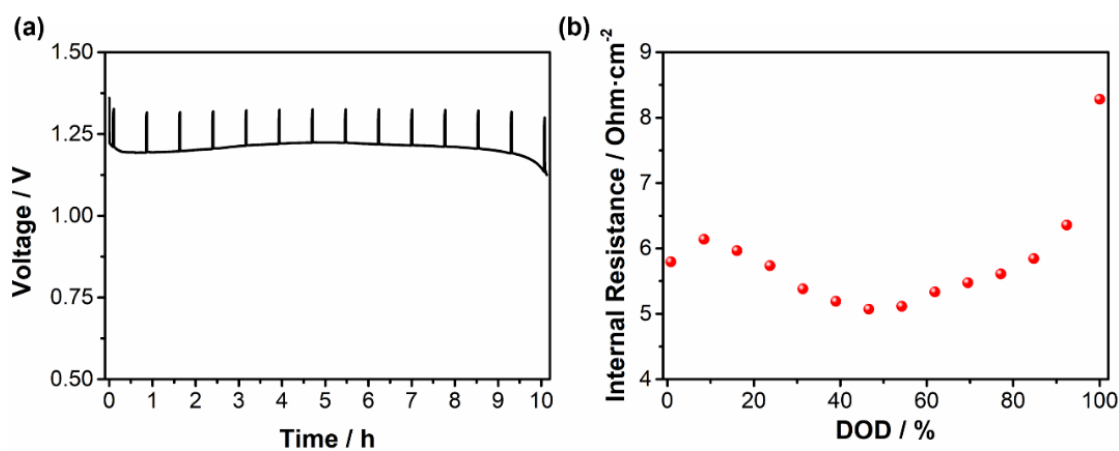


**Figure 6 - 9.** Voltage profile of a galvanostatic intermittent titration technique measurement at  $20 \text{ mA cm}^{-2}$  for a semi-solid electrode containing  $1 \text{ Kg}_{\text{Zn}} \text{ L}^{-1}$  and  $70 \text{ g}_{\text{C}} \text{ L}^{-1}$ , and (b) the resulting evolution of the internal resistance with the depth of discharge.

Thus, different behavior for the specific power is anticipated when the cells are almost discharge ( $> 90 \%$  DOD). In general, the specific power increases while flowability decreases, with increasing carbon content. Electrodes containing  $80 \text{ mg}_{\text{carbon}} \text{ mL}_{\text{electrode}}^{-1}$  were able to deliver *ca.*  $100 \text{ mW cm}^{-2}$  at  $100 \text{ mA cm}^{-2}$  (1 V).

Electrochemical data and voltage efficiencies are shown in **Figure 6-10**.

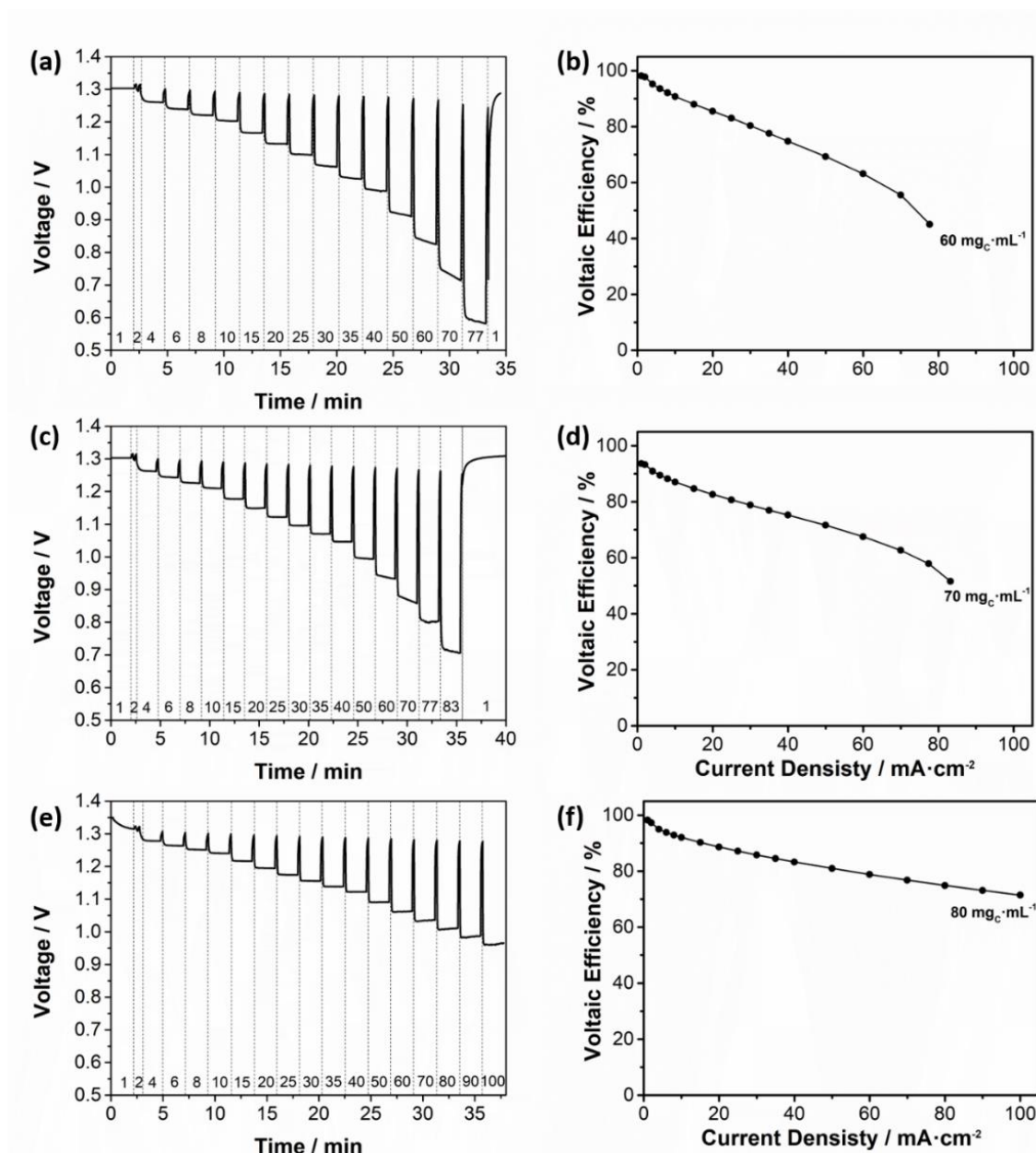


**Figure 6 - 10** Voltage profile of a Zn – air cell using a semi-solid electrode that contains 0.5 kg<sub>Zn</sub> L<sub>electrode</sub><sup>-1</sup> and 60 mg<sub>c</sub>· mL<sup>-1</sup> at different current densities: 1, 2, 4, 6, 8, 10, 15, 20, 25, 30, 35, 40, 50, 60 and 77 mA·cm<sup>-2</sup> (a) and the voltaic efficiency (b). Voltage profile of a Zn – air cell using a semi-solid electrode that contains 0.5 kg<sub>Zn</sub> L<sub>electrode</sub><sup>-1</sup> and 70 mg<sub>c</sub>· mL<sup>-1</sup> at different current densities: 1, 2, 4, 6, 8, 10, 15, 20, 25, 30, 35, 40, 50, 60, 77 and 83 mA·cm<sup>-2</sup> (c) and the voltaic efficiency (d). Voltage profile of a Zn – air cell using a semi-solid electrode that contains 0.5 kg<sub>Zn</sub> L<sub>electrode</sub><sup>-1</sup> and 80 mg<sub>c</sub>· mL<sup>-1</sup> at different current densities: 1, 2, 4, 6, 8, 10, 15, 20, 25, 30, 35, 40, 50, 60, 70, 80, 90 and 100 mA·cm<sup>-2</sup> (e) and the voltaic efficiency (f).

However, we were unable to remove semi-solid electrodes containing 80 mg mL by applying our simple removal protocol (tap water), while electrodes containing lower carbon contents ( $60\text{--}70 \text{ mg}_{\text{carbon}} \text{ mL}_{\text{electrode}}^{-1}$ ) were easily removed. In general, this home-made device using a low-cost  $\text{MnO}_x$ -based air-breathing electrode and semi-flowable semi-solid Zn electrodes ( $60\text{--}70 \text{ mg}_{\text{carbon}} \text{ mL}_{\text{electrode}}^{-1}$ ) is demonstrated to operate at current densities in the range of  $50 \text{ mA cm}^{-2}$ . At this current density, a specific power value of  $> 50 \text{ mW cm}^{-2}$  was delivered without a critical loss in voltage efficiency ( $> 80 \%$ ), which are remarkable values considering the thickness of the electrode ( $> 100 \text{ mAh cm}^{-2}$ ). Since the three main elements of the cell, i.e. Mn-based air-breathing electrode, microporous separator, and stainless-steel current collector (**Figure 6-11**) are inexpensive, power costs ( $\text{USD kW}^{-1}$ ) rapidly decay in the range of  $1\text{--}5 \text{ mA cm}^{-2}$ . Stainless steel is an inexpensive material commonly used for negative current collector in primary batteries. **Figure 6-11** shows the excellent electrochemical performance of the systems using stainless steel current collector.

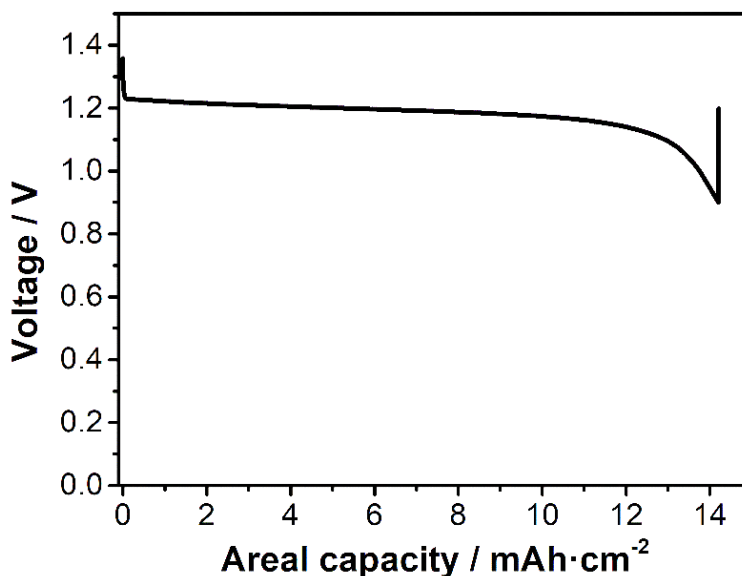


**Figure 6 - 11.** Voltage profile of a Zn-Air battery using stainless steel as current collector.

The evolution of the cost of power with the current density was calculated taking the following cost of the materials: 2.7 USD·m<sup>-2</sup>, 5.9 USD·m<sup>-2</sup> and 18 USD·m<sup>-2</sup> for separator<sup>38</sup>, negative current collector<sup>39</sup> and air-cathode<sup>40,41</sup>, respectively. The cost of power (USD W<sup>-1</sup>) was calculated as a function of the current density (d) by **Equation 6-2**:

$$\frac{USD}{W} = \left[ \frac{A}{V \cdot C} \right] \cdot \frac{USD}{A} = \left[ \frac{1}{V \cdot d} \right] \cdot \frac{USD}{A} \quad [6 - 2]$$

A: area of reactor; W: power; C: current; V: voltage; d: current density

$$\frac{USD}{W} = \left( \frac{A}{V \cdot C} \right) \cdot \left[ \left( \frac{USD}{A} \right)_{Separator} + \left( \frac{USD}{A} \right)_{CurrentCollector} + \left( \frac{USD}{A} \right)_{AirCathode} \right]$$

$$\frac{USD}{W} = \left[ \frac{1}{V \cdot d} \right] \cdot \left[ \frac{USD}{A} \right]_{Reactor}$$

A: area of reactor; W: power; C: current; V: voltage; d: current density, **Equation 6-3**

$$\frac{USD}{W} = \left[ \frac{m^2}{V \cdot A} \right] \cdot \frac{USD}{m^2} = \left[ \frac{1}{V \cdot d} \right] \cdot \frac{USD}{m^2} \quad [6 - 3]$$

m<sup>2</sup>: area of reactor; W: power; A: current; V: voltage; d: current density

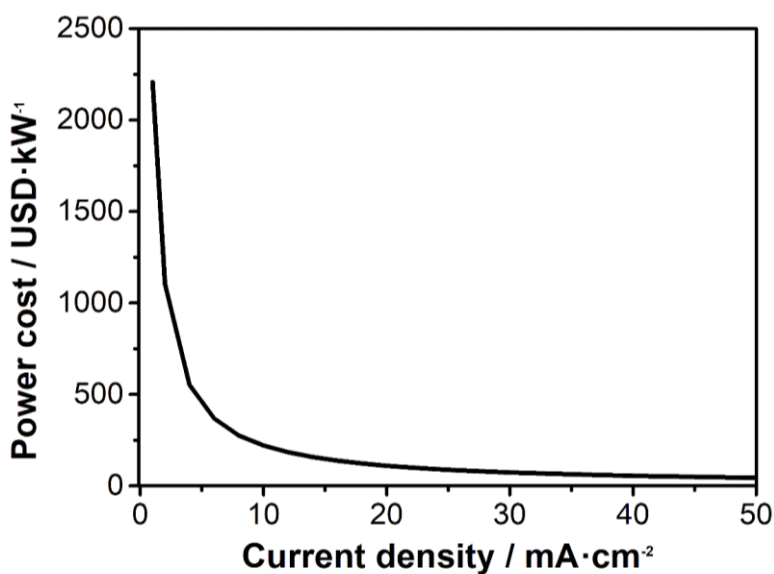


**Figure 6 - 12 Evolution of power cost with current density**

Thus, the values of current density demonstrated in this work result in a cost of power below 100 USD kW<sup>-1</sup> (**Figure 6-12**), approaching the asymptote in the curve of power cost vs. current density.

### **6.3.5 Boosting the specific power by implementing redox mediators**

Incremental improvements in the specific power can be achieved by optimizing the formulation of semi-solid electrode. However, the use of conventional conductive particles for providing electrical conductivity requires physical contact between carbon particles for reaching electrical percolation. The presence of high contents of carbon both hinders ionic conductivity and reduces flowability, so that innovative strategies are of high interest. In this context, we explored the use of a molecular wire to support electrical conductivity. When a reversible redox species is dissolved in the electrolyte and its redox potential is above that of the oxidation of Zn metal, spontaneous charge transfer reaction can take place between oxidized dissolved species and reduced Zn metal. As a result, Zn metal is oxidized, and dissolved species are reduced. The reduced dissolved species can then diffuse to the carbon network, where they are oxidized being able to react again with Zn metal (**Figure 6-13a**). The 2,6 dihydroxyanthraquinone (2,6-DHAQ) has been used in alkaline aqueous redox flow batteries,<sup>42</sup> showing a redox potential of ca. – 0.7 V vs SHE, which is above the redox potential of Zn/ZnO(– 1.25 V vs SHE). Thus, charge transfer reaction between 2,6-DHAQ and Zn should thermodynamically occur since  $E_{\text{reduction}} > E_{\text{oxidation}}$  ( $\Delta G < 0$ ). Indeed, 2,6-DHAQ has been recently used as molecular wire for metal hydrides in redox flow batteries.<sup>43</sup> Considering the redox potentials, dissolved 2,6-DHAQ should be able to be reduced to 2,6-DHAQ<sup>2-</sup> while Zn metal oxidizes to ZnO. If so, the reduced anthraquinone can transport these charges by diffusing across the porous electrode to

the current collector, where the applied potential drives its oxidation back to its neutral state transferring the charges originated from the Zn metal. In other words, 2,6-DHAQ can act as a molecular wire (**Figure 6-13a**). **Figure 6-13b** shows the evolution of cell voltage as a function of the applied current density for semi-solid electrode containing  $60 \text{ mg mL}^{-1}$ ,  $70 \text{ mg mL}^{-1}$  and  $60 \text{ mg mL}^{-1}$  in the presence of dissolved 2,6-DHAQ ( $0.5 \text{ kg}_{\text{Zn}} \text{ L}_{\text{electrode}}^{-1}$  for all of them).

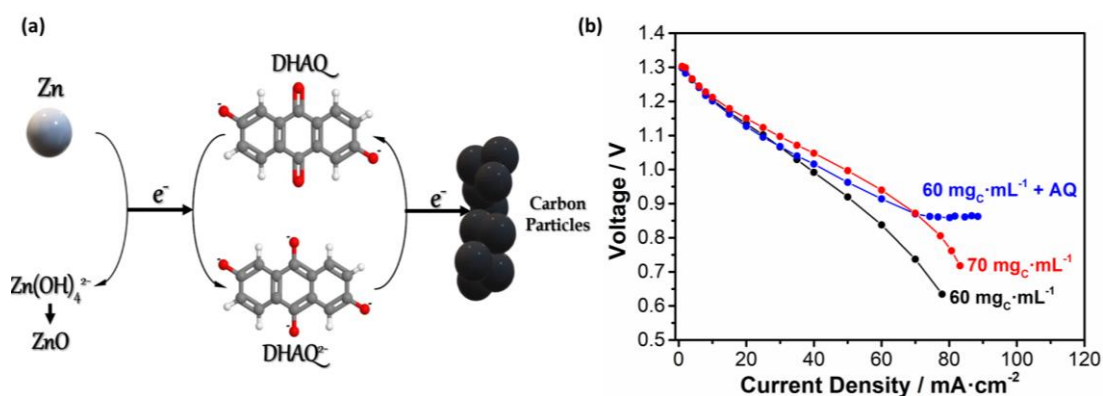


**Figure 6 - 13.** (a) Scheme of 2,6-dihydroxyanthraquinone acting as molecular wiring for mechanically rechargeable semi-solid Zinc-Air battery. (b) Comparison of the operating voltage when 2,6-dihydroxyanthraquinone is included into the formulation of the electrode.

Considering that the open cell voltage (Zn-Air) was *ca.* 1.45 V and the difference between the redox potential of Zn/ZnO and 2,6-DHAQ/2,6-DHAQ $^{2-}$  is *ca.* 0.55 V, the reduced 2,6-DHAQ (after spontaneous reaction with Zn) should be re-oxidized at the current collector when the operating cell voltage is 0.9 V. In **Figure 6-13b**, for the same amount of carbon ( $60 \text{ mg mL}^{-1}$ ), the performance for the semi-solid in the presence of 2,6-DHAQ starts to improve at *ca.* 0.95 V, which confirms the function of the molecular wire for this semi-solid electrode. Indeed, the presence of 2,6-DHAQ was able to outperform an excess of carbon in the semi-solid electrode, i.e.  $60 \text{ mg mL}^{-1}$  with mediators versus  $70 \text{ mg mL}^{-1}$  without mediator. Above the value of  $70 \text{ mA cm}^{-2}$  (0.88 V), the specific power of the semi-solid containing 2,6-DHAQ was remarkable

compared to semi-solid electrode containing even more amount of carbon. It should be noted that we were not able to apply current density above  $90 \text{ mA cm}^{-2}$  due to limitation of the instrument when operating below 1 V. Therefore, the use of molecular wire not only enables the use of less amount of carbon, which is very beneficial for the flowability, but it increases the specific power compared with semi-solid electrodes containing higher amounts of carbon. It should be noted that self-discharge does not occur when the semi-solid is stored outside the cell before injection. In addition, there is much room for improvement in terms of specific power by combining engineering and colloidal chemistry in future studies

### **6.3.6 Projected specific energy and energy density of mechanically rechargeable Zn-Air batteries based on semi-solid electrodes**

Engineering aspects obviously play an important role for the practical energy density of the proposed technology. We conducted a theoretical analysis to assess the potential of the concept. The influence of two critical parameters, i.e. thickness of air-breathing electrode and thickness of the semi-solid electrode, on the energy density and specific energy was analyzed for two Zn contents,  $2 \text{ kg}_{\text{zn}} \text{ L}^{-1}$  (demonstrated in this work) and  $3 \text{ kg}_{\text{zn}} \text{ L}^{-1}$  (target for future works). The contribution of casing that is rather large in our home-made prototypes is not considered to elucidate the intrinsic values. We consider that the contribution of casing should be addressed at a later stage (after reaching higher Technology Readiness Level), while intrinsic values provide a better idea of the potential of this technology. **Figure 6-14** reveal three important points. I) The use of a thick electrodes, as in our work, is beneficial for all studied cases. This is due to that fact that the volume losses of inactive elements, e.g. current collector, and separator, are minimized with increasing areal capacity. II) The energy density

increases as the thickness of the air-breathing electrode decreases. This is due to that fact that  $O_2$  is in the air so that the volume of the air-breathing electrode does not limit the charge storage capacity of the cell. And III) the benefit of using thick semi-solid electrodes is reduced with decreasing thickness of the air-breathing electrode. This is due to the volume of inactive elements decreases with decreasing thickness of air-breathing electrode, so that the positive impact of thick semi-solid electrode is buffered. This latter point may be of interest for higher power applications that requires thinner semi-solid electrodes.

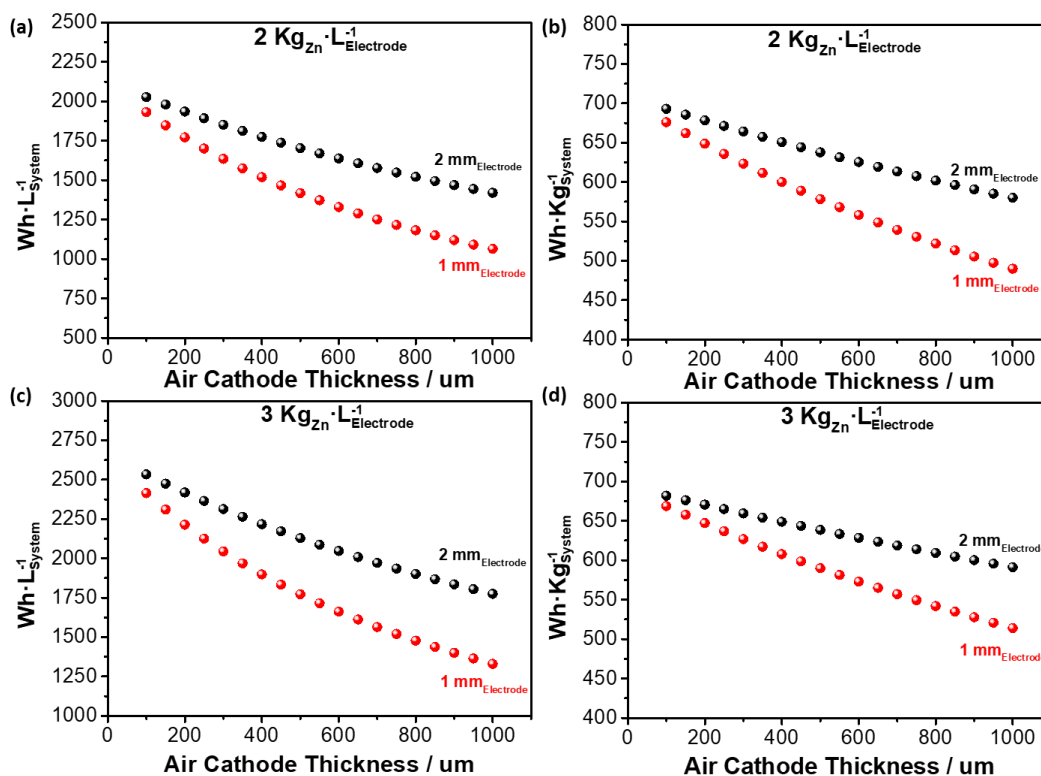


**Figure 6 - 14. Theoretical estimation of energy density for Zn-Air batteries using semi-solid electrodes. Comparison between two different Zinc content in the electrode: (a) and (b) for  $2 \text{ kg}_{\text{zn}} \text{ L}^{-1}$ , and (c) and (d) for  $3 \text{ kg}_{\text{zn}} \text{ L}^{-1}$ . Thickness of Celgard separator and stainless-steel current collector are  $25 \mu\text{m}$  and  $12 \mu\text{m}$ , respectively.**

In this work, the thickness of the air-breathing electrode and the Zn content in the semi-solid electrodes were 0.5 mm and  $2 \text{ kg L}^{-1}$ , respectively. This results in values of ca.  $1703 \text{ Wh L}^{-1}$  and  $638 \text{ Wh kg}^{-1}$  when 100 % utilization rates are achieved. If the

utilization rate is reduced to 84 % (demonstrated here), the energy density only decreases to 1430 Wh L<sup>-1</sup>. It should be noted that energy density only decreases 5 % with respect to the energy density of the electrode (1500 Wh L<sup>-1</sup>) when including separator, current collector and air-breathing electrode are also considered. For a Zn content of 3 kg L<sup>-1</sup> and a utilization rate of 80 %, the energy density would be 1700 Wh L<sup>-1</sup>, which indicates both Zn content and utilization rate are relevant to achieve high values of energy density.

### **6.3.7 Zn semi-solid electrodes as potential energy vector**

The mechanically-rechargeable Zn–Air battery can be considered as a refillable primary Zn – Air battery that uses Zn as renewable energy carrier (**Figure 6-15a**). The spent ZnO can be easily dissolved in e.g. mild acid media and transported in liquid phase to the regeneration site. By the mature and well-established Zn electrowinning process<sup>44,45</sup>, Zn<sup>2+</sup> ions are reduced to metal Zn using energy from renewable sources. Zn semi-solid electrode can be prepared and stored in sealed containers for their transportation. Refilling of the device can be conducted directly from these containers. The most critical point here is the self-discharge during storage / transportation. Due to the strong alkaline media used in this work, spontaneous reaction of Zn and water is kinetically slow. To evaluate the self-discharge rate, Zn particles were stored in 6 M KOH for 24 h and then, the loss of Zn was determined.

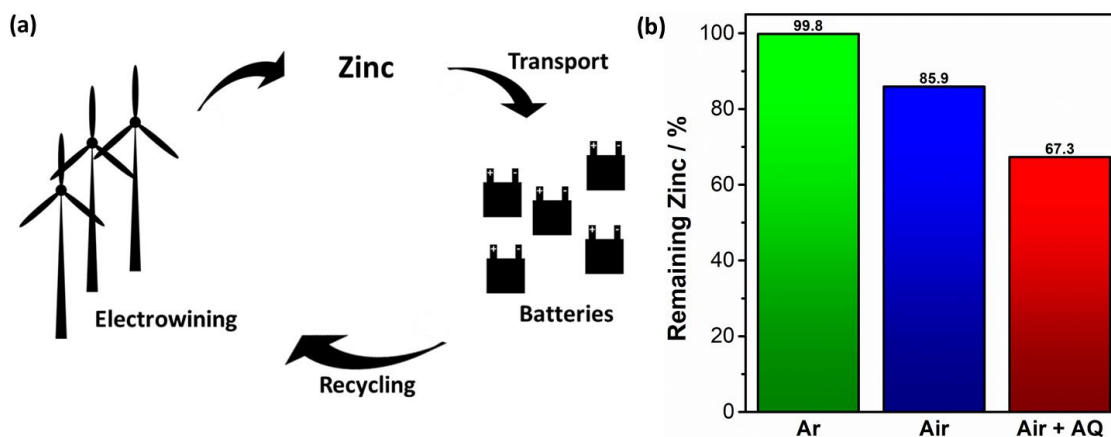


*Figure 6 - 15. (a) Scheme of metallic zinc as energy carrier used in mechanically-rechargeable Zn–Air batteries. (b) Results of experiments for determining the amount of zinc that remains when it is stored in different media: Argon, Air and Air with 2,6-DHAQ.*

Due to the higher solubility of zincates at increasing KOH concentration, Zn particles were rinsed with 12 M KOH after storage, dried it and weighted it. When the suspension of Zn was stored under protected atmosphere (Ar-filled), the loss of Zn was negligible (0.2 wt.%) (**Figure 6-15b**). However, when the suspension of Zn was purged with air, a loss of 14.1 wt.% was observed after 24 h. When the suspension of Zn contained redox wire (anthraquinone), the kinetics between oxygen reduction and Zn oxidation increased, and the loss of Zn increased up to 32.7 wt.%. Considering that low-cost microporous are often used in Zn-Air batteries, slow diffusion of oxygen from the air-breathing electrode to the negative electrode cannot be avoided. It should be noted that self-discharge that occurs by diffusion of oxygen or the charged molecular wire is prevented by storing the semi-solid electrode in containers before its use. Importantly, exclusion of air from the containers storing Zn semi-solid electrodes should be considered for storage and transport.

## 6.4 Conclusions

In summary, success of the concept of a mechanically-rechargeable Zn–Air battery has been locked by the poor practical energy density of semi-flowable Zn electrodes ( $\approx 150 \text{ Wh L}^{-1}$ ) due to the formation of passivating ZnO. This concept has been long desired since it overcomes the most demanding challenges of Zn–Air batteries (reversible oxygen reaction and Zn reaction) by decoupling the charge and discharge process of a Zn–Air battery in the two processes in separate device. However, the low practical energy densities have been so far achieved in practice. In our work, the use of electrically conducting flowable semi-solid electrodes unlocks the achievement of higher practical volumetric capacities (*ca.*  $1500 \text{ Wh L}^{-1}$ ) using a 3-D printed home-made primary Zn–Air battery cell. The cells were mechanically recharged several times, thus successfully demonstrating the feasibility of the concept. These values were achieved by comprising flowability of the semi-solid electrodes, while their semi-flowability still enables eventual substitution of electrode (in contrast to continuous flow for redox flow batteries). This opens up a new research direction in the field of energy storage, in which Zn-based semi-solid electrodes become a new type of renewable fuel. In contrast to gas and liquid fuel, Zn semi-flowable “fuel” is easier to be stored, transported, used in an electrochemical cell due to its semi-solid nature (active material is solid and easier to be confined). This battery concept has the potential to become a fitting power source for a number of emerging and demanding applications such as drones, in which safety, fast charge and high energy density are essential. Nevertheless, intensive efforts are required to be devoted from neighboring fields such as colloidal chemistry, chemical engineering, and mechanical engineering to make this concept more competitive.

## 6.5 References

1. Lee, J.-S. *et al.* Metal-Air Batteries with High Energy Density: Li-Air versus Zn-Air. *Adv. Energy Mater.* **1**, 34–50 (2011).
2. Li, Y. & Dai, H. Recent advances in Zinc-air batteries. *Chem. Soc. Rev.* **43**, 5257–5275 (2014).
3. Mainar, A. R. *et al.* An overview of progress in electrolytes for secondary zinc-air batteries and other storage systems based on zinc. *J. Energy Storage* **15**, 304–328 (2018).
4. Liu, Q., Pan, Z., Wang, E., An, L. & Sun, G. Aqueous metal-air batteries: Fundamentals and applications. *Energy Storage Mater.* **27**, 478–505 (2020).
5. Hosseini, S., Masoudi Soltani, S. & Li, Y. Y. Current status and technical challenges of electrolytes in zinc–air batteries: An in-depth review. *Chem. Eng. J.* **408**, 127241 (2021).
6. Group, T. C. & Foller, P. C. Improved slurry zinc/air systems as batteries for urban vehicle propulsion. *J. Appl. Electrochem.* **16**, 527–543 (1986).
7. Sapkota, P. & Kim, H. Zinc-air fuel cell, a potential candidate for alternative energy. *J. Ind. Eng. Chem.* **15**, 445–450 (2009).
8. Evans, J. W., Savaskan, G. & Engineering, M. A zinc-air cell employing a packed bed anode. *J. Appl. Electrochem.* **21**, 105–110 (1991).
9. Korall, M. J., Harats, Y., Sassen, J. & Goldstein, J. R. US5418080A. (1994).
10. Cooper, J. F. *et al.* Demonstration of zinc/air fuel battery to enhance the range and mission of fleet electric vehicles: Preliminary results in the refueling of a multicell module. *Intersoc. Energy Convers. Eng. Conf. CA (United States)* 7–12 (1994).
11. Goldstein, J., Brown, I. & Koretz, B. New Developments in the Electric Fuel Zinc-Air System. *Int. Power Sources Symp.* (1999).
12. J. R. Goldstein. B. Koretz. *Intersoc. Energy Convers. Eng. Conf.* 28, 2.279 (1993).
13. J. Noring, S. Gordon, A. Maimoni, M. S. and J. F. C. Mechanically refuelable

- zinc/air electric vehicle cells. *Electromechanical Soc. Meet. Honolulu, HI*, 16–21 (1993).
14. Selvakumaran, D., Pan, A., Liang, S. & Cao, G. A review on recent developments and challenges of cathode materials for rechargeable aqueous Zn-ion batteries. *J. Mater. Chem. A* **7**, 18209–18236 (2019).
  15. Wang, F. *et al.* Highly reversible zinc metal anode for aqueous batteries. *Nat. Mater.* **17**, 543–549 (2018).
  16. Petrescu, M. I., Ghica, G. V & Buzatu, T. Recovery of zinc and manganese from spent batteries by reductive leaching in acidic media. *J. Power Sources* **247**, 612–617 (2014).
  17. J. R. Goldstein, N. Lapidot, M. Aguf, I. G. and M. G. Electric Fuel Zinc-Air System: Zinc Regeneration Update. *Electrochem. Soc. Pennington, NJ* 97(18), 881 (1997).
  18. Electric Fuel. <https://electric-fuel.com/>.
  19. Powerzinc. <http://www.powerzinc.com/>.
  20. Metallic Power. <http://www.metallicpower.com/>.
  21. Smedley, S. Zinc air fuel cell for industrial and specialty vehicles. *IEEE Aerosp. Electron. Syst. Mag.* **15**, 19–21 (2000).
  22. The Leader in Zinc Air Battery Technology - Zinc8 Energy Solutions. <https://www.zinc8energy.com/>.
  23. Koretz, B., Goldstein, J. R. & Gektin, I. Electric Fuel™ Zinc-Air Battery Regeneration Technology presented. in *Annual Meeting of the Applied Electrochemistry Division of the German Chemical Society* (1995).
  24. J.Cherepy, N., Krueger, R. & Cooper, J. F. A Zinc / Air Fuel Cell for Electric Vehicles. *Annual Battery Conference. Long Beach, CA* (1999).
  25. Duduta, M. *et al.* Semi-solid lithium rechargeable flow battery. *Adv. Energy Mater.* **1**, 511–516 (2011).
  26. Ventosa, E. *et al.* Non-aqueous semi-solid flow battery based on Na-ion chemistry. P2-type  $\text{Na}_x\text{Ni}_{0.22}\text{Co}_{0.11}\text{Mn}_{0.66}\text{O}_2\text{-NaTi}_2(\text{PO}_4)_3$ . *Chem. Commun.* **51**, 7298–7301 (2015).

27. Li, Z. *et al.* Aqueous Semi-Solid Flow Cell : Demonstration and Analysis. 2–7 (2013).
28. Fan, F. Y. *et al.* Polysulfide Flow Batteries Enabled by Percolating Nanoscale Conductor Networks. *Nano Lett* **14**, (2014).
29. Muñoz-Torrero, D., Palma, J., Marcilla, R. & Ventosa, E. Al-Ion Battery Based on Semisolid Electrodes for Higher Specific Energy and Lower Cost. *ACS Appl. Energy Mater.* **3**, 2285–2289 (2020).
30. 24M Technologies.
31. Liu, J. & Wang, Y. Preliminary study of high energy density Zn/Ni flow batteries. *J. Power Sources* **294**, 574–579 (2015).
32. Zhu, Y. G. *et al.* High-energy and high-power Zn–Ni flow batteries with semi-solid electrodes. *Sustain. Energy Fuels* **4**, 4076–4085 (2020).
33. Liu, Y. *et al.* A Renewable Sedimentary Slurry Battery: Preliminary Study in Zinc Electrodes. *iScience* **23**, (2020).
34. Narayanan, T. M., Zhu, Y. G., Gençer, E., McKinley, G. & Shao-Horn, Y. Low-cost manganese dioxide semi-solid electrode for flow batteries. *Joule* **5**, 2934–2954 (2021).
35. Perez-Antolin, D., Trócoli, R., Palma, J. & Ventosa, E. The injectable battery. A conceptually new strategy in pursue of a sustainable and circular battery model. *J. Power Sources* **480**, 228839 (2020).
36. Zuo, Y. *et al.* A high areal capacity solid-state zinc-air battery via interface optimization of electrode and electrolyte. *Chem. Eng. J.* **430**, 132996 (2022).
37. Jung, C. Y., Kim, T. H., Kim, W. J. & Yi, S. C. Computational analysis of the zinc utilization in the primary zinc-air batteries. *Energy* **102**, 694–704 (2016).
38. Patry, G., Romagny, A., Martinet, S. & Froelich, D. Cost modeling of lithium-ion battery cells for automotive applications. *Energy Sci. Eng.* **3**, 71–82 (2015).
39. Li, Z. *et al.* Air-Breathing Aqueous Sulfur Flow Battery for Ultralow-Cost Long-Duration Electrical Storage. *Joule* **1**, 306–327 (2017).
40. Carlson, E. J., Kopf, P., Sinha, J., Sriramulu, S. & Yang, Y. Cost Analysis of PEM Fuel Cell Systems for Transportation: September 30, 2005. (2005).

41. Toussaint, G., Stevens, P., Akrou, L., Rouget, R. & Fourgeot, F. Development of a Rechargeable Zinc-Air Battery. *ECS Trans.* **28**, 25–34 (2010).
42. Lin, K. *et al.* Alkaline quinone flow battery. *Science (80-. )*. **349**, 1529–1532 (2015).
43. Páez, T. *et al.* The Redox-Mediated Nickel–Metal Hydride Flow Battery. *Adv. Energy Mater.* 2102866 (2021) doi:10.1002/AENM.202102866.
44. St-Pierre, J. & Piron, D. L. Electrowinning of zinc from alkaline solutions. *J. Appl. Electrochem.* **16**, 447–456 (1986).
45. Saba, A. E. & Elsherief, A. E. Continuous electrowinning of zinc. *Hydrometallurgy* **54**, 91–106 (2000).



**Chapter 7. Regenerative Electrochemical  
Ion Pumping Cell Based on Semi-Solid  
Electrodes for Sustainable Li Recovery**

The results obtained in this chapter have been published in an international peer-reviewed journal (Desalination, IF:9.501). Basic information about this publication can be found as follows.

**D. Perez-Antolin**, C. Irastorza, S. Gonzalez, R. Moreno, E. Garcia-Quismondo, J. Palma, J. Lado, E. Ventosa. (2022). Regenerative electrochemical ion pumping cell based on semi-solid electrodes for sustainable Li recovery. *Desalination*. 553, 115764 DOI: 10.1016/j.desal.2022.115764.

<https://www.sciencedirect.com/science/article/pii/S0011916422002193>

## 7.1 Introduction

The lithium demand has been increasing in the last years, mainly due to the growth of portable electronics powered by Li-ion batteries. If projections are fulfilled, the penetration of electric vehicles will boost lithium demand in near future. In this sense, different financial studies estimated a total lithium demand of 278 kt of Lithium Carbonate Equivalents (LCE) in 2018, for which demand associated to lithium-ion batteries (LIB's) represents 58% of that amount.<sup>1</sup> These studies also project the total lithium demand to reach 2.20 Mt LCE in 2030. The 10-fold increase in lithium demand with respect to 2018 is mainly triggered by battery applications related with the electric mobility. This estimation is supported by a recent report published by the International Energy Agency that indicates an increase of the vehicle battery capacity from 170 GWh per year (2020) to 1.5 TWh in 2030 following the Stated Policies Scenario, and even reaching the 3 TWh in a Sustainable Development Scenario.<sup>2</sup> Currently, there are two main lithium sources; *i*) brines of high-altitude salt flats known as “salars” (which are mainly found in Bolivia, Argentina and Chile), and *ii*) hard rock spodumene deposits. Salars are usually located in areas of geothermal activity and present relatively high concentration of dissolved lithium (30-150 mg L<sup>-1</sup>).<sup>3</sup> In salars, the lime-soda evaporation is the most employed extraction process. This practice basically consists on pumping the brines from under the saline crust to solar evaporation ponds from which concentrated brine is treated with precipitation agents, e.g. sodium carbonate, for obtaining first lithium carbonate and then lithium hydroxide.<sup>3</sup> Here the main drawbacks associated to lithium extraction from brines are the long processing times, the low lithium recovery efficiency, the weather dependency and the high consumption of water.<sup>4</sup> These limitations affect the lithium global production capacity from brine, estimated 120.5 Ktons/year<sup>4</sup> which, according to predictions, will not be enough to cover the lithium market demand in the

near future.<sup>5,6</sup> In this context, the quest for more convenient technology has become of great interest. Thus, emerging technologies are expected to involve environmentally friendly methodologies looking for reducing wastes production, maximizing the areal capacity of evaporating ponds and minimizing the chemicals consumption.<sup>7</sup>

Different approaches have been explored to tackle this challenge searching for a relatively high selective separation that consumes a moderate amount of energy at a reasonable cost. In this regard, the electrochemical technologies have recently attracted the attention of the scientific community.<sup>3,5,6,8-13</sup> Ions from a stream are captured by selective electrodes through electrochemical reactions which enables the production of a diluted stream and a concentrated stream. First electrochemical technologies employed capacitive electrodes in which ion separation is driven by the formation of the electrical double layer (EDL).<sup>9,14-19</sup> However, this physical and non-selective process leads to limited ion storage capacity and a low separation factor.<sup>9</sup> More recently, the use of Faradaic intercalation materials was proposed for electrochemical ion pumping.<sup>20,21</sup> These materials, typically used in batteries for energy storage,<sup>8,21,22</sup> are able to intercalate selectively certain ions within their structures as a result of a redox reaction. Consequently, intercalation electrodes present high ion selectivity and specific charge capacity with respect to capacitive electrodes<sup>22,23</sup> which results from the bulk redox reactions in contrast with surface confined reactions for capacitive materials. However, same as in batteries, insertion of ions into the bulk of intercalation materials leads to accelerated degradation in comparison to capacitive processes,<sup>9</sup> which may compromise the techno-economic feasibility and sustainability of Faradaic-based ion separation systems.

Faradaic intercalation materials are usually fixed on the electrode surface located inside the electrochemical reactor forming a porous and immobile film. Recently, intercalation materials have been deployed in the field of redox flow batteries in the form of flowable

“semi-solid electrodes” (mixture of solid intercalation material, carbon additive and electrolyte in the absence of binder).<sup>24,25</sup> By doing this, solid Faradaic intercalation materials can be stored in external reservoirs and pumped into the reactor for energy conversion enabling decoupling of energy and power. Despite semi-solid electrodes were conceived for redox flow batteries, their unique feature can be of great interest for other applications.

Herein an innovative electrochemical ion pumping cell concept having easily exchangeable Faradaic semi-solid electrodes is proposed for facilitating regeneration and direct reuse of the system. The use of semi-solid electrodes containing intercalation materials allows simple substitution of the spent Faradaic electrodes when it reaches its end of life. Two cell designs are developed for implementing the proposed concept of Regenerative Electrochemical Ion Pumping Cell (REIPC): *i*) a configuration using two Li-selective intercalation materials and an ion-selective membrane and *ii*) a membrane-free configuration using one Li-selective and one Na-selective intercalation materials. Both prototypes were fabricated delivering good ion separation properties and, more importantly, being easily regenerated by replacing Faradaic materials in the form of semi-solid electrodes and, thus, enabling the reuse of the entire system.

## 7.2 Experimental Procedures

### 7.2.1 Reagents and materials

Lithium Iron Phosphate ( $\text{LiFePO}_4$ , Advanced Lithium Electrochemistry), Carbon black KetjenBlack EC-600 JD (Azelis and AkzoNovel polymer chemicals), Lithium Manganese Oxide ( $\text{LiMn}_2\text{O}_4$ , Nanomyte NEI Corporation), Lithium Chloride ( $\text{LiCl}$ , Alfa Aesar), Sodium Chloride ( $\text{NaCl}$ , Sigma Aldrich), Potassium Chloride ( $\text{KCl}$ , Sigma Aldrich), Magnesium Chloride ( $\text{MgCl}_2$ , Alfa Aesar) were used as received.

Potassium Nickel Hexacyanoferrate ( $\text{KNi}[\text{Fe}(\text{CN})_6]$ ) was synthesized following the route described by [11], briefly, 120 mL of  $\text{Ni}(\text{NO}_3)_2 \cdot 6 \text{H}_2\text{O}$  (Alfa Aesar) 0.1 M and 120 mL of  $\text{K}_3\text{Fe}(\text{CN})_6$  0.05 M (Alfa Aesar) were added simultaneously to 60 mL of water while stirring at 70 °C forming a brown precipitate. The suspension was sonicated for 30 min at 70 °C and rested overnight. The precipitate was filtrated and washed with distilled water, and subsequently dried in vacuum at 70 °C. X-ray diffraction pattern of the obtained materials confirming that the synthesis was carried out successfully is provided in **Figure 7-1**.

Expanded graphite (Sigracell TF6) was used as current collector, Celgard 3501 as separator, and Fumasep FAA-3-30 as selective anionic exchange membrane (AEM). The external case of the battery was fabricated by 3D-Printing machine (MakerBot Replicator™ 2X) using ABS as plastic material.

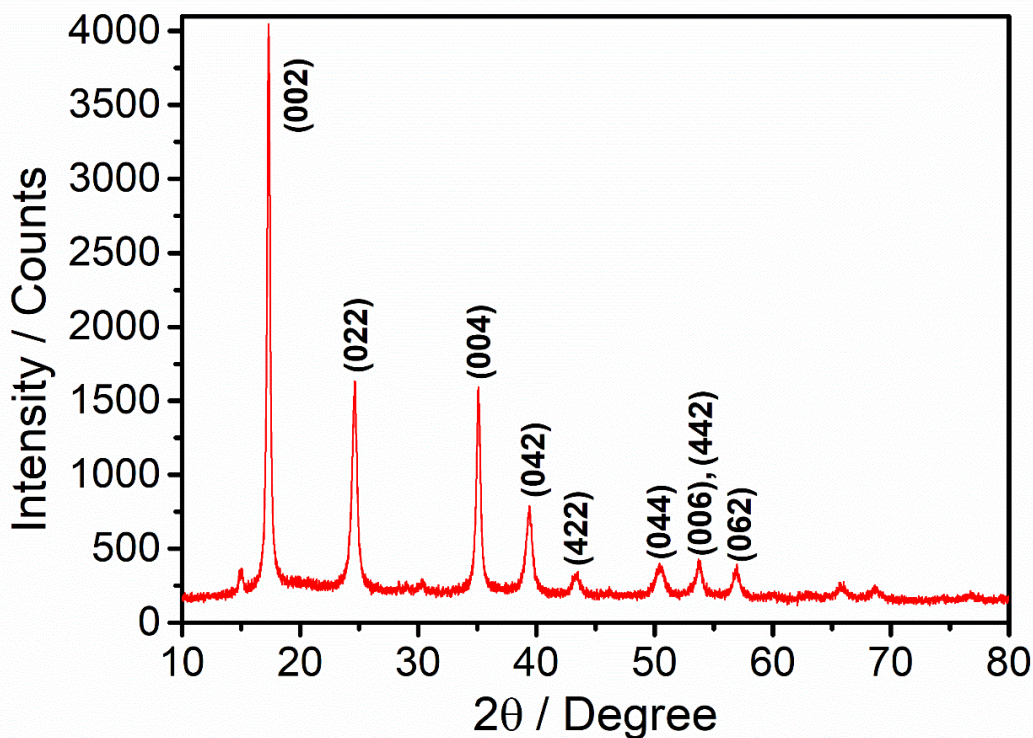


*Figure 7 - 1. XRD pattern of Potassium Nickel Hexacyanoferrate ( $\text{KNi}[\text{Fe}(\text{CN})_6]$ ) matching the diffraction previously reported for this materials.<sup>26</sup>*

## 7.2.2 Preparation of semi-solid electrodes

Semi-solid electrodes containing a mixture of the active material and carbon black additive (77 wt.%, and 23 wt.%, respectively) and electrolyte (6 mL) were prepared directly in a syringe by stirring with a high-shear homogenizer (Ultra-Turrax IKA T18-Basic) during three periods of 10 minutes resting 5 minutes between periods. The electrolyte used for each experiment had the same composition as the initial brine solution.

## 7.2.3 Electrochemical cell

A filter-pressed type electrochemical cell was designed using the following elements: 3-D printed end-plates, current collectors made of expanded graphite, Viton gaskets with the intentionally cavities for allocating the semi-solid electrodes and Celgard 3501 separator for confining solid particles. Moreover, another gasket was used for allowing

the electrolyte flow through the mentioned cell. This description corresponds to half-cell configuration since the same layers were used for the other half-cell that allowed to assemble the complete device. Where AEM was used, it was located in the middle of the water-flow-channel. A Masterflex® L/S® peristaltic pump with two heads was used for pumping the electrolyte flow through the device at  $100 \text{ mL} \cdot \text{min}^{-1}$ .

### **7.2.3.1 Configuration of the Regenerative Electrochemical Ion Pumping Cell (REIPC)**

The cell consists of four different chambers; 1) injectable positive electrode confined by an expanded-graphite bipolar current collector, a gasket with a  $5 \text{ cm}^2$  area, 2 mm thickness gap and a microporous separator (Celgard, C3501); 2) compartment for the solution to be deionized/concentrated, separated by an anion exchange membrane from the 3) other solution compartment; 4) injectable negative electrode confined in a similar way as the positive electrode by a current collector, gasket, and microporous separator. (**Figure 7-2**).

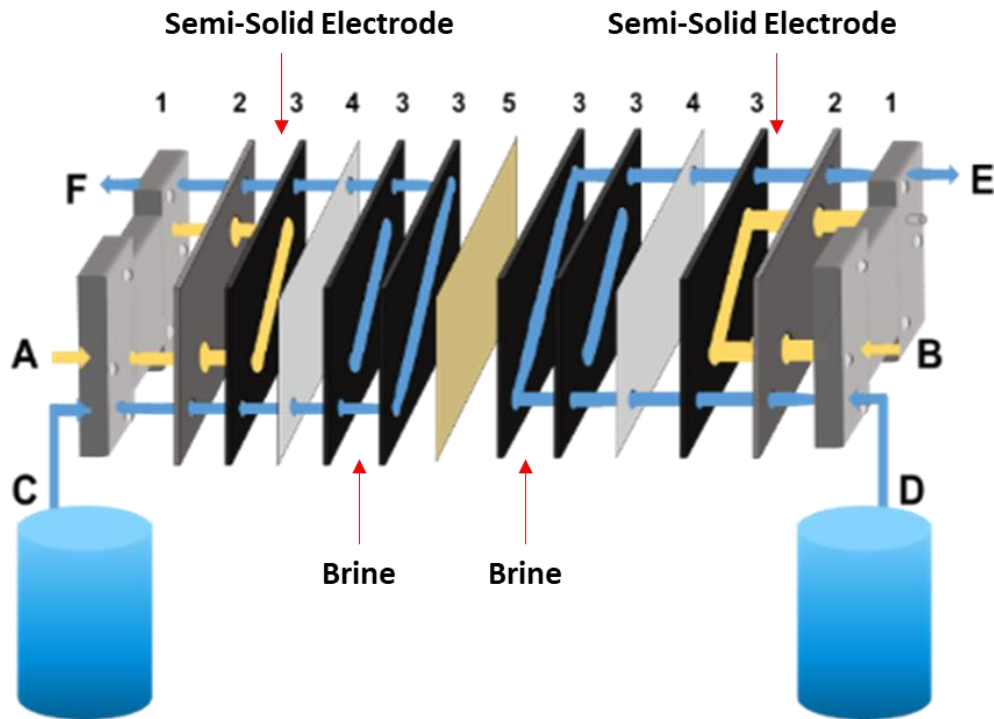
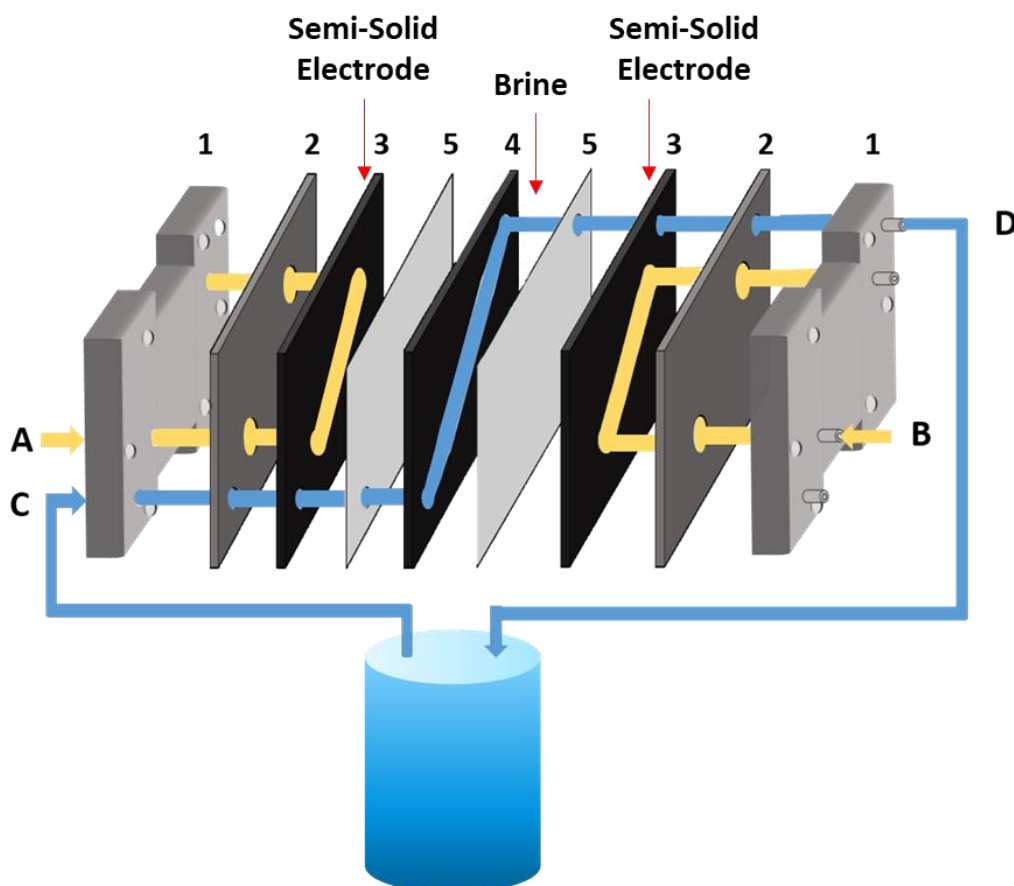


Figure 7 - 2. Flow diagram of Ion Pumping Injectable Cell 1. 3D Printed ABS Endplate; 2. Graphite Current Collector; 3. Viton Gasket; 4. Microporous Separator C3501; 5. Anion Exchange Membrane (AEM).

### 7.2.3.2 Configuration of the Membrane-Free Regenerative Electrochemical Ion Pumping Cell (MF-REIPC)

The cell consists of three different chambers; 1) injectable positive electrode confined by an expanded-graphite bipolar current collector, a gasket with a 5 cm<sup>2</sup> area, 2 mm thickness gap and a microporous separator (Celgard, C3501); 2) compartment for the solution to be deionized/concentrated, 3) injectable negative electrode confined in a similar way as the positive electrode by a current collector, gasket, and microporous separator. (Figure 7-3).



*Figure 7 - 3. Flow diagram Membrane Free Ion Pumping Injectable Cell 1. 3D Printed ABS Endplate; 2. Graphite Current Collector; 3 and 4. Viton Gasket; 5. Microporous Separator C3501.*

## 7.2.4 Electrochemical measurements

Galvanostatic measurements were carried out using an EC-Biologic potentiostat. The proof of concept for the REIPC containing  $\text{LiFePO}_4 - \text{FePO}_4$  was performed by cycling the system between 0.35 V and -0.35 V at  $2 \text{ mA cm}^{-2}$ . Regarding the demonstration of the REIPC electrode substitution, the cell was cycled between 0.5 V and -0.5 V at  $2 \text{ mA cm}^{-2}$  after each substitution of the electrode (even for those with capacitive behavior). In the case of the proof of concept for the asymmetrical configuration, the  $\text{LiFePO}_4 - \text{LiMn}_2\text{O}_4$  REIPC was cycled between 0 V and 0.8 V at  $2 \text{ mA cm}^{-2}$ . Moreover, the  $\text{LiMn}_2\text{O}_4 - \text{KNi}[\text{Fe}(\text{CN})_6]$  Membrane-Free REIPC (MF- REIPC) was cycled between 0 V and 1 V at  $1 \text{ mA cm}^{-2}$ .

Ion chromatography (IC) analysis (930 Compact IC Flex, Metrohm) was performed to evaluate the variation of the lithium concentration in the electrolytes and determined the lithium adsorption capacity ( $SAC_{Li}$ ). Additionally, Flame photometer (Corning 410) was used for measuring the concentration of lithium and sodium in the electrolytes of Membrane-Free Regenerative Electrochemical Ion Pumping system.

### 7.2.5 Figures of merit

Five figures of merit are defined to assess the performance of the prototypes:

The efficiency of the system ( $\eta$ ) is defined as the ratio between the change in concentration of cations effectively achieved for the stream and the theoretical change in concentration of cations corresponding to the charge consumed by the system, following the **Equations 7-1 and 7-2**, for lithium capturing and releasing process respectively <sup>27</sup>.

$$\eta = \frac{C_i \cdot V - |Q|/F}{C_f \cdot V} \quad [7-1]$$

$$\eta = \frac{C_f \cdot V}{C_i \cdot V + |Q|/F} \quad [7-2]$$

In which  $C_i$  and  $C_f$  ( $\text{mol L}^{-1}$ ) are the initial and the final concentrations, respectively,  $V$  is the volume of the electrolyte solution (L),  $Q$  (C) is the charge consumed by the system and  $F$  is the Faraday constant.

The lithium adsorption capacity ( $SAC$ ) is defined as the amount of Li removed per mass of Faradaic intercalation material, and was calculated using the **Equation 7-3**:

$$SAC_{Li} = \frac{m_{Li}}{m_e} \quad [7-3]$$

Where  $m_{Li}$  (mg) is the amount of lithium removed and  $m_e$  (g) the mass of the limiting electrode.

The adsorption areal capacity (AAC) is defined as the amount of Li removed per electrode area and was calculated using the **Equation 7-4**.

$$AAC = \frac{m_{Li}}{A} \quad [7-4]$$

where A (cm<sup>2</sup>) is the area occupied by the electrode limited by the gasket.

The energy consumption is defined as the net energy consumed by the systems to remove a mole of Li<sup>+</sup>. The calculation differs depending on configuration of the systems. D) In symmetrical systems, e.g. LiFePO<sub>4</sub> – FePO<sub>4</sub>, the device is separating ions in a continuous mode so that there is no need for half-cycles. Thus, the energy consumption is defined as the energy needed for one half-cycle normalized by the amount of Li<sup>+</sup> recovered in such a half-cycle. On the one hand, energy is stored in an asymmetrical system, i.e. energy is consumed and released during the charge process and discharge process respectively. Therefore, the second half-cycle does not consume energy, but it releases it. Therefore, the net energy consumption is calculated as the difference between the energy applied and released normalized by the amount of Li<sup>+</sup> recovered during the entire cycle.

The selectivity coefficient of lithium ions versus sodium ions (K<sub>Li,Na</sub>) is defined as the change in Li concentration normalized by the total change in concentration of cations (**Equation 7-5**). This coefficient varies between 0 and 1.

$$K_{Li,Na} = \frac{\Delta C_{Li}}{\Delta C_{Li} + \Delta C_{Na}} \quad [7-5]$$

Li recovery rate (R<sub>Li</sub>) is defined as the mass of Li recovered (ΔC<sub>Li</sub>) per area of electrode (A) and unit of time (t), as describe in **Equation 7-6**.

$$R_{Li} = \frac{\Delta C_{Li}}{A * t} \quad [7-6]$$

## 7.3 Results and Discussion

### 7.3.1 The concept of Regenerative Electrochemical Ion Pumping Cell (REIPC)

The Electrochemical Ion Pumping Cell (EIPC) is a device that makes use of ion uptake and release driven by redox reactions occurring in Faradaic materials (typically used in batteries) for driving ion separation in a stream. By doing this, the concentration of targeted ions in a solution is modified. The EIPC concept has been proposed to improve the separation of Li-ions in the lithium capturing process using brines<sup>10,28</sup>. Since there are several metal cations in this type of streams, e.g.  $\text{Li}^+$ ,  $\text{Na}^+$ ,  $\text{K}^+$ , the EIPC needs selectivity towards Li-ions. This selectivity is achieved by using one of two following options: i) two Li-selective Faradaic electrodes and an AEM or ii) two Faradaic electrodes each one having selective towards different cations without membrane. Each option requires a specific setup and operating mode offering intrinsic advantages and disadvantages. **Figure 7-4a** illustrates the necessary steps in an EIPC containing ion-selective membrane to concentrate Li-ions. The intercalation materials used in the two electrodes are selective towards Li-ions being separated by an AEM. During the first step (first half-cycle), Li-ions are captured in compartment A by electrode A as Li-ions are released in compartment B from electrode B. To maintain electro-neutrality, anions move from compartment A to compartment B. As a result, the concentration of Li-ions in the streams exiting compartment A and compartment B is diluted and concentrated, respectively. In the second step (second half-cycle), the opposite processes occur; concentration of Li-ions increases in compartment A while it decreases in compartment B. **Figure 7-4b** shows the steps for an EIPC containing two intercalation materials, each of which is selective towards a different cation. In this case, two streams (one concentrated and one diluted) are not continuously obtained as in the previous operating

mode. In the first step (first half-cycle), Li-ions are released from electrode B while another cation (e.g. Na-ions) is captured by electrode A resulting in one single stream with higher concentration of Li-ion and lower concentration of Na-ions. In the second step (second half-cycle), Li-ions are captured by electrode B while Na-ions are released from electrode A resulting in a stream with lower concentration of Li-ion and higher concentration of Na-ions.

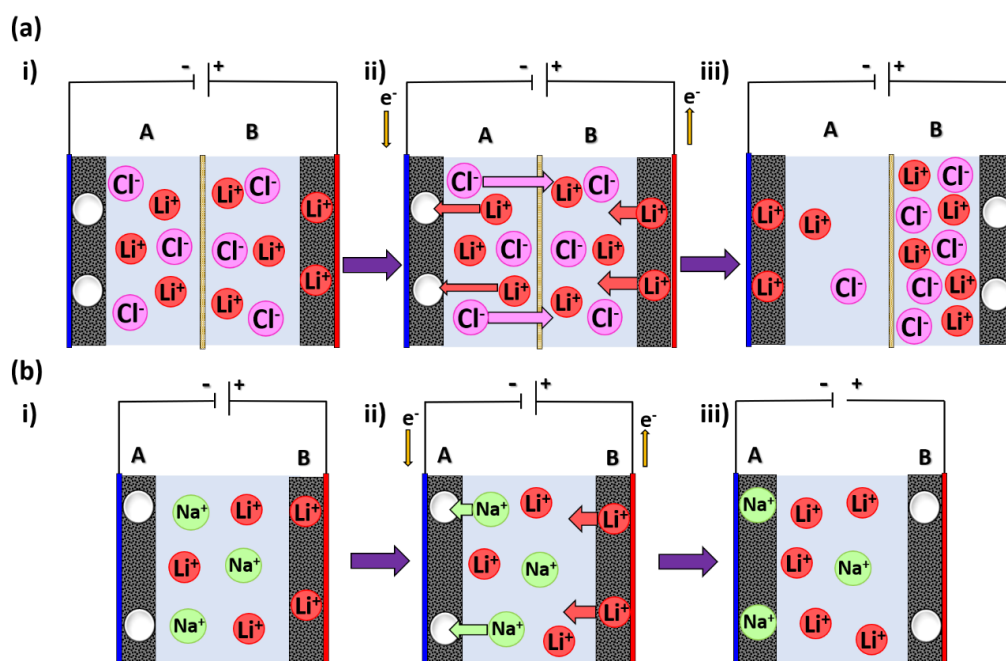


**Figure 7 - 4. Illustration of two operating modes for the EIPC for the first half-cycle resulting in the concentration of Li-ions. (a). EIPC with ion-selective exchange membrane (b) Membrane free EIPC.**

In both configurations of the EIPC above-explained, ion-capturing Faradaic materials are fixed onto the current collectors, which are sealed inside the cell. Degradation of these materials and/or occurrence of parasitic reactions leading to charge unbalancing between positive and negative electrode materials, e.g. oxygen reduction reaction, are responsible for reaching end-of-life and for the need for recycling of the entire system. In contrast to conventional cell configurations, the REIPC concept proposes that an electrochemical cell is pre-assembled. Cavities are intentionally created next to the current collectors,

which are then filled with semi-solid electrodes (**Figure 7-5**). Once semi-solid electrodes are injected, the electrochemical cell is sealed and operated normally until it reaches its end-of-life. The flowable nature of semi-solid electrodes (**Chapter 3, Figure 3-1.**) allows for direct and easy replacing of spent electrodes at the end-of-their-life by fresh electrodes through a dejecting-reinjecting process (**Figure 7-5**). In this fashion, spent electrodes are directly recovered, and the entire cell is reused. It should be noted that flowable semi-solid electrodes remain static during operation of the REIPC. Only the stream of Li brine flows through a compartment that is located between the two electrodes. Confinement of semi-solid electrodes is proposed through the use of microporous separators and gaskets, avoiding by size exclusion that particles of the electrode are dragged into the flowing solution. It should be also noted that previous reports related to the use of semi-solid electrodes for ion separation requires continuous flow of slurry <sup>29</sup>. That configuration does not offer as many techno-economically advantages as REIPC, mainly due to degradation of the devices (erosion by the flowing suspended particles) and high energy consumption (pumping of viscous and dense fluids).

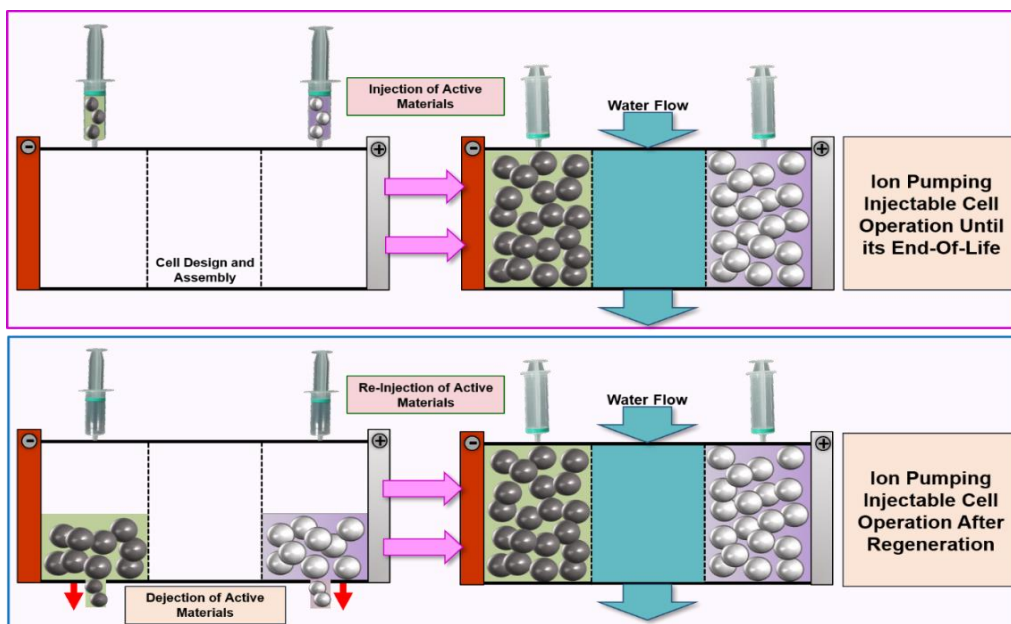


**Figure 7 - 5. Process of substitution (injection and dejection) of the semi-solid electrodes into a pre-assembled cell for their use in ion pumping applications.**

Pictures of the actual device shows (**Figure 7-6a**) the different elements of the cell, (**Figure 7-6b**) the injection of semi-solid electrodes in the cell, and (**Figure 7-6d**) the final assembled systems including peristaltic pumps. Simplified schemes of the system are shown in **Figure 7-2** and **Figure 7-3**.

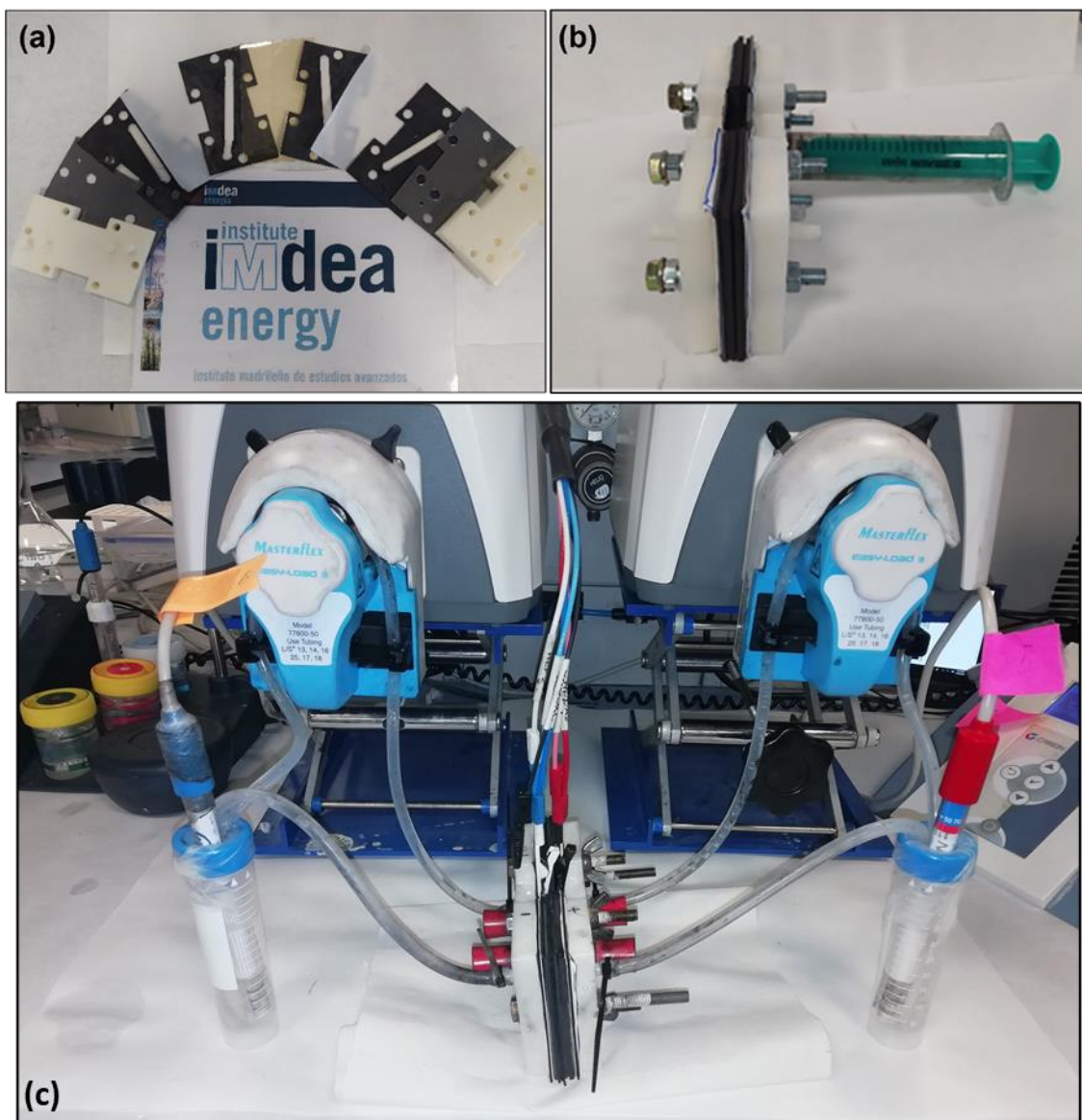


**Figure 7 - 6.** Pictures of (a) the different components of the Regenerative Electrochemical Ion Pumping Cell (3D Printed ABS Endplate, Graphite Current Collector, Viton Gasket, Microporous Separator C350, Anion Exchange Membrane (AEM), (b) regeneration process by dejection / injection of semi-solid electrode from / into the assembled REIP cell, (c) operating REIP system.

### 7.3.2 Membrane-Containing Regenerative Electrochemical Ion Pumping Cell (MC-REIPC)

A MC-REIPC was assembled using an anion-selective membrane and two Li-selective Faradaic materials (LiFePO<sub>4</sub> (LFP) and FePO<sub>4</sub> (FP)) in the form of flowable semi-solid electrodes. First, one LFP semi-solid electrode was injected and oxidized inside the cell to obtain the de-intercalated material (FP) (**Figure 7-2** path A). Prior to use, since both electrodes (positive and negative) are in the same oxidation state, (reduced form in our case) it is necessary to oxidize the positive one. In the case of symmetrical LFP configuration, one electrode of LFP is oxidized to FP. The electrode oxidation methodology was performed as follows: once the electrode was injected, an electrolyte flow was passed through the rest of the cell and a current density of 5 mA·cm<sup>-2</sup> was applied for 4 hours. By proceeding in this way, the electrode suffered the oxidation process while hydrogen evolution reaction takes place in the opposite side. Since the hydrogen reaction ( $4\text{H}_2\text{O} + 4\text{e}^- \rightarrow 2\text{H}_2 + 4\text{OH}^-$ ) leads to an increase in the pH value, a great amount of volume (50 mL) of electrolyte was used to avoid any limitation. This “activation” step might be skipped if active materials are injected in its oxidized and reduced forms

Then, the second flowable semi-solid electrode (LFP) was injected in the opposite side of the cell (**Figure 7-2** path B). Once electrodes were injected and “activated”, the electrolyte solution was pumped from two solution tanks using a peristaltic pump passing through the cell by independent paths (**Figure 7-2** path CF and path DE). The proof-of-concept was performed using a batch configuration (also known as recirculation mode) in which the electrolyte was returning to the feed solution containers after completing the flow circuit.

Our hypothesis here is that the use of the MC-REIPC equipped with semi-solid electrodes enables an easy regeneration of the system through substitution of spent Faradaic materials. Thus, several subsequent regenerations that consisted of dejection and reinjection of semi-solid electrodes were performed in an REIPC cell using LFP-FP semi-solid electrodes to demonstrate this major advantage (**Figure 7-7**).

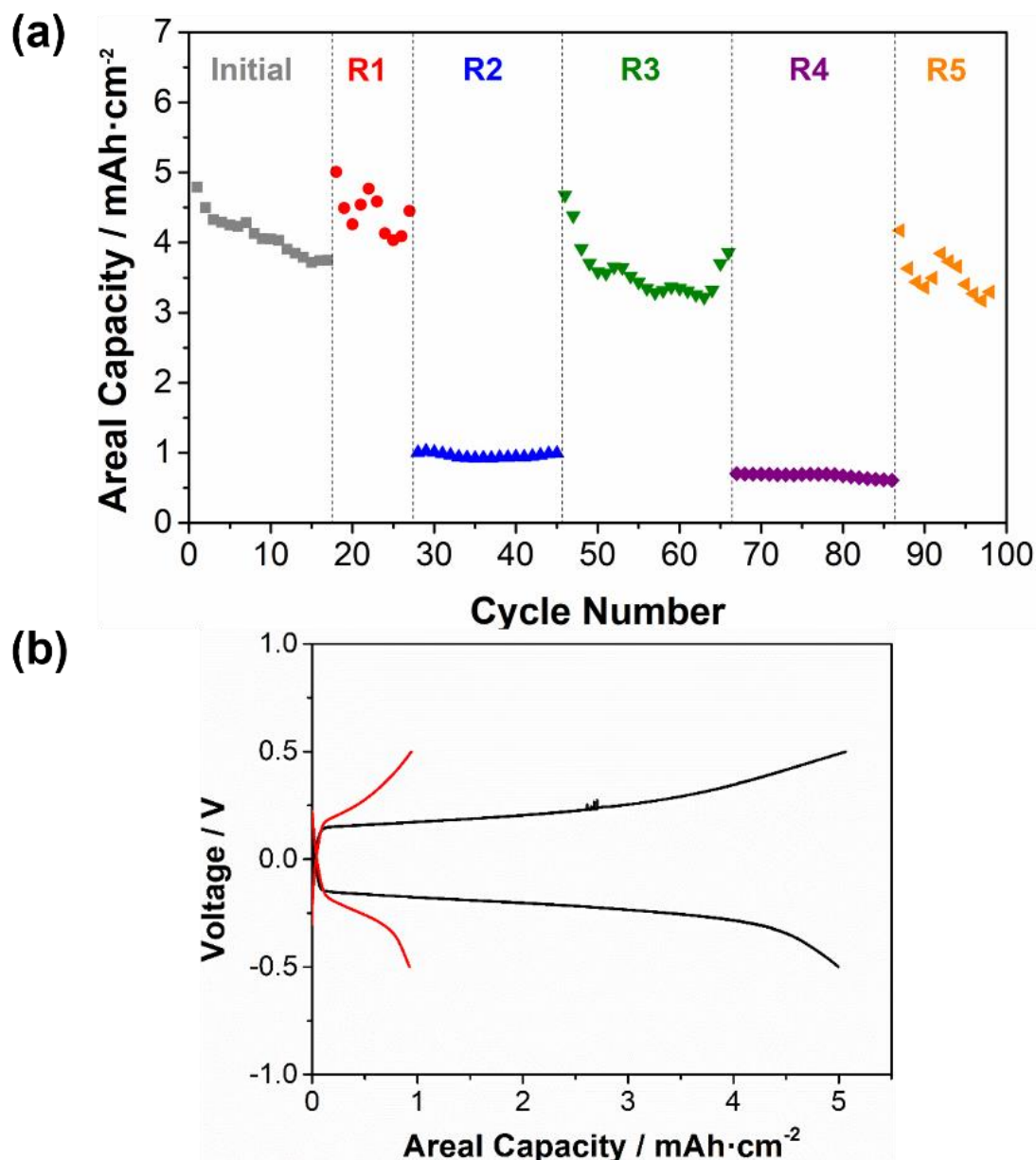


*Figure 7 - 7. Performance of the REIPC LFP-FP cell. (a) after several injections and reinjections with activated carbon and LFP. (b) Comparison between capacitive (Activated Carbon-Activated Carbon, red line) and Faradaic (LFP-FP, black line) REIPC Cells.*

**Figure 7-7a** shows the results of an experiment designed to visualize the effective replacement of semi-solid electrode:

**R1)** LFP semi-solid electrode was replaced by a fresh one. An increase of *ca.* 30 % in charge storage capacity was observed which means that the battery almost fully recovered the initial capacity after the replacement of electrode.

**R2)** LFP semi-solid electrode was replaced by activated carbon semi-solid electrode leading to an enormous capacity drop, which also shows the limited contribution of the activated carbon to the charge storage in comparison with LFP (**Figure 7-7b**).

**R3)** Both semi-solid electrodes were again replaced by fresh LFP and FP semi-solid electrodes. Charge storage capacity increased to the initial values (3-4 mAh cm<sup>2</sup>).

**R4)** LFP semi-solid electrode was again replaced by activated carbon semi-solid electrode leading again to a substantial decrease of the capacity.

**R5)** In the last regeneration, fresh LFP semi-solid electrode was injected recovering value of capacity in the order of 3-4 mAh cm<sup>-2</sup>.

**Figure 7-7b** displays the voltage profiles of the cell initially assembled and after the replacement of one LFP semi-solid electrode by activated carbon semi-solid electrode. Prolonged measurements of REIPC (without regeneration processes) showed excellent cycle stability at 3 mAh cm<sup>-2</sup> delivering capacity fading of 0.0048 % per cycle and 0.0016 % per hour, with an exceptional coulombic efficiency >99 % over at least 50 cycles and 150 h (**Figure 7-8**).

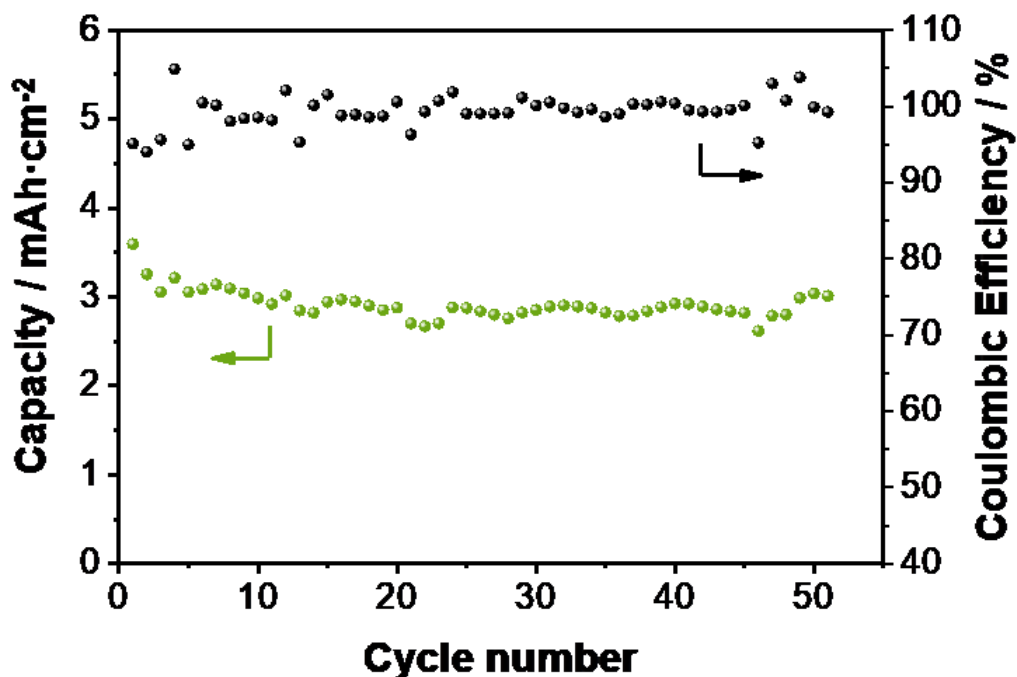


*Figure 7 - 8. Cycling experiment probing the stability of the system. Note that noisy coulombic efficiency is attributed to the temperature fluctuations during this experiment. Temperature affects ionic conductivity. At lower temperature, the cycle process may be finished before it is complete due to the overpotential induced by the higher ionic resistance. The following cycle, the cell starts partially charged, so that it consumes less charge during charging process, while it releases more charge during discharge process due to the accumulated charge in the previous cycle.*

Importantly, results displayed in **Figure 7-7** confirmed that the easy recycling process of the active materials for our REIPC system enables direct reuse of the cell after reaching end-of-life of the electrodes.

### **7.3.2.1 Techno-Economic Analysis**

Since all the expensive components of the cell such as ion-selective membranes and current collectors are reused, the concept of REIPC contributes significantly to cost reductions. Regarding the cost analysis of the REIPC, it is important to make a distinction between the Capital Cost (CAPEX) and Operational Cost (OPEX). The Installation Cost, considered as part of the capital cost without depreciation, was calculated based on the prices of the materials involved in the process such as active material (including carbon,

lithium iron phosphate and electrolyte needed for making the injectable electrodes) and inactive material (current collectors, separators, and the selective anion exchange membrane). The methodology for this calculation of the installation cost (materials of the device) is the same that **Chapter 4**. As illustrated in **Figure 7-9**, much of the inactive materials is contributing to the total installation cost, mainly due to the high cost of the exchange membrane (200 US\$ m<sup>-2</sup>). Here it must be stressed the importance of the REIPC configuration based on injectable/dejectable electrodes that enables the easy replacement of the cheap active materials while reusing the costly inactive material. Thus, it is estimated that 95 % of the total cost of the REIPC system could be saved by using injectable electrodes.

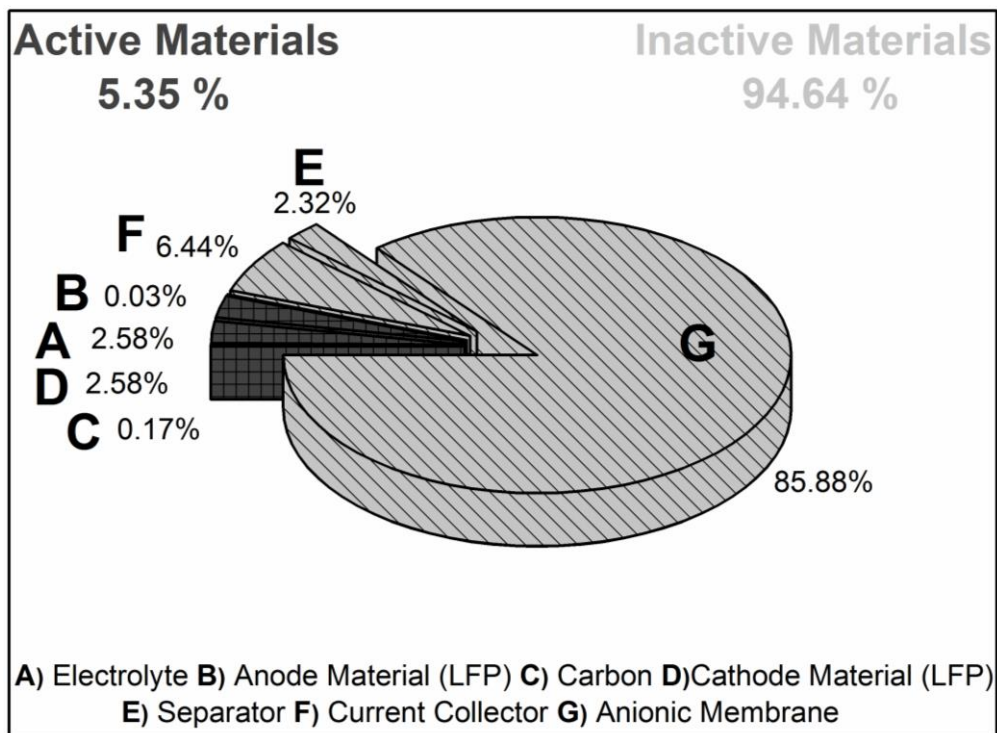


**Figure 7 - 9.** Contribution of different elements to cost of a REIPC: inactive and active materials.

The areal capacity defines how much active material is used per area of systems. Thus, for a given area (given cost of inactive materials), the higher the areal capacity, the higher the installation cost (US\$ m<sup>-2</sup>) as shown in **Figure 7-10**.

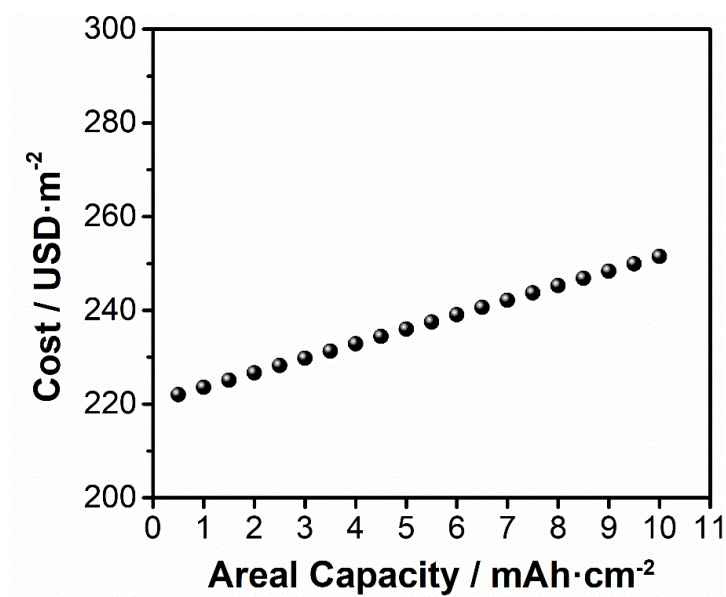


*Figure 7 - 10. Installation costs per area of device as a function of the areal capacity.*

Although inactive materials cost does not change, the higher the capacity (mAh cm<sup>-2</sup>), the higher the price of the installation. With the aim of evaluating properly the production of lithium recovered, the price of the system was defined in terms of USD per kilogram of lithium recovered/released. Assuming that a high ion-separation efficiency ( $\eta=100\%$ ), the installation cost per kg Li is calculated as a function of the areal capacity from **Figure 7-10** through the Faraday constant and molecular mass (**Figure 7-11**).

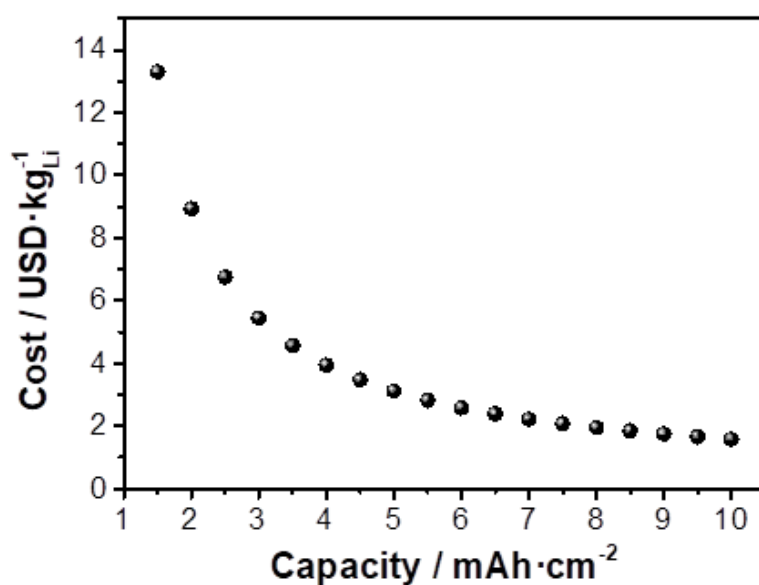


*Figure 7 - 11. Installation cost per Kg of Li as a function of the areal capacity.*

The influence of the current density was also analyzed. Results shown in **Figure 7-12** indicate that the cost of the materials for the REIPC system will depend on the current density applied. The analysis of the price of the materials required to build this kind of installation shows that the selection of the operational mode is highly relevant because it is directly related to the capital costs of the system.

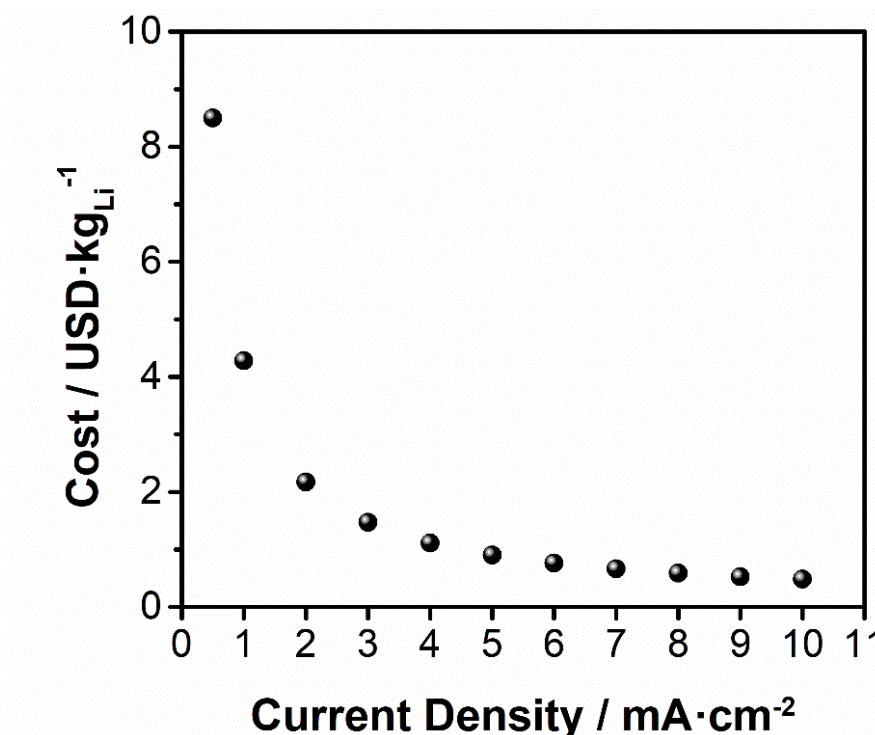


*Figure 7 - 12. Operational costs of the system per kg of lithium recovered as a function of the current density.*

Thus, a proper selection of the current rate can result in a cost reduction of more than 70 % when increasing the current density from 0.5 mA cm<sup>-2</sup> to 2 mA cm<sup>-2</sup>. Moreover, the economic analysis indicated that the prices seem to reach a plateau for the highest current densities (8-10 mA cm<sup>-2</sup>).

**7.3.2.2 Regenerative Electrochemical Ion Pumping Cell having an ion-selective membrane: Asymmetric configuration.  $\text{LiFePO}_4$  -  $\text{LiMn}_2\text{O}_4$**

According to our estimations a cost reduction of 95 % is achieved in each regeneration by implementing the REIPC concept. It should be noted that the symmetrical configuration using LFP-FP semi-solid electrodes do not effectively store energy while capturing ions since both electrodes have the same standard redox potentials leading to a nominal cell voltage of 0 V. To store energy, two ion-intercalation materials having different redox potentials should be employed. Indeed, energy storage in ion separation systems represent an additional benefit of this technology. In this new configuration, the lithium ions were released from the LFP electrodes (3.4 V vs.  $\text{Li}/\text{Li}^+$ ) in the charging step and intercalated in the Manganese Oxide ( $\text{Mn}_2\text{O}_4$ , MO) electrode (previously oxidized from Lithium Manganese Oxide,  $\text{LiMn}_2\text{O}_4$ , LMO) that presents a higher electrode potential (3.9 V vs.  $\text{Li}/\text{Li}^+$ ). In the discharging process, the opposite reactions take place, and the stored charge is being released.

The cell voltage profile displayed in **Figure 7-13a** which has a battery-like voltage profile confirms the behavior of the asymmetrical electrochemical ion pumping system, delivering an average discharge cell voltage of 0.28 V. Its stability is shown in **Figure 7-13b**. For more than one hundred cycles, the cell delivers a capacity fading of  $4 \cdot 10^{-5}$  % per cycle and  $3 \cdot 10^{-5}$  % per hour (**Figure 7-13b**) and reversible specific energy of 8.9 Wh  $\text{kg}_{\text{LMO}}$ . Thus, this successful measurement demonstrates the versatility of the REIPC technology for using different electrode materials and configurations (symmetric vs asymmetric cell). This allows for the recovery of part of the energy stored in the electrodes, thus reducing the energy consumption. This configuration might represent a low energy consumption alternative to the symmetric configuration (LFP-FP) cell.

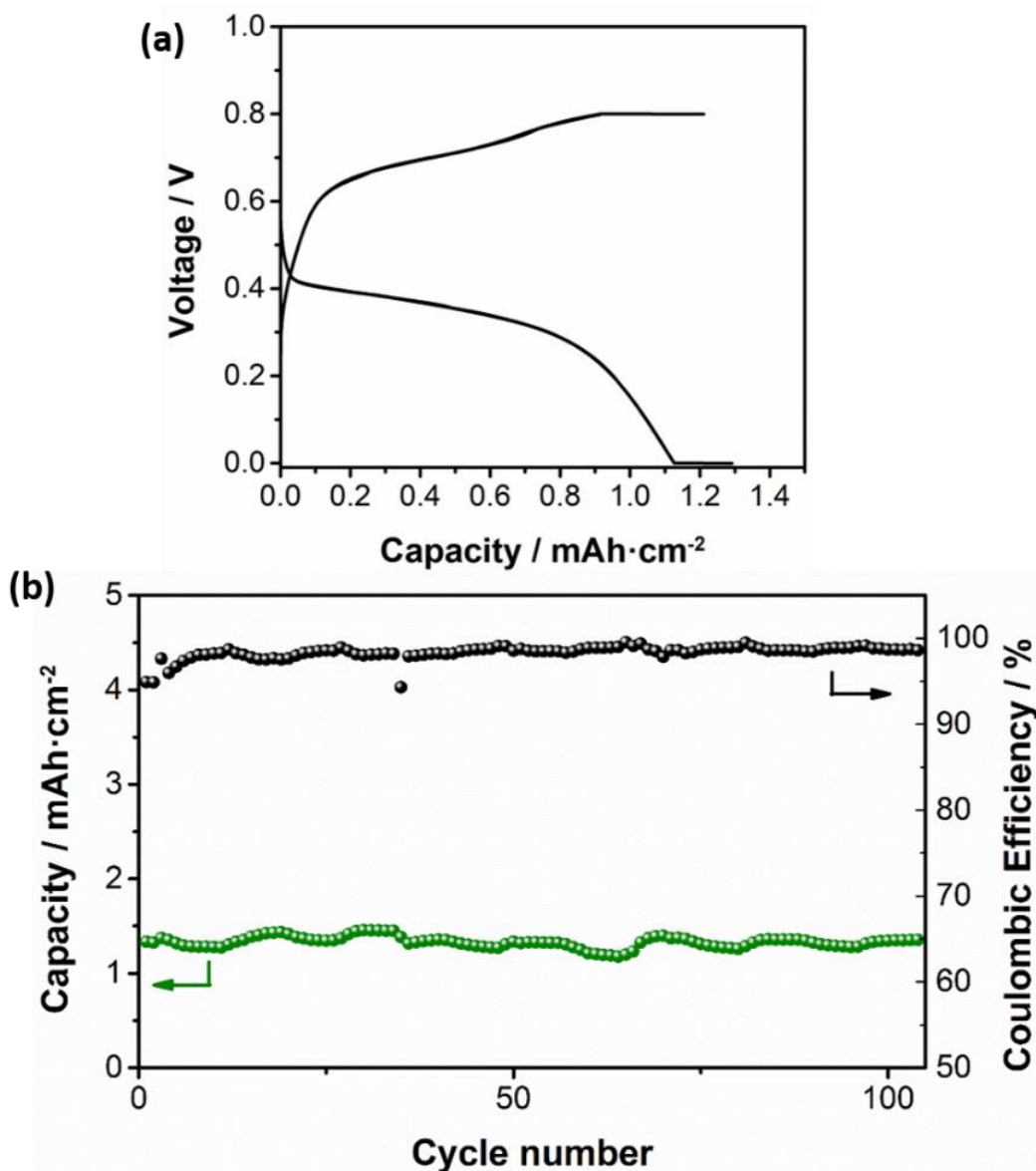
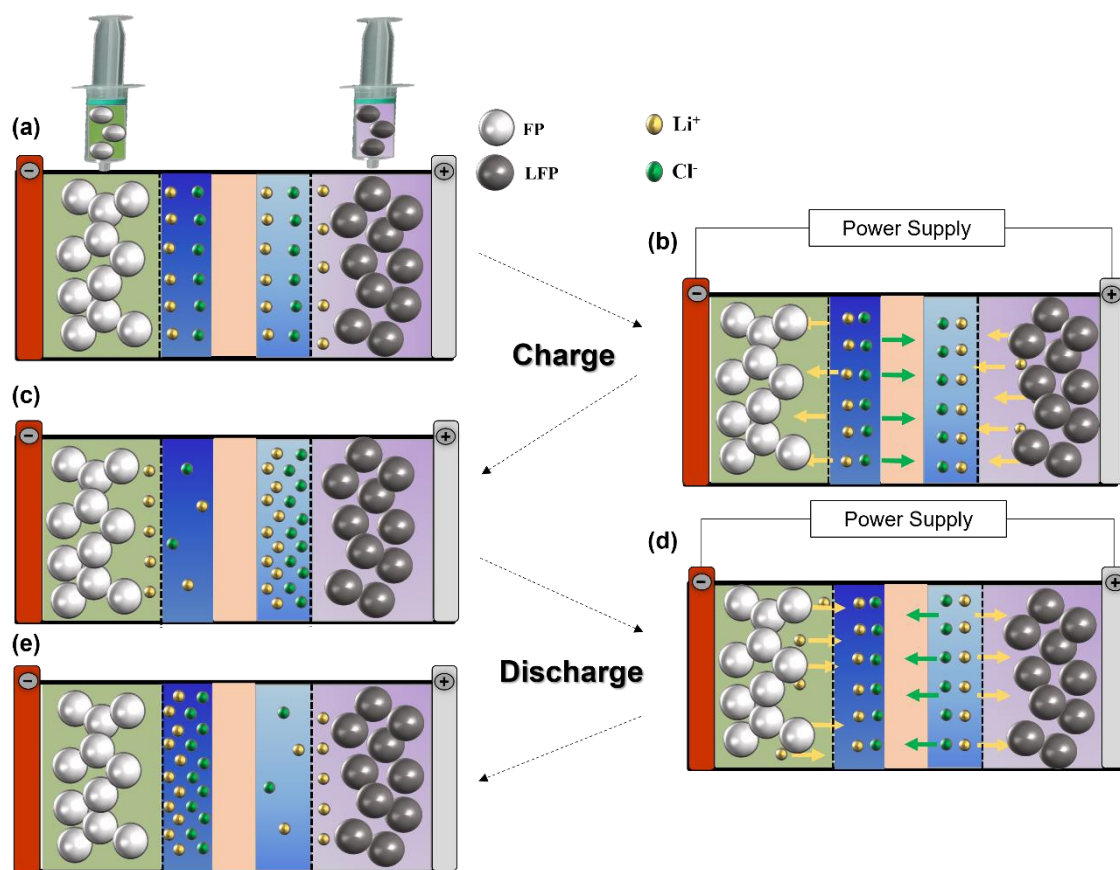


Figure 7 - 13. (a) Voltage profile and (b) cyclability test of the REIPC using an asymmetrical system (LFP-MO).

### 7.3.2.3 Ion separation capacity membrane-containing configuration (LFP-FP).

After the evaluation of charge storage capacity and regeneration capacities, the ion separation capability of the proposed concept was investigated. The selectivity of LFP towards Li-ions has been exploited for selective lithium extraction in the presence of other metal cations<sup>3,8,12,30</sup>. The ion separation process consists of two steps as discussed generally in **Figure 7-4a**, and specifically for the case of LFP-FP in **Figure 7-14**.



**Figure 7 - 14.** Graphical explanation for the movement of the ions ( $\text{Cl}^-$  and  $\text{Li}^+$ ) in the REIPC system with symmetrical LFP configuration. (a-c) Charging process, concentration of the solution in the positive side and dilution in the negative. (c-e) Discharging process, dilution of the solution in the negative side and concentration in the positive.

In the first step (half-cycle) LFP semi-solid electrode is oxidized releasing Li-ions and FP is simultaneously reduced capturing Li-ions while  $\text{Cl}^-$  ions move from FP compartment to LFP side through the AEM. In this way, two streams containing different Li-ion concentrations are obtained: Li-ion concentrated stream in the LFP compartment and Li-ion diluted stream in the FP side. In this configuration, the REIPC can be operated continuously resulting in two streams. Qualitatively, variations in the concentration of LiCl were monitored using the ionic conductivity of the two streams. **Figure 7-15a** shows the evolution of the cell voltage together with the ionic conductivity of the streams in both compartments during one full cycle. During the first half cycle, the conductivity in compartment A increased while conductivity in compartment B decreased. In the second

half cycle, the opposite trend was observed. This clearly shows the ability of the device to concentrate LiCl in one compartment and dilute it in the same magnitude in the other compartment. **Figure 7-15b** shows that this behavior was stable over longer periods of time.

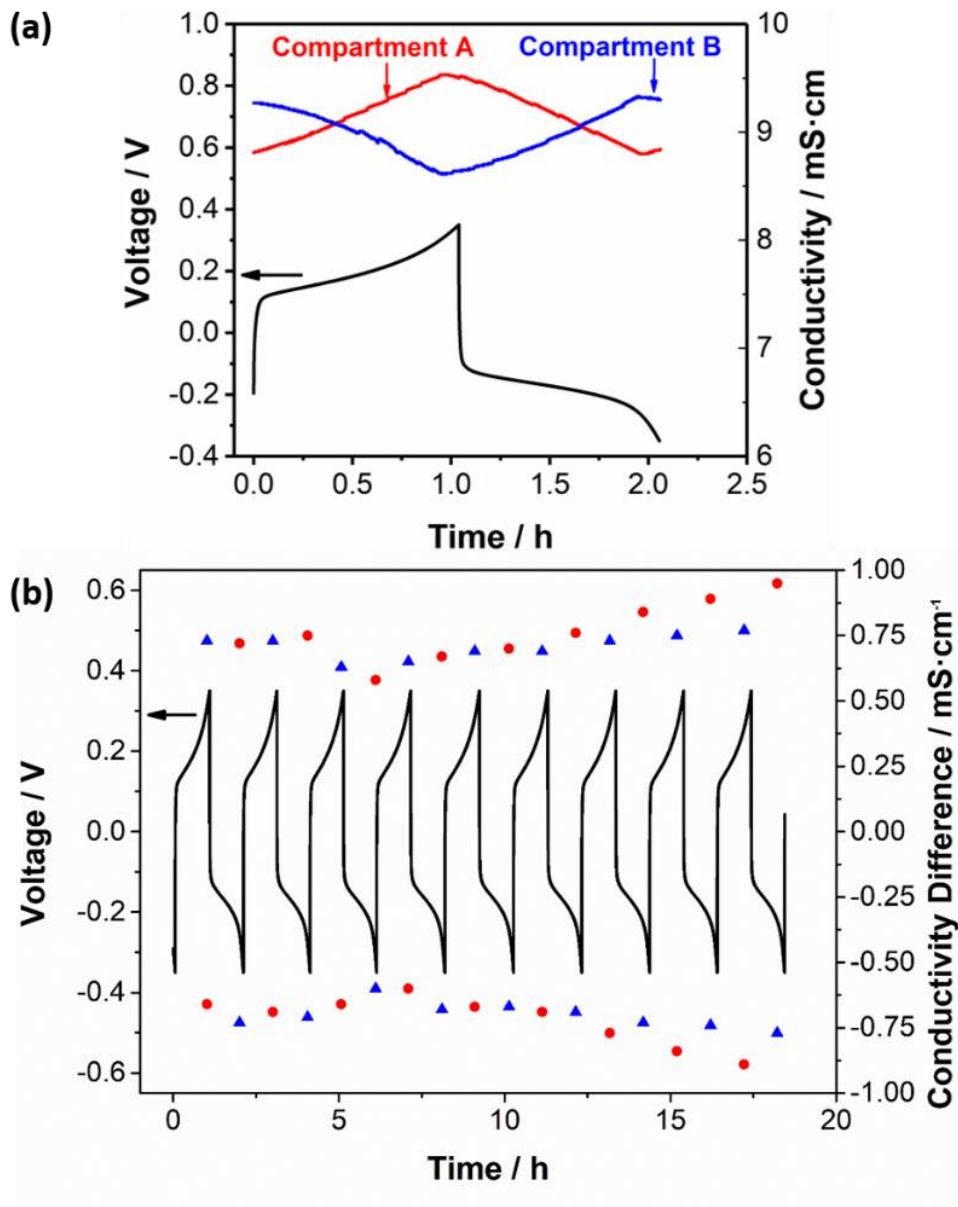


**Figure 7 - 15.** Evolution of cell voltage and ionic conductivity of the symmetrical REIPC during (a) one full cycle and (b) ca. 20 h. Blue triangles and red circles represent the conductivity difference values in each one of the compartments at the end of each one of the charging/discharging cycles.

A quantitative assessment of the ion removal capacity of our cell was conducted using Ion Chromatography (IC). With this aim, samples were taken in each tank before and after one half-cycle, and subsequently analyzed by IC.

A lithium adsorption capacity ( $SAC_{Li}$ ) of  $27 \text{ mg}_{Li} \text{ g}_{LFP}^{-1}$  and an areal adsorption capacity (AAC) of  $9 \text{ g}_{Li} \cdot \text{m}^{-2}$  were obtained along with a  $\eta$  of 80 % when operating the system at  $3 \text{ mA cm}^{-2}$ . Note that these figures of merits are defined in the Experimental Section. Whereas these values are comparable to the values reported in literature <sup>10</sup>, the use of semi-solid electrode allows not only an easy regeneration of the system but also the achievement of unprecedented values of areal capacities ( $3\text{-}4 \text{ mAh cm}^{-2}$ ), which is a key parameter for practical implementation of this electrochemical technology reducing installation cost per kg of Li (**Figure 7-11**) and minimizing ion mixing between half-cycles.

Furthermore, Li permeability tests were conducted for the anion selective membrane used in this work. A permeability experiment consisting of filling up a two cell bodies with LiCl 0.2 M and MilliQ water respectively, separated by a Fumasep FAA-3-30 AEM was performed. **Figure 7-16** shows the evolution of the ion concentrations analyzed by ion chromatography after 24 h and 48 h. The results indicate that not only chlorides but also lithium ions were able to cross the membrane from the LiCl compartment to the H<sub>2</sub>O chamber. The static-mode experiment performed in the two cell bodies has a selectivity of 97.4 % (calculated as the ratio between the initial Li<sup>+</sup> in the LiCl solution and the lithium found in the water side). There are reasons to believe that in the real flow-type REIPC system, the pressure applied by the streams to the membrane produced an increment of the amount of lithium going through the membrane.

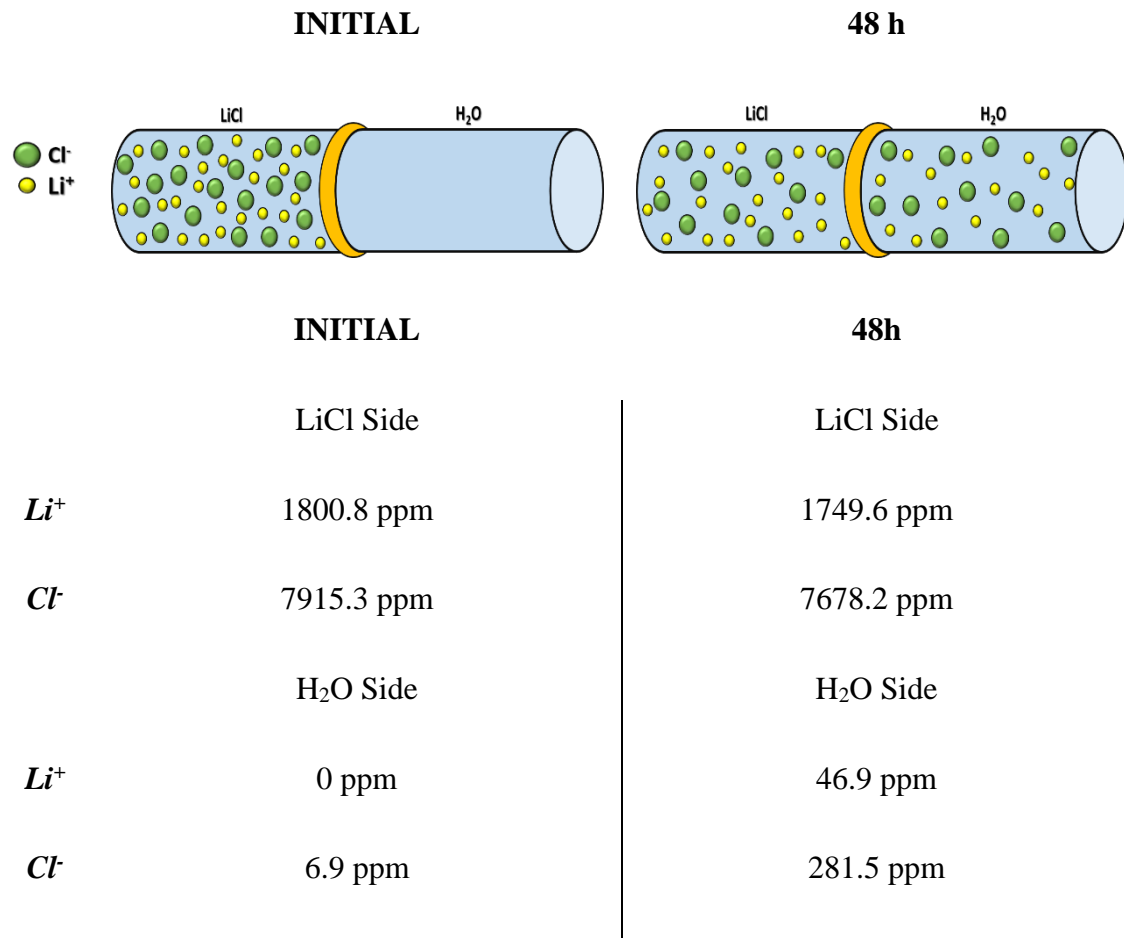


Figure 7 - 16. Experiment showing the permeability of the anion exchange membrane to the lithium ions.

Thus, anion selective membrane are not only expensive elements (**Techno-economic analysis**), but their ability to confine small cations such as Li-ion is not sufficiently high. This motivated us to extend the concept of REIPC to a membrane-free configuration: The Membrane-Free Regenerative Ion Pumping Cell (MF-REIPC).

### 7.3.3 Membrane-Free Regenerative Electrochemical Ion Pumping Cell (MF-REIPC)

Selectivity towards specific ions is also achieved by using two ion-selective Faradaic materials without the need for ion-selective membranes, as discussed above<sup>23,31</sup>. As a result, this section is dedicated to developing a Membrane-Free Regenerative Electrochemical Ion Pumping Cell (MF-REIPC). This concept consists of an

asymmetrical cell configuration that introduces a significant cost reduction by removing the ion-selective membrane while having the ability of separating specific ions and storing energy (**Figure 7-4b**). **Figure 7-3** describes the different elements in the cell design for this concept. The Faradaic materials selected for this system were Nickel Hexacyanoferrate ( $\text{KNiFe}(\text{CN})_6$ , NiHCF) and Lithium Manganese Oxide ( $\text{LiMn}_2\text{O}_4$ , LMO). By using a Na-selective material, i.e. NiHCF,<sup>26</sup> and a Li-selective material, i.e. LMO, the ion-selective membrane is no longer needed to provide ion selectivity to the system.<sup>5</sup>

In this concept, the process started by injecting a LMO semi-solid electrode in the pre-assembled cell followed by oxidation of LMO ( $\text{LiMn}_2\text{O}_4$ ) to MO ( $\text{Mn}_2\text{O}_4$ ). Once the oxidation process was completed, a NiHCF semi-solid electrode was injected in the opposite compartment. Ion removal in the MF-REIPC consists of two steps: in the charge step, Li-ions are released by the LMO electrode in the stream leading to an increase in Li-ion concentration in the stream. Simultaneously, the NiHCF electrode captures Na-ions resulting in a decrease in Na-ion concentration in the stream. (**Figure 7-17** (a-c)). In the discharge step, the opposite process takes place i.e., Na-ions are released, and Li-ions are captured (**Figure 7-17** (d-e)) leading to a Na-ion concentrated and Li-ion diluted stream.

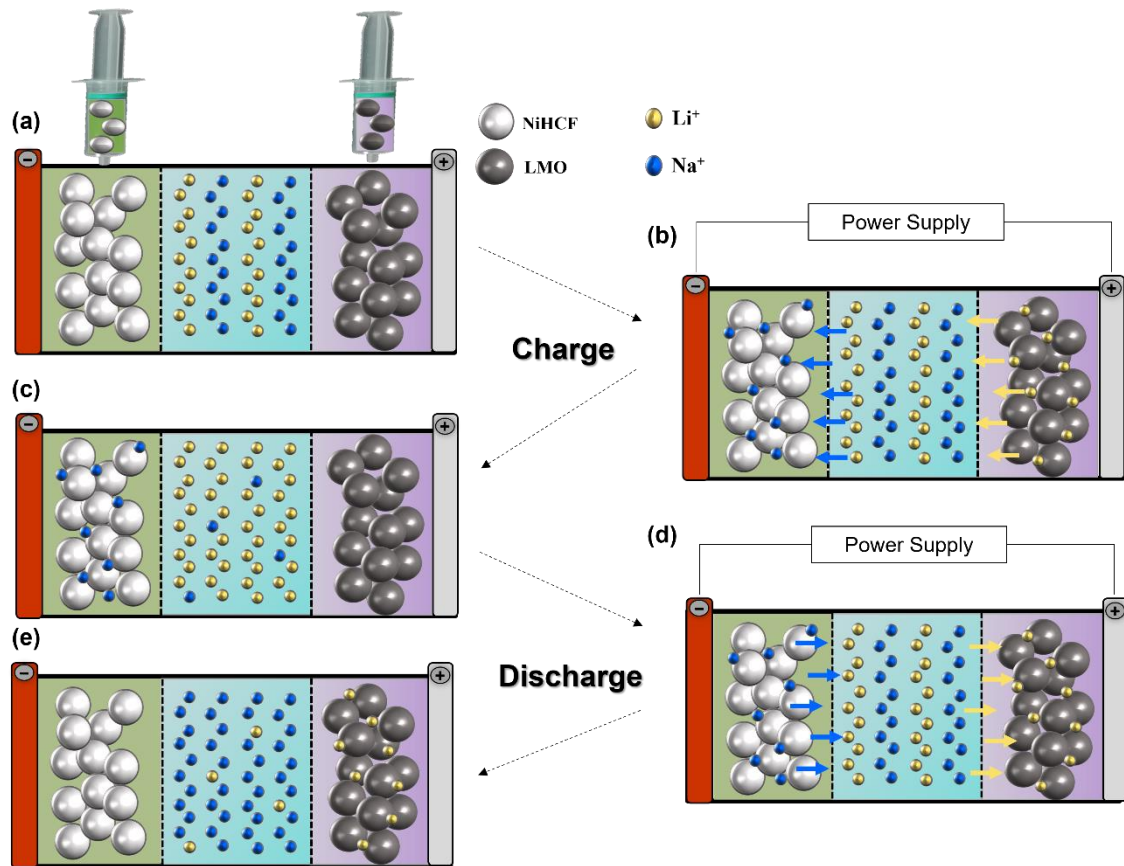


*Figure 7 - 17. Graphical explanation for the movement of the ions ( $\text{Na}^+$  and  $\text{Li}^+$ ) in the MF-REIPC system with LMO-NiHCF electrodes. (a-c) Charging process, concentration of lithium ions in the solution. (c-e) Discharging process, concentration of sodium ions in the solution.*

Since the distinct feature of the proposed technology is the possibility of regenerating the system by substituting the spent semi-solid electrodes once the battery reaches its end-of-life, regeneration capability of the system was first evaluated. A MF-REIPC using MO-NiHCF active materials was studied for ion separation in a stream containing 0.1M NaCl and 0.1M LiCl in one single solution tank (**Figure 7-3**). It should be noted that a batch configuration with only one tank, instead of using two tanks, was set up. The initially assembled MF-REIPC system having NiHCF and MO semi-solid electrodes was run for 28 cycles (**Figure 7-18**).

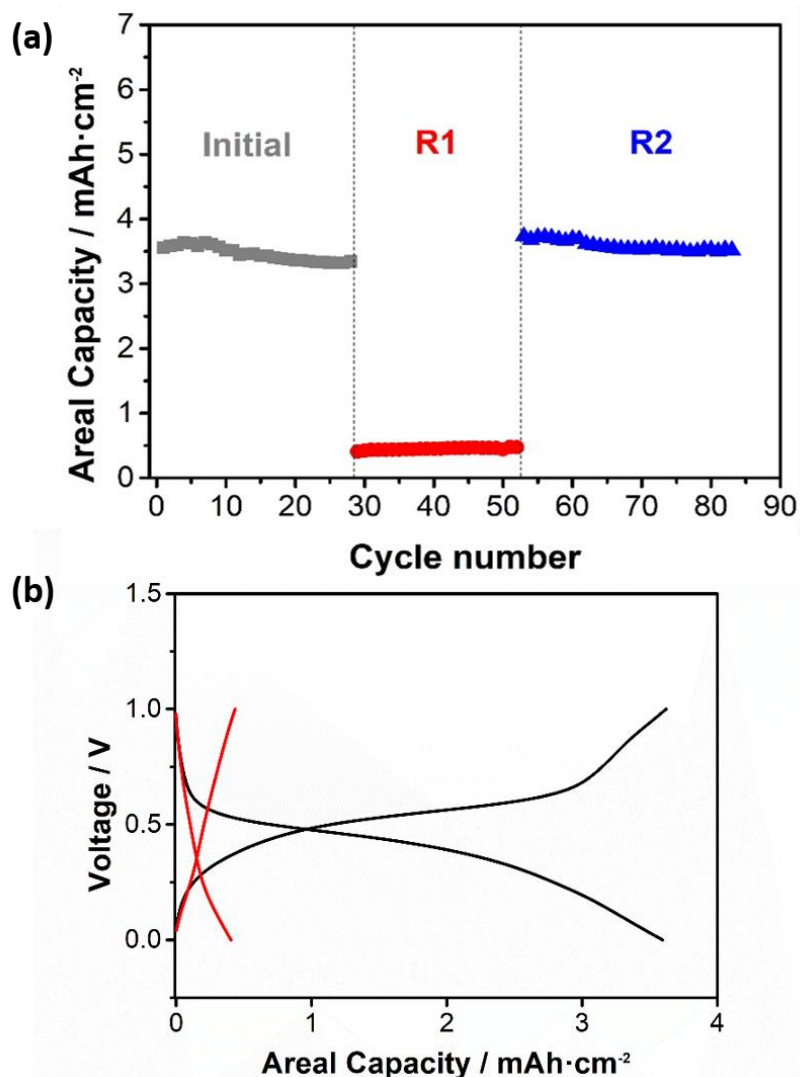


*Figure 7 - 18. (a) Evolution of the areal capacity of the MFREIPC MO-NiHCF cell with the number of cycles. Regenerations were conducted in cycle 28 (carbon-based semi-solid electrode replaced NiHCF semi-solid electrode) and cycle 52 (fresh semi-solid electrodes). (b) Comparison between capacitive (Activated Carbon-Activated Carbon, red line) and Faradaic (MO-NiHCF, black line) MF-REIPC.*

Then, the following regenerations were carried out (**Figure 7-18a**): R1) LMO was replaced by a semi-solid electrode that only contained carbon additive (without Faradaic material). Consequently, the Faradaic behavior initially observed (cycle 1-28) turned into a capacitive behavior (cycle 29-52) leading to a sloppier voltage profile (**Figure 7-18b**). As the specific charge capacity of carbon additive is lower than that of LMO, the charge capacity of the system decreased by 75 % when carbon semi-solid electrode replaced

LMO semi-solid electrode. R2) The carbon-based semi-solid electrode was replaced by a fresh LMO semi-solid electrode while the NiHCF semi-solid electrode was substituted by a fresh one having the same formulation. **Figure 7-18a** shows that the system was able to recover the initial charge capacity value ( $3.5 \text{ mAh cm}^{-2}$ ). These results confirm the versatility and robustness of the proposed concept as demonstrated by the possibility of replacing electrode active materials for the same assembled cell. **Figure 7-19** shows the long-term stability of the system delivering a capacity fading of  $0.13 \text{ \% cycle}^{-1}$  and  $0.22 \text{ \% h}^{-1}$  over 160 cycles and 1,000 h. It should be noted that we did not observe any coloring or suspended particles after 6 weeks operating in batch (using the same solution), which confirmed that Celgard separator effectively confines solid materials. Future studies will explore whether the use of Celgard is more effective to confine solid materials in the electrodes compared to the conventional use of binder.

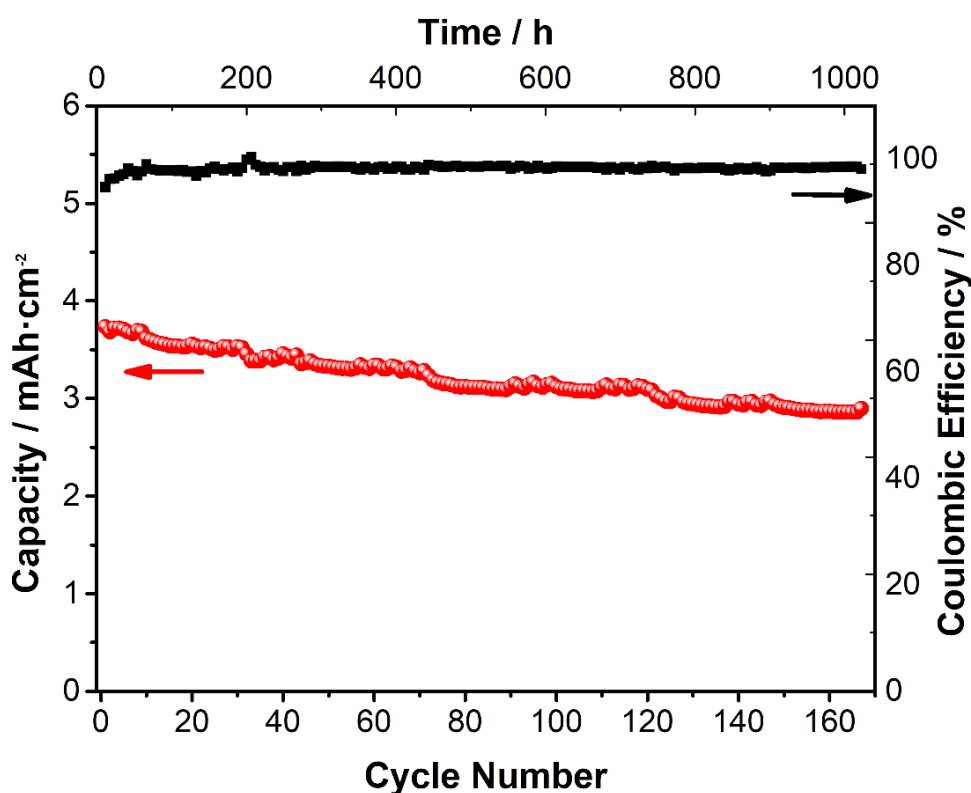


*Figure 7 - 19. Cycling experiment probing the stability of the MF-REIPC system after being regenerated.*

The ion separation capacities of the system were first evaluated using a solution containing only Na-ions and Li-ions, and then a solution emulating the brine of Atacama Lake (43 mM Li<sup>+</sup>, 757 mM Na<sup>+</sup>, 102 mM K<sup>+</sup> and 66 mM Mg<sup>2+</sup>)<sup>11</sup>. **Figure 7-21a** shows the evolution of the efficiency as a function of the ratio between concentration of Na-ions and Li-ions. As expected, increasing ratio of Na:Li led to an increase in the efficiency for Na-ions and a decreased for Li-ions. Thus, the efficiency for brine samples in which the concentration of Li-ions is lower than that of Na-ions will be determined by the selectivity of the Li-capturing material (LMO in our case). The Li selectivity (normalized values varying between 0 and 1, **Equation 7-5**) followed similar trend as the Li efficiency, since it decreased with increasing concentration of Na-ions at 0.5 mA cm<sup>-2</sup> (**Figure 7-20**). Since the Li selectivity is determined by the intrinsic selectivity of the intercalations materials, the results indicate that there is room for improvement by optimizing electrode parameters and operating conditions.

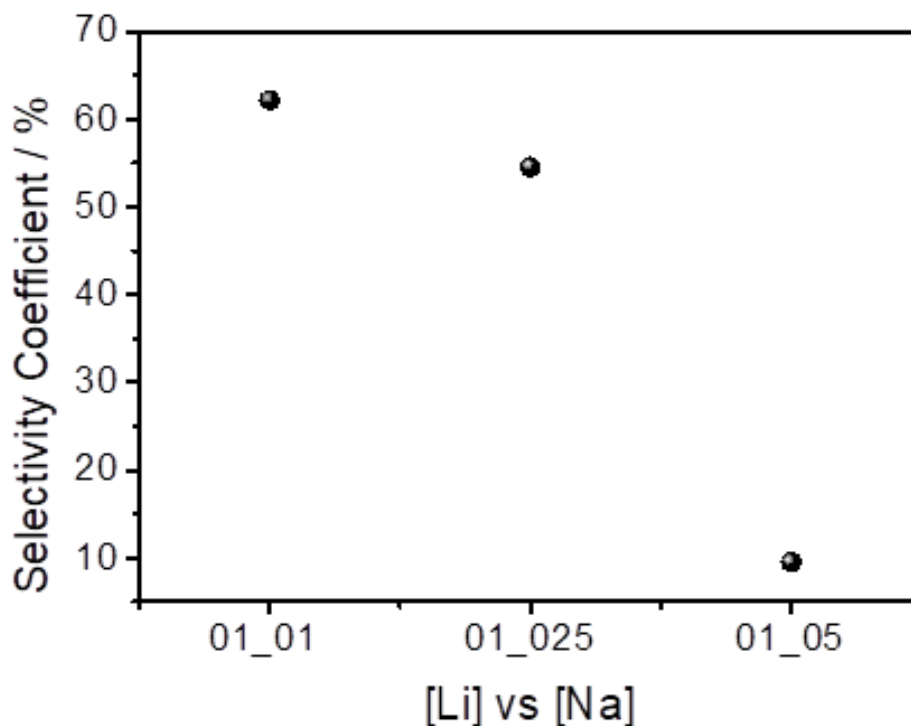


*Figure 7 - 20. Experimental selectivity coefficient obtained as a function the concentration ratio of Li-Na.*

The influence of the current density, which is critical for the cost, was also evaluated (**Figure 7-21b**). The efficiency for both Li-ions and Na-ions increased with increasing current density (from 0.25 to 0.5 mA·cm<sup>-2</sup>), which is attributed to the kinetics of ion-intercalation processes. As current density increases, the kinetically hindered processes are unfavored making LMO and NiHCF more selective towards Li-ions and Na-ions, respectively. Unfortunately, another 2-fold increase in current density from 0.5 to 1 mA cm<sup>-2</sup> did not result in further improvement in efficiency likely due to the occurrence of parasitic reaction such as oxygen evolution reaction. When working with solutions containing 0.1 M LiCl and 0.25 M NaCl at 0.5 mA cm<sup>-2</sup>, the efficiencies were above 90 % (94 % and 92 % for Na-ions and Li-ions, respectively), achieving an areal capacity of 2.6 mAh cm<sup>-2</sup>, SAC<sub>Li</sub> of 16.2 mgLi·g<sub>NiHCF</sub><sup>-1</sup>, AAC of 4 g<sub>Li</sub> m<sup>-2</sup> and energy consumption of 15.6 Wh·mol<sup>-1</sup>.

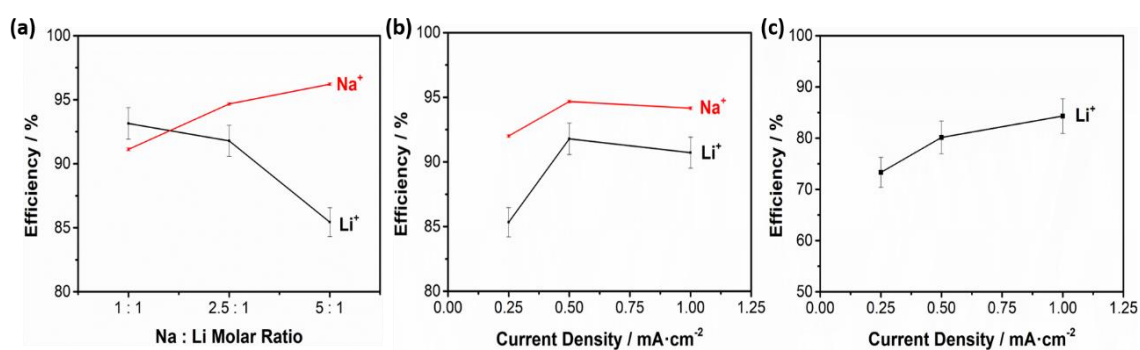


**Figure 7 - 21. Efficiencies obtained with MF-REIPC (a) Effect of the Na:Li ions ratio in the solution for a current density of 0.5 mA·cm<sup>-2</sup> (b) Effect of the current density for a Na:Li ratio of 2.5:1 (c) Impact of the presence of additional cations on Lithium capturing using Atacama brine solution. Charge steps were carried out at constant current density to avoid potential interfering of oxygen evolution reaction, so that the influence of the current density on the efficiency process was evaluated for the discharge step.**

Comparison of the performances achieved in this work with other values reported in the literature (**Table 7-1**) suggests that the proposed REIP systems is competitive with other non-regenerative systems.

**Table 7 - 1. Comparison between this work and others state-of-the-art systems.**

<i>Ref</i>	<i>Electrodes</i>	<i>Efficiency/ %</i>	<i>mg Li / g<sub>electrode</sub></i>	<i>Selectivity Li-Na / %</i>	<i>Energy consumption Wh/mol</i>	<i>Stability</i>
<sup>32</sup>	LMO - MO	89	22 <sub>LMO</sub>	0.996	18	5 cycles
<sup>5</sup>	NiHCF - MO	71	25.4	0.982	3.6	83 % (100 cycles)
<sup>27</sup>	NiHCF - MO	75	39	13 <sub>(first cycle)</sub>	11.3	-
<sup>27</sup>	NiHCF - LFP	-	-	0.112	8.7	9 cycles
<i>Our Work</i>	NiHCF - MO	90	16.2 <sub>NiHCF</sub>	0.62	15.6	80 % 160 cycles (> 1000 h)

In the literature, many different selectivity terms are used. In our view, the normalized selectivity is the most useful one since it goes from 0 to 1 so that it is easier to interpret whether the selectivity is good, compared to absolute values. These values are provided directly in ref [27] while we need to recalculate the normalized selectivity for ref [32] and ref [5] from their absolute values for all values to be comparable. The calculation of normalized selectivity for ref and ref were conducted as follows

$$K_{normalized} = \frac{X}{X+1} \cdot 100; \text{ where } X = K_{\frac{Li}{Na}, reported} = \frac{C_{Li}}{C_{Na}}; \quad [7-6]$$

Finally, a solution emulating the brine of Atacama was studied (**Figure 7-21c**). Only Li-ions were analyzed in this case due to the difficulties of measuring reliably both Li-ions and Na-ions with such a large difference in concentration by flame photometry. The efficiency increased continuously in the range of 0.25 – 1 mA cm<sup>-2</sup>, while the ion separation capacity showed a maximum at 0.5 mA cm<sup>-2</sup>. At this current density, an efficiency of 81 %, an ion separation capacity of 0.17 g<sub>Li</sub> m<sup>-2</sup> h<sup>-1</sup>, specific capacity of 61.6

$\text{mAh} \cdot \text{g}_{\text{NiHCF}}^{-1}$  and consumption of  $27 \text{ Wh L}^{-1}$  was obtained. Note that our calculations include both steps (charge and discharge). Again, whereas these values are comparable to the values reported in literature,<sup>33</sup> the use of semi-solid electrode allows not only easy regeneration of the systems but also achievement of unprecedented values of areal capacities ( $3\text{-}4 \text{ mAh cm}^{-2}$ ), which is a key parameter for practical implementation of this electrochemical technology reducing installation cost per kg of Li (**Figure 7-11**). For continuous Li recovery, an electro-valve controlled by a programmable logic controller (PLC) could swap the streams to achieve continuous Li extraction. A small mixing of Li-rich and Li-poor solutions occurs upon the swapping decreasing the overall efficiency would be expected, as experienced before by Palagonia et al.<sup>27</sup> Moreover, we could anticipate that our high areal capacity electrodes, able to retain a larger amount of Li per area, will help minimizing these losses. It should be noted that, in our experiment, solution exchange was not carried out between half-cycles. As a consequence, the energy consumption ( $27 \text{ Wh mol}_{\text{Li}}^{-1}$ ) was higher than some of the previous values reported in the literature. Small volumes were used to reliably measure the concentration changes, so that the concentration during Li uptake step continuously decreases. This detrimental decrease in Li concentration during Li uptake step does not occur when large volumes of brine are employed as in report in the literature. This highlights the difficulties when benchmarking performance, especially in terms of energy consumption. In any case, our prototype delivered competitive electrochemical and ion separation performances, whereas providing the ability of easy regeneration when reaching end-of-life.

## 7.4 Conclusions

A new ion capturing and separation device, REIPC, which consists of an electrochemical cell equipped with injectable battery type electrodes able to selectively capture and concentrate the ions of interest, was successfully demonstrated. The injectable electrodes enable improving the recyclability and direct reuse of the cell without affecting negatively to the electrochemical performance. In this sense, the techno-economic analysis indicated that a 95 % of the fabrication cost is reduced in each regeneration of the semi-solid electrodes by recycling the passive components of the cell. Additionally, the operation of the REIPC is based on electrochemical phenomena, which does not require the use of extraction agents to elute the ion captured from the active material. These aspects represent a tremendous impact of this technology from the sustainability point of view with respect to the precipitation and ion exchange resins processes.

Furthermore, the REIPC system developed in this research is exceptionally versatile since it can be equipped with different kinds of electrodes allowing to capture different types of ions. Thus, our results showed that modifications in cell voltage and ion selectivity can be achieved by simply replacing the active materials. Indeed, we showed that the combination of different electrode materials and/or membranes opens the possibility to store energy while capturing ions (asymmetrical configuration). Furthermore, a membrane-free configuration using two electrodes selective to different ions (as it is the case of the MF-REIPC system equipped with LMO and NiHFC electrodes) accomplished a remarkable performance, not only when tested in dual electrolytes, but also when running experiments using solutions that emulate typical Atacama's brine compositions. Hence, this versatility opens the path for exploring the application of this technology to other solutions to be treated in different fields such as battery recycling, water treatment plants, waste valorization, agricultural business, or pharmaceutical applications.

## 7.5 References

1. Lithium 2019 recharge - Canaccord Genuity. <http://cdn.ceo.ca.s3-us-west-2.amazonaws.com/1eo071m-Canaccord - Neo Lithium Corp Researn Note - Sept 2019.pdf>.
2. Energy Agency, I. Global EV Outlook 2020 Entering the decade of electric drive?
3. Calvo, E. J. Electrochemical methods for sustainable recovery of lithium from natural brines and battery recycling. *Curr. Opin. Electrochem.* **15**, 102–108 (2019).
4. Meshram, P., Pandey, B. D. & Mankhand, T. R. Extraction of lithium from primary and secondary sources by pre-treatment, leaching and separation: A comprehensive review. *Hydrometallurgy* **150**, 192–208 (2014).
5. Trócoli, R., Erinmwingbovo, C. & La Mantia, F. Optimized Lithium Recovery from Brines by using an Electrochemical Ion-Pumping Process Based on  $\lambda$ -MnO<sub>2</sub> and Nickel Hexacyanoferrate. *ChemElectroChem* **4**, 143–149 (2017).
6. Kong, L. & Liu, X. Emerging electrochemical processes for materials recovery from wastewater: Mechanisms and prospects. *Front. Environ. Sci. Eng.* **14**, 1–14 (2020).
7. Lithium Extraction Technologies. Tech 2018S11. Nexant, November 2018. <https://www.nexanteca.com/file/137456/download?token=NeqrmzjJ>.
8. Pasta, M., Battistel, A. & La Mantia, F. Batteries for lithium recovery from brines. *Energy Environ. Sci.* **5**, 9487–9491 (2012).
9. Suss, M. E. & Presser, V. Water Desalination with Energy Storage Electrode Materials. *Joule* **17**, 10–15 (2018).
10. Battistel, A., Palagonia, M. S., Brogioli, D., La Mantia, F. & Trócoli, R. Electrochemical Methods for Lithium Recovery: A Comprehensive and Critical Review. *Advanced Materials* vol. 32 1905440 (2020).
11. Trócoli, R., Battistel, A. & La Mantia, F. Nickel Hexacyanoferrate as Suitable Alternative to Ag for Electrochemical Lithium Recovery. *ChemSusChem* **8**, 2514–2519 (2015).
12. Kim, J. S. *et al.* An Electrochemical Cell for Selective Lithium Capture from

- Seawater. *Environ. Sci. Technol.* **49**, 9415–9422 (2015).
13. Yoon, H., Lee, J., Kim, S. & Yoon, J. Review of concepts and applications of electrochemical ion separation (EIONS) process. *Separation and Purification Technology* vol. 215 190–207 (2019).
  14. Huang, Z. H., Yang, Z., Kang, F. & Inagaki, M. Carbon electrodes for capacitive deionization. *J. Mater. Chem. A* **5**, 470–496 (2017).
  15. Liu, Y. *et al.* Review on carbon-based composite materials for capacitive deionization. *RSC Adv.* **5**, 15205–15225 (2015).
  16. Wouters, J. J., Tejedor-Tejedor, M. I., Lado, J. J., Perez-Roa, R. & Anderson, M. A. Influence of metal oxide coatings on the microstructural and electrochemical properties of different carbon materials. *J. Electrochem. Soc.* **163**, A2733–A2744 (2016).
  17. Wouters, J. J., Isabel Tejedor-Tejedor, M., Lado, J. J., Perez-Roa, R. & Anderson, M. A. Influence of metal oxide coatings, carbon materials and potentials on ion removal in capacitive deionization. *J. Electrochem. Soc.* **165**, E148–E161 (2018).
  18. Santos, C. *et al.* Interconnected metal oxide CNT fibre hybrid networks for current collector-free asymmetric capacitive deionization. *J. Mater. Chem. A* **6**, 10898–10908 (2018).
  19. Lado, J. J., Zornitta, R. L., Vázquez Rodríguez, I., Malverdi Barcelos, K. & Ruotolo, L. A. M. Sugarcane Biowaste-Derived Biochars as Capacitive Deionization Electrodes for Brackish Water Desalination and Water-Softening Applications. *ACS Sustain. Chem. Eng.* **7**, 18992–19004 (2019).
  20. Yu, F. *et al.* Faradaic reactions in capacitive deionization for desalination and ion separation. *J. Mater. Chem. A* **7**, 15999–16027 (2019).
  21. Lee, J., Kim, S. & Yoon, J. Rocking Chair Desalination Battery Based on Prussian Blue Electrodes. *ACS Omega* **2**, 1653–1659 (2017).
  22. Singh, K., Porada, S., de Gier, H. D., Biesheuvel, P. M. & de Smet, L. C. P. M. Timeline on the application of intercalation materials in Capacitive Deionization. *Desalination* **455**, 115–134 (2019).
  23. Singh, K. *et al.* Nickel hexacyanoferrate electrodes for high mono/divalent ion-

- selectivity in capacitive deionization. *Desalination* **481**, 114346 (2020).
24. Duduta, M. *et al.* Semi-solid lithium rechargeable flow battery. *Adv. Energy Mater.* **1**, 511–516 (2011).
  25. Ventosa, E. *et al.* Non-aqueous semi-solid flow battery based on Na-ion chemistry. P2-type  $\text{Na}_x\text{Ni}_{0.22}\text{Co}_{0.11}\text{Mn}_{0.66}\text{O}_2\text{-NaTi}_2(\text{PO}_4)_3$ . *Chem. Commun.* **51**, 7298–7301 (2015).
  26. Porada, S., Shrivastava, A., Bukowska, P., Biesheuvel, P. M. & Smith, K. C. Nickel Hexacyanoferrate Electrodes for Continuous Cation Intercalation Desalination of Brackish Water. *Electrochim. Acta* **255**, 369–378 (2017).
  27. Palagonia, M. S., Brogioli, D. & La Mantia, F. Lithium recovery from diluted brine by means of electrochemical ion exchange in a flow-through-electrodes cell. *Desalination* **475**, (2020).
  28. Guolang, Z. *et al.* Progress in electrochemical lithium ion pumping for lithium recovery. *Artic. J. Energy Chem.* **59**, 431–445 (2020).
  29. Hatzell, K. B., Boota, M. & Gogotsi, Y. Materials for suspension (semi-solid) electrodes for energy and water technologies. *Chem. Soc. Rev.* **44**, 8664–8687 (2015).
  30. Trócoli, R., Battistel, A. & Mantia, F. La. Selectivity of a lithium-recovery process based on  $\text{LiFePO}_4$ . *Chem. - A Eur. J.* **20**, 9888–9891 (2014).
  31. Shi, W. *et al.* Berlin green-based battery deionization-highly selective potassium recovery in seawater. *Electrochim. Acta* **310**, 104–112 (2019).
  32. Zhao, M. Y. *et al.* Study on lithium extraction from brines based on  $\text{LiMn}_2\text{O}_4/\text{Li}_{1-x}\text{Mn}_2\text{O}_4$  by electrochemical method. *Electrochim. Acta* **252**, 350–361 (2017).
  33. Zhao, X., Yang, H., Wang, Y. & Sha, Z. Review on the electrochemical extraction of lithium from seawater/brine. *J. Electroanal. Chem.* **850**, 113389 (2019).





## **Chapter 8. Final Conclusions and Future Challenges**

## 8.1 Final conclusions

This doctoral thesis has contributed to the development of innovative battery technologies based on the use of semi-solid electrodes. The work performed during this doctoral thesis has demonstrated the feasibility for these technologies for their use in different applications. Despite each chapter of the work has its specific conclusions, this last chapter pretend to unify them paying attention to the most relevant findings and results.

1. The unique features of semi-solid electrodes enable easy tuneability of their properties by changing their formulation. On the one hand, their thixotropic nature that are assessed by standard rheometer allows them to be easily injected into a preassembled cell. On the other hand, ionic and electrical properties that are evaluated by a proposed method that combines Electrochemical Impedance Spectroscopy and a membrane-free cell are also tunable as the formulation of the semi-solid electrode determine both properties.

2. An innovative battery concept based on semi-solid electrodes is proposed: The Injectable Battery. This concept lies on the use of flowable semi-solid electrode to facilitate recycling of the system. By replacing the semi-solid electrode by dejection / reinjection, reuse of the inactive materials of the cell is enabled. This feasibility of this concept is demonstrated, not only for aqueous battery system ( $\text{Zn} - \text{LiFePO}_4$ ,  $\text{LiTi}_2(\text{PO}_4)_3 - \text{LiFePO}_4$ ,  $\text{LiFePO}_4 - \text{FePO}_4$ , or  $\text{Zn} - \text{MnO}_2$ ), but also for non-aqueous battery chemistry ( $\text{Li} - \text{LiFePO}_4$ ). On the economical perspective, the cost of the consecutive regenerated batteries is reduced due to the reuse of inactive materials. In addition, since the fabrication of a new injectable cell is not necessary, manufacturing cost will decrease too.

3. The injectable battery is especially interesting for cheap battery chemistries for which the contribution of inactive materials to the cost is large, e.g.  $\text{Zn} - \text{MnO}_2$ . For this battery chemistry, i.e. the  $\text{Zn} - \text{MnO}_2$  battery, the spontaneous Hydrogen Evolution

Reaction at the zinc electrode changes the pH of the mild-acidic electrolyte (2 M ZnSO<sub>4</sub> and 0.1 M MnSO<sub>4</sub>). An innovative hybrid system flow (negative) / semi-solid (positive) mitigates the pH variations. In addition, a float charging protocol compensates the pH increase of the electrolyte due to the oxidation of Mn<sup>2+</sup> additive dissolved in the electrolyte and the Oxygen Evolution Reaction occurring at the positive electrode at 1.8 V.

**4.** While the concept of mechanically rechargeable battery has been long desired, the practical values of energy density has prevented its success. The use of semi-solid electrodes improves the practical volumetric capacity of the mechanically-rechargeable Zn – Air battery (*ca.* 1500 Wh L<sup>-1</sup>). In addition, the use of 2,6 dihydroxyanthraquinone as “molecular wiring” inside the zinc semi-solid electrodes allows an enhancement of the flowability of the electrodes as well as increases its specific power, reaching values of 66 mW cm<sup>-2</sup> at 77 mA cm<sup>-2</sup>.

**5.** A new ion capturing, and separation device equipped with injectable semi-solid electrodes is able to selectively capture and concentrate the ions of interest. The versatile design of the cell allows the use of different systems, not only regarding the active materials for the semi-solid electrodes, but also the cell configuration can be modified (membrane-containing or membrane-free system). Changing active materials permits different capturing ions, thanks to the selectivity of each intercalation material to specific ions. On the other hand, each configuration enables different operational modes: when membrane-containing is used, two streams (concentrated/diluted) are obtained at the same time. However, for the membrane-free configuration, only one stream is flowing, being concentrated, or diluted depending on the state-of-charge of the system.

## 8.2 Future challenges

While the proof-of-concept for various technologies based on semi-solid electrodes were explored and successfully demonstrated along this doctoral thesis, several aspects require intensive effort for these concepts to become more competitive. Below, few important aspects to be addressed are listed.

1. Further fundamental understanding of the properties of semi-solid electrodes, extending the number of phenomena (mass transport, double layer charging, electron, and ion transfer, etc) and parameters (diffusion coefficients and electron-transfer coefficients) to be included. To achieve this, the development of analytical techniques will also be required, e.g. electrical conductivity in the presence of active materials.
2. Extending the concept of injectable battery based on semi-solid electrodes to promising battery chemistries, e.g. sodium – ion, lithium – sulfur, or lithium – air.
3. Regarding the concept applied for Zn – Air batteries, different research disciplines like colloidal chemistry, chemical engineering and mechanical engineering are required to boost their performances. Additionally, engineering effort will need to be devoted to the injection / removal system.
4. The Regenerative Electrochemical Ion Pumping Injectable Cell open up a whole range of possibilities for investigating the potential of this technology with different solutions for its application in different fields such as battery recycling, water treatment plants, waste valorization, agricultural business, or pharmaceutical applications. In addition, further fundamental understanding regarding ion transport through semi-solid electrodes is of great interest since the intrinsic properties of this type of electrodes may be very beneficial considering the low concentration of ions.



## **Appendix A. Scientific Contributions**

## **Publications:**

- **D. Perez-Antolin**, R. Trócoli, J. Palma, E. Ventosa. (2020). The injectable battery. A conceptually new strategy in pursue of a sustainable and circular battery model. *Journal of Power Sources*, 480, 228839. DOI: 10.1016/j.jpowsour.2020.228839 (IF:9.127).
- **D. Perez-Antolin**, I. Sáez-Bernal, A. Colina, E. Ventosa. (2022). Float-charging protocol in rechargeable Zn–MnO<sub>2</sub> batteries: unraveling the key role of Mn<sup>2+</sup> additives in preventing spontaneous pH changes. *Electrochemistry Communications*, 107271. DOI: 10.1016/j.elecom.2022.107271 (IF:4.724).
- **D. Perez-Antolin**, C. Irastorza, S. Gonzalez, R. Moreno, E. Garcia-Quismondo, J. Palma, J. Lado, E. Ventosa. (2022). Regenerative electrochemical ion pumping cell based on semi-solid electrodes for sustainable Li recovery. *Desalination*, 553, 115764. DOI: 10.1016/j.desal.2022.115764 (IF:9.501).
- **D. Perez-Antolin**, W. Schuhmann, J. Palma, E. Ventosa (2022). Semi-Flowable Zn Semi-Solid Electrodes as Renewable Energy Carrier for Refillable Zn–Air Batteries. *Journal of Power Sources*, (IF:9.127). Accepted: 14/04/2022.

## **Patents:**

- International Patent Application: E. Ventosa, **D. Pérez**, G. García, J. Palma, “An Alkaline Flow Battery Assembly”. Application Number: PCT/ES2020/070277. Priority date: 06/06/2019.
- International Patent Application: J. Lado, E. Ventosa, **D. Perez-Antolin**, E. García-Quismondo, J. Palma, “Recyclable Electrode”. Application Number: PCT/EP2021/073842. Priority date: 31/08/2020.

## **Conference Contributions:**

- **D. Perez-Antolin**, R. Trócoli, J. Palma, E. Ventosa. “*La Batería Inyectable. Una Nueva Estrategia En La Búsqueda De Un Modelo De Baterías Circular Y Sostenible*”. XXIV Congreso De La Sociedad Iberoamericana De Electroquímica (2020). Póster contribution.
- **D. Perez-Antolin**, J. Palma, E. Ventosa “*Flowable semi-solid electrodes enable a concept for battery sustainability*”. 2<sup>nd</sup> Congress of the Interdivisional Group on Chemistry for Renewable Energy of the Italian Chemical Society – SCI. ENERCHEM. Padova, Italy (2020). Oral contribution.
- **D. Perez-Antolin**, J. Palma, E. Ventosa “*Zinc Semi-Solid Electrodes as New Form of Fuel for Electro-mobility*”. 7<sup>th</sup> Annual Workshop of Young Researchers held in IMDEA Energy Institute (2019). Oral contribution.
- **D. Perez-Antolin**, J. Palma, E. Ventosa “*Prolonging Cycle Life in Aqueous Based Organic Redox Flow Batteries: A Symmetrical Configuration.*” 6<sup>th</sup> Annual Workshop of Young Researchers held in IMDEA Energy Institute (2018). Poster contribution.

## **Co-supervision of Bachelor/Master theses**

- Julio Verdejo. Master’s degree in industrial engineering. “Mejora de la economía circular en baterías Li-ion de vehículos eléctricos.” Presented in 30/04/2020 at Universidad Rey Juan Carlos.
- Cristina Irastorza. Master’s degree in industrial engineering. “Desarrollo de baterías reciclables para aplicaciones medioambientales.” Presented in 23/06/2020 at Universidad Rey Juan Carlos.

## Appendix A. Scientific Contributions

- Laura Sillero Moreno. Master's degree in industrial engineering. "Batería reinyectable Zn-MnO<sub>2</sub> de bajo coste para aplicaciones de almacenamiento de energía." Presented in 27/01/2021 at Universidad Rey Juan Carlos.
- Inés Sáez Bernal. Bachelor's degree in chemistry. "Química de baterías avanzadas: Baterías Inyectables". Presented in 11/03/2021 at Universidad de Burgos.
- Sara González Plaza. Bachelor's degree in chemistry. "Baterías desaladoras sostenibles." Presented in 24/06/2021 at Universidad de Burgos.
- Inés Sáez Bernal, Master's degree in Advanced Chemistry. "Baterías libres de forma basadas en electrodos semi-sólidos." Planned for 07/2022 at Universidad de Burgos.



## **Appendix B. List of Figures and Tables**

## Chapter 1. Introduction

### Figures

<i>Figure 1 - 1. Installed power capacity. Adapted with permission from [1].</i>	2
<i>Figure 1 - 2. Scheme of the charge process of a supercapacitor. Movement of cations (red) and anions (blue).</i>	6
<i>Figure 1 - 3. Time of energy release and power rate for (a) Energy storage applications and (b) Energy storage systems. Adapted with permission from [25].</i>	8
<i>Figure 1 - 4. History of batteries. Timeline illustrating milestones achieved in the field of batteries in the last 200 years.</i>	10
<i>Figure 1 - 5. Illustration of the elements of a Metal - Air battery.</i>	12
<i>Figure 1 - 6. Scheme of an all-Vanadium redox flow battery.</i>	13
<i>Figure 1 - 7. Representation of specific capacity and operating redox potential of various materials for Li-ion batteries, adapted with permission from [45].</i>	15
<i>Figure 1 - 8. Scheme of a semi-solid redox flow battery.</i>	25
<i>Figure 1 - 9. Different configurations of static battery (a) Conventional thin electrodes vs. (b) Thick electrodes. Adapted with permission from [115].</i>	27
<i>Figure 1 - 10. Illustration of the manufacturing process of conventional electrodes. Adapted from [119].</i>	28
<i>Figure 1 - 11. Drawing representing the tortuosity of a porous media.</i>	29

### Tables

<i>Table 1 - 1. Comparison of the key performance indicators of state-of-art static batteries and flow batteries: Lithium-ion vs. All-vanadium.</i>	17
<i>Table 1 - 2. Key performance indicators for post-lithium-ion battery technologies. Adapted with permission from [48].</i>	22
<i>Table 1 - 3. Value of “<math>\gamma</math>” for different materials [123].</i>	30

## Chapter 3. Semi-solid electrodes for static batteries

### Figures

<i>Figure 3 - 1. Rheological behavior of a semi-solid electrode containing LFP, carbon additive, and electrolyte.</i>	52
<i>Figure 3 - 2. Cell design for (a) Conventional battery and (b) Separator-free configuration for determination of electrical properties of semi-solid electrodes.</i>	53

Figure 3 - 3. Design scheme of the separator-free symmetrical cell containing (A) Expanded graphite, (B) Gasket and (C) ABS 3D printed case. _____	54
Figure 3 - 4. (a) Typical Nyquist plot for mixed ionic and electronic conductors, and (b) Equivalent electrical circuit. _____	56
Figure 3 - 5. Nyquist plot for relevant mixed ionic and electronic transport. _____	58
Figure 3 - 6. Nyquist plots of the EIS measurements for semi-solid electrodes containing 10, 30, 50, 70 and 90 mg <sub>carbon</sub> mL <sup>-1</sup> . _____	59
Figure 3 - 7. Electrical and ionic conductivities for semi-solid electrodes containing 10, 30, 50, 70 and 90 mg <sub>carbon</sub> mL <sup>-1</sup> . _____	60
Figure 3 - 8. Nyquist plot of EIS measurements of semi-solid electrodes containing: (a) 53 mg mL <sup>-1</sup> carbon additive and 0 mg mL <sup>-1</sup> stabilizer. (b) 53 mg mL <sup>-1</sup> carbon additive and 1.5 mg mL <sup>-1</sup> stabilizer. (c) 53 mg mL <sup>-1</sup> carbon additive and 2.3 mg mL <sup>-1</sup> stabilizer. (d) 42 mg mL <sup>-1</sup> carbon additive and 0 mg mL <sup>-1</sup> stabilizer. (e) 42 mg mL <sup>-1</sup> carbon additive and 1.5 mg mL <sup>-1</sup> stabilizer. (f) 42 mg mL <sup>-1</sup> carbon additive and 2.3 mg mL <sup>-1</sup> stabilizer. _____	61
Figure 3 - 9. (a) Ionic, electrical, and total conductivity of a semi-solid electrode for 42 mg mL <sup>-1</sup> carbon additive. (b) Ionic, electrical, and total conductivity of a semi-solid electrode for 53 mg mL <sup>-1</sup> carbon additive. _____	62

## Chapter 4. The injectable battery. A conceptually new strategy in pursue of a sustainable and circular battery model

### Figures

Figure 4 - 1. General illustration of life cycle of battery materials and components, adapted with permission from [18]. Red and blue arrows show the path for the mechanical-hydrometallurgical recycling route of active and inactive materials, respectively. Green arrows represent the new path for the recycling of the injectable battery. Recycling of inactive materials is not required for injectable battery since battery cells are reused, while shredding and mechanical separation are not necessary since spent electrodes are extracted without damaging the cells. _____	71
Figure 4 - 2. Photograph of the semi-solid electrode after dismantling the cell. _____	73
Figure 4 - 3. Illustration of the injectable battery concept. (a) The preassembled cell is fabricated, which is (b) filled with semi-solid electrode. After end-of-life (several years), the injectable battery regenerated by (c) removing the spent semi-solid electrodes, (d-e) having the cell ready for injecting fresh one. _____	76
Figure 4 - 4. Schematic representation of the cell design of the Zn – LiFePO <sub>4</sub> injectable battery. _____	78

Figure 4 - 5. (a) Photograph of a semi-solid electrode. (b) Voltage profile of an injected Zn – LiFePO <sub>4</sub> battery in the 1 <sup>st</sup> and 50 <sup>th</sup> cycle for the initial battery and after 4 subsequent regenerations (R1, R2, R3 and R4) at 1C (2.5 mA cm <sup>-2</sup> ). (c) Variation of the internal resistance of the injectable battery with respect to initial value when semi-solid electrodes are substituted.	79
Figure 4 - 6. Schematic representation of the cell design of the aqueous super-concentrated Zn – LiFePO <sub>4</sub> , FePO <sub>4</sub> – LiFePO <sub>4</sub> and LiTi <sub>2</sub> (PO <sub>4</sub> ) <sub>3</sub> – LiFePO <sub>4</sub> injectable battery.	80
Figure 4 - 7. (a) Voltage profile and (b) evolution of the areal capacity with cycles for the super-concentration Zn – LiFePO <sub>4</sub> injectable battery in 21 m LiTFSI and 1 m ZnTFSI.	80
Figure 4 - 8. (a) Voltage profile and (b) evolution of the areal capacity with cycles for the LiTi <sub>2</sub> (PO <sub>4</sub> ) <sub>3</sub> – LiFePO <sub>4</sub> injectable battery.	81
Figure 4 - 9. Energy and coulombic efficiency of aqueous (a) LiTi <sub>2</sub> (PO <sub>4</sub> ) <sub>3</sub> – LiFePO <sub>4</sub> and (b) super-concentrated Zn - LiFePO <sub>4</sub> injectable battery operated at 1 mA cm <sup>-2</sup> and 2 mA cm <sup>-2</sup> , respectively.	82
Figure 4 - 10. Voltage profile and differential voltage curves of the aqueous FePO <sub>4</sub> – LiFePO <sub>4</sub> injectable battery for the 1 <sup>st</sup> and 300 <sup>th</sup> cycle at 2 mA cm <sup>-2</sup> . Electrode thickness: 2 mm and 1 mm for FePO <sub>4</sub> and LiFePO <sub>4</sub> semi-solid electrode, respectively.	84
Figure 4 - 11. Comparison of capacity retentions for the LiTi <sub>2</sub> (PO <sub>4</sub> ) <sub>3</sub> – LiFePO <sub>4</sub> , the super-concentrated Zn – LiFePO <sub>4</sub> and the FePO <sub>4</sub> – LiFePO <sub>4</sub> injectable batteries. An average capacity decay of 0.15, 0.13 and 0.08 % cycle <sup>-1</sup> , respectively, was calculated for the last 200 cycles.	84
Figure 4 - 12. Voltage profile of a FePO <sub>4</sub> – LiFePO <sub>4</sub> injected battery with an electrode porosity of 70 vol% cycled at C/14 (1 mA cm <sup>-2</sup> ) reaching a utilization rate of LiFePO <sub>4</sub> of 140 mAh g <sup>-1</sup> for the limiting side (the 1 mm-thick electrode vs the 2 mm-thick electrode).	88
Figure 4 - 13. Normalized voltage profile of a FePO <sub>4</sub> – LiFePO <sub>4</sub> injected battery with low electrode porosity (70 vol%) cycled at 1 mA cm <sup>-2</sup> and high electrode porosity (90 vol%) at 2 mA cm <sup>-2</sup> .	88
Figure 4 - 14. (a) Contributions of different elements to the cost of materials for the aqueous LiTi <sub>2</sub> (PO <sub>4</sub> ) <sub>3</sub> – LiFePO <sub>4</sub> battery. (b) Evolution of the contribution of inactive materials, which represents the reduction in battery costs, as a function of the active materials cost for an aqueous battery (neutral pH electrolyte). The values were calculated using prices of materials shown in Table 4-2.	89
Figure 4 - 15. Evolution of cost of materials as a function of the areal capacity and electrode porosity for an aqueous LiTi <sub>2</sub> (PO <sub>4</sub> ) <sub>3</sub> – LiFePO <sub>4</sub> battery.	93
Figure 4 - 16. Evolution of (a) energy density and (b) specific energy as a function of the areal capacity and electrode porosity for the aqueous LiTi <sub>2</sub> (PO <sub>4</sub> ) <sub>3</sub> – LiFePO <sub>4</sub> .	94
Figure 4 - 17. Schematic representation of the cell design of the non-aqueous Li – LiFePO <sub>4</sub> injectable battery.	95

Figure 4 - 18. (a) Voltage profile and (b) evolution of the area capacity with cycles for 4 subsequent regenerations for the non-aqueous Li – LiFePO <sub>4</sub> injectable battery electrode. ____	96
Figure 4 - 19. Energy and coulombic efficiency of Li - LiFePO <sub>4</sub> 0.3 mA cm <sup>-2</sup> . _____	97
Figure 4 - 20. Contributions of different elements to the cost of materials for a non-aqueous Li – LiFePO <sub>4</sub> battery. _____	98
Figure 4 - 21. Evolution of (a) Energy density and (b) Specific energy as a function of the areal capacity and electrode porosity for a non-aqueous Li – LiFePO <sub>4</sub> battery. _____	98

## **Tables**

Table 4 - 1. Comparison of electrochemical performance of state-of-the-art aqueous LiFePO <sub>4</sub> -based batteries. _____	86
Table 4 - 2. Prices of materials for the analysis of costs _____	91

## **Chapter 5. Implementation of injectable semi-solid electrodes for an ultra-low-cost aqueous battery chemistry: The injectable Zn-MnO<sub>2</sub> battery**

### **Figures**

Figure 5 - 1 Cyclability test of an injectable Zn – MnO <sub>2</sub> battery using semi-solid electrodes at 0.5 C. _____	112
Figure 5 - 2 Scheme of the battery cell design for the hybrid-flow injectable Zn - MnO <sub>2</sub> battery. _____	114
Figure 5 - 3 Internal design of the cell. _____	115
Figure 5 - 4 (a) Cyclability test of the hybrid system: injected MnO <sub>2</sub> - Zn-foil with electrolyte flow. (b) Voltage profiles of 1 <sup>st</sup> , 250 <sup>th</sup> and 500 <sup>th</sup> cycles. _____	116
Figure 5 - 5 Photograph of the negative zinc electrode after 500 cycles. _____	117
Figure 5 - 6 (a) Scheme of the Zn-MnO <sub>2</sub> cell assembled in a UV-Vis Cuvette. (b) Picture of the cell filled with electrolyte containing pH indicator. Green color indicates that the pH value is between 3 and 5. _____	118
Figure 5 - 7 Spontaneous evolution of the electrolyte pH without the application of an external bias. _____	119
Figure 5 - 8. Pictures of evaluation of a solution when Zn particles are added. _____	120
Figure 5 - 9. Pictures of the cuvette cell after open circuit voltage (left) and when a constant voltage of 1.7 V, 1.8 V, 1.9 V and 2.0 V was applied to the cell. Zn foil and MnO <sub>2</sub> electrode are located at the left and right side of the cuvette. Right: scheme of the electrochemical reaction taking place at the positive electrode. _____	123

*Figure 5 - 10. Accumulated charge consumed with time when a constant voltage of 1.8 V is applied during one hour in four systems: Graphite as positive electrode with (blue) and without (pink)  $Mn^{2+}$  additive in the electrolyte, and  $MnO_2$  electrode as positive side with (black) and without (red)  $Mn^{2+}$  additive in the electrolyte.* \_\_\_\_\_ 125

*Figure 5 - 11. Pictures of the electrolyte after a constant voltage of 1.7 V, 1.8 V 1.9 V and 2.0 V was applied for 2 h.* \_\_\_\_\_ 127

*Figure 5 - 12 Evolution of the charge capacity when a float charging protocol is applied (1.8 V for 15 min). Inset: color of the electrolyte at the beginning, after 22 h at open circuit voltage (spontaneous drift towards alkaline values) and after 300 cycles implementing the float charging protocol. Total duration of the experiment was >160 h.* \_\_\_\_\_ 128

*Figure 5 - 13. Coulombic efficiency for a Zn- $MnO_2$  cell when a float charging protocol is applied (1.8 V for 15 min.* \_\_\_\_\_ 129

*Figure 5 - 14. Voltage profiles for full cycles when a float charging protocol is applied (1.8 V for 15 min).* \_\_\_\_\_ 130

## **Tables**

*Table 5 - 1. Changes in pH for 6 solution (20 mL) before and 2 minutes after the addition of Zn particles.* \_\_\_\_\_ 121

*Table 5 - 2. Volume of electrolyte necessary for long-life battery* \_\_\_\_\_ 122

*Table 5 - 3. Estimation of number of protons spontaneously consumed based on the corrosion rate of Zn, the amount of  $Mn^{2+}$  necessary to correct the pH change, and concentration assuming  $10 \mu L cm^{-2}$  of electrolyte for long-life battery.* \_\_\_\_\_ 126

## **Chapter 6. Semi-flowable Zn semi-solid electrodes as renewable energy carrier for refillable Zn – air batteries**

### **Figures**

*Figure 6 - 1. Design of the semi-solid Zn-air device fabricated using 3-D Fused Deposition Modeling Printing. (a) Packed cell (negative end-plate view). (b) Packed cell (positive end-plate view). (c) Internal part of the cell.* \_\_\_\_\_ 146

*Figure 6 - 2. (a) Electrical and ionic resistivities of semi-solid electrodes containing different carbon contents (10, 30, 50, 70, 90  $mg \cdot mL^{-1}$ ) (b) Schematic representation of the working principle of the mechanically-rechargeable semi-solid Zn-Air battery. (i) A pre-assembled electrochemical cell is filled with flowable semi-solid Zn electrode. (ii) The cell is sealed and ready to deliver energy in static (non-flow) configuration. (iii) The sealed cell reaches full state of discharge. (iv) The spent semi-solid Zn electrode is removed from the cell, which is then*

- ready to be refilled in step (i). (c) Voltage profile of 5 subsequent refilling using a semi-solid electrode containing 0.1 kgZn Lelectrode – 1 in 6 M KOH. \_\_\_\_\_ 147
- Figure 6 - 3. Removal of the semi-solid electrode from a filled battery cell. (i) Initially, the cell is filled with a semi-solid electrode. (ii) Air pressure is applied inside the cell through the one of the inlets, and the semi-solid electrode starts to come out of the cell. (iii) Finally, all the spent semi-solid electrode is removed from the cell, which is then empty and ready for being used again. \_\_\_\_\_ 148
- Figure 6 - 4. Refilling process of a battery cell using semi-solid electrodes. (i) Initially, the cell is empty, and the syringe that contains the semi-solid electrode is connected to the inlet. (ii) Pressure is applied to the syringe and the semi-solid electrode is introduced inside the cell. (iii) Finally, the cell is fulfilled by the semi-solid electrode. It should be noted that a modified version of the cell displayed in Figure 6-1 was used here. The air-breathing electrode is replaced by a glass plate to visualize the filling process of the cavity left inside the cell. \_\_\_\_ 149
- Figure 6 - 5. (a) Voltage profiles of three subsequent injections. (b) Energy density evolution for semi-solid electrodes with different zinc content ( $0.1 \text{ kg}_{\text{Zn}} \text{ L}^{-1}$ ,  $0.33 \text{ kg}_{\text{Zn}} \text{ L}^{-1}$ ,  $1 \text{ kg}_{\text{Zn}} \text{ L}^{-1}$ ,  $2 \text{ kg}_{\text{Zn}} \text{ L}^{-1}$  and  $2.5 \text{ kg}_{\text{Zn}} \text{ L}^{-1}$ ). \_\_\_\_\_ 150
- Figure 6 - 6. Voltage profiles of 100 % discharged batteries with different Zn content. (a)  $0.1 \text{ kg}_{\text{Zn}} \text{ L}^{-1}$  (b)  $0.33 \text{ kg}_{\text{Zn}} \text{ L}^{-1}$  (c)  $1 \text{ kg}_{\text{Zn}} \text{ L}^{-1}$  (d)  $2 \text{ kg}_{\text{Zn}} \text{ L}^{-1}$  (e)  $2.5 \text{ kg}_{\text{Zn}} \text{ L}^{-1}$ . \_\_\_\_\_ 151
- Figure 6 - 7. X-ray computed tomography (a) Cross section of semi-solid electrodes at different Depth-Of-Discharge (0 %, 50 % and 100 %). (b) Top-view of electrodes at different semi-solid heights (top, bottom, and middle) with different DOD. (c) Cross section of two electrodes with different Zn content ( $1 \text{ kg}_{\text{Zn}} \text{ L}^{-1}$  and  $2 \text{ kg}_{\text{Zn}} \text{ L}^{-1}$ ) at 100 % DOD. \_\_\_\_\_ 152
- Figure 6 - 8. Performance of semi-solid electrodes with different formulation in terms of (a) Evolution of the operating voltage (b) Evolution of the specific power with the applied current density for a Zn content of  $0.5 \text{ kg} \text{ L}^{-1}$ . \_\_\_\_\_ 154
- Figure 6 - 9. Voltage profile of a galvanostatic intermittent titration technique measurement at  $20 \text{ mA cm}^{-2}$  for a semi-solid electrode containing  $1 \text{ Kg}_{\text{Zn}} \text{ L}^{-1}$  and  $70 \text{ g}_{\text{C}} \text{ L}^{-1}$ , and (b) the resulting evolution of the internal resistance with the depth of discharge. \_\_\_\_\_ 155
- Figure 6 - 10 Voltage profile of a Zn – air cell using a semi-solid electrode that contains  $0.5 \text{ kg}_{\text{Zn}} \text{ Lelectrode} - 1$  and  $60 \text{ mg}_{\text{C}} \cdot \text{mL}^{-1}$  at different current densities: 1, 2, 4, 6, 8, 10, 15, 20, 25, 30, 35, 40, 50, 60 and  $77 \text{ mA} \cdot \text{cm}^{-2}$  (a) and the voltage efficiency (b). Voltage profile of a Zn – air cell using a semi-solid electrode that contains  $0.5 \text{ kg}_{\text{Zn}} \text{ Lelectrode} - 1$  and  $70 \text{ mg}_{\text{C}} \cdot \text{mL}^{-1}$  at different current densities: 1, 2, 4, 6, 8, 10, 15, 20, 25, 30, 35, 40, 50, 60, 77 and  $83 \text{ mA} \cdot \text{cm}^{-2}$  (c) and the voltaic efficiency (d). Voltage profile of a Zn – air cell using a semi-solid electrode that contains  $0.5 \text{ kg}_{\text{Zn}} \text{ Lelectrode} - 1$  and  $80 \text{ mg}_{\text{C}} \cdot \text{mL}^{-1}$  at different current densities: 1, 2, 4, 6, 8, 10, 15, 20, 25, 30, 35, 40, 50, 60, 70, 80, 90 and  $100 \text{ mA} \cdot \text{cm}^{-2}$  (e) and the voltaic efficiency (f). \_\_\_\_\_ 156

<i>Figure 6 - 11. Voltage profile of a Zn-Air battery using stainless steel as current collector. _</i>	<i>157</i>
<i>Figure 6 - 12 Evolution of power cost with current density_____</i>	<i>158</i>
<i>Figure 6 - 13. (a) Scheme of 2,6-dihydroxyanthraquinone acting as molecular wiring for mechanically rechargeable semi-solid Zinc-Air battery. (b) Comparison of the operating voltage when 2,6-dihydroxyanthraquinone is included into the formulation of the electrode. 160</i>	
<i>Figure 6 - 14. Theoretical estimation of energy density for Zn-Air batteries using semi-solid electrodes. Comparison between two different Zinc content in the electrode: (a) and (b) for 2 kg<sub>zn</sub> L<sup>-1</sup>, and (c) and (d) for 3 kg<sub>zn</sub> L<sup>-1</sup>. Thickness of Celgard separator and stainless-steel current collector are 25µm and 12µm, respectively. _____</i>	<i>162</i>
<i>Figure 6 - 15. (a) Scheme of metallic zinc as energy carrier used in mechanically-rechargeable Zn-Air batteries. (b) Results of experiments for determining the amount of zinc that remains when it is store in different media: Argon, Air and Air with 2,6-DHAQ. _____</i>	<i>164</i>

## **Chapter 7. Regenerative electrochemical ion pumping cell based on semi-solid electrodes for sustainable Li recovery**

### **Figures**

<i>Figure 7 - 1. XRD pattern of Potassium Nickel Hexacyanoferrate (KNi[Fe(CN)<sub>6</sub>]) matching the diffraction previously reported for this materials. <sup>26</sup> _____</i>	<i>177</i>
<i>Figure 7 - 2. Flow diagram of Ion Pumping Injectable Cell 1. 3D Printed ABS Endplate; 2. Graphite Current Collector; 3. Viton Gasket; 4. Microporous Separator C3501; 5. Anion Exchange Membrane (AEM)._____</i>	<i>179</i>
<i>Figure 7 - 3. Flow diagram Membrane Free Ion Pumping Injectable Cell 1. 3D Printed ABS Endplate; 2. Graphite Current Collector; 3 and 4. Viton Gasket; 5. Microporous Separator C3501. _____</i>	<i>180</i>
<i>Figure 7 - 4. Illustration of two operating modes for the EIPC for the first half-cycle resulting in the concentration of Li-ions. (a). EIPC with ion-selective exchange membrane (b) Membrane free EIPC._____</i>	<i>184</i>
<i>Figure 7 - 5. Process of substitution (injection and dejection) of the semi-solid electrodes into a pre-assembled cell for their use in ion pumping applications. _____</i>	<i>185</i>
<i>Figure 7 - 6. Pictures of (a) the different components of the Regenerative Electrochemical Ion Pumping Cell (3D Printed ABS Endplate, Graphite Current Collector, Viton Gasket, Microporous Separator C350, Anion Exchange Membrane (AEM), (b) regeneration process by</i>	

<i>dejection / injection of semi-solid electrode from / into the assembled REIP cell, (c) operating REIP system.</i>	186
<i>Figure 7 - 7. Performance of the REIPC LFP-FP cell. (a) after several injections and reinjections with activated carbon and LFP. (b) Comparison between capacitive (Activated Carbon-Activated Carbon, red line) and Faradaic (LFP-FP, black line) REIPC Cells.</i>	188
<i>Figure 7 - 8. Cycling experiment probing the stability of the system. Note that noisy coulombic efficiency is attributed to the temperature fluctuations during this experiment. Temperature affects ionic conductivity. At lower temperature, the cycle process may be finished before it is complete due to the overpotential induced by the higher ionic resistance. The following cycle, the cell starts partially charged, so that it consumes less charge during charging process, while it releases more charge during discharge process due to the accumulated charge in the previous cycle.</i>	190
<i>Figure 7 - 9. Contribution of different elements to cost of a REIPC: inactive and active materials.</i>	191
<i>Figure 7 - 10. Installation costs per area of device as a function of the areal capacity.</i>	192
<i>Figure 7 - 11. Installation cost per Kg of Li as a function of the areal capacity.</i>	192
<i>Figure 7 - 12. Operational costs of the system per kg of lithium recovered as a function of the current density.</i>	193
<i>Figure 7 - 13. (a) Voltage profile and (b) cyclability test of the REIPC using an asymmetrical system (LFP-MO).</i>	195
<i>Figure 7 - 14. Graphical explanation for the movement of the ions (<math>Cl^-</math> and <math>Li^+</math>) in the REIPC system with symmetrical LFP configuration. (a-c) Charging process, concentration of the solution in the positive side and dilution in the negative. (c-e) Discharging process, dilution of the solution in the negative side and concentration in the positive.</i>	196
<i>Figure 7 - 15. Evolution of cell voltage and ionic conductivity of the symmetrical REIPC during (a) one full cycle and (b) ca. 20 h. Blue triangles and red circles represent the conductivity difference values in each one of the compartments at the end of each one of the charging/discharging cycles.</i>	197
<i>Figure 7 - 16. Experiment showing the permeability of the anion exchange membrane to the lithium ions.</i>	199

Figure 7 - 17. Graphical explanation for the movement of the ions ( $\text{Na}^+$  and  $\text{Li}^+$ ) in the MF-REIPC system with LMO-NiHCF electrodes. (a-c) Charging process, concentration of lithium ions in the solution. (c-e) Discharging process, concentration of sodium ions in the solution. 201

Figure 7 - 18. (a) Evolution of the areal capacity of the MFREIPC MO-NiHCF cell with the number of cycles. Regenerations were conducted in cycle 28 (carbon-based semi-solid electrode replaced NiHCF semi-solid electrode) and cycle 52 (fresh semi-solid electrodes). (b) Comparison between capacitive (Activated Carbon-Activated Carbon, red line) and Faradaic (MO-NiHCF, black line) MF-REIPC. \_\_\_\_\_ 202

Figure 7 - 19. Cycling experiment probing the stability of the MF-REIPC system after being regenerated. \_\_\_\_\_ 203

Figure 7 - 20. Experimental selectivity coefficient obtained as a function the concentration ratio of Li-Na. \_\_\_\_\_ 204

Figure 7 - 21. Efficiencies obtained with MF-REIPC (a) Effect of the Na:Li ions ratio in the solution for a current density of  $0.5 \text{ mA}\cdot\text{cm}^{-2}$  (b) Effect of the current density for a Na:Li ratio of 2.5:1 (c) Impact of the presence of additional cations on Lithium capturing using Atacama brine solution. Charge steps were carried out at constant current density to avoid potential interfering of oxygen evolution reaction, so that the influence of the current density on the efficiency process was evaluated for the discharge step. \_\_\_\_\_ 205

## **Tables**

Table 7 - 1. Comparison between this work and others state-of-the-art systems. \_\_\_\_\_ 206



## **Appendix C. Acronyms**

2,6-DHAQ	2,6-Dihydroxyanthraquinone
ABS	Acrylonitrile Butadiene Styrene
AAC	Adsorption Areal Capacity
AC	Alternating Current
$I_0$	Amplitude of Sinusoidal Current Signal
$E_0$	Amplitude of Sinusoidal Voltage Signal
$\omega$	Angular Frequency
AEM	Anionic Exchange Membrane
$\alpha$	Bruggeman Coefficient
C	Capacitance
CAPEX	Capital Cost
Q	Charge consumed
CAES	Compressed Air Energy Storage
$\gamma$	Correcting Parameter for Bruggeman Equation
I	Current
DOD	Depth of Discharge
$D_0$	Diffusion Coefficient
$D_{\text{eff}}$	Effective Diffusion Coefficient
$\eta$	Efficiency of the System (REIPC)
EDL	Electrical Double Layer
$R_e$	Electrical Resistance
EIS	Electrochemical Impedance Spectroscopy
EIPC	Electrochemical Ion Pumping Cell
CE	Electrostatic Capacitors
F	Faraday Constant
$C_f$	Final Concentration
f	Frequency
FDM	Fused Deposition Modelling
HER	Hydrogen Evolution Reaction
$Z''$	Imaginary part of Impedance
Z	Impedance
L	Inductance

$C_i$	Initial Concentration
IEA	International Energy Agency
IC	Ion Chromatography
$R_i$	Ionic Resistance
FP	Iron Phosphate
KPI	Key Performance Indicator
LiTFSI	Lithium (I) bis(trifluoromethanesulfonyl)imide
$SAC_{Li}$	Lithium Adsorption Capacity
LCE	Lithium Carbonate Equivalent
LFP	Lithium Iron Phosphate
LMO	Lithium Manganese Oxide
$R_{li}$	Lithium recovery Rate
LTP	Lithium Titanium phosphate
LAB	Lithium-Air Battery
LIB	Lithium-Ion Battery
LSB	Lithium-Sulfur Battery
MO	Manganese Oxide
MF-REIPC	Membrane-Free Regenerative Electrochemical Ion Pumping Cell
$E_{ocv}$	Open Circuit Voltage
OPEX	Operational Cost
OER	Oxygen Evolution Reaction
$\phi$	Phase Shift
PTFE	Polytetrafluoroethylene
$\varepsilon$	Porosity
NiHCF	Potassium Nickel Hexacyanoferrate
$Z'$	Real part of Impedance
REIPC	Regenerative Electrochemical Ion Pumping Cell
R	Resistance
$K_{LiNa}$	Selectivity Coefficient of Li vs Na
SIB	Sodium-Ion Battery
SSB	Solid-State Battery
SHE	Standard Hydrogen Electrode

## Appendix C. Acronyms

SMES	Superconducting Magnetic Energy Storage
SNG	Synthetic Natural Gas
TES	Thermal Energy Storage
$\tau$	Tortuosity
UPS	Uninterrupted Power Supply
E	Voltage
V	Volume of Electrolyte
ZnTFSI	Zinc (II) bis(trifluoromethanesulfonyl)imide
ZAFC	Zinc-Air Fuel Cell

